University of Massachusetts Amherst
ScholarWorks@UMass Amherst

Doctoral Dissertations 1896 - February 2014

1-1-1989

The Sagittarius B2 molecular cloud : an extreme case of a galactic center giant molecular cloud.

Dariusz C. Lis
University of Massachusetts Amherst

Follow this and additional works at: https://scholarworks.umass.edu/dissertations_1

Recommended Citation

Lis, Dariusz C., "The Sagittarius B2 molecular cloud : an extreme case of a galactic center giant molecular cloud." (1989). *Doctoral Dissertations 1896 - February 2014*. 1767.
https://scholarworks.umass.edu/dissertations_1/1767

This Open Access Dissertation is brought to you for free and open access by ScholarWorks@UMass Amherst. It has been accepted for inclusion in Doctoral Dissertations 1896 - February 2014 by an authorized administrator of ScholarWorks@UMass Amherst. For more information, please contact scholarworks@library.umass.edu.

UMASS/AMHERST
312066007581529

THE SAGITTARIUS B2 MOLECULAR CLOUD
AN EXTREME CASE OF A GALACTIC CENTER GIANT MOLECULAR CLOUD

A Dissertation Presented

by

DARIUSZ C. LIS

Submitted to the Graduate School of the
University of Massachusetts in partial fulfilment
of the requirements for the degree of

DOCTOR OF PHILOSOPHY

May 1989

Department of Physics and Astronomy

© Copyright by Dariusz C. Lis 1989

All Rights Reserved

THE SAGITTARIUS B2 MOLECULAR CLOUD
AN EXTREME CASE OF A GALACTIC CENTER
GIANT MOLECULAR CLOUD

A Dissertation Presented

by

DARIUSZ C. LIS

Approved as to style and content by:

Paul F. Goldsmith, Chairman

William M. Irvine

John Y. Kwan

Robert L. Dickman

R. Krotkov

Robert V. Krotkov

Robert B. Hallock

Robert B. Hallock, Department Head
Department of Physics and Astronomy

ACKNOWLEDGMENTS

It has been a pleasure to be associated for almost four years with the staff of the Five College Radio Astronomy Observatory. My time spent at FCRAO was not only intellectually stimulating, but enjoyable as well. I especially would like to thank my advisor, Paul Goldsmith, who suggested my thesis project and while being extremely helpful, allowed me a large degree of independence in carrying it out. I would like to thank Bill Irvine, who invited me to Amherst for the summer of 1985, for his continuous support of my graduate research, as well as for observing and meeting related travel funds. I also would like to thank Bob Dickman for his patience in solving problems which occurred during my late night observing at Quabbin. All my committee members contributed valuable suggestions to this work. My special thanks go to Susan Kleinmann for her help with Eroff and to Chun Ming Leung for providing me with his continuum radiation transfer code. Part of this Research was conducted using Cornell National Supercomputer Facility, a resource of the Center for Theory and Stimulation in Science and Engineering at Cornell University.

ABSTRACT

THE SAGITTARIUS B2 MOLECULAR CLOUD AN EXTREME CASE OF A GALACTIC CENTER GIANT MOLECULAR CLOUD

MAY 1989

DARIUSZ C. LIS

Ph.D., UNIVERSITY OF MASSACHUSETTS

Directed by: Paul F. Goldsmith

I develop a model of the Sagittarius B2 molecular cloud based on the $J=1\rightarrow0$ and $2\rightarrow1$ transitions of ^{13}CO and $C^{18}O$, as well as on the far-infrared and submillimeter continuum emission from the dust, in order to determine the physical conditions in this source. The total mass of the cloud is dominated by an envelope which consists of a constant density component and a power law component with a radial exponent of -2. The virial mass of the cloud is a factor of ~ 2 higher than the molecular mass, suggesting that Sgr B2 is close to virial equilibrium. The Sgr B2(M) and (N) continuum sources are situated inside small dense cores embedded in the extended clouds. The middle source is much more luminous than the northern source. The observed change in the middle-to-north peak flux ratio between 350 μ and 1300 μ is primarily a result of the difference in luminosity. In order to compare Sgr B2 with other Galactic Center clouds I observed the $J=1\rightarrow0$ transition of ^{13}CO in two selected Galactic Center fields centered on the G1.1-0.1 and G359.4-0.1 continuum sources. The molecular clouds observed there seem to be distinctively different from Sgr B2. They have similar sizes, but their mean H_2 densities, column densities and masses are a factor of ~ 3 lower than in Sgr B2. The relatively dense gas present over the inner several pc of Sgr B2 seems to be absent in other Galactic Center clouds. The far-infrared optical depth is also reported to be low, suggesting that very dense cores with embedded continuum sources similar to Sgr B2(M) and (N) do not exist in these objects. The disruptive tidal forces acting on all the clouds have similar magnitude. Sgr B2, however, seems to be much closer to the tidally limited density. The smaller Galactic Center clouds, although not as dense as Sgr B2, are distinctively different from the disk clouds in terms of line width and mean density. The high density seems to be a common characteristic of all Galactic Center GMCs. It may simply reflect the higher density of the interstellar medium from which the clouds formed.

TABLE OF CONTENTS

ACKNOWLEDGEMENTS.......... iv
ABSTRACT.......... v
LIST OF TABLES.......... viii
LIST OF FIGURES.......... ix

CHAPTER

I. INTRODUCTION.......... 1

II. CO ISOTOPE STUDIES AND MASS OF THE EXTENDED CLOUD.. 4
- A. Observations.......... 4
- B. Molecular Abundances.......... 5
- C. Molecular Mass and Density Distribution.......... 9
- D. Dynamical Mass and Virial Equilibrium.......... 12
- E. Conclusion.......... 17

III. CONTINUUM STUDIES OF THE CORE.......... 50
- A. Observations.......... 51
- B. Model of Sgr B2(M).......... 55
- C. Model of Sgr B2(N).......... 61
- D. Comparison with Constant Temperature Analysis.......... 62
- E. Conclusion.......... 65

IV. MULTITRANSITION CO ISOTOPE STUDIES.......... 105
- A. Observations.......... 105
- B. Monte Carlo Simulations.......... 109
- C. Thermal Balance.......... 112
- D. Final Models.......... 116
- E. Conclusion.......... 120

V. CONDITIONS IN THE CORE OF THE CLOUD.......... 178
- A. HC_3N in Ground Vibrational State.......... 178
- B. Vibrationally Excited HC_3N.......... 186
- C. Conclusion.......... 189

VI. COMPARISON WITH OTHER GALACTIC CENTER CLOUDS.......... 231
- A. Observations.......... 231
- B. G1.1-0.1.......... 232
- C. G359.4-0.1.......... 235
- D. Conclusion.......... 237

VII. CONCLUSION.......... 269

APPENDIX: DETAILS OF THE DUST MODEL CALCULATIONS.......... 274

BIBLIOGRAPHY.......... 276

LIST OF TABLES

2.1 Line Parameters of ^{13}CO $J = 1 \rightarrow 0$ emission in Sgr B2 19

2.2 Line Parameters of $C^{18}O$ $J = 1 \rightarrow 0$ emission in Sgr B2 26

2.3 Density Distribution in Sgr B2 Envelope 30

2.4 Sgr B2 Mass Estimates by Different Methods 31

3.1 JCMT Beam Sizes and Calibration Factors 68

3.2 Observed Flux Densities from Sgr B2(M) 69

3.3 Observed Flux Densities from Sgr B2(M) 70

3.4 Observed Middle-to-North Peak Flux Ratios 71

3.5 Model Parameters for Models of Sgr B2(M) Core 72

3.6 Predicted Fluxes from Model Clouds Given in Table 3.5 73

3.7 Model Parameters for Models of Sgr B2(M) Core 74

3.8 Combined Models of Sgr B2 75

3.9 Column Densities at the Position of Sgr B2(M) 76

4.1 Line Parameters of ^{13}CO $J = 2 \rightarrow 1$ Emission in Sgr B2 122

4.2 Line Parameters of $C^{18}O$ $J = 2 \rightarrow 1$ Emission in Sgr B2 124

4.3 Line Parameters of ^{13}CO and ^{12}CO $J = 3 \rightarrow 2$ Emission in Sgr B2 125

4.4 Line Parameters of ^{12}CO $J = 1 \rightarrow 0$ Emission in Sgr B2 126

4.5 Summary of CO Isotope Observations of Sgr B2 127

4.6 Monte Carlo Predictions for $T_g = T_d$ 128

4.7 Parameters of Final Cloud Models 129

5.1 Line Parameters of HC_3N $J = 5 \rightarrow 4$ Emission in Sgr B2 192

5.2 Line Parameters of HC_3N $J = 12 \rightarrow 11$ emission in Sgr B2 193

5.3 HC_3N Excitation Temperatures and Column Densities 195

5.4 Results of Statistical Equilibrium Calculations 196

5.5 Frequencies, Energies and Line Strengths of Observed Lines 197

5.6 Integrated Intensities of HC_3N and HNCO Transition 198

6.1 Line Parameters of ^{13}CO $J = 1 \rightarrow 0$ Emission in G1.1-0.1 239

6.2 Line Parameters of ^{13}CO Emission in G359.4-0.1 (A) 241

6.3 Line Parameters of ^{13}CO Emission in G359.4-0.1 (B) 242

LIST OF FIGURES

2.1 A contour map of the ^{13}CO $J = 1 \rightarrow 0$ integrated intensity in Sgr B2............. 32
2.2 ^{13}CO $J = 1 \rightarrow 0$ spectra in Sgr B2.. 34
2.3 A contour map of the C^{18}O $J = 1 \rightarrow 0$ integrated intensity in Sgr B2............. 36
2.4 C^{18}O $J = 1 \rightarrow 0$ spectra in Sgr B2.. 38
2.5 Correlation between ^{13}CO and C^{18}O integrated intensities.......................... 40
2.6 Observed spectra and antenna temperature ratio at the (4,1) position........... 42
2.7 Obseved spectra and antenna temperature ratio at the (0,0) position............ 44
2.8 First mass derivative as function of the projected distance 46
2.9 C^{18}O integrated intensity as a function of the projected distance 48
3.1 A contour map of the 1300 μ continuum emission in Sgr B2........................ 77
3.2 Observed spectrum of the IR emission from Sgr B2..................................... 79
3.3 A contour map of the 1100 μ continuum emission in Sgr B2........................ 81
3.4 A contour map of the 800 μ continuum emission in Sgr B2.......................... 83
3.5 A contour map of the 450 μ continuum emission in Sgr B2.......................... 85
3.6 A contour map of the 350 μ continuum emission in Sgr B2.......................... 87
3.7 The effect of the optical depth on the IR spectrum 89
3.8 The effect of the central luminosity on the IR spectrum............................... 91
3.9 The effect of the central source temperature on the IR spectrum 93
3.10 The effect of the grain emissivity on the IR spectrum 95
3.11 Temperature distribution for Sgr B2 (M) models... 97
3.12 The geometry of Sgr B2 models... 99
3.13 Predicted spectra for constant temperature models.. 101
3.14 Predicted spectra for complete cloud models... 103
4.1 A contour map of the ^{13}CO $J = 2 \rightarrow 1$ integrated intensity in Sgr B2............. 130
4.2 ^{13}CO $J = 2 \rightarrow 1$ integrated intensity for $\Delta\alpha = 0$... 132
4.3 ^{13}CO $J = 2 \rightarrow 1$ spectra in Sgr B2.. 134
4.4 A Contour map of the C^{18}O $J = 2 \rightarrow 1$ integrated intensity in Sgr B2............ 136
4.5 C^{18}O $J = 2 \rightarrow 1$ integrated intensity for $\Delta\alpha = 0$... 138
4.6 C^{18}O $J = 2 \rightarrow 1$ spectra in Sgr B2.. 140
4.7 A contour map of the ^{12}CO $J = 3 \rightarrow 2$ integrated intensity in Sgr B2............. 142

4.8 ^{12}CO $J = 3 \rightarrow 2$ spectra in Sgr B2 144
4.9 ^{13}CO $J = 3 \rightarrow 2$ spectra in Sgr B2 146
4.10 A contour map of the ^{12}CO $J = 1 \rightarrow 0$ integrated intensity in Sgr B2 148
4.11 ^{12}CO $J = 1 \rightarrow 0$ spectra in Sgr B2 150
4.12 Parabolic fit to the cooling rate coefficient a 152
4.13 Parabolic fit to the cooling rate coefficient b 154
4.14 Kinetic temperature for different cooling rates 156
4.15 Kinetic temperature for different turbulent heating rates 158
4.16 Heating rates as a function of the distance from the center 160
4.17 $C^{18}O$ $J = 1 \rightarrow 0$ integrated intensity for MC models 162
4.18 ^{13}CO $J = 1 \rightarrow 0$ integrated intensity for MC models 164
4.19 $C^{18}O$ $J = 2 \rightarrow 1$ integrated intensity for MC models 166
4.20 ^{13}CO $J = 2 \rightarrow 1$ integrated intensity for MC models 168
4.21 ^{13}CO and $C^{18}O$ model spectra 170
4.22 An average excitation temperature as a function of projected distance 172
4.23 Correlation between ^{13}CO and $C^{18}O$ integrated intensities for MC models 174
4.24 ^{13}CO to $C^{18}O$ antenna temperature ratio 176
5.1 A contour map of the HC_3N $J = 5 \rightarrow 4$ integrated intensity in Sgr B2 199
5.2 HC_3N $J = 5 \rightarrow 4$ spectra in Sgr B2 201
5.3 A contour map of the HC_3N $J = 12 \rightarrow 11$ integrated intensity in Sgr B2 203
5.4 HC_3N $J = 12 \rightarrow 11$ spectra in Sgr B2 205
5.5 Contours of constant 12→11 to 5→4 integrated intensity ratio 207
5.6 Integrated intensity ratio as a function of density 209
5.7 Integrated intensity per unit hydrogen column density 211
5.8 A contour map of the SO 2_3-1_2 integrated intensity in Sgr B2 213
5.9 A contour map of HNCO 5_{05}-4_{04} integrated intensity in Sgr B2 215
5.10 HC_3N $J = 12 \rightarrow 11$ spectra in ν_7 (1e) state 217
5.11 HC_3N $J = 12 \rightarrow 11$ spectra in ν_7 (1f) state 219
5.12 HC_3N $J = 12 \rightarrow 11$ spectra in $2\nu_7$ state 221
5.13 A multiple Gaussian fit to the (0,1) spectrum from Figure 5.12 223
5.14 Possible detection of the $J = 12 \rightarrow 11$ HC_3N transition in ν_6 (1e) state 225
5.15 Rotation diagram for HC_3N 227

5.16 Rotation diagram for HNCO 229
6.1 ^{13}CO $J = 1 \rightarrow 0$ spectra in G1.1-0.1 243
6.2 A spatial-velocity map of G1.1-0.1 for a cut with $\Delta\alpha = 0$ 245
6.3 A contour map of ^{13}CO integrated intensity in G1.1-0.1 247
6.4 C^{18}O, ^{13}CO, and ^{12}CO spectra at the (2,10) position in G1.1-0.1 249
6.5 C^{18}O, ^{13}CO, and ^{12}CO spectra at the (10,12) position in G1.1-0.1 251
6.6 Kinetic temperature of the gas for different velocity dispersions 253
6.7 Integrated intensity of ^{13}CO emission in G1.1-0.1 255
6.8 ^{13}CO spectra showing the -120 km s^{-1} component of G359.4-0.1 257
6.9 The -120 km s^{-1} component of G359.4-0.1 259
6.10 C^{18}O, ^{13}CO, and ^{12}CO spectra at the (-2,4) position in G359.4-0.1 261
6.11 ^{13}CO spectra showing the -45 M component of G359.4-0.1 263
6.12 The -45 km s^{-1} component of G359.4-0.1 265
6.13 C^{18}O, ^{13}CO, and ^{12}CO spectra at the (4,2) position in G359.4-0.1 267

CHAPTER I

INTRODUCTION

Giant Molecular Clouds are a major mass component of the interstellar medium, and have a fundamental influence on galactic evolution, as it appears that all massive star formation occurring at the present time is associated with them (Blitz 1980). There are ~ 3000 - 4000 GMCs in the molecular ring between 4 and 8 kpc from the Galactic Center. A typical size of a GMC complex, approximately 40 pc, and a typical mass of 5×10^5 $M_\odot$, yield an average H_2 density of ~ 300 cm^{-3} (Solomon and Sanders 1980). The highest concentration of molecular material occurs at the Galactic Center. Possibly due to strong tidal forces caused by high mass concentration, the clouds there have densities and masses much higher than the values characteristic of constituents of the galactic disk. Several of them (Scoville 1980) have masses exceeding 10^6 $M_\odot$, diameters in the range 50 - 100 pc, and infrared luminosities of ~ 10^7 $L_\odot$. The total mass of the GMC complex at the Galactic Center is estimated to be ~ 5×10^7 $M_\odot$, approximately 10 times the total mass of HI in the nuclear disk (~ 2 kpc in diameter).

The Galactic Center region has been a target of extensive continuum and molecular line studies. Radio continuum data often have impressive resolution and sensitivity (Downes *et al.* 1976). Molecular data, however, is limited to surveys with typical resolution of ~ 6′ corresponding to 15 pc at a distance of 8.5 kpc (Bally *et al.* 1986, Heiligman 1987, Dame *et al.* 1987). Detailed studies of Galactic Center GMCs other than Sgr B2 with high angular resolution have never been undertaken. Even in the best studied case of Sgr B2, the data is mostly limited to several characteristic positions within the cloud.

The giant molecular cloud associated with the compact H II region Sgr B2 is a prototype of Galactic Center clouds. Situated ~ 120 pc from the Galactic Center, it represents an extreme case of a molecular cloud in terms of mass and column density. Nearly half of the known interstellar molecules were first detected toward this source, and almost all of them were later observed there. Molecular studies of Scoville, Solomon, and Penzias (1975) revealed the existence of a moderately dense region, ~ 45 pc in diameter, with an average H_2 density of ~ 1250 cm^{-3} traced out by CO emission. A variety of different molecular species are observed in a 5 pc diameter core with an average density of ~ 10^5 cm^{-3}, elongated parallel to the galactic plane (Cummins, Linke, and Thaddeus 1986). Radio continuum studies (Benson and Johnston 1984) show ~ 10 compact H II regions distributed in three groups: northern (N), middle (M), and southern (S). Sgr B2 is also a strong source of infrared emission (Harvey, Campbell, and Hoffmann 1977; Righini, Joyce, and Simon 1976; Gatley *et al.* 1977). This is powered by massive young stars which also maintain ionized regions. The total number of Lyman continuum photons from the northern and middle sources is estimated to be in excess of 10^{50} s^{-1} (Garey 1986). One of the most interesting results of the early high resolution continuum studies of Sgr B2 is a striking difference between distribution of the 53 μ continuum emission (Harvey, Campbell, and Hoffman 1977) and the 1300 μ continuum emission (Goldsmith, Snell, and Lis 1987). The 1300 μ emission peaks at the position of Sgr B2(N), where no excess 53 μ emission is observed. It has been suggested that the observed change in the middle-to-north peak flux ratio is caused by the fact that the northern source is situated behind the dust cloud associated with Sgr B2(M), and that its emission is, therefore, attenuated by cold foreground dust (Thronson and Harper 1986; Goldsmith, Snell, and Lis 1987).

The goal of this project is to develop a model of the Sgr B2 molecular cloud consistent with the molecular line and continuum data, as well as to determine the influence of the Galactic Center environment on the structure of GMCs in this region. Because of the complex structure of Sgr B2, the model is developed iteratively. Based on the simple analysis of the $J=1\rightarrow0$ transitions of ^{13}CO and $C^{18}O$, the density distribution in the envelope is first derived in Chapter II. Because of its low dipole moment and fractional abundance, $C^{18}O$ turns out to be a very good tracer of the total H_2 column density along the line of sight. The $J=1\rightarrow0$ transition does not trace, however, the very dense and hot gas in the core of the cloud. This is a result of the large partition function and small beam filling factor there. The conditions in the immediate vicinity of the radio continuum sources are, therefore, determined by modeling the submillimeter and millimeter continuum emission from the dust (Chapter III). The dust models give estimates of densities and sizes of the northern and middle cores, as well as luminosities of the continuum sources. The dust emission also allows for independent determination of H_2 column density. An absolute calibration of the density distribution derived in Chapter II can now be carried out. Knowledge of the density, velocity dispersion and dust temperature allows for determination of the kinetic temperature of the gas (Chapter IV). This leads back to the molecular emission. The emission in the $J=1\rightarrow0$ and $2\rightarrow1$ transitions of ^{13}CO and $C^{18}O$ from the models consistent with the continuum data is calculated using the Monte Carlo method and the results are compared with the observational data. Conditions in the central region of the cloud (~ 10 pc in diameter) are determined through the statistical equilibrium analysis of the $J=5\rightarrow4$ and $12\rightarrow11$ transitions of HC_3N in Chapter V. In Chapter VI the the parameters derived from models of molecular line and continuum emission in Sgr B2 are compared with conditions in other Galactic Center clouds based on the $J=1\rightarrow0$ observations of ^{13}CO. The results of this work are summarized in Chapter VII.

CHAPTER II

CO ISOTOPE STUDIES AND MASS OF THE EXTENDED CLOUD

In the present chapter I address the issues of molecular abundances in the Sgr B2 cloud, as well as the density distribution and molecular and dynamical masses of the complex. Due to the low permanent dipole moment of the CO isotopes, their rotational transitions are easily thermalized by collisions even at relatively low densities, and the emission provides information about the bulk of molecular material distributed along the line-of-sight. This property together with their relatively low optical depth makes ^{13}CO and $C^{18}O$ particularly useful for studying the extended cloud, ~ 45 pc in diameter, with an average H_2 density of ~ 2500 cm^{-3}. Molecules with higher dipole moments are excited only at the relatively high densities characteristic of the central region, which is ~ 10 pc in diameter.

A. Observations

The original set of data was taken between October and December 1986, using the 14 m FCRAO radome enclosed telescope at New Salem, Massachusetts. Additional ^{13}CO data were taken in May and June 1988 in order to extend the existing map and fully sample the center of the cloud. The receiver system employed a cooled Schottky barrier diode mixer and a quasi-optical single sideband filter with cold image termination. The typical system temperature (referred to above the Earth's atmosphere) at the low elevations characteristic of Sgr B2 was 800 K (SSB). Saturn was used for pointing and calibration. The beam efficiency (product of the forward scattering and spillover efficiency and the coupling efficiency to a uniform source filling the main beam) was determined to be 0.45 at 110 GHz. The ^{13}CO emission (Figures 2.1 and Table 2.1) was observed at 275 positions with 42″ spacing centered on the position of the Sgr B2(M) continuum source ($\alpha_{1950} = 17^h44^m10.5^s$, $\delta_{1950} = -28°22'05''$). The 42″ spacing is equivalent to 1.8 pc, assuming 8.5 kpc for the distance to the Galactic Center (Kerr and Lynden-Bell 1986). The integration time was 90 s for the first set of data and 120 s for the second set of data, giving a typical rms fluctuation level of ~ 0.2 K after smoothing the spectra to 2 km s^{-1} velocity resolution (a typical signal-to-noise ratio of ~ 10:1 for off-center positions, and 30:1 at the cloud center). A sample of five ^{13}CO spectra from a north-south cut is shown in Figure 2.2. The C^{18}O emission (Figures 2.4 and Table 2.2) was observed at 155 positions, having 30″ spacing in the central region and 1′ spacing away from the center. The integration time varied from 300 s to 1500 s depending on weather conditions and intensity of the observed line. A sample of five C^{18}O spectra from a north-south cut is shown in Figure 2.4. Additional high signal-to-noise spectra were obtained at the (0,0) and (4,1) positions (offsets of positions are with respect to Sgr B2(M), in minutes of arc) in order to determine the ^{13}CO to C^{18}O abundance ratio as a function of velocity. At the (0,0) position the rms temperatures achieved for a 3 km s^{-1} velocity resolution element were 0.035 K and 0.026 K for ^{13}CO and C^{18}O respectively. At the (4,1) position the corresponding values were 0.042 K and 0.020 K for 2 km s^{-1} velocity resolution.

B. Molecular Abundances

Because the antenna efficiencies and beam filling factors should be nearly the same for both transitions which differ in frequency by only 420 MHz, the observed intensity ratio is equal to the abundance ratio provided that the ^{13}CO line is optically thin, and both lines are in LTE. The ^{13}CO and C^{18}O integrated intensities (Figure 2.5) show a linear correlation for C^{18}O integrated intensities smaller than ~ 15 K km s^{-1}

(uncorrected for beam efficiency). For higher integrated intensities the curve flattens, indicating saturation of the ^{13}CO line. The effect seems to be important only for positions close to the center of the cloud. The average ^{13}CO to C^{18}O integrated intensity ratio weighted by the inverse of the square of its error for 80 positions with C^{18}O integrated intensities between 5 and 15 K km s^{-1} is 9.0 ± 1.9 . The average unweighted ratio based on the same data is 10.4 ± 2.8 (the errors represent one standard deviation). The results are not very sensitive to the fitting range. The ratios for 110 points with C^{18}O integrated intensities between 0 and 20 K km s^{-1} are 8.7 ± 1.7 and 10.2 ± 3.4, for weighted and unweighted averages respectively.

Knowing the ^{13}CO to C^{18}O intensity ratio in the optically thin case I can correct the ^{13}CO integrated intensities at the center of the cloud for the effect of saturation, as well as estimate a profile average optical depth of ^{13}CO. If R_{obs} is the observed intensity ratio and R_{thin} is the ratio in the optically thin case as derived above, the profile averaged optical depth, τ, is given by

$$\frac{1-\exp(-\tau)}{\tau} = \frac{R_{obs}}{R_{thin}} . \qquad (2.1)$$

The integrated intensity ratio of 6.2 observed at the peak of the emission yields a profile-averaged ^{13}CO optical depth of ~ 1 in the 0 - 100 km s^{-1} velocity range. The conclusion of low ^{13}CO optical depth for off-center positions is further supported by lack of variation in the antenna temperature with LSR velocity. The average ratio over 36 channels with high signal to noise ratio at the (4,1) position (Figure 2.6) is 8.5 ± 1.6, statistically consistent with the previous value. At the (0,0) position (Figure 2.7), on the contrary, the ^{13}CO to C^{18}O ratio drops from 10.1 ± 0.8 in a presumably optically thin component between 80 and 100 km s^{-1} (average over 7 channels with 3 km s^{-1} velocity resolution) to 3.1 at the line center. The line center ^{13}CO optical depth at the peak of the emission is ~ 3. Careful inspection of Figure 2.5 shows that the points with very low $C^{18}O$ integrated intensities tend to lie above the best fit line. Although the observational errors are large due to the low signal-to-noise ratio of the weak $C^{18}O$ lines, the effect could be real and caused by non-LTE excitation of $C^{18}O$ at the edge of the cloud. Because the kinetic temperature in the outer regions of the cloud is still expected to be relatively high, ^{13}C fractionation (*cf.* below) is unlikely to be responsible for the observed effect. Based on the above data, I adopt the value of 9.0 ± 1.9 as the average ^{13}CO to $C^{18}O$ abundance ratio in Sagittarius B2. This value is very close to the galactic plane average of 10 ± 1 (Penzias 1981), as well as to the value of 11.6 ± 1.3 given for Sgr A (Penzias 1980). *cf.*e value of 16 ± 5 in Sgr B2 given by Penzias (1980) seems to be too high, although the large error of this value makes it statistically consistent with our data.

Watson, Anicich and Huntress (1976) and Langer (1976, 1977) have suggested that the ^{13}CO abundance should be enhanced in relatively cold regions by the chemical isotopic fractionation reaction

$$^{12}CO + {}^{13}C^{+} \rightarrow {}^{13}CO + {}^{12}C^{+} \,. \qquad (2.2)$$

The reverse reaction is endothermic ($\Delta E / k = 35$ K) so at low temperatures the abundance of ^{13}CO is enhanced. Since the average kinetic temperature in Sgr B2 is higher than in dark clouds one would expect the ^{12}CO to ^{13}CO fractionation there to be less than in colder disk clouds. A relatively low ^{12}CO to ^{13}CO abundance ratio in Galactic Center clouds (23 compared to 69 in the disk clouds) is indicated by observations (Penzias 1980). Because $C^{18}O$ is not affected by chemical fractionation, a reduced ^{12}CO to ^{13}CO ratio produced by chemical fractionation of ^{13}C should be accompanied by an enhanced ^{13}CO to $C^{18}O$ ratio. The observed constancy of the ^{13}CO to $C^{18}O$ ratio as a function of position within Sgr B2 suggests that the ^{13}C is not fractionated. Isotope fractionation via reaction (2.2) will also be suppressed by the relatively high gas temperatures, greater than 25 K, present throughout Sgr B2 (Scoville, Solomon, and Penzias 1975; Goldsmith, Snell, and Lis 1987).

The peak $C^{18}O$ column density in the $J = 1$ level, within the velocity range 0 to 100 km s^{-1}, is 3×10^{16} cm^{-2}, 77% of this being between 50 and 75 km s^{-1}. The total $C^{18}O$ column density (0-100 km s^{-1}) is 1×10^{17} cm^{-2} assuming 20 K for an average excitation temperature along the line-of-sight. The total ^{13}CO column density is determined to be 9×10^{17} cm^{-2}, assuming the same excitation temperature, and the ^{13}CO to $C^{18}O$ abundance ratio of 9 as derived above.

The H_2 column density at the same position derived from the 1300 μ continuum data (Goldsmith, Snell, and Lis 1987) is 2.2×10^{24} cm^{-2}. An independent confirmation of a large H_2 column density comes from the shape of the far-infrared continuum spectrum of the core of the cloud (Erickson *et al.* 1977). Assuming that the grain emissivity depends on frequency as a power law with exponent ϵ, Erickson *et al.* derive 100 μ optical depths of 1.6, and 1.2 for ϵ equal to 1.5 and 1, respectively. If the grain emissivity is equal to unity for $\lambda = a$, and the grain radius, a, is 0.1 μ, I derive the grain emissivity at 100 μ to be 3×10^{-5} and 10^{-3} for the above values of ϵ. The H_2 column density is given by

$$N_{H_2} = \frac{2a\rho R_{gd}}{3m_H} \frac{\tau_{100}}{Q_{100}} . \tag{2.3}$$

With the grain density, $\rho = 3$ g cm^{-3}, and the gas to dust ratio by mass, $R_{gd} = 100$, I obtain the following formula

$$N_{H_2} = 1.2 \times 10^{21} \frac{\tau_{100}}{Q_{100}} , \tag{2.4}$$

which gives a H_2 column density of 6.4×10^{25} cm^{-2} and 1.4×10^{24} cm^{-2} for $\varepsilon = 1.5$ and 1, respectively. Taking 1×10^{24} cm^{-2} as a conservative lower limit for the H_2 column density, I derive an upper limit for the ^{13}CO to H_2 abundance ratio in Sagittarius B2 equal to 10^{-6}. This is a factor of 2 lower than the value characteristic of local clouds (Dickman 1978). Because the ^{12}CO to ^{13}CO ratio is lower by a factor of 3 in Sgr B2 than in the disk (Penzias 1980), the ^{12}CO fractional abundance in Sgr B2 is at least a factor of 6 lower than in the disk. Irvine, Goldsmith, and Hjalmarson (1987), assuming an H_2 column density of 2×10^{23} cm^{-2}, conclude that the molecular abundances in Sgr B2 are similar to those in several disk clouds. However, if the peak H_2 column density is higher, as suggested by the continuum data, the fractional abundances of many molecular species in Sgr B2 will be *lower* than in the disk sources studied by Irvine, Goldsmith, and Hjalmarson. One possible explanation for lower molecular abundances may be a greater effect of sticking of molecular material to dust grains caused by the high density. Because the circulation time scale is longer than for typical lower density clouds in the disk, the average rate at which the molecular material is returned to the gas phase as a result of interaction with the interstellar UV field at the boundaries of the molecular cloud is slower than for the disk clouds. Since the average density in Sgr B2 is high, the depletion time scale is relatively short (*cf.* Boland and de Jong 1982). This combination of factors could result in a greater fraction of molecular material being depleted onto grain surfaces. The wide variety of molecular species detected in Sgr B2 may thus be to a large degree a result of the very large column density rather than a particularly large fractional abundance of these species.

C. Molecular Mass And Density Distribution

Assuming a ^{13}CO fractional abundance of 10^{-6}, as discussed in section B, I derive the total mass of the 27.5 × 27.5 pc region for which both $C^{18}O$ and ^{13}CO data are available to be 4.0×10^6 $M_\odot$. The first derivative of the mass contained inside the region with a projected distance from the center, r, as a function of this distance (Figure 2.8) increases for $r < 15$ pc. This suggests that the mass outside of the region mapped is a significant fraction of the total mass of the complex.

The functional dependence of the $C^{18}O$ integrated intensity on the projected distance from the center of the cloud can provide information about density distribution within the cloud. The variation of the integrated intensity with projected offset is shown in Figure 2.9, and exhibits a prominent central peak together with a smoothly falling large scale distribution. This indicates a core-envelope structure for the cloud. The $C^{18}O$ integrated intensity is fairly constant for $r > 5$ pc suggesting existence of an envelope with small density gradient. The sharp increase in the integrated intensity for $r < 5$ pc can be attributed to a core. A single power law density distribution is unable to reproduce observed flattening of the distribution for large values of r. I fit the data in Figure 2.9 with a two component model of the cloud, consisting of a constant density component and a power law density component extending inward to radius r_o and outward to radius R. I thus have the following density distribution for the model cloud:

$$n(r) = \begin{cases} n_1 + n_2 & r \le r_0 \\ n_1 \left[\dfrac{r}{r_0} \right]^{-\alpha} + n_2 & R \ge r > r_0 \end{cases} \tag{2.5}$$

Results of the computations for six density distributions with $\alpha = 1.5, 1.7, 2.0, 2.5, 3.0$ and ∞ are presented in Table 2.3 (models A to E respectively). Because the central position is characterized by much higher signal-to noise-ratio than any other position I require the integrated intensity at the center of the model cloud convolved with 45 $''$ beam to be equal to the observed value of 37.8 K km s^{-1}. Due to scatter in the data caused mostly by the non-spherical shape and clumpiness of the cloud, it is difficult to find a unique solution to the problem. It appears that models with low values of α (models A and B) have difficulty reproducing the data between ~ 3 and 10 pc, predicting too high integrated intensities in this region. Models with $\alpha \geq 3$ (models E and F) fail to reproduce the data for $r \leq 3$ pc, predicting too high integrated intensities in this region. A good fit to the data is achieved for models with $\alpha \approx 2.0 - 2.5$ (models C and D). A general trend is that higher values of α are accompanied by larger core radii and lower central densities. The outer radius of the cloud (~ 22.5 pc) is rather arbitrary. It has been selected based on several points with non-detections in the northern part of the region.

In the above calculations I assumed that the excitation temperature does not vary with the distance from the cloud center. The $C^{18}O$ integrated intensity is, therefore, simply proportional to the total molecular column density. I believe this to be a good approximation for the CO isotopes, which are easily thermalized due to its low dipole moment. The magnitude of the errors introduced by this assumption will be checked in Chapter IV.

Based on the models with good fit to the data I estimate the total mass within a 22.5 pc radius of Sgr B2 to be ~ 6×10^6 $M_{\odot}$. My 45″ beam does not allow for studying very dense small concentrations which may exist in the core because the beam filling factor of these fragments and their contribution to the total intensity of the CO isotope lines would be relatively small. It has to pointed out that the molecular mass estimate given above involves significant uncertainties introduced by $C^{18}O$ excitation temperature and fractional abundance used in the calculations. It is very difficult to give an error for this estimate. The true mass of the cloud should be within a factor of 2 of that given above. The functional form of the density distribution should be much less uncertain, provided that the $C^{18}O$ fractional abundance and kinetic temperature do not vary significantly throughout the envelope. The discrepancy between the observed line profiles and results of the microturbulent models discussed in Chapter IV, together with the results of the SE models of HC_3N emission presented in Chapter V, suggest that the coherent structures traced by ^{13}CO emission may consist of small clumps of the type discussed by Kwan and Sanders (1986). If this is the case the derived density distribution would refer to a mean density in the envelope, being a combination of the internal density inside clumps and their volume filling factor. The kinetic temperature of the gas in the clumpy model would also be significantly higher than the value suggested by ^{12}CO data (*cf.* Kwan and Sanders 1986). It is impossible to estimate qualitatively how the clumpy structure of the envelope would affect the derived mass and column density. The effect, however, may be significant.

D. Dynamical Mass And Virial Equilibrium

The dynamical mass of the cloud can be estimated using the virial theorem (*cf.* Dickman and Clemens 1983). Ignoring external pressure, rotation, and thermal energy of the gas I obtain the following formula

$$M_{vir} = \frac{3\beta R\sigma^2}{G} , \tag{2.6}$$

where σ is the line-of-sight velocity dispersion, R is the radius of the cloud, and β depends on the density distribution inside the cloud. Determination of the line-of-sight velocity dispersion is a non-trivial problem. The $C^{18}O$ line profile averaged over the region mapped yields values of σ ranging from 7.0 km s^{-1} using the velocity range 50 to 75 km s^{-1}, to 20.7 km s^{-1} using the velocity range 10 to 100 km s^{-1}, and 24.9 km s^{-1} using the velocity range 0 to 110 km s^{-1}. The last value gives a dynamical mass estimate of 16×10^6 $M_\odot$, taking 22.5 pc for the outer radius of the cloud, and $\beta = 1.6$ as determined for the best fit model clouds with $\alpha = 2$ - 2.5, as discussed in section B. The largest contribution to the dispersion clearly comes from the low level emission at extreme velocities. Using the $J = 1 \rightarrow 0$ transition of $C^{18}O$ or ^{13}CO (as opposed to higher transitions) for determination of σ can be misleading since these lines can be contaminated by emission coming from regions along the line of sight which are not associated with Sgr B2. In fact, the ^{12}CO spectra show low level emission with antenna temperature of ~ 1 to 2 K in the velocity range -100 to 200 km s^{-1}. Higher transitions of either isotope should be much less susceptible to this effect because the gas distributed along the line of sight is characterized by relatively low excitation temperature so it contributes less to higher transitions than it does to the $J = 1 \rightarrow 0$ transition. The value of 16×10^6 $M_\odot$ given above is, therefore, an *upper limit* to the dynamical mass of the cloud.

Due to scatter of the data in Figure 2.9, the estimate of the cloud radius given above can involve significant uncertainties, which lead to an uncertainty in the dynamical mass of the cloud as given by equation (2.3). In order to avoid this problem as well as to make our results easier to compare with previous work I compute the virial mass using the method of Solomon *et al.* (1987). The size parameter $S = 7.4$ pc determined from ^{13}CO data and the velocity dispersion $\sigma = 25$ km s^{-1} yield a virial mass of 9×10^6 $M_\odot$, assuming a projection factor of 2.9 which is appropriate for a power law density distribution with $\alpha = 1$ [*cf.* equation (2) of Solomon *et al.*]. Sgr B2 is situated far above the best fit line in the size-line width diagram defined by clouds studied by Solomon *et al.* The average surface density (~ 4×10^3 $M_\odot$ pc^{-2}) is about two orders of magnitude higher than the typical value (170 $M_\odot$ pc^{-2}). Sgr B2 clearly does not obey the standard mass-line width and mass-radius relations characteristic of GMCs in the galactic disk.

An alternative algorithm for computing the virial mass from observational data has been proposed by Langer *et al.* (1989). The virial mass of the cloud is given by the following formula

$$M = 640\, r_{hm}\, {v_{rms}}^2\, D_{kpc}\ , \tag{2.7}$$

where D_{kpc} is the distance to the cloud in kpc and the harmonic mean size, r_{hm}, in minutes of arc, is defined as

$$r_{hm} = \frac{\left(\sum\limits_{i,n} T_{in}\right)^2}{2 \sum\limits_{j<k,n,p} \dfrac{T_{jn}T_{kp}}{r_{jk}}}\ . \tag{2.8}$$

The rms velocity dispersion is

$$v_{rms} = \left\{ \frac{\sum\limits_{i,n} T_{in} {v_{zin}}^2 - \left(\sum\limits_{i,n} T_{in} v_{zin} / \sum\limits_{i,n} T_{in}\right)^2}{\sum\limits_{i,n} T_{in}} \right\}^{\frac{1}{2}}\ . \tag{2.9}$$

The first summation index denotes spatial coordinates and the second a velocity channel. When applied to our data this method gives a virial mass of 14 × 10^6 $M_\odot$.

The three methods discussed above give a virial mass of Sgr B2 between 9 and 16 × 10^6 $M_\odot$ with an average of ~ 13 × 10^6 $M_\odot$, approximately a factor of 2 higher than the molecular mass estimate given in the previous section (6 × 10^6 $M_\odot$). The uncertainties involved are very difficult to estimate for any of the method of virial mass determination used. The differences between the three estimates suggest that an error of about a factor of 2 does not seem unreasonable. The virial mass of the cloud is, therefore, quite close to the molecular mass estimate given in the previous section taking into account uncertainties involved in both methods of mass determination (for example, the not well known fractional abundances, and errors in determining the velocity dispersion). I conclude that Sgr B2 is close to virial equilibrium, similar to GMC complexes in the first quadrant of the galactic disk (Dame *et al.* 1986; Solomon *et al.* 1987).

Several mechanisms could be playing a role in determining the distinctive high density and line width for Sgr B2, with the cloud conforming to the virial equilibrium that is the rule among GMCs. Tidal forces can have a major effect on molecular clouds, especially in the inner galaxy (Stark and Blitz 1978). The differential rotation sets a lower limit to the mean density for a cloud to be bound (Bania, Stark, and Heiligman 1986). Extrapolation to the 120 pc galactocentric distance of Sgr B2 is highly uncertain but scaling the tidally limited density as R^{-2} (Stark and Blitz 1978) yields $n_T = 3\times10^4$ cm^{-3}. This is greater than the density I derive for the region outside the central ~ 2 pc core of Sgr B2. This could indicate that the gravitational potential so close to the Galactic Center is not so simply behaved as assumed, or that the outer parts of Sgr B2 are, in fact not gravitationally bound as suggested by Oort (1977). One can estimate the magnetic field strength required for magnetic support of the cloud, which for regions with mainly nonthermal motions is given by

$$B = 3\left[\frac{5}{G}\right]^{\frac{1}{2}}\frac{\sigma^2}{R} = 84\,\frac{\sigma^2}{R}\ (\mu G)\,, \tag{2.10}$$

where the velocity dispersion, σ, is in km s^{-1}, and the cloud radius, R, is in pc (Myers and Goodman 1988). Taking $\sigma = 25$ km s^{-1} and $R = 22.5$ pc I obtain $B = 2300$ μG. This very large value reflects the large velocity dispersion for a cloud the size of Sgr B2, but there is no presently available observational data that can decide the issue of magnetic support for this cloud.

The fragments or clumps of molecular material surrounding the core of Sgr B2 are potentially valuable probes of its dynamical state. The observed line width of the ^{13}CO lines increases with the projected distance from the center of the cloud (compare Figures 2.6a and 2.7a). High and low velocity components in the ^{13}CO spectra are more often observed at off-center positions, suggesting that fragments existing in the cloud envelope are in a randomly oriented orbits about the center of mass, rather than participating in a systematic flow such as collapse. An estimate of the dynamical mass of the cloud can be obtained from the analysis of small clumps with LSR velocities higher than 100 km s^{-1} observed in the ^{13}CO maps. For a set of N small clumps in elliptical orbits around the center of the cloud, the dynamical mass is given by

$$M_{dyn} = \frac{\gamma}{GN} \sum_{i=1}^{N} r_i \Delta v_{zi}{}^2 , \tag{2.11}$$

where Δv_{zi} is the radial velocity shift of the $i-th$ clump from the mean line velocity, r_i its projected distance from the center of the cloud, and γ depends on the geometry of the system and the orbit parameters. Bahcall and Tremaine (1981) addressed the problem for a spherical system of test particles in the gravitational potential of a massive central object. In the absence of any specific information on the distribution of eccentricities, their preferred estimator of the mass gives $\gamma = 24/\pi$. This leads to the mass estimate of 3.8×10^7 $M_\odot$, when applied to the data for four clumps observed in the ^{13}CO spectra. It should be pointed out, however, that the observational data has a significant statistical bias. Clumps with small velocity offsets from the line center are blended with the emission from the core and are, therefore, undetectable. Due to this effect I observe only clumps with large velocity offsets (~ 45 km s^{-1}) which are likely to be close to the pericenters of their orbits. In this case the parameter γ is much smaller, typically on the order of unity. Setting $\gamma = 1$ gives to a lower limit of 5×10^6 $M_\odot$ for the mass of the cloud which agrees well with the mass determination given above. Additional observations with higher sensitivity will be required to more fully explore this method of determining molecular cloud mass.

E. Conclusion

The present observations of the CO isotopes in the Sgr B2 molecular cloud give a ^{13}CO to $C^{18}O$ abundance ratio of 9.0 ± 1.9, consistent with the average ratio in the disk and other Galactic Center sources. Comparison of the ^{13}CO column density based on the present data with H_2 column density based on the 1300 μ continuum data gives an upper limit of 10^{-6} for the ^{13}CO fractional abundance, a factor of 2 lower than the local value. The $^{12}CO/H_2$ abundance ratio is a factor of 6 lower than the local value due to the lower ^{12}CO to ^{13}CO ratio. The H_2 column density suggested by the continuum data for Sgr B2 leads to the conclusion that abundances of many molecular species in addition to the CO isotopes may be lower than in local clouds. Our observations suggest a two component structure for the cloud, with a constant density component and a component with density having a power law dependence on the distance from the cloud center with an exponent between -2 and -2.5 . Based on our model calculations I derive the outer radius of the cloud to be ~ 22.5 pc, and the total mass of the cloud of ~ 6×10^6 $M_\odot$. The virial mass of the cloud is ~ 13×10^6 $M_\odot$, suggesting that the complex is close to virial equilibrium as are GMC complexes in the disk. The velocity dispersion and virial mass reported here are higher than these found in previous studies of the cloud (Scoville, Solomon, and Penzias 1975), mostly due to broader velocity range used in computing the integrated intensities. I believe that most of the emission in the 0 - 100 km s^{-1} velocity range comes from the regions dynamically bound to the core of the cloud.

The mass and line width of Sgr B2 are greater than those of disk GMCs of similar size. In a sample of 1427 molecular cloud and cloud cores in the inner galaxy (Scoville *et al.* 1987), there are objects with diameters between 10 and 150 pc. Sgr B2 cannot be, therefore, considered as an outstanding object in terms of its size. It is the high H_2 density *and* large virial mass that make this cloud exceptional. Virial masses of clouds in the sample of Scoville *et al.* (1987) range from 2×10^5 to 4×10^6 $M_\odot$ compared to 9 -16×10^6 $M_\odot$ for Sgr B2. The mean density of a disk GMC of diameter 45 pc is only 165 cm^{-3} compared to ~ 2500 cm^{-3} for Sgr B2. An equally complete set of data does not exist for the Galactic Center clouds. Although the region has been mapped in a number of molecular transitions (Bally *et al.* 1987), qualitative data including virial masses, mean densities and velocity dispersions are not available. From very limited data obtained for several Galactic Center clouds (Chapter VI) it appears, however, that Sgr B2 is exceptional even in the population of Galactic Center GMCs.

Table 2.1. - Line Parameters of ^{13}CO $J = 1 \rightarrow 0$ Emission in Sgr B2.

$\Delta\alpha$	$\Delta\delta$	V_{mean}	σ_V	$\int T_A^* dv$	T_A^*	σ_T
5.0	5.0	49.9	24.4	135.8	2.6	0.21
4.0	5.0	50.1	26.3	127.1	1.9	0.19
3.0	5.0	47.1	27.5	135.8	2.3	0.19
2.0	5.0	49.7	29.2	129.5	2.2	0.18
1.0	5.0	53.6	26.4	146.3	2.6	0.18
0.0	5.0	55.9	24.7	128.9	1.9	0.17
-1.0	5.0	48.7	23.0	86.5	2.0	0.18
-2.0	5.0	45.1	22.2	72.5	1.7	0.16
-3.0	5.0	46.0	21.7	64.0	1.4	0.21
-4.0	5.0	45.8	21.8	43.9	1.0	0.20
-5.0	5.0	47.9	22.8	35.8	0.9	0.21
5.0	4.0	45.8	25.0	163.0	2.9	0.22
4.0	4.0	44.8	25.3	166.8	2.3	0.22
3.0	4.0	47.1	26.0	164.8	2.7	0.18
2.0	4.0	50.9	25.4	148.8	2.6	0.19
1.0	4.0	52.7	25.4	164.6	2.5	0.18
0.0	4.0	53.6	24.0	140.2	2.0	0.20
-1.0	4.0	52.9	21.3	99.6	1.9	0.18
-2.0	4.0	55.0	17.8	70.9	1.7	0.17
-3.0	4.0	49.1	20.2	70.3	1.7	0.17
-4.0	4.0	49.4	19.9	71.4	1.5	0.16
-5.0	4.0	49.2	18.0	48.6	1.2	0.19
5.0	3.0	47.5	25.2	164.0	2.5	0.19
4.0	3.0	48.2	24.5	170.2	2.7	0.17
3.0	3.0	50.3	24.3	154.3	3.0	0.17
2.0	3.0	53.0	24.1	153.3	2.8	0.19
1.0	3.0	53.1	24.0	181.4	3.2	0.14
0.0	3.0	56.0	21.9	169.0	3.4	0.17
-1.0	3.0	57.8	20.3	129.7	3.2	0.18
-2.0	3.0	55.2	19.8	111.6	2.5	0.19
-3.0	3.0	55.4	20.4	94.0	2.3	0.19
-4.0	3.0	52.3	18.4	81.3	1.8	0.19
-5.0	3.0	52.5	11.8	54.2	1.7	0.18
5.0	2.0	47.7	26.0	137.4	2.4	0.16
4.0	2.0	51.0	25.3	124.9	2.1	0.17
3.0	2.0	52.3	24.6	135.9	2.4	0.17
2.0	2.0	52.8	24.2	150.2	2.4	0.17
1.0	2.0	57.2	22.7	177.8	3.8	0.17
0.0	2.0	61.9	20.9	164.8	4.3	0.17
-1.0	2.0	64.7	18.9	137.4	3.5	0.15
-2.0	2.0	61.2	21.0	111.8	2.8	0.17
-3.0	2.0	56.9	20.7	107.7	2.5	0.18
-4.0	2.0	55.7	19.3	91.4	2.3	0.18
-5.0	2.0	55.7	14.3	69.4	2.3	0.21
5.0	1.0	49.0	24.4	145.5	2.6	0.17

continued on next page

Table 2.1. - Continued.

$\Delta\alpha$	$\Delta\delta$	V_{mean}	σ_V	$\int T_A^* dv$	T_A^*	σ_T
4.0	1.0	50.1	24.1	131.7	2.2	0.17
3.0	1.0	49.7	24.2	134.7	2.4	0.18
2.0	1.0	53.6	23.4	124.5	2.3	0.15
1.0	1.0	59.5	21.9	159.1	4.1	0.18
0.0	1.0	66.3	19.8	197.4	5.2	0.15
-1.0	1.0	67.6	20.1	172.3	4.7	0.19
-2.0	1.0	66.5	18.0	120.1	3.4	0.21
-3.0	1.0	60.8	21.2	119.1	3.0	0.16
-4.0	1.0	56.2	19.5	105.0	2.6	0.21
-5.0	1.0	55.0	12.7	75.9	2.3	0.20
5.0	0.0	50.7	24.1	153.5	2.6	0.21
4.0	0.0	47.3	25.3	154.5	2.4	0.19
3.0	0.0	48.5	23.3	131.4	2.2	0.24
2.0	0.0	52.2	22.7	116.1	2.0	0.21
1.0	0.0	59.7	20.7	159.5	3.7	0.23
0.0	0.0	64.6	19.5	240.5	6.2	0.14
-1.0	0.0	64.7	22.0	190.0	4.4	0.21
-2.0	0.0	65.7	19.8	124.4	3.5	0.26
-3.0	0.0	62.8	21.7	130.3	3.1	0.18
-4.0	0.0	55.3	16.6	94.0	3.3	0.27
-5.0	0.0	52.8	14.7	88.7	2.5	0.25
5.0	-1.0	46.5	23.9	144.1	2.5	0.23
4.0	-1.0	44.3	24.7	164.8	2.7	0.24
3.0	-1.0	46.6	24.3	148.5	2.5	0.20
2.0	-1.0	55.5	19.8	112.6	2.5	0.22
1.0	-1.0	60.6	19.8	162.5	4.1	0.19
0.0	-1.0	62.7	20.1	158.0	3.8	0.19
-1.0	-1.0	62.8	22.7	165.4	4.3	0.20
-2.0	-1.0	65.9	20.1	122.7	3.5	0.23
-3.0	-1.0	57.3	22.1	129.6	3.1	0.20
-4.0	-1.0	54.2	19.6	110.7	3.1	0.24
-5.0	-1.0	53.3	19.0	98.8	2.6	0.26
5.0	-2.0	43.9	23.6	142.5	2.4	0.26
4.0	-2.0	43.6	25.5	162.8	2.9	0.27
3.0	-2.0	46.9	23.9	116.2	2.2	0.18
2.0	-2.0	55.8	22.0	125.6	2.3	0.22
1.0	-2.0	57.8	21.1	115.8	2.6	0.22
0.0	-2.0	62.7	21.7	143.8	3.0	0.18
-1.0	-2.0	62.4	23.7	142.2	3.4	0.17
-2.0	-2.0	62.9	23.5	132.6	3.2	0.24
-3.0	-2.0	58.5	21.1	155.5	3.6	0.21
-4.0	-2.0	58.2	18.9	110.9	3.2	0.22
-5.0	-2.0	49.5	20.1	110.5	2.6	0.22
5.0	-3.0	43.3	21.8	131.8	2.7	0.20
4.0	-3.0	44.0	25.1	145.6	2.8	0.25

continued on next page

Table 2.1. - Continued.

$\Delta\alpha$	$\Delta\delta$	V_{mean}	σ_V	$\int T_A^* dv$	T_A^*	σ_T
3.0	-3.0	49.1	24.1	135.9	2.6	0.22
2.0	-3.0	57.0	20.9	113.3	2.4	0.20
1.0	-3.0	60.1	17.8	102.8	2.6	0.17
0.0	-3.0	59.1	17.7	117.1	3.2	0.22
-1.0	-3.0	62.7	22.5	137.1	3.6	0.21
-2.0	-3.0	57.8	24.3	137.9	3.7	0.24
-3.0	-3.0	59.1	22.1	144.7	3.3	0.24
-4.0	-3.0	54.5	18.3	100.4	3.0	0.23
-5.0	-3.0	47.9	18.8	91.9	2.5	0.24
5.0	-4.0	45.0	21.4	115.0	2.2	0.22
4.0	-4.0	47.4	20.9	108.8	2.1	0.23
3.0	-4.0	48.1	20.8	114.6	2.2	0.22
2.0	-4.0	51.7	20.5	118.3	2.8	0.23
1.0	-4.0	60.3	20.4	107.5	2.6	0.26
0.0	-4.0	60.0	18.1	88.8	2.9	0.22
-1.0	-4.0	63.5	22.1	103.8	2.5	0.22
-2.0	-4.0	61.8	22.0	101.9	3.1	0.19
-3.0	-4.0	58.5	25.0	138.3	3.5	0.20
-4.0	-4.0	53.2	24.3	129.8	2.5	0.18
-5.0	-4.0	48.3	23.4	108.8	1.9	0.18
5.0	-5.0	48.9	22.0	94.3	2.1	0.26
4.0	-5.0	49.8	21.0	96.3	2.0	0.25
3.0	-5.0	47.7	22.3	88.5	1.8	0.24
2.0	-5.0	49.5	20.9	86.0	2.2	0.28
1.0	-5.0	50.3	24.0	98.3	2.4	0.25
0.0	-5.0	59.4	25.2	92.3	2.3	0.31
-1.0	-5.0	63.5	24.2	89.1	1.9	0.27
-2.0	-5.0	57.8	25.2	91.1	2.0	0.32
-3.0	-5.0	53.8	26.5	94.9	1.9	0.37
-4.0	-5.0	53.6	25.0	86.7	1.7	0.34
-5.0	-5.0	47.9	22.7	79.3	1.9	0.30
6.0	6.0	42.7	28.6	110.9	1.9	0.14
5.0	6.0	50.3	28.8	110.3	1.6	0.18
4.0	6.0	50.0	29.3	81.2	1.6	0.20
3.0	6.0	45.2	28.7	85.5	1.6	0.16
2.0	6.0	53.7	30.5	92.6	1.9	0.14
1.0	6.0	52.6	30.0	100.1	1.7	0.15
0.0	6.0	55.3	27.5	93.1	1.4	0.10
-1.0	6.0	43.1	23.4	40.1	1.0	0.13
-2.0	6.0	15.6	0.0	23.4	0.9	0.12
-3.0	6.0	16.2	0.0	15.0	0.6	0.13
-4.0	6.0	39.6	28.1	25.1	0.7	0.09
-5.0	6.0	13.0	0.0	20.4	0.8	0.08
-6.0	6.0	-38.9	0.0	4.9	0.6	0.11
6.0	5.0	44.4	27.3	113.3	1.9	0.14

continued on next page

Table 2.1. - Continued.

$\Delta\alpha$	$\Delta\delta$	V_{mean}	σ_V	$\int T_A^* dv$	T_A^*	σ_T
6.0	4.0	45.5	25.1	128.1	2.7	0.16
6.0	3.0	44.0	25.8	134.9	2.5	0.14
6.0	2.0	44.9	26.9	143.0	2.3	0.13
6.0	1.0	47.6	25.6	145.9	2.7	0.09
6.0	0.0	48.6	24.4	144.2	2.3	0.14
6.0	-1.0	45.8	21.4	117.2	2.1	0.19
6.0	-2.0	44.3	18.9	124.5	2.7	0.18
6.0	-3.0	45.5	20.5	122.8	2.6	0.17
6.0	-4.0	41.8	20.0	111.6	2.6	0.22
6.0	-5.0	45.9	23.4	116.1	1.8	0.19
6.0	-6.0	49.9	22.2	51.8	1.3	0.22
5.0	-6.0	49.2	24.9	103.8	2.1	0.28
4.0	-6.0	49.3	22.4	79.7	1.8	0.22
3.0	-6.0	49.3	23.2	104.5	2.3	0.23
2.0	-6.0	44.9	22.0	134.5	3.1	0.30
1.0	-6.0	49.2	23.3	106.9	2.6	0.22
0.0	-6.0	55.5	24.2	97.1	2.4	0.25
-1.0	-6.0	52.4	25.2	104.7	2.4	0.26
-2.0	-6.0	58.5	23.9	104.9	2.4	0.17
-3.0	-6.0	52.5	24.6	119.3	2.6	0.16
-4.0	-6.0	50.5	24.5	133.7	2.8	0.19
-5.0	-6.0	46.6	23.4	126.8	2.8	0.19
-6.0	-6.0	43.5	21.1	110.2	3.4	0.34
-6.0	5.0	11.8	0.0	17.6	0.9	0.17
-6.0	4.0	17.0	0.0	24.7	0.8	0.16
-6.0	3.0	39.5	0.0	20.9	1.1	0.16
-6.0	2.0	49.6	9.7	57.3	2.1	0.19
-6.0	1.0	48.4	12.8	65.6	2.2	0.20
-6.0	0.0	45.7	17.5	81.2	2.3	0.22
-6.0	-1.0	44.1	14.9	65.6	2.0	0.19
-6.0	-2.0	44.3	14.2	64.8	2.2	0.19
-6.0	-3.0	48.2	19.0	76.0	2.2	0.28
-6.0	-4.0	40.0	17.4	117.6	2.9	0.24
-6.0	-5.0	37.1	13.5	82.4	2.4	0.23
7.0	6.0	34.1	28.8	70.9	1.8	0.25
7.0	5.0	39.3	28.4	80.9	1.7	0.33
7.0	4.0	37.6	23.4	90.3	1.8	0.30
7.0	3.0	44.3	26.7	101.3	1.9	0.26
7.0	2.0	45.2	25.3	128.6	2.9	0.24
7.0	1.0	48.2	24.2	120.0	2.5	0.30
7.0	0.0	46.1	22.8	115.4	2.2	0.24
7.0	-1.0	51.0	23.9	123.0	2.2	0.22
7.0	-2.0	44.2	18.9	110.3	2.4	0.22
7.0	-3.0	43.5	21.7	82.3	1.8	0.22
7.0	-4.0	48.2	23.6	100.4	2.3	0.27

continued on next page

Table 2.1. - Continued.

$\Delta\alpha$	$\Delta\delta$	V_{mean}	σ_V	$\int T_A^* dv$	T_A^*	σ_T
7.0	-5.0	49.3	22.6	124.8	2.6	0.25
7.0	-6.0	54.9	23.0	60.4	1.2	0.26
0.0	0.0	64.7	20.4	239.5	5.8	0.07
2.5	2.5	50.3	23.9	136.4	2.7	0.28
1.5	2.5	51.3	24.8	169.1	3.2	0.20
0.5	2.5	54.9	23.4	199.5	3.8	0.21
-0.5	2.5	58.0	21.3	151.6	3.6	0.19
-1.5	2.5	56.8	16.8	89.1	2.5	0.22
-2.5	2.5	54.0	20.6	107.5	2.7	0.21
2.5	1.5	51.5	25.4	153.6	2.4	0.20
1.5	1.5	53.8	24.0	197.1	3.8	0.22
0.5	1.5	58.5	22.9	180.0	4.6	0.25
-0.5	1.5	63.2	20.5	169.1	4.6	0.18
-1.5	1.5	66.7	18.0	106.1	3.6	0.29
-2.5	1.5	58.6	19.9	102.0	3.0	0.19
2.5	0.5	46.2	22.2	120.1	2.3	0.27
1.5	0.5	55.4	23.4	162.8	4.0	0.22
0.5	0.5	62.0	21.0	180.4	4.7	0.22
-0.5	0.5	67.0	20.5	216.3	6.0	0.19
-1.5	0.5	72.0	12.4	116.1	3.9	0.37
-2.5	0.5	64.5	18.4	127.9	3.6	0.23
2.5	-0.5	50.3	22.3	116.4	2.1	0.20
1.5	-0.5	54.7	20.4	129.9	3.3	0.20
0.5	-0.5	61.2	19.8	173.2	4.7	0.17
-0.5	-0.5	64.0	21.0	244.5	5.7	0.20
-1.5	-0.5	64.9	20.7	156.7	4.7	0.27
-2.5	-0.5	62.3	22.6	122.3	3.1	0.22
2.5	-1.5	47.0	22.6	116.9	2.1	0.24
1.5	-1.5	56.9	20.2	131.4	3.0	0.23
0.5	-1.5	60.8	19.4	158.5	4.1	0.20
-0.5	-1.5	63.8	21.2	157.6	3.9	0.20
-1.5	-1.5	64.0	23.6	156.5	4.1	0.26
-2.5	-1.5	61.7	21.1	122.6	3.5	0.26
2.5	-2.5	49.0	23.3	117.0	2.1	0.29
1.5	-2.5	55.6	19.5	109.9	2.5	0.26
0.5	-2.5	56.2	21.9	124.4	3.3	0.21
-0.5	-2.5	63.1	22.8	164.3	3.5	0.25
-1.5	-2.5	59.2	25.5	157.5	3.7	0.25
-2.5	-2.5	61.5	21.1	131.4	3.7	0.22
5.5	4.5	46.9	24.9	147.3	3.6	0.36
4.5	4.5	42.8	24.3	165.1	3.5	0.38
3.5	4.5	46.7	25.8	185.3	3.3	0.43
2.5	4.5	47.3	27.9	186.5	3.4	0.41
1.5	4.5	51.5	27.9	138.1	2.7	0.43
0.5	3.5	51.4	26.0	161.0	2.8	0.40

continued on next page

Table 2.1. - Continued.

$\Delta\alpha$	$\Delta\delta$	V_{mean}	σ_V	$\int T_A^* dv$	T_A^*	σ_T
0.5	4.5	51.6	25.5	160.7	3.1	0.43
-0.5	4.5	51.5	24.9	141.2	2.9	0.37
-1.5	4.5	49.0	24.2	68.1	1.9	0.45
-2.5	4.5	43.1	23.3	87.6	2.1	0.45
-3.5	4.5	45.5	20.9	67.2	2.0	0.36
5.5	3.5	43.8	25.2	161.0	3.2	0.36
4.5	3.5	43.3	24.5	208.0	4.0	0.44
3.5	3.5	44.3	25.9	188.7	2.9	0.40
2.5	3.5	46.9	25.3	199.4	3.2	0.40
1.5	3.5	50.3	25.2	206.8	3.4	0.36
-0.5	3.5	51.5	25.1	162.2	3.1	0.43
-1.5	3.5	51.0	21.5	95.8	2.6	0.34
-2.5	3.5	49.6	15.6	44.8	1.7	0.39
-3.5	3.5	46.0	20.0	82.5	2.0	0.38
5.5	2.5	44.3	26.2	151.9	2.8	0.37
4.5	2.5	44.0	25.0	180.2	3.2	0.35
3.5	2.5	48.9	24.8	172.9	3.0	0.39
-3.5	2.5	51.0	22.0	114.6	3.0	0.34
5.5	1.5	42.1	26.4	151.1	3.0	0.31
4.5	1.5	48.2	25.5	138.4	3.0	0.37
3.5	1.5	49.5	24.9	155.8	2.8	0.41
-3.5	1.5	55.7	21.6	127.6	3.1	0.31
5.5	0.5	48.8	25.0	154.3	2.7	0.35
4.5	0.5	47.6	23.8	168.2	3.2	0.34
3.5	0.5	48.6	24.5	172.1	2.8	0.34
-3.5	0.5	55.6	22.5	147.0	3.5	0.36
5.5	-0.5	46.9	22.9	150.0	2.9	0.32
4.5	-0.5	47.0	25.3	182.5	3.1	0.33
3.5	-0.5	45.6	23.8	166.6	3.2	0.36
-3.5	-0.5	59.6	22.2	149.0	4.2	0.36
5.5	-1.5	43.6	20.7	149.2	3.9	0.39
4.5	-1.5	43.5	23.8	182.6	3.1	0.35
3.5	-1.5	43.9	23.2	170.9	3.4	0.37
-3.5	-1.5	56.5	22.5	164.6	4.0	0.38
5.5	-2.5	42.7	18.1	96.7	2.5	0.38
4.5	-2.5	42.8	23.6	166.6	3.1	0.40
3.5	-2.5	41.4	24.6	149.2	3.1	0.36
-3.5	-2.5	58.3	19.6	163.8	4.9	0.31
5.5	-3.5	45.3	21.2	144.6	3.0	0.39
4.5	-3.5	40.2	21.3	159.7	3.3	0.38
3.5	-3.5	45.1	23.1	139.6	2.9	0.37
2.5	-3.5	47.0	22.5	132.1	2.7	0.42
1.5	-3.5	56.2	21.7	134.1	3.2	0.34
0.5	-3.5	58.7	20.0	123.7	3.3	0.34
-0.5	-3.5	61.9	19.6	134.8	4.0	0.32

continued on next page

Table 2.1. - Continued.

$\Delta\alpha$	$\Delta\delta$	V_{mean}	σ_V	$\int T_A^* dv$	T_A^*	σ_T
-1.5	-3.5	61.2	22.8	149.4	4.8	0.31
-2.5	-3.5	60.5	24.1	151.3	4.2	0.44
-3.5	-3.5	56.2	22.6	172.8	4.7	0.32
-4.5	-3.5	51.0	18.2	113.1	4.1	0.34
-5.5	-3.5	44.8	17.4	102.3	2.8	0.34
-6.5	-3.5	41.8	19.8	139.1	3.6	0.46
-7.5	-3.5	33.9	13.9	77.4	3.1	0.38

The entries in the table are: offsets from the cloud center (arcminutes), mean line velocity, velocity dispersion (km s^{-1}), integrated intensity between 0 and 100 km s^{-1} (K km s^{-1}), peak antenna temperature corrected for atmospheric attenuation and warm losses, but not corrected for the beam efficiency (K), and rms noise in the spectrum (K). The conversion factor from ^{13}CO integrated intensity to H_2 column density is 2.8×10^{21} cm^{-2} (K km $s^{-1})^{-1}$ (including a correction for η_{FSS} and coupling to a uniform source filling the main beam, $\eta_{FSS}\eta_C = 0.45$).

Table 2.2. - Line Parameters of $C^{18}O$ $J=1\rightarrow0$ Emission in Sgr B2.

$\Delta\alpha$	$\Delta\delta$	V_{mean}	σ_V	$\int T_A^* dv$	T_A^*	σ_T
0.0	6.0	51.9	22.5	7.0	0.2	0.07
6.0	5.0	43.0	26.3	10.3	0.2	0.05
5.0	5.0	44.9	24.3	10.2	0.4	0.06
4.0	5.0	44.6	26.0	13.3	0.3	0.07
3.0	5.0	37.5	24.5	11.3	0.4	0.06
2.0	5.0	42.0	26.1	16.6	0.4	0.06
1.0	5.0	45.3	26.0	11.1	0.3	0.07
0.0	5.0	54.4	21.0	10.6	0.3	0.08
-1.0	5.0	50.9	23.5	8.9	0.3	0.06
-2.0	5.0	42.9	22.2	6.6	0.2	0.05
-3.0	5.0	36.0	20.5	4.8	0.2	0.04
-4.0	5.0	13.0	0.0	1.9	0.2	0.04
-5.0	5.0	49.8	28.2	4.7	0.2	0.10
6.0	4.0	42.6	21.7	9.8	0.3	0.05
5.0	4.0	43.0	22.8	16.5	0.4	0.07
4.0	4.0	42.0	25.6	17.2	0.3	0.06
3.0	4.0	39.3	24.8	16.3	0.5	0.05
2.0	4.0	40.3	24.2	14.4	0.4	0.06
1.0	4.0	52.2	22.6	11.0	0.4	0.07
0.0	4.0	46.7	22.1	14.1	0.4	0.07
-1.0	4.0	52.4	22.5	5.3	0.3	0.06
-2.0	4.0	48.1	16.9	6.2	0.3	0.05
-3.0	4.0	43.7	13.5	3.0	0.2	0.09
-4.0	4.0	43.4	25.3	7.5	0.2	0.04
-5.0	4.0	70.7	0.0	3.1	0.4	0.14
6.0	3.0	44.6	20.9	10.1	0.3	0.04
5.0	3.0	42.2	17.8	13.8	0.4	0.08
4.0	3.0	37.6	10.4	8.9	0.3	0.09
3.0	3.0	52.2	22.9	14.7	0.4	0.08
2.0	3.0	55.3	24.9	14.9	0.4	0.06
1.0	3.0	53.1	24.7	16.5	0.4	0.07
0.0	3.0	60.4	15.5	16.1	0.5	0.05
-1.0	3.0	55.2	19.3	12.0	0.3	0.05
-2.0	3.0	55.4	14.0	10.4	0.3	0.05
-3.0	3.0	53.2	21.0	11.3	0.3	0.06
-4.0	3.0	48.9	0.0	5.1	0.3	0.05
0.5	2.5	50.2	17.6	16.6	0.6	0.17
0.0	2.5	56.8	22.2	19.7	0.7	0.17
-0.5	2.5	51.4	18.8	14.6	0.7	0.16
6.0	2.0	45.1	25.5	12.9	0.3	0.05
5.0	2.0	44.6	24.9	16.6	0.4	0.08
4.0	2.0	46.5	24.4	9.7	0.3	0.06
3.0	2.0	52.5	24.8	14.5	0.4	0.07
2.0	2.0	51.9	24.3	14.0	0.4	0.06
1.0	2.0	58.8	19.9	21.2	0.7	0.07

continued on next page

Table 2.2. - Continued.

$\Delta\alpha$	$\Delta\delta$	V_{mean}	σ_V	$\int T_A^* dv$	T_A^*	σ_T
0.5	2.0	52.3	20.5	23.3	0.7	0.16
0.0	2.0	76.3	0.0	14.4	0.7	0.07
-0.5	2.0	58.3	18.4	17.6	0.5	0.20
-1.0	2.0	63.1	17.1	17.8	0.6	0.07
-2.0	2.0	61.5	9.8	11.5	0.5	0.05
-3.0	2.0	55.5	16.4	11.4	0.5	0.05
-4.0	2.0	53.5	16.3	9.5	0.4	0.05
-5.0	2.0	58.7	15.9	6.2	0.3	0.08
1.0	1.5	61.0	16.8	18.6	0.8	0.19
0.5	1.5	60.5	0.0	12.1	0.7	0.19
0.0	1.5	63.7	18.9	14.2	0.7	0.18
-0.5	1.5	62.7	21.0	23.8	0.9	0.18
-1.0	1.5	67.9	15.1	20.2	0.9	0.16
6.0	1.0	46.7	23.4	11.7	0.3	0.06
5.0	1.0	45.7	24.2	15.9	0.3	0.07
4.0	1.0	50.6	21.8	11.1	0.3	0.05
3.0	1.0	50.0	24.5	11.6	0.3	0.07
2.0	1.0	53.8	19.6	11.9	0.4	0.05
1.0	1.0	59.5	18.6	24.6	1.0	0.11
0.5	1.0	60.9	18.8	19.4	1.2	0.12
0.0	1.0	76.6	0.0	22.5	1.1	0.09
-0.5	1.0	68.3	15.5	25.0	1.1	0.15
-1.0	1.0	61.8	22.4	34.6	1.1	0.08
-2.0	1.0	72.8	0.0	13.3	0.7	0.06
-3.0	1.0	57.0	18.8	13.5	0.4	0.06
-4.0	1.0	52.5	16.4	12.7	0.5	0.04
-5.0	1.0	49.6	13.2	11.4	0.4	0.07
0.0	0.5	64.7	18.4	30.8	1.3	0.17
-0.5	0.5	69.1	16.6	31.7	1.4	0.17
-1.0	0.5	64.3	23.2	21.0	0.7	0.19
6.0	0.0	46.1	22.1	14.4	0.3	0.05
5.0	0.0	47.9	25.8	20.9	0.3	0.05
4.0	0.0	45.7	25.3	17.4	0.4	0.04
3.0	0.0	48.6	24.7	18.0	0.3	0.04
2.0	0.0	52.7	23.3	13.1	0.3	0.04
1.0	0.0	59.8	17.9	24.4	0.8	0.05
0.0	0.0	65.4	12.0	37.8	1.6	0.03
-0.5	0.0	60.4	20.3	31.7	1.2	0.19
-1.0	0.0	70.6	9.6	26.0	1.0	0.08
-2.0	0.0	67.2	15.4	14.9	0.6	0.06
-3.0	0.0	63.6	18.0	12.2	0.4	0.05
-4.0	0.0	55.5	12.2	12.4	0.4	0.05
-5.0	0.0	54.5	12.9	11.6	0.4	0.03
0.0	-0.5	62.5	17.1	28.4	1.2	0.17
-0.5	-0.5	65.6	16.4	27.6	0.9	0.15

continued on next page

Table 2.2. - Continued.

$\Delta\alpha$	$\Delta\delta$	V_{mean}	σ_V	$\int T_A^* dv$	T_A^*	σ_T
-1.0	-0.5	61.3	22.9	27.3	1.0	0.20
6.0	-1.0	49.9	20.2	12.1	0.3	0.06
5.0	-1.0	39.9	21.5	16.7	0.4	0.07
4.0	-1.0	41.7	23.2	15.9	0.3	0.07
3.0	-1.0	44.1	21.5	10.8	0.3	0.08
2.0	-1.0	58.2	13.4	9.3	0.4	0.06
1.0	-1.0	61.7	3.9	13.1	0.8	0.22
1.0	-1.0	61.9	11.9	19.2	0.8	0.07
0.0	-1.0	63.7	14.5	19.0	0.9	0.08
-0.5	-1.0	56.5	25.9	26.3	0.7	0.14
-1.0	-1.0	63.0	20.9	26.2	0.8	0.08
-2.0	-1.0	66.8	20.5	13.5	0.5	0.06
-3.0	-1.0	59.1	22.1	12.7	0.4	0.07
-4.0	-1.0	50.5	18.1	11.6	0.4	0.05
-5.0	-1.0	57.1	8.1	9.9	0.4	0.09
0.0	-1.5	52.4	24.9	24.0	0.8	0.21
6.0	-2.0	46.6	21.5	17.2	0.4	0.07
5.0	-2.0	39.5	23.4	17.3	0.4	0.07
4.0	-2.0	38.1	24.5	11.8	0.3	0.06
3.0	-2.0	50.5	20.8	15.1	0.4	0.11
3.0	-2.0	45.5	22.0	15.2	0.3	0.07
2.0	-2.0	54.0	18.9	14.1	0.4	0.05
1.0	-2.0	54.0	19.1	11.3	0.4	0.05
0.0	-2.0	55.1	22.7	18.7	0.5	0.06
-1.0	-2.0	61.7	19.8	20.3	0.6	0.06
-2.0	-2.0	67.0	18.0	11.5	0.5	0.06
-3.0	-2.0	57.4	20.4	18.0	0.5	0.07
-4.0	-2.0	57.1	18.5	12.1	0.5	0.05
-5.0	-2.0	6.6	0.0	5.0	0.3	0.09
6.0	-3.0	40.2	18.4	15.7	0.5	0.07
5.0	-3.0	42.3	21.8	16.5	0.4	0.07
4.0	-3.0	40.3	20.6	11.4	0.3	0.05
3.0	-3.0	48.4	24.6	18.2	0.3	0.06
2.0	-3.0	53.2	23.5	12.5	0.3	0.06
1.0	-3.0	54.3	20.5	13.0	0.5	0.05
0.0	-3.0	59.6	13.7	9.9	0.5	0.05
-1.0	-3.0	68.6	14.6	12.6	0.4	0.07
-2.0	-3.0	57.0	23.8	13.7	0.5	0.04
-3.0	-3.0	59.4	22.0	16.5	0.5	0.06
-4.0	-3.0	51.3	24.4	14.4	0.5	0.05
-5.0	-3.0	45.3	10.3	6.9	0.3	0.08
6.0	-4.0	44.1	21.6	18.0	0.4	0.09
5.0	-4.0	42.2	21.3	16.4	0.3	0.06
4.0	-4.0	48.3	23.9	10.5	0.2	0.05
3.0	-4.0	50.4	19.4	10.5	0.4	0.06

continued on next page

Table 2.2. - Continued.

$\Delta\alpha$	$\Delta\delta$	V_{mean}	σ_V	$\int T_A^* dv$	T_A^*	σ_T
2.0	-4.0	52.5	12.2	8.4	0.4	0.05
1.0	-4.0	53.4	23.9	14.3	0.4	0.06
0.0	-4.0	57.6	17.3	11.9	0.4	0.05
-1.0	-4.0	59.5	25.0	15.4	0.4	0.06
-2.0	-4.0	64.4	15.5	13.4	0.6	0.09
-3.0	-4.0	56.9	25.1	15.2	0.4	0.06
-4.0	-4.0	53.0	19.7	12.2	0.5	0.07
-5.0	-4.0	35.8	19.3	6.4	0.4	0.12
6.0	-5.0	45.9	19.0	9.1	0.3	0.08
5.0	-5.0	47.3	21.4	11.3	0.3	0.06
4.0	-5.0	49.7	15.8	7.1	0.3	0.05
3.0	-5.0	51.6	6.1	7.9	0.3	0.05
2.0	-5.0	44.9	21.4	13.6	0.6	0.08
1.0	-5.0	53.0	17.1	9.6	0.4	0.06
0.0	-5.0	58.5	22.0	9.7	0.4	0.04
-1.0	-5.0	64.2	4.5	6.8	0.4	0.05
-2.0	-5.0	56.0	22.5	12.2	0.4	0.05
-3.0	-5.0	61.2	20.3	14.4	0.4	0.05
-4.0	-5.0	50.6	23.1	14.8	0.4	0.06
-5.0	-5.0	66.3	48.8	-7.1	0.6	0.22

The entries in the table are: offsets from the cloud center (arcminutes), mean line velocity, velocity dispersion (km s^{-1}), integrated intensity between 0 and 100 km s^{-1} (K km s^{-1}), peak antenna temperature corrected for atmospheric attenuation and warm losses, but not corrected for the beam efficiency (K), and rms noise in the spectrum (K). The conversion factor from $C^{18}O$ integrated intensity to H_2 column density is 2.7×10^{22} cm^{-2} (K km $s^{-1})^{-1}$ (including a correction for η_{FSS} and coupling to a uniform source filling the main beam, $\eta_{FSS}\eta_C = 0.45$).

Table 2.3. - Density Distribution in Sgr B2 Envelope[a] .

Model	r_o(pc)	n_1(cm^{-3})	n_2(cm^{-3})	α	β	$M(M_\odot)$
A	0.25	3.4×10^5	2.2×10^3	1.5	1.59	7.1×10^6
B	0.75	9.2×10^4	2.2×10^3	1.7	1.59	6.7×10^6
C	1.25	5.5×10^4	2.2×10^3	2.0	1.59	6.3×10^6
D	1.5	5.3×10^4	2.2×10^3	2.5	1.60	5.9×10^6
E	2.0	3.95×10^4	2.4×10^3	3.0	1.60	6.2×10^6
F	3.0	3.5×10^4	2.9×10^3	∞	1.64	7.0×10^6

[a] The density distribution consists of two components, the first of which is a constant density component (n_1). The second is a power law component $[n_2(r_o/r)^\alpha]$, extending inward to r_o, and outward to R, together with extension $n = n_2$ for $r \le r_o$. For all models the outer radius of the cloud, R, is equal to 22.5 pc. The parameter β is is defined in equation (2.6). The integrated intensities from the model cloud have been convolved with a 45″ FWHM beam.

Table 2.4. - Sgr B2 Mass Estimates by Different Methods.

Method	$M(M_\odot)$
Column density	6×10^6
Virial theorem[a]	$< 16 \times 10^6$
Virial theorem[b]	9×10^6
Virial theorem[c]	14×10^6
Projected mass[d]	$> 5 \times 10^6$

[a] As given by equation (2.6).

[b] Method of Solomon *et al.* (1987).

[c] Method of Langer *et al.* (1989).

[d] As given by equation (2.11).

Figure 2.1. - A contour map of the ^{13}CO $J = 1 \rightarrow 0$ integrated intensity in Sgr B2. The integrated intensity in the velocity range 0 - 100 km s^{-1} has been corrected for atmospheric attenuation and warm losses (not corrected for forward scattering and spillover and coupling efficiencies). The contour levels are: 50, 80, 110, 140, 160, 180 and 200 K km s^{-1}. The conversion factor from ^{13}CO integrated intensity to H_2 column density is 2.8×10^{21} cm^{-2} (K km $s^{-1})^{-1}$ (including a correction for η_{FSS} and coupling to a uniform source filling the main beam, $\eta_{FSS}\eta_C = 0.45$). The coordinates of the (0,0) position are: $\alpha_{1950} = 17^h 44^m 10.5^s$, $\delta_{1950} = -28°22'05''$.

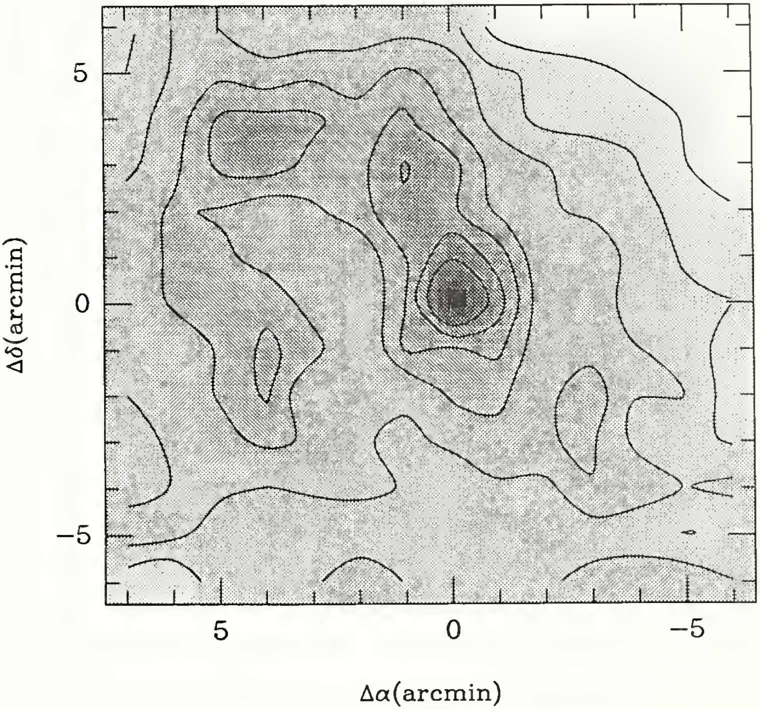
5
0
−5
Δδ(arcmin)
5
0
−5
Δα(arcmin)

Figure 2.2. - ^{13}CO $J = 1 \rightarrow 0$ spectra in Sgr B2. The spectra are from a north-south cut with 1′ spacing. The main velocity component is clearly self-absorbed at the VLSR of ~ 62 km s^{-1} for the three central position (compare optically thin C^{18}O lines at the corresponding positions shown in Figure 2.4). The line center optical depth at the center of the cloud is ~ 3 assuming the ^{13}CO to C^{18}O abundance ratio of 9, as discussed in the text. The velocity component with the VLSR of ~ 90 km s^{-1} is also present in the C^{18}O spectra. The ^{13}CO emission in this component is presumably optically thin even at the center of the cloud.

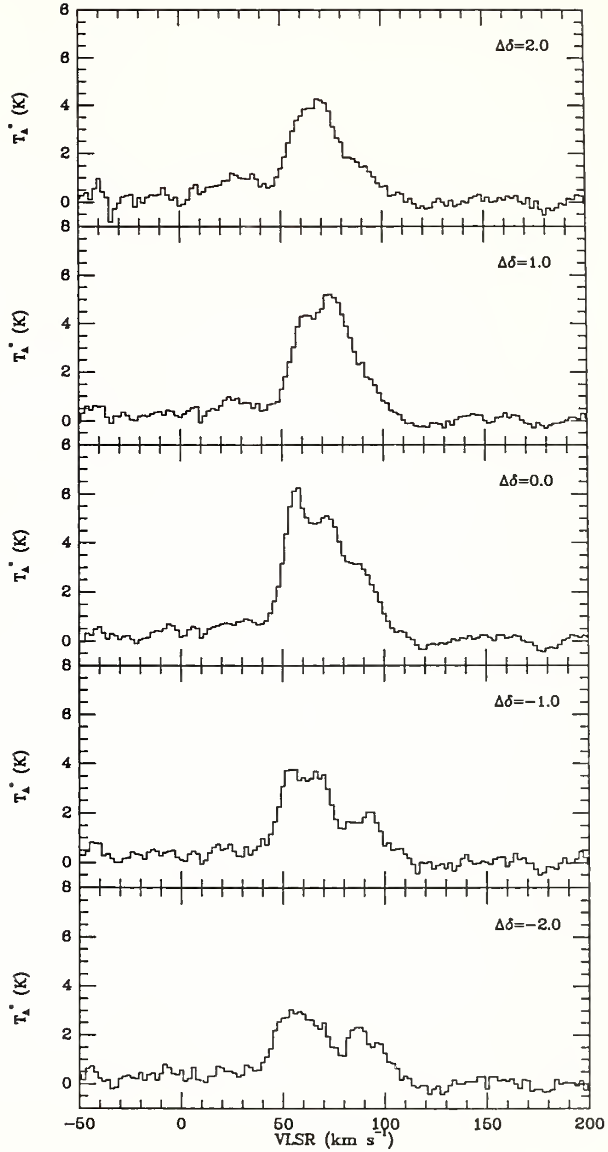
Δδ=2.0
Δδ=1.0
Δδ=0.0
Δδ=−1.0
Δδ=−2.0
T$_A^*$ (K)
8
6
4
2
0
−50
0
50
100
150
200
VLSR (km s^{-1})

Figure 2.3. - A contour map of the $C^{18}O$ $J = 1 \rightarrow 0$ integrated intensity in Sgr B2. The integrated intensity in the velocity range 0 - 100 km s^{-1} has been corrected for atmospheric attenuation and warm losses (not corrected for forward scattering and spillover and coupling efficiencies). The contour levels are: 10, 14, 18, 22, 26 and 30 K km s^{-1}. The conversion factor from $C^{18}O$ integrated intensity to H_2 column density is 2.7×10^{22} cm^{-2} (K km $s^{-1})^{-1}$ (including a correction for η_{FSS} and coupling to a uniform source filling the main beam, $\eta_{FSS}\eta_C = 0.45$). The coordinates of the (0,0) position are: $\alpha_{1950} = 17^h44^m10.5^s$, $\delta_{1950} = -28°22'05''$.

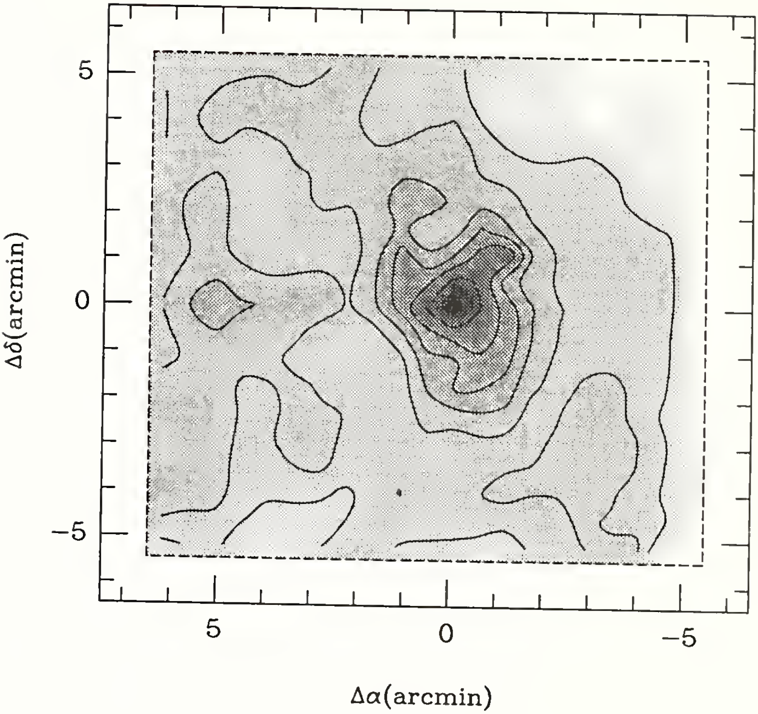
5
0
−5
Δδ(arcmin)
5
0
−5
Δα(arcmin)

Figure 2.4. - $C^{18}O$ $J = 1 \rightarrow 0$ spectra in Sgr B2. The spectra are from a north-south cut with 1′ spacing. Notice a Gaussian shape of the main velocity component with the VLSR of ~ 62 km s^{-1}. The feature with the VLSR of ~ 140 km s^{-1} is a line of SO_2.

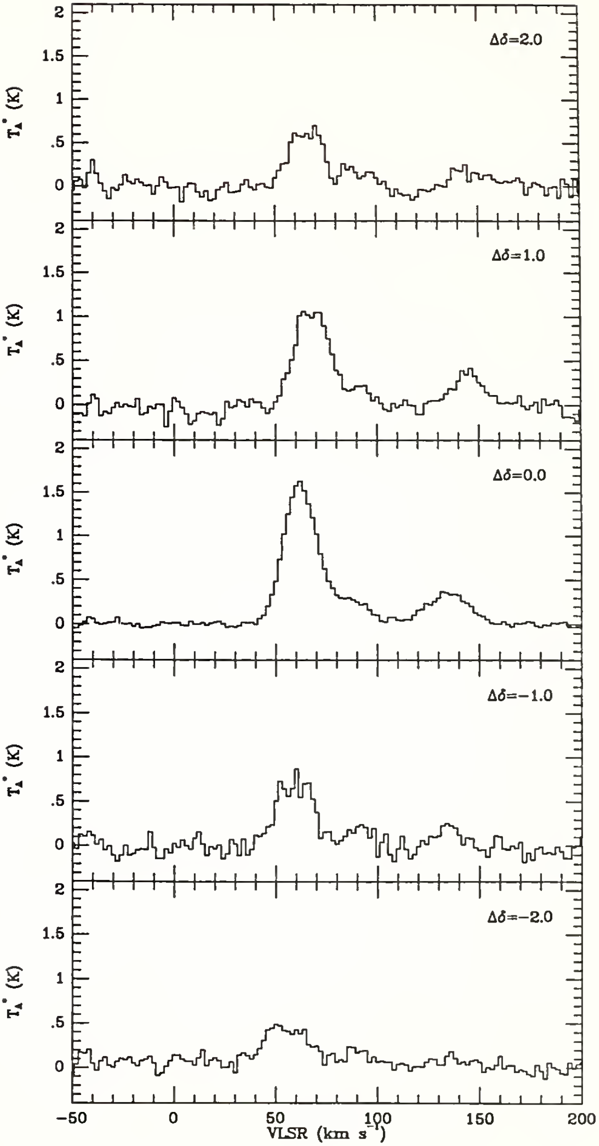
Δδ=2.0
Δδ=1.0
Δδ=0.0
Δδ=−1.0
Δδ=−2.0
T_A^* (K)
2
1.5
1
.5
0
−50
0
50
100
150
200
VLSR (km s^{-1})

Figure 2.5. - Correlation between ^{13}CO and C^{18}O integrated intensities. The dashed line corresponds to the intensity ratio of 9.0 as discussed in the text. The lower ratio observed for C^{18}O integrated intensities greater than ~ 20 K km s^{-1} is indicative of saturation of the ^{13}CO line. The fact that for low C^{18}O integrated intensities the points tend to lie above the constant ratio line may suggest non-LTE C^{18}O excitation at the edge of the cloud. The data used in the weighted average are indicated by filled squares.

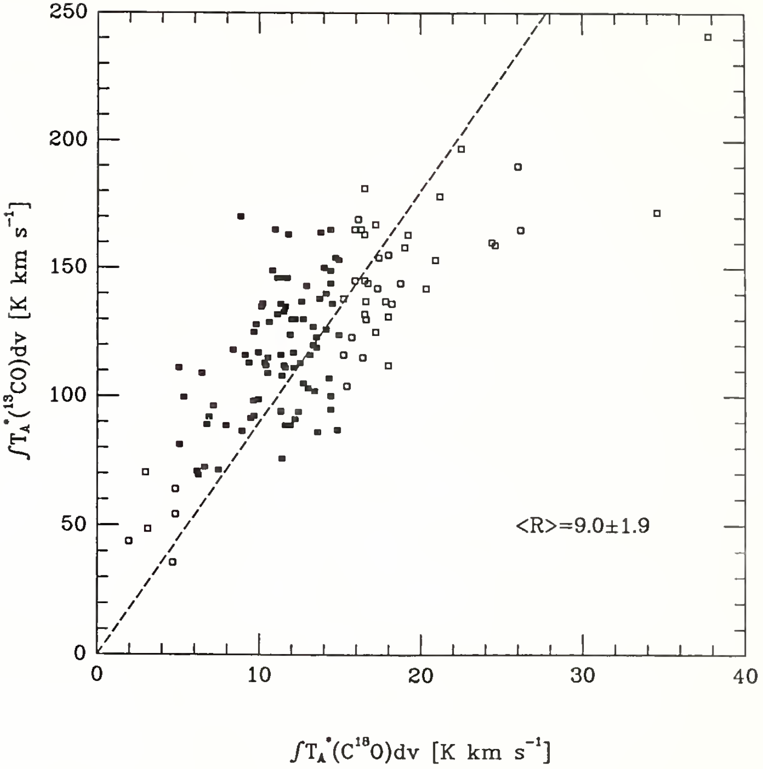
250
200
150
100
50
0
0
10
20
30
40
$\int T_A^*(^{13}CO)dv$ [K km s^{-1}]
$\int T_A^*(C^{18}O)dv$ [K km s^{-1}]
<R>=9.0±1.9

Figure 2.6. - Observed spectra and antenna temperature ratio at the (4,1) position. (a) ^{13}CO and C^{18}O spectra. The solid line corresponds to the ^{13}CO antenna temperature. The dashed line is the C^{18}O antenna temperature multiplied by the average abundance ratio of 9 as discussed in the text. The spectrometer coverage is -95 to 255 km s^{-1}. (b) The ^{13}CO to C^{18}O antenna temperature ratio. The average ratio of 8.5 ± 2.2 is statistically consistent with the value obtained from Figure 2.5. The constancy of the observed ratio suggests a low optical depth of ^{13}CO.

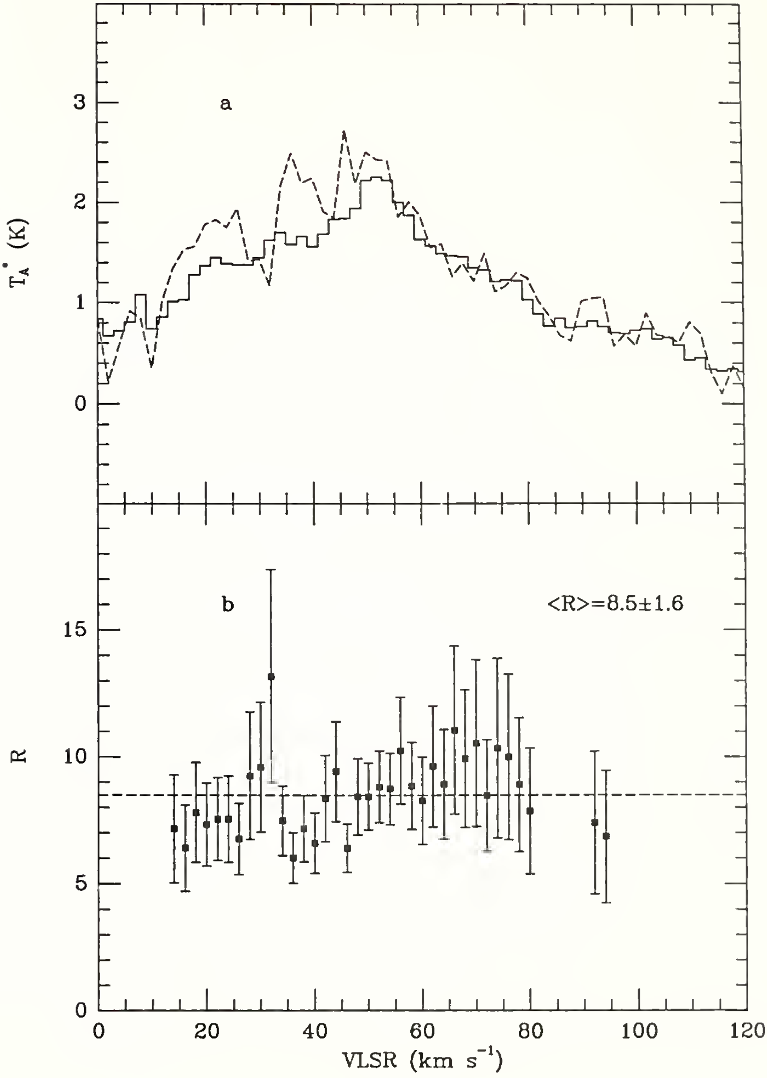
a
b
T_A^* (K)
3
2
1
0
R
15
10
5
0
<R>=8.5±1.6
0
20
40
60
80
100
120
VLSR (km s^{-1})

Figure 2.7. - Observed spectra and antenna temperature ratio at the (0,0) position. (a) ^{13}CO and C^{18}O spectra. The solid line corresponds to the ^{13}CO antenna temperature. The dashed line is the C^{18}O antenna temperature multiplied by the average abundance ratio of 9 as discussed in the text. (b) The ^{13}CO to C^{18}O antenna temperature ratio. The ratio of 10.1 ± 0.8 determined for presumably optically thin component between 80 and 100 km s^{-1} is consistent with the average value from Figure 2.5. The line center ratio of 3.1 gives a line center ^{13}CO optical depth of ~ 3, assuming a ^{13}CO to C^{18}O abundance ratio of 9.

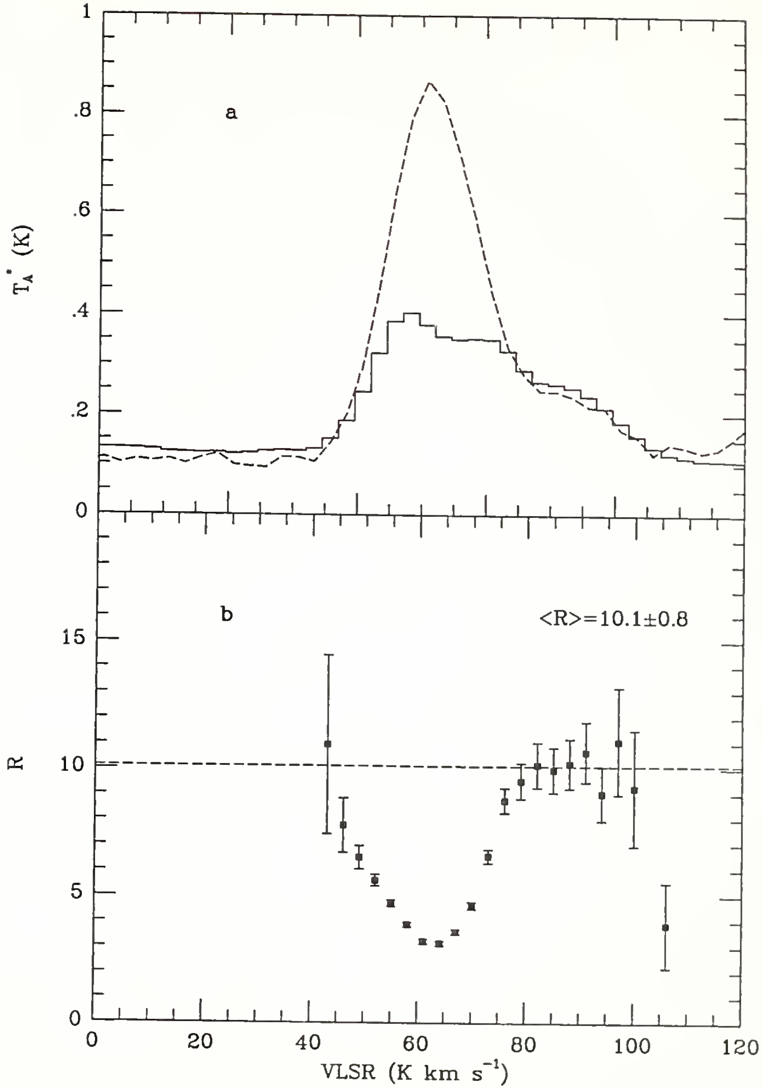
1
.8
.6
.4
.2
0
T_A^* (K)
a
b
<R>=10.1±0.8
15
10
5
0
R
0
20
40
60
80
100
120
VLSR (K km s^{-1})

Figure 2.8. - First mass derivative as a function of the projected distance. The value plotted is the first derivative of the mass contained in a region with the projected distance from the center smaller than r. Assuming that the column density is only a function of the projected distance from the cloud center, dM/dr is proportional to $r\int T_A^* dv$. The fact that dM/dr is an increasing function of r for $r \leq 15$ pc suggests that the mass outside of the region mapped is a significant fraction of the total mass of the cloud. The dashed line corresponds to the model with $\alpha = 2.5$ and the solid line to the model with $\alpha = 2$.

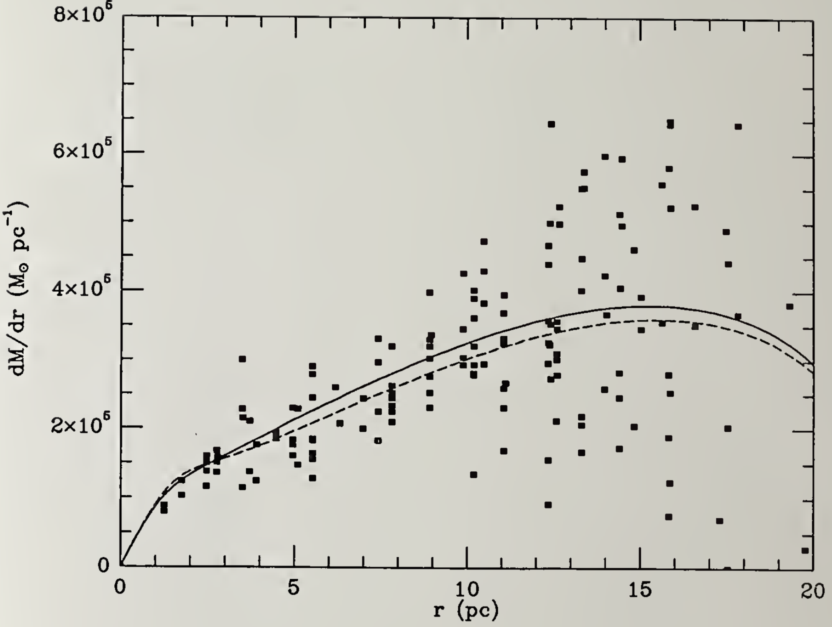
8×10⁵
6×10⁵
4×10⁵
2×10⁵
0
dM/dr ($M_\odot$ pc^{-1})
0
5
10
15
20
r (pc)

Figure 2.9. - $C^{18}O$ integrated intensity as a function of the projected distance. The uniform integrated intensity distribution for $r > 5$ pc is indicative of the constant density component. The central peak for $r < 5$ pc is produced by the power law density component (*cf.* eq. [2.5]). The dashed line corresponds to the model with $\alpha = 2.5$ and the solid line to the model with $\alpha = 2$.

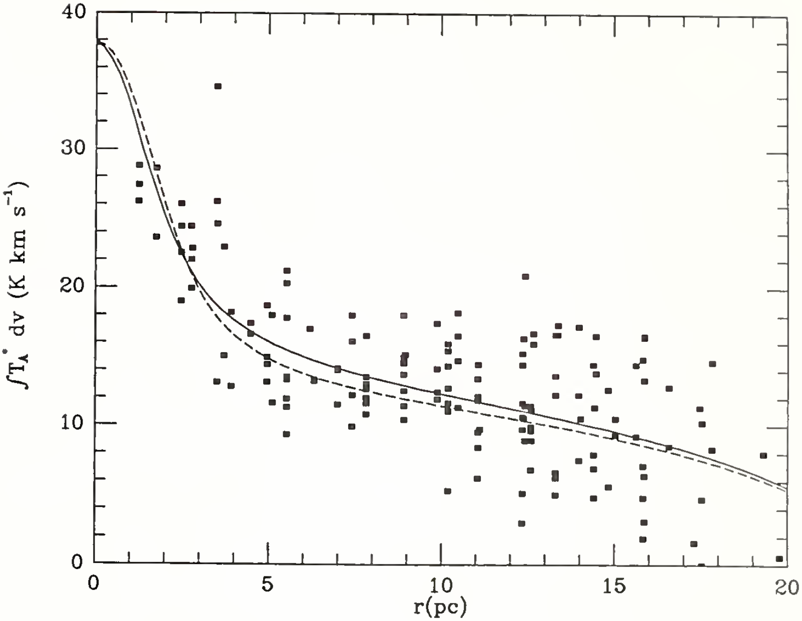
40
30
20
10
0
0
5
10
15
20
r(pc)
$\int T_A^* \, dv$ (K km s^{-1})

CHAPTER III

CONTINUUM STUDIES OF THE CORE

Submillimeter and millimeter continuum emission from warm dust can be a very useful probe of physical conditions in GMC cores. Careful modeling of the distribution and intensity of the observed emission over a wide range of wavelengths can provide information about densities and temperatures in the core, as well as luminosities of powering sources in star forming regions.

Within the core of Sgr B2, ~ 3 pc in diameter, there are two major concentrations of compact H II regions (Benson and Johnston 1986), the northern (N) and middle (M) sources, separated by ~ 2.5 pc which are embedded in an extended region of ionized gas (e.g., Kapitzky and Dent 1974). The implied stellar luminosities for the two sources are each ~ 5×10^6 $L_\odot$ (Benson and Johnston 1986). One of the most interesting results of the early high resolution continuum studies of Sgr B2 is a striking difference between distribution of the 53 μ continuum emission (Harvey, Campbell, and Hoffman 1977) and the 1300 μ continuum emission (Goldsmith, Snell, and Lis 1987). The 1300 μ emission peaks at the position of Sgr B2(N), where no 53 μ emission in excess of that expected from the distribution surrounding Sgr B2(M) is observed. It has been suggested that the observed change in the middle-to-north peak flux ratio is caused by the fact that the northern source is situated behind the dust cloud associated with Sgr B2(M), and that its emission is, therefore, attenuated by cold foreground dust (Thronson and Harper 1986; Goldsmith, Snell, and Lis 1987).

In the present chapter I present results of the high angular resolution observations of the dust emission from the core at 1300 μ, 1100 μ, 800 μ, 450 μ, and 350 μ, and discuss the constraints that the data impose on models of the cloud.

A. Observations

The 1300 μ data were taken on three days in 1988 February and March, using the 14 m FCRAO antenna. The receiver system comprised two cooled Schottky diode receivers sensitive to orthogonal linear polarizations with an IF bandwidth of approximately 500 MHz. The LO frequency of 230.2 GHz was selected to keep both upper and lower sidebands free of any strong line emission. The only features with $T_A{}^*$ greater than 1 K in the portions of the Orion spectral scan (Sutton *et al.* 1985) corresponding to the upper and lower sidebands are a pair of lines from $HCOOCH_3$. Lower lying transitions of this molecule have been detected in Sgr B2 by Cummins, Linke, and Thaddeus (1986), with about one-tenth the intensity of the lines seen in Orion. Although the rotational temperature of molecules in certain portions of Sgr B2 can be much higher than derived by Cummins, Linke, and Thaddeus (*cf.* Goldsmith *et al.* 1987), it is unlikely that the lines at 228 GHz could be more than twice as strong as the Cummins, Linke, and Thaddeus intensity of ~ 0.2 K. The pair of lines would contribute at most an antenna temperature of 6 mK averaged over the full double-sideband bandwidth. Identified spectral lines, therefore, do not make a significant contribution to the observed 1300 μ flux density.

The data consist of 45 positions with 15″ spacing and 16 positions with 20″ spacing centered at the position of Sgr B2(M) continuum source ($\alpha_{1950} = 17^h 44^m 10.5^s$, $\delta_{1950} =$ -28°22′05″). The size of the region mapped is 1′ × 2′. The receivers were tuned for double sideband operation. A typical double sideband system temperature referred to above the Earth's atmosphere at the low elevation characteristic of Sgr B2 was 1400 - 2000 K. A 4 minute integration time gave an observed rms fluctuation level of ~ 40 mK (1σ). The antenna pointing and efficiency were checked by observations of Saturn at an elevation ~ 5° higher than that of Sgr B2. The FWHM beam size was measured to be 23″, and the main beam efficiency was ~ 0.1, assuming a source temperature of 145 K (Werner *et al.* 1978). The relatively low efficiency is due to reflective and scattering losses of the radome, as well as the surface errors of the dish. The resulting conversion from the observed antenna temperature to the unpolarized flux density in a 23″ beam is 185 Jy K^{-1}.

A contour map of the emission, presented in Figure 3.1, shows a qualitative agreement with the first data set obtained in 1986 (Goldsmith, Snell and Lis 1987), with the exception of a small difference in declination of the peak of the emission. Each of the two data sets with 15″ spacing which are averaged in Figure 3.1 shows the same distribution of the emission. The peak antenna temperature of 0.29 K (equivalent to a flux density of 56 Jy) is observed at the (0,50″) position corresponding approximately to the location of the Sgr B2(N) continuum source. The antenna temperature observed at the position of the Sgr B2 (M) source is 0.24 K (equivalent to 44 Jy). The Sgr B2 molecular cloud contains a number of H II regions which are strong sources of the free-free emission. The contribution of the free-free emission to the observed continuum flux at different wavelengths is clearly seen from the plot of the observed flux density in a 60″ beam as a function of frequency (*cf.* Figure 3.2 taken from Goldsmith, Snell and Lis 1987). The total flux density is between 50 and 75 Jy at frequencies of 1.67 GHz to 85 GHz (Bieging 1976; Downes *et al.* 1978; Kapitzky and Dent 1974; Downes, Maxwell, and Rinehart 1970; Gordon *et al.* 1986). The contributions from dust and free-free emission are readily separable in Figure 3.2. The free-free flux density can be conservatively extrapolated to 1300 μ using a ν^{o}

dependence. The free-free contribution at this wavelength is ~ 25 Jy in a 60″ beam, less than 20% of the total flux density measured.

The 1100 μ, 800 μ, 450 μ and 350 μ data were taken on 2 days in 1988 July, using the 15 m James Clerk Maxwell Telescope at Mauna Kea, Hawaii. The receiver system employed the helium cooled UKT14 bolometer together with the 1100 μ, 800 μ, 450 μ, and 350 μ broad band filters with resolving power of ~ 5. The data consists of four azimuth - elevation raster maps, 33 × 33 points in size with 5″ spacing, centered on the position of the Sgr B2(M) continuum source obtained by chopping between the source and a reference position offset by 80″ in azimuth (Figures 3.3 - 3.6). Uranus (less than 5° away from Sgr B2) was used for pointing and calibration. At each frequency a raster map of Uranus, with 11 × 11 points separated by 5″ was obtained before and after the Sgr B2 observation. The maximum pointing shift between two observations separated by ~ 30 min in time was smaller than 4″. By fitting a two-dimensional Gaussian to the Uranus maps the main beam size and the conversion from the output voltage to the unpolarized flux density were determined. The beam was slightly elongated in the azimuthal direction (a typical semi-major to semi-minor axis ratio of ~ 1.2). The average beam sizes and conversions from output voltage to unpolarized flux density are given in Table 3.1. The peak fluxes in the telescope beam and in 30″ and 60″ beams are given in Tables 3.2 and 3.3 for the middle and northern sources, respectively.

The flux densities obtained with a bolometer and broad band filter can be contaminated by spectral line emission. The contamination, however, should not be significant in the present case due to the relatively small chopper throw (80″) used for the observations. Emission from low energy transitions is rather extended in Sgr B2, so the line contributions to the flux density in the main and reference beams will cancel out or at least be significantly reduced. Emission from high energy transitions can be confined to relatively small region, but the lines are usually weak and do not make significant contribution to the broad band continuum flux. In this regard, the use of a heterodyne spectrometer provides a distinct advantage over thermal detectors with filters having a resolving power of only a few. As an example I estimate the contribution of the $J=2\rightarrow1$ transition of ^{12}CO to the total flux density in the 1100 μ filter. The $J=1\rightarrow0$ transition observed at FCRAO has a peak radiation temperature of ~ 20 K, and equivalent width of ~ 40 km s^{-1}. Since ^{12}CO lines are optically thick the radiation temperature of the $J=2\rightarrow1$ transition is expected to be approximately the same as that of the $J=1\rightarrow0$ transition. Assuming a FWHM beam width of 20″ one gets a peak flux density

$$S = \frac{2k}{\lambda^2}\Omega_M T_R \ , \tag{3.1}$$

equal to ~ 500 Jy. The equivalent line width in frequency units is ~ 0.03 GHz. For a filter with central wavelength of 1100 μ and a resolving power of 5 one gets an equivalent bandwidth of ~ 55 GHz. The flux density of the $J=2\rightarrow1$ transition of ^{12}CO averaged over the whole filter bandwidth is, therefore, ~ 0.3 Jy. This will be further reduced due to small chopper throw used for observations. The contribution from weaker lines is rather difficult to estimate. In the spectral line tables of Lovas (1987) there are ~ 30 lines in the frequency range 240 - 300 GHz (approximately corresponding to the bandwidth of our 1000 μ filter) with radiation temperature higher than 3 K in the OMC-1 molecular cloud and ~ 200 lines with the radiation temperature between 1 K and 3 K. Each of the "strong" lines contributes ~ 10 % of the flux of the ^{12}CO 2→1 line (the radiation temperature of the ^{12}CO 2→1 line in OMC-1 is ~ 70 K), and each of the "weak" lines contributes ~ 3 % of the ^{12}CO 2→1 flux, I obtain the total flux from all lines equal to ~ 10 times the flux from the ^{12}CO 2→1 line. The total line contribution to the continuum flux in our 1100 μ filter is, therefore, negligible. The conclusion is true for other filters, assuming that the density of lines does not vary significantly with wavelength.

The Sgr B2(M) and (N) sources are quite well separated, and each is partially resolved. The regular beam patterns at 1100 μ and 800 μ allow for source size estimation. The observed source diameters are clearly larger than the antenna beam size, and assuming a Gaussian source shape, I derive a mean size of 18″ (0.75 pc) and 12″ (0.5 pc) for the middle and northern source, respectively. The 0.5 pc diameter of the northern source is a factor of ~ 2 bigger that that found by Carlstrom and Vogel (1989) from 3.4 mm interferometric measurements. This difference may be in part a result of antenna performance but may also reflect the extended low level emission which is present in the Carlstrom and Vogel data. The middle-to-north peak flux ratio referred to a 30″ FWHM beam increases from 0.86 at 1100 μ to > 1.22 at 350 μ (Table 3.4). The observed increase of this ratio as a function of frequency has to be explained by a model of the source.

B. Model of Sgr B2(M)

An acceptable model of the source should be able to reproduce the observed spectrum of the continuum emission, as well as the change in the middle-to-north peak flux ratio. I have modeled the source structure using the radiative transfer code of Egan, Leung, and Spagna (1988). The equation of radiative transfer in spherical geometry is solved with a Newton-Raphson iterative scheme. The transfer problem is cast as a two-point boundary value problem. By introducing two auxiliary functions, the anisotropy factor f_ν, and the configuration function ζ_ν, the equation is transformed into a quasi-diffusion form. The quasi-diffusion method operates in two parts. First the radiation field is assumed to be isotropic, and accordingly the initial values for f_ν, ζ_ν, and the temperature profile of the cloud are fixed. The linearized moment equations of radiative transfer are solved for the mean intensity J_ν. The coupled, linearized moment and energy balance equations are then solved for corrections to the mean intensity and the temperature profile. The source function S_ν is calculated, and the angular distribution of the radiation field is calculated by a ray tracing technique. The process is repeated until the convergence is achieved. The code has proved to converge quite rapidly, usually within seven to ten iterations, even for models with very high optical depth.

Because the position of Sgr B2(M) coincides with the peak of the $J = 1 \rightarrow 0$ transitions of ^{13}CO and $C^{18}O$, I have assumed that the middle source is situated at the center of the molecular cloud traced by the molecular emission. The absence of a molecular peak corresponding to Sgr B2(N) suggest that the northern source is a very small and dense clump of material situated somewhere inside the extended cloud. The absence of the 53 μ continuum emission from the northern source suggest that the clump is located at the far side of the envelope. Because the optical depth through the envelope is low at submillimeter wavelengths, the northern source is easily visible. For wavelengths shorter than ~ 100 μ, however, the envelope becomes optically thick and the emission from the northern source is attenuated by cold foreground dust. Because the separation between the two sources is large compared compared to the core sizes, I solved the radiation transfer equation for each source independently, assuming no interaction between the two sources. For Sgr B2(M) I assumed the density distribution in the envelope in the form discussed in Chapter II. The very small source diameter at submillimeter wavelengths suggest that the continuum emission comes from a small core embedded in the extended cloud, which due to small beam filling factor and high temperature does not show up in the $C^{18}O$ emission. The core was assumed to have a Gaussian density distribution with a FWHM diameter, r_{in}, and peak central H_2 density,

d_{in}. Other important input parameters of the model are: the luminosity of the central object for wavelengths longer than 912 Å (L), the 100 μ optical depth from the center to the edge of the cloud (τ), and the parameter X, scaling the envelope density distribution derived in Chapter II. The absorption efficiency, $Q(\lambda)$, at far infrared wavelengths is also a very important parameter of the model. Comparing the flux density at 1300 μ with the 1 mm data of Westerbrook *et al.* (1976) and the 350 μ data of Righini, Simon, and Joyce (1976) one finds a $\nu^{1.5}$ dependence of Q on frequency. This frequency dependence has been used in the model calculations for wavelengths longer than 100 μ. For wavelengths between 0.1 μ and 100 μ I used a ν^1 frequency dependence, as suggested by theoretical calculations of Draine and Lee (1984). The above formula gives $Q = 2.1 \times 10^{-5}$ at 1300 μ. I included one grain component with radius $a = 0.1$ μ, density $\rho = 3$ g cm^{-3}, and used the standard gas-to-dust ratio of 100 by mass.

The effects of different input parameters on the observed spectrum from a model cloud are shown in Figures 3.7 - 3.10. The solid line in each figure represents Model C from Table 3.5, which is a good model of the middle source, as discussed below. Figure 3.7 shows models with the 100 μ optical depth of 2.3 (dotted line), 3.1 (solid line), and 3.9 (dashed line). Increasing optical depth results in higher flux density at long wavelengths, and lower flux density at short wavelengths. The peak of the observed spectrum is shifted to longer wavelengths. For models presented in Figure 3.7 the 1100 μ flux in a 60″ beam is 118 Jy, 156 Jy, and 193 Jy, for $\tau = 2.3$, 3.1, and 3.9, respectively. The long wavelength flux density is, therefore, approximately proportional to the 100 μ optical depth. The short wavelength flux density changes faster than the optical depth. The corresponding flux densities at 50 μ are: 12.9 kJy, 9.1 kJy, and 6.5 kJy. The wavelength of the peak of the spectrum is also approximately proportional to the optical depth. The corresponding values are 95 μ, 110 μ, and 120 μ. The effect of the central luminosity on the observed spectrum is shown in Figure 3.8. The long wavelength part of the spectrum is only slightly affected by the luminosity. The model luminosities are 5.6×10^6 $L_{\odot}$ (dotted line), 7.5×10^6 $L_{\odot}$ (solid line), and 9.4×10^6 $L_{\odot}$ (dashed line). The 1100 μ flux density changes from 144 Jy to 166 Jy. To the first approximation the effect is also linear. The peak flux in a 60″ beam increases with L. The corresponding values are 23 kJy, 28 kJy, and 33 kJy. The wavelength of the peak decreases from 120 μ to 100 μ, and the short wavelength flux density also increases. The corresponding flux densities at 50 μ are: 6.4 kJy, 9.1 kJy, and 11.9 kJy. The observed spectrum is almost uneffected by the temperature of the central source, as shown in Figure 3.9 for models with $T = 40000$ K (solid line), and 20000 K (dashed line). Finally, models with different long wavelength emissivity laws are presented in Figure 3.10. The slopes of the grain emissivity law for wavelengths longer than 100 μ are: -1.75 (dotted line), -1.5 (solid line), and -1.25 (dashed line). Only the long wavelength flux density is affected. The 1100 μ flux density changes from 88 Jy to 272 Jy.

The input parameters to the model described above were varied to obtain the 1100 μ fluxes of ~ 75 Jy and 101 Jy in 19.4″ and 30″ beams (the wavelength of 1100 μ was chosen because of the very regular beam pattern, which allows for direct comparison of the results of the model calculations with observations), and the peak flux density of 27 - 28 kJy at 100 μ in a 60″ beam. The 100 μ flux density is slightly lower than the value of 30 kJy reported by Gatley *et al.* (1978). The northern source, however, will also contribute to the total flux in a 60″ beam. These values of input parameters give a correct flux distribution in a 60″ beam for wavelengths between 20 μ and 1300 μ. Because the source size determination involves some uncertainty (compare the 0.5 pc diameter of the northern core based on the 1100 μ and 800 μ JCMT data with the 0.2 pc diameter determined by Carlstrom and Vogel from the 3.4 mm interferometric measurements) I have taken the core size as a free parameter and run models for five core sizes ranging from 0.3 to 0.75 pc. The parameters of corresponding models are given in Table 3.5. The 100 μ, 800 μ, and 1100 μ flux densities are given in Table 3.6.

The core size is a critical parameter of the model. As one can see from Table 3.5 the luminosity of the central source and density in the core are both functions of the core diameter. The observed flux density at submillimeter and millimeter wavelengths is mainly a function of the column density averaged over the telescope beam. For small cores one has to increase the density in order to compensate for the smaller beam filling factor. This results in a higher 100 μ optical depth from the center to the edge of the cloud, and accordingly in a lower 100 μ flux. In order to increase the 100 μ flux to the required value one has to increase the stellar luminosity at the center of the cloud. The core size, density in the core, 100 μ optical depth, and stellar luminosity are, therefore, strongly correlated. The core size has also clear implications for the H_2 density in the envelope, and CO isotope abundances discussed in Chapter II. One could think that because the molecular emission in the $J=1\rightarrow0$ transition of the CO isotopes comes mostly from the envelope (high temperature and small beam filling factor in a 45″ beam make the contribution from the core negligible), and the continuum emission comes almost entirely from the core, it would be difficult to draw any conclusions about the envelope based on the continuum data. It is true that the continuum emission in a small beam (~ 20″) is dominated by the core. For bigger beams, however, the contribution from the envelope increases as the beam filling factor of the core decreases. A 30″ beam seems to be a proper choice for this type of studies, as it contains a significant fraction of the emission from the envelope and at the same time is small enough to resolve the northern and middle sources. Once a model with correct 1100 μ flux density in a 19.4″ beam is obtained, the flux in a 30″ beam can be adjusted by changing the density in the envelope. The parameter X in Table 3.5 is a value by which the density in the envelope determined in Chapter II has to be scaled in order to obtain the correct flux density in a 30″ beam. As one can see from Table 3.5, *X* is another parameter that critically depends on the core size. For small cores, the density in the envelope has to be higher in order to provide the extra flux needed in a 30″ beam. Models with small core sizes are, therefore, characterized by higher H_2 column density through the envelope (Table 3.9). The model with 0.75 pc core diameter suggested by the JCMT data is consistent with the ^{13}CO abundance observed in the local clouds. Knowledge of the true value of the diameter of the middle core is essential for determining molecular abundances and cloud mass, as well as to address the issue of cloud virialization. Single dish or interferometric data with angular resolution better than ~ 10″ are necessary to resolve the remaining ambiguity.

The temperature distributions in the models presented in Table 3.5 are shown in Figure 3.11. The increasing luminosity affects the dust temperature in inner ~ 1 pc. For bigger distances from the center the dust temperature is barely affected by the conditions in the core. This effect is caused by the fact that higher luminosities are accompanied by higher 100 μ optical depths.

Scoville and Kwan (1976) presented a simple analytic solution to an upper limit of the dust temperature in a molecular cloud, assuming no intervening opacity between the central source and the grain in consideration. If the grain emissivity varies as λ^{-1} the maximum dust temperature is given by

$$T_d(r) = 49^\circ\, q^{-0.2} \left[\frac{2\times10^{17}\,cm}{r}\right]^{0.4} \left[\frac{L}{10^5}\right]^{0.2}, \tag{3.2}$$

where q is the grain emissivity at 50 μ. The above formula gives temperatures significantly higher than the radiation transfer code of Egan, Leung, and Spagna (1988) (*cf.* Figure 3.11). This results from the very large IR optical depth through the cloud.

The 100 μ optical depth from the center of the cloud in model C is equal to unity for $r \sim 0.02$ pc. This suggest that the analytic formula of Scoville and Kwan has little application for clouds with very large IR optical depths.

The calculations were performed assuming the dust emissivity law with a slope of -1.5 in the far infrared. Satisfactory models can be obtained for other slopes of the emissivity law. Steeper slopes will result in a lower flux at millimeter wavelengths. In order to keep the same flux at 1100 μ, one would have to increase the dust column density. This would result in higher 100 μ optical depth and higher luminosity would be required to keep the same flux at 100 μ.

C. Model of Sgr B2(N)

Because of the absence of a corresponding peak of the $C^{18}O$ emission in the $J = 1 \rightarrow 0$ transition, I assumed Sgr B2(N) to be a small clump of material situated behind the molecular cloud associated with Sgr B2(M). I assumed the source to have a Gaussian density distribution with a low density envelope. The envelope was introduced for simplicity of calculations, to keep the same outer radius of the cloud and the same radial grid as for Sgr B2(M) models discussed in the previous section. It does not affect the final dust temperature distribution in the core (*cf.* more detailed discussion in the appendix). I used the same emissivity law with the slope of -1.5 in the far infrared, and the same central source temperature of 40000 K. For the reasons discussed in the previous section I ran models with three different core radii of 0.25 pc, 0.4 pc, and 0.5 pc. Having the specific intensity as a function of the offset from the center of the cloud for northern and middle source models, I calculated the combined flux in different beams assuming the geometry shown in Figure 3.12. The specific intensity along a given line of sight is simply a sum of two components: a contribution from the middle source, $I_M(p)$, and a contribution from the northern source, $I_N(p')$, attenuated by foregroud dust characterized by an optical depth, τ_{fg}:

$$I(p,\theta) = I_M(p) + I_N(p')\exp(-\tau_{fg}) \,. \tag{3.3}$$

For any model of the middle source from Table 3.5, the parameters of the northern source were varied to give the middle-to-north flux ratios at 1100 μ equal to those obtained from the observational data (Table 3.4). The parameters of final Sgr B2(N) models are given in Table 3.7. The final characteristics of combined models of the northern and middle sources are given in Table 3.8. The northern source with a 0.5 pc core diameter gives a good fit to the data for middle source models with core diameters of 0.4 - 0.6 pc (Models BC, CC, and DD). For bigger middle core sizes (Model ED) the column density through the envelope at the position of the northern source is too low, resulting in too low flux density in a 30″ beam (middle-to-north flux ratio in a 30″ beam to high). For smaller middle core sizes (Model AC) the column density through the envelope at the position of the northern source is too high, resulting in too low flux density in a 30″ beam (middle-to-north flux ratio in a 30″ beam to low). Although the change in the middle-to-north flux density ratio is rather small and the observational data itself involve some uncertainties, the trend is well defined and it allows for rejecting models with extreme middle core diameters. Similarly, a preferred range of the middle core diameter for a 0.4 pc diameter of the northern core is 0.3 - 0.5 pc. For a 0.25 pc diameter of the northern core the middle-to-north peak flux ratio in a 30″ beam is too high even for smallest size of the middle core given in Table 3.4.

D. Comparison with Constant Temperature Analysis

The analysis of the dust emission presented in the previous sections of this chapter is quite complicated and requires a lot of computer time. The continuum emission from dust is often analyzed in terms of a simple model with constant dust temperature along the line of sight. The flux density at a frequency, ν, is simply given by

$$S_\nu = \Omega B_\nu(T) \, (1 - e^{-\tau_o Q_\nu / Q_o}) \, , \tag{3.4}$$

where Ω is an effective solid angle of the source, $B_\nu(T)$ is the Planck function at an average dust temperature, T, τ_o is the optical depth at a selected frequency, and Q_ν is the grain emissivity which is usually assumed to be a power law with an exponent, β. The values of Ω, T, τ_o, and β are adjusted in order to obtain the best fit to the observed spectrum. The method was applied to Sgr B2 by Gordon (1988) who derives an average dust temperature of 36 K, effective solid angle of 4.4×10^{-8} sr, emissivity law exponent of -2.0, 1300 μ emissivity of 6.9×10^{-6}, and total H_2 column density of 1.6×10^{23}, assuming grain radius $a = 0.1$ μ and density $\rho = 1$ g cm^{-3}.

Because the H_2 column density derived by Gordon significantly differs from results of my model calculations (Table 3.9), I have applied the method of Gordon to the data in Figure 3.2 in order to derive the source parameters for Sgr B2(M) independently. I have used the same emissivity law as discussed in section B. Because the data represents the flux density in a 60″ beam, I have fixed the effective solid angle Ω in equation (3.4) and varied only the average dust temperature and 100 μ optical depth. The results are presented in Figure 3.13. The three lines correspond the the dust temperatures of 31 K (dotted line), 32 K (short dashed line), and 33 K (long dashed line). The corresponding 100 μ optical depths are 1.15, 1.0, and 0.85, respectively. The dashed-dotted line corresponds to the parameters given by Gordon. The H_2 column density is given by eq. (2.3). Using the same grain parameters as discussed in previous sections I derive H_2 column densities of 1.4, 1.2, and 1.0×10^{24} cm^{-2} in a 60″ beam for the three models, respectively. These are about an order of magnitude higher than the value given by Gordon (1988). It is not clear what value of the gas to dust ratio was used by Gordon. Using the values of a, γ, Q, and τ, given in the paper by Gordon, I derive an H_2 column density of $3.5 \times 10^{22} R_{gd}$, where R_{gd} is the gas to dust ratio by mass. Using the gas to dust ratio of 100 one gets an H_2 column density of 3.5×10^{24}, a factor of 30 higher than the value derived by Gordon based on the same data. For a comparison H_2 column densities in different beams for Models A-D are given in Table 3.9. They are entirely consistent with the results of the simple analysis presented above. The simple models do not fit the observed spectrum perfectly. The biggest discrepancy occurs at short wavelengths. The flux density at 30 μ is an order of magnitude lower than the observed value. This is caused by the fact that short wavelength emission comes from hot dust in the vicinity of the continuum sources. The spectrum from a cloud with a distribution of dust temperatures along the line of sight is always broader than the one given by a model with constant dust temperature. For comparison, predicted spectra for Models A-D are shown in Figure 3.14. They fit the observational data very well. The fitted temperature of ~ 32 K represents an average dust temperature along the line of sight and does not have an important physical meaning. As one can see from Figure 3.11 dust temperature decreases monotonically with the distance from the center of the cloud. The value of 32 K corresponds to a relatively small region, ~ 1 pc from the center. The situation is different for the gas kinetic temperature which, as discussed in Chapter IV, is almost constant over most of the envelope. As far as H_2 column density is concerned, I consider the predictions of simple model to be quite accurate taking into account all the simplifications involved.

Although the model of Gordon fits the data as well as my simple model, there are some significant differences in the model predictions. The optical depth of 0.06 at 1300 μ derived by Gordon, together with his emissivity law, leads to an extremely high 100 μ optical depth of 10. This comes from the fact that in constant temperature model the flux density is independent of the optical depth once the emission becomes optically thick. The short wavelength optical depth can, therefore, be artificially increased without affecting the spectrum. The situation is different for complete models described in previous sections. Because of the steep temperature gradient through the cloud, the short wavelength flux is strongly decreased if the optical depth at short wavelengths is overestimated. The simple model is, therefore, not sensitive to short wavelength emission, and one has to be extremely careful choosing the functional form of the grain emissivity law.

E. Conclusion

Based on the model calculations I conclude that the diameter of the northern core is between 0.4 and 0.5 pc. This leads to a middle core diameter of 0.3 - 0.6 pc. The important conclusion is that diameters of the middle core bigger than 0.6 pc are rather unlikely, as they result in too high middle-to-north peak flux ratio in a 30″ beam. This has clear implications for the molecular abundances in the cloud. For all models with good fit to the observational data, the parameter X which scales the density in the envelope is somewhat bigger than unity. This seems to confirm the conclusion of the high H_2 column density through the envelope drawn in Chapter II.

Another important result of the calculations is that the luminosity of the northern source is rather low, $1 - 2 \times 10^6\ L_\odot$, compared to $\sim 5 \times 10^6\ L_\odot$ given by Benson and Johnston (1986) based on free-free emission from compact H II regions. The free-free emission data, however, may involve significant uncertainty. New VLA observations of Gaume and Claussen (1988) suggest much lower luminosities of both northern and middle sources than the original data of Benson and Johnston. The uncertainty of the middle source luminosity based on the model calculations can be estimated from Figure 3.8. The 100 μ flux density in a 60″ beam, which is a sensitive function of this luminosity, changes by ~ 20% for a 25% change in the luminosity. The scatter of the observational data is quite significant around this wavelength. Assuming calibration errors of ~ 25%, one gets a luminosity error of ~ 30%. In order to estimate the uncertainty of the northern source luminosity I ran additional models with luminosities of this source higher and lower by 25% compared to model CB. I adjusted the 100 μ optical depth to keep the same middle-to-north flux ratio at 1100 μ for all three models. The middle-to-north flux ratio changes by ~ 5% at 450 μ and ~ 7% at 350 μ for a 25% change in the northern source luminosity. This is about the order of observational errors in our data. The corresponding change at 100 μ is ~ 30%. Luminosities of the northern source much higher than our estimates are inconsistent with observations. For example a model with northern source luminosity a factor of 3 higher than that in model CB and the same middle-to-north ratio at 1100 μ predicts ratios of 0.9 and 1.04 at 450 μ and 350 μ, respectively. These ratios are significantly lower than the observed values. The very high northern source luminosity of ~ 10^7 $L_\odot$ suggested by Thronson and Harper (1986) seems to be completely ruled out by the model calculations. The foreground attenuation plays an important role in decreasing the observed flux density from the northern source at wavelengths shorter than ~ 100 μ. It is essential for explaining the absence of the 53 μ emission associated with Sgr B2(N). The extinction *cannot* explain, however, the observed change in the middle-to-north peak flux ratio between 1100 μ and 350 μ, *where the optical depth is still low.* The middle source luminosity based on the model calculations is ~ 1 - 2 × 10^7 $L_\odot$, somewhat higher than that suggested either by Benson and Johnston, or Gaume and Claussen. One possible way to lower the middle source luminosity would be to change the slope of the far infrared grain emissivity law. If the slope were less steep one would have to decrease the 100 μ optical depth in order to get the same flux density at millimeter wavelengths. The lower optical depth would result in a higher 100 μ flux density. In order to lower the 100 μ flux density to the required value one would have to decrease the luminosity of the middle source. A clear conclusion of the model calculations is that the middle source luminosity is an order of magnitude higher than that of the northern source, unless the grain properties in the two regions are significantly different. In this context it is very interesting that the vibrationally excited molecules peaks at the position of the northern source (Goldsmith *et al.* 1987). If the molecules are really excited by radiation, as suggested by Goldsmith *et al.*, the emission should peak at the position of the middle source, where a stronger radiation field is present. The high H_2 density of 1 - 2 × 10^7 cm^{-3} present in the northern core is still too low for collisional excitation of vibrational transitions of HC_3N. The fact that the emission of vibrationally excited molecules peak at the position of the northern source seems to indicate a real chemical difference between the two regions. One possibility, suggested by Carlstrom and Vogel (1989), is that the middle source is more evolved than the northern source and has had enough time to destroy molecules in its immediate vicinity, where the strong radiation field is present. HC_3N emission and its implications are further discussed in Chapter V.

Comparison of the model predictions with results of a simple analysis based on constant dust temperature suggests that the simple technique gives satisfactory predictions for the total column density along the line of sight, provided that reasonable form of grain emissivity law is chosen.

Model calculations suggest the total core masses of 1.5 - 4.1 × 10^4 $M_\odot$, and 3 -10 × $10^4 M_\odot$ for the middle and northern cores, respectively. These are very small fractions of the total mass of the cloud, 5 - 10 × 10^6 $M_\odot$.

Table 3.1. - JCMT Beam Sizes and Calibration Factors.

λ	$\theta(FWHM)^a$	$C_\theta{}^b$	$C_{30}{}^c$	$C_{60}{}^d$
1100	19.4	32	77	300
800	16.4	65	220	880
450	16.3	298	1010	4040
350	20.4	1040	2250	9000

[a] The mean FWHM beam width determined by fitting a two dimensional Gaussian to Uranus maps. The beam is slightly elongated in azimuthal direction (a typical semi-major to semi-minor axis ratio of 1.2).

[b] The conversion from the output voltage to the unpolarized flux density in the telescope beam for a source much smaller than the main beam based on the observation of Uranus. The flux from Uranus was assumed to be 50 Jy, 97 Jy, 210 Jy, and 300 Jy for 1100 μ, 800 μ, 450 μ, and 350 μ filters, respectively (JCMT calibration program).

[c] The conversion from the output voltage to the unpolarized flux density in a 30″ beam, calculated according to the formula $C_{30} = C_\theta\ (30/\theta)^2$. Because of the errors in determination of θ, C_{30} can involve may involve significant uncertainty.

[d] The conversion from the output voltage to the unpolarized flux density in a 60″ beam, calculated according to the formula $C_{60} = C_\theta\ (60/\theta)^2$.

Table 3.2. - Observed Flux Densities from Sgr B2 (M).

λ	S_θ[a]	S_{30}[b]	S_{60}[c]	R[d]
1100	79.	105.	210	1.33
800	227	343	783	1.51
450	1192	1919	4686	1.61
350	3962	>3780[e]	>9090[e]	-

[a] Flux density in the telescope beam.

[b] Flux density in a 30″ beam.

[c] Flux density in a 60″ beam.

[d] Ratio of the fluxes in a 30″ and actual telescope beams.

[e] 350 μ flux in large beams is affected by a row of bad pixels present in the data (*cf.* Figure 3.6).

Table 3.3. - Observed Flux Densities from Sgr B2 (N).

λ	S_θ[a]	S_{30}[b]	S_{60}[c]	R[d]
1100	103	123	225	1.19
800	284	370	801	1.30
450	1070	1646	4323	1.54
350	3141	>3173[e]	>8370[e]	-

[a] Flux density in the telescope beam.

[b] Flux density in a 30″ beam.

[c] Flux density in a 60″ beam.

[d] Ratio of the fluxes in a 30″ and actual telescope beams.

[e] 350 μ flux in large beams is affected by a row of bad pixels present in the data (*cf.* Figure 3.6).

Table 3.4. Observed Middle-to-North Peak Flux Ratios.

λ	M/N_{θ}[a]	M/N_{30}[b]
1300	0.80	-
1100	0.76	0.85
800	0.80	0.93
450	1.11	1.17
350	1.26	1.19[c]

[a] Referred to the telescope beam.

[b] Referred to a 30″ beam.

[c] 350 μ flux ratio in a 30″ beam is affected by bad pixels in the data and represents a lower limit to the true ratio.

Table 3.5. - Model Parameters for Models of Sgr B2(M) Core.

Model	r_{in}[a]	d_{in}[b]	X[c]	L[d]	L_1[e]	τ_{100}[f]	M_{core}[g]
A	0.3	9.4×10^6	1.6	1.4×10^7	2.3×10^7	4.4	1.5×10^4
B	0.4	5.6×10^6	1.4	$9. \times 10^6$	1.5×10^7	3.6	2.1×10^4
C	0.5	3.9×10^6	1.1	7.5×10^6	1.3×10^7	3.1	2.9×10^4
D	0.6	3.2×10^6	0.8	$6. \times 10^6$	1.0×10^7	2.9	4.1×10^4
E	0.75	2.4×10^6	0.5	$5. \times 10^6$	8.5×10^6	2.6	6.0×10^4

[a] FWHM diameter of a Gaussian core (pc).

[b] Central H_2 density in the core assuming a gas to dust ratio of 100 by mass (cm^{-3}).

[c] Factor scaling the density distribution in the envelope determined in Chapter II.

[d] Luminosity of the central star for wavelengths longer than 912 Å ($L_\odot$). The stellar temperature does not affect the results and has been set to 40000 K.

[e] Total luminosity of the central star ($L_\odot$).

[f] 100 μ optical depth from the center to the edge of the cloud.

[g] Total mass of the core ($M_\odot$).

Table 3.6. - Predicted Fluxes From Models from Table 3.5.

Model	$S\,(100\mu)^a$	$S_\theta(1100\,\mu)^b$	R^c
A	27.4	75.3	1.35
B	27.0	74.8	1.34
C	28.1	74.2	1.34
D	27.1	75.2	1.34
E	27.3	74.9	1.37

[a] 100 μ flux density in a 60″ beam (kJy).

[b] 1100 μ flux density in a 19.4″ beam (Jy).

[c] Ratio of flux densities in 30″ and 19.4″ beams.

Table 3.7. - Model Parameters for Models of Sgr B2(N) Core.

Model	r_{in}[a]	d_{in}[b]	L[c]	L_1[d]	τ_{100}[e]	M_{core}[f]
A	0.25	3.6×10^7	$5. \times 10^6$	8.5×10^6	11.7	3.4×10^4
B	0.4	1.7×10^7	$1. \times 10^6$	1.7×10^6	9.2	6.5×10^4
C	0.4	1.8×10^7	$1. \times 10^6$	1.7×10^6	9.6	6.9×10^4
D	0.5	1.3×10^7	$6. \times 10^5$	1.0×10^6	8.4	9.7×10^4
E	0.5	1.3×10^7	$6. \times 10^5$	1.0×10^6	8.6	9.7×10^4

[a] FWHM diameter of a Gaussian core (pc).

[b] Central H_2 density in the core assuming a gas to dust ratio of 100 by mass (cm^{-3}).

[c] Luminosity of the central heating source for wavelengths longer than 912 Å ($L_\odot$).

[d] Total luminosity of the central heating source ($L_\odot$). The stellar temperature does not affect the results and has been set to 40000 K.

[e] 100 μ optical depth from the center to the edge of the cloud.

Table 3.8. - Combined Models of Sgr B2.

Model	r_M[a]	r_N[b]	$M\,(30/\theta)$[c]	$N\,(30/\theta)$[d]	$M/N\,(30)$[e]	$M/N\,(\theta)$[f]
Observed Value			1.34	1.21	0.86	0.77
AA	0.3	0.25	1.35	1.15	0.90	0.76
AB*	0.3	0.4	1.35	1.21	0.86	0.77
BB*	0.4	0.4	1.34	1.20	0.87	0.78
CB*	0.5	0.4	1.34	1.18	0.88	0.78
DC	0.6	0.4	1.34	1.16	0.89	0.77
EC	0.75	0.4	1.37	1.14	0.94	0.78
AD	0.3	0.5	1.35	1.26	0.82	0.77
BD	0.4	0.5	1.34	1.24	0.83	0.77
CD*	0.5	0.5	1.34	1.23	0.84	0.77
DE*	0.6	0.5	1.34	1.21	0.86	0.77
EE	0.75	0.5	1.37	1.19	0.90	0.78

[a] Diameter of the middle core (pc).

[b] Diameter of the northern core (pc).

[c] 1100 μ flux ratio in 30″ and telescope beams for the middle source.

[d] 1100 μ flux ratio in 30″ and telescope beams for the northern source.

[e] 1100 μ middle-to-north flux ratio in a 30″ beam.

[f] 1100 μ middle-to-north flux ratio in the telescope beam.

* Denotes a good model of the source.

Table 3.9. - Column Densities at the Position of Sgr B2(M).

Model	$N_{H_2}(23'')$	$N_{H_2}(45'')$	$N_{H_2}(60'')$	M_{total}
A	2.5×10^{24}	1.8×10^{24}	1.5×10^{24}	1.0×10^{7}
B	2.6×10^{24}	1.7×10^{24}	1.4×10^{24}	8.8×10^{6}
C	2.6×10^{24}	1.5×10^{24}	1.2×10^{24}	6.9×10^{6}
D	2.7×10^{24}	1.4×10^{24}	1.1×10^{24}	5.0×10^{6}
E	2.8×10^{24}	1.3×10^{24}	0.9×10^{24}	3.2×10^{6}

The H_2 column densities (cm^{-2}) at the position of Sgr B2(M) in 23″, 45″, and 60″ FWHM beams for final models of the source and the total mass of the cloud ($M_\odot$).

Figure 3.1. - A contour map of the 1300 μ continuum emission in Sgr B2. The FWHM beam size and main beam efficiency are determined to be 23″ and 0.1, respectively. The conversion from the antenna temperature corrected for atmospheric attenuation and warm losses to unpolarized flux density is 185 Jy K^{-1}. The peak antenna temperatures are 0.29 K and 0.24 K for the northern and middle sources, respectively. This corresponds to flux densities of 56 Jy and 44 Jy. The contour levels are 0.9, 0.8, 0.7, 0.6, and 0.5 of the peak flux density. The dashed line represents a boundary of the region for which the data is available. The coordinates of the (0,0) position are: $\alpha_{1950} = 17^h 44^m 10.5^s$, $\delta_{1950} = -28°22'05''$.

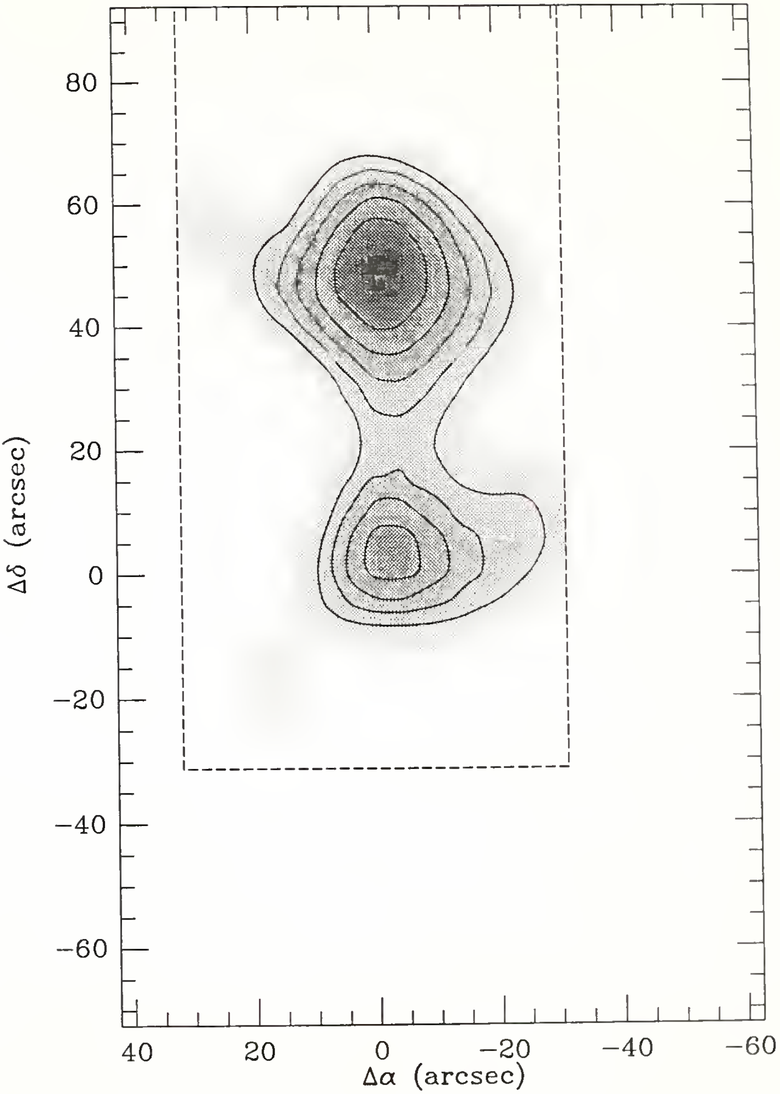
80
60
40
20
0
−20
−40
−60
Δδ (arcsec)
40
20
0
−20
−40
−60
Δα (arcsec)

Figure 3.2. - Observed spectrum of the IR emission from Sgr B2. The figure has been taken from Goldsmith, Snell, and Lis (1987). The data refer to a 60″ beam except for the three longest wavelength points which were taken with 77″, 135″, and 70″ beams, respectively. The wavelengths and references for the data are: (1) 2.8 cm (Downes *et al.* 1976); (2) 1.9 cm (Kapitzky and Dent 1974); (3) 1 cm (Downes, Maxwell, and Rinehart 1970); (4) 1.3 mm (Goldsmith, Snell, and Lis 1987); (5) 1 mm (Westerbrook *et al* 1976); (6) 350 μ (Righini, Simon, and Joyce 1976); (7) 175 μ, 100 μ, and 53 μ (Harvey, Campbell, and Hoffman 1977); (8) 155 μ and 125 μ (Thronson and Harper 1986); (9) 100 μ, 50 μ and 30 μ (Gatley *et al.* 1978).

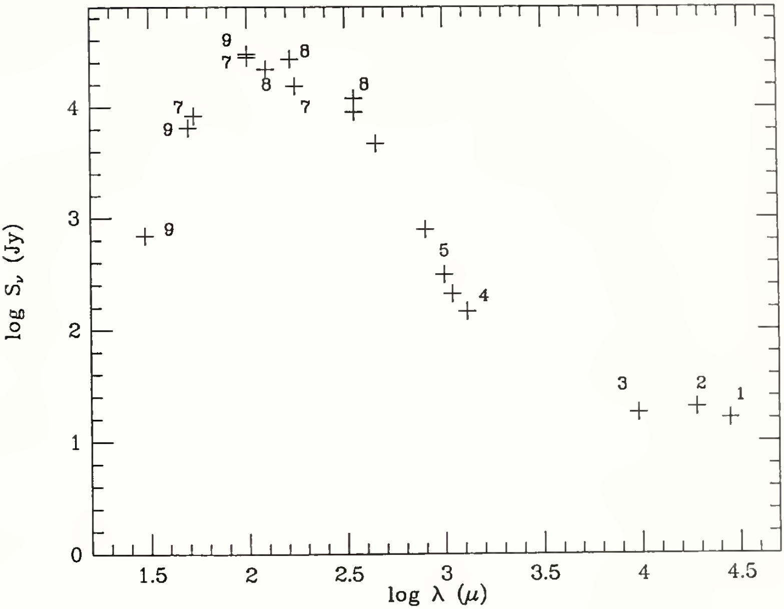
log S_ν (Jy)
log λ (μ)
0
1
2
3
4
1.5
2
2.5
3
3.5
4
4.5
9
7
9
7
8
8
7
8
7
9
9
5
4
3
2
1

Figure 3.3. - A contour map of the 1100 μ continuum emission in Sgr B2. The FWHM beam size is 19.4″. The conversion from the output voltage to unpolarized flux density is 32 Jy V^{-1}. The peak flux densities from the northern and middle sources are 103 Jy and 79 Jy, respectively. The contour levels are 0.9, 0.8, 0.7, 0.6, 0.5, 0.4, 0.3, 0.2, and 0.1 of the peak flux density. The dashed line represents a boundary of the region for which the data is available. The coordinates of the (0,0) position are: α_{1950} = $17^h 44^m 10.5^s$, δ_{1950} = -28°22′05″.

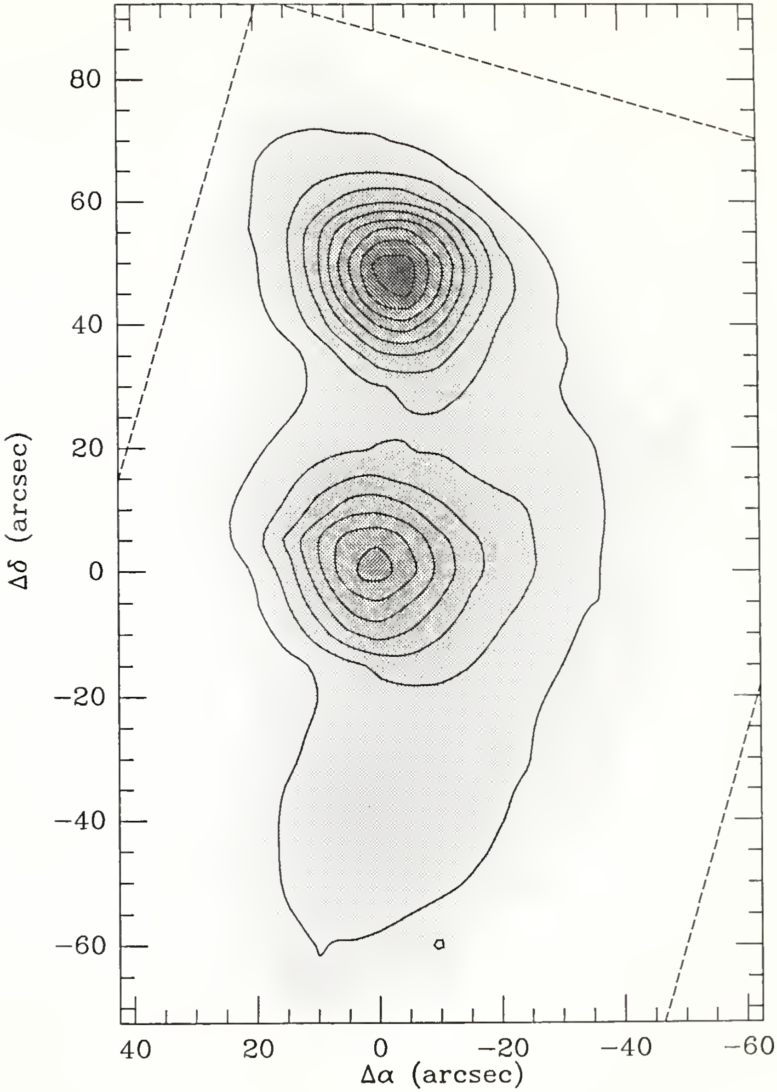
80
60
40
20
0
−20
−40
−60
Δδ (arcsec)
40
20
0
−20
−40
−60
Δα (arcsec)

Figure 3.4. - A contour map of the 800 μ continuum emission in Sgr B2. The FWHM beam size is 16.4″. The conversion from the output voltage to unpolarized flux density is 65 Jy V^{-1}. The peak flux densities from the northern and middle sources are 284 Jy and 227 Jy, respectively. The contour levels are 0.9, 0.8, 0.7, 0.6, 0.5, 0.4, 0.3, 0.2, and 0.1 of the peak flux density. The dashed line represents a boundary of the region for which the data is available. The coordinates of the (0,0) position are: α_{1950} = $17^h44^m10.5^s$, δ_{1950} = -28°22′05″.

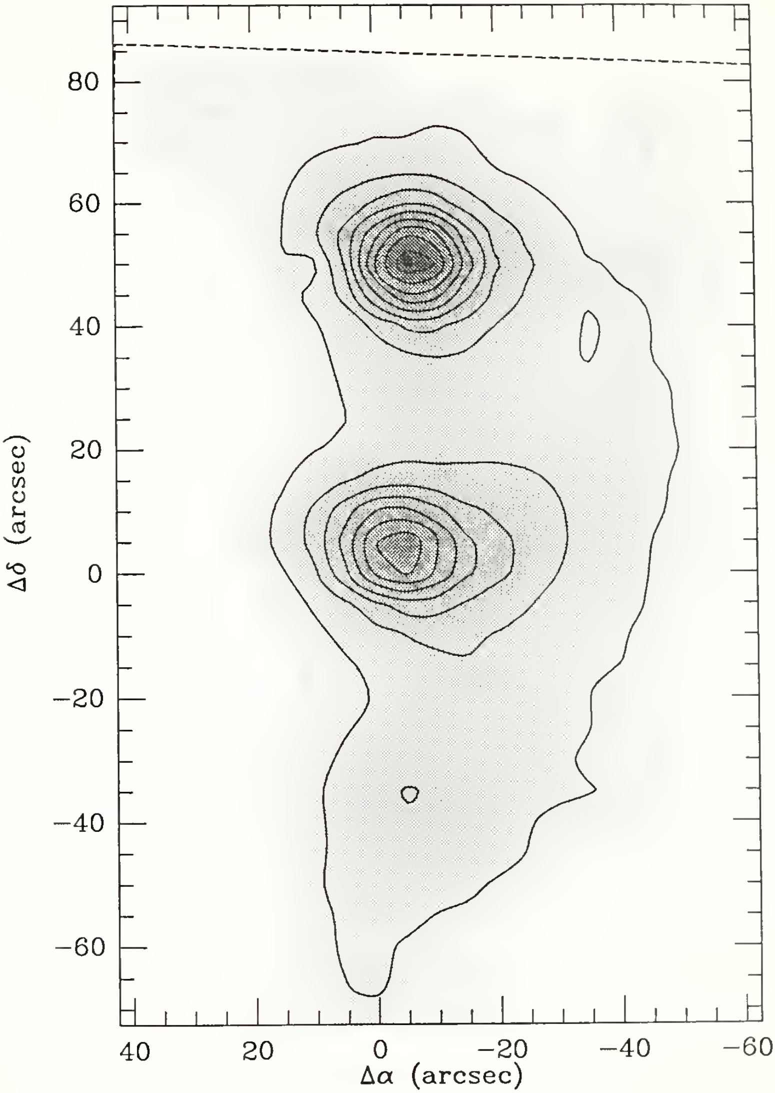
80
60
40
20
0
−20
−40
−60
Δδ (arcsec)
40
20
0
−20
−40
−60
Δα (arcsec)

Figure 3.5. - A contour map of the 450 μ continuum emission in Sgr B2. The FWHM beam size is 16.3″. The conversion from the output voltage to unpolarized flux density is 300 Jy V^{-1}. The peak flux densities from the northern and middle sources are 1070 Jy and 1192 Jy, respectively. The contour levels are 0.9, 0.8, 0.7, 0.6, 0.5, 0.4, 0.3, 0.2, and 0.1 of the peak flux density. The dashed line represents a boundary of the region for which the data is available. The coordinates of the (0,0) position are: α_{1950} = $17^h 44^m 10.5^s$, δ_{1950} = -28°22′05″.

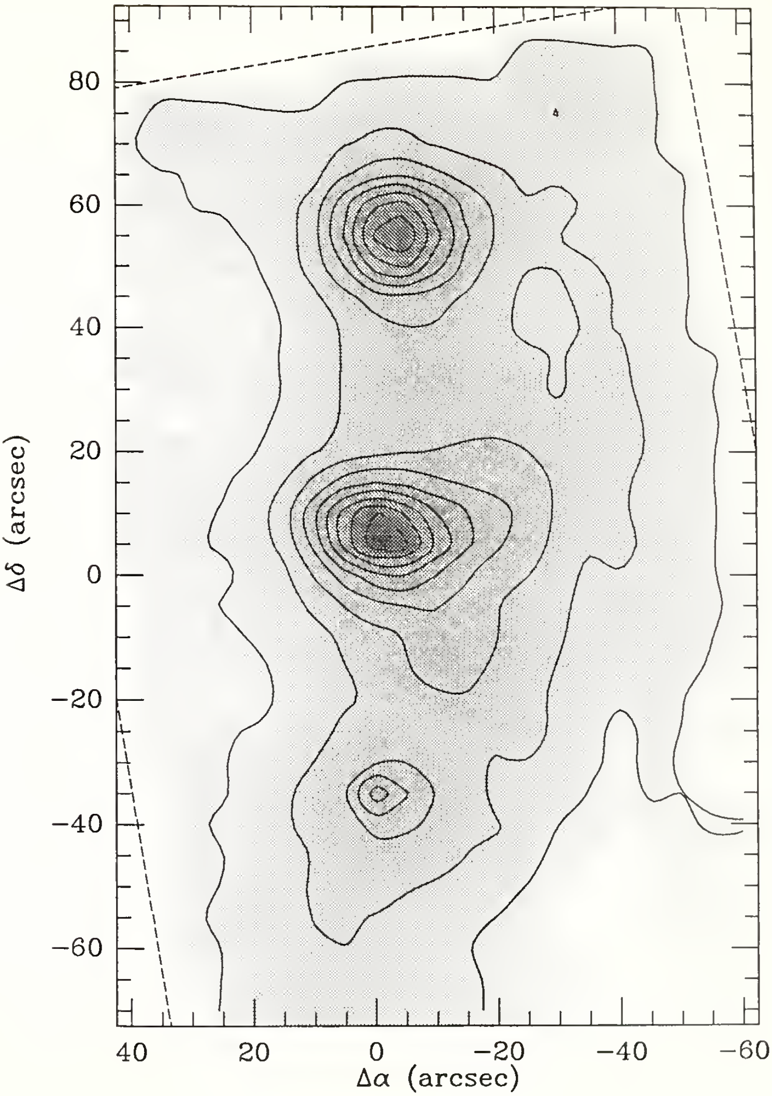
80
60
40
20
0
−20
−40
−60
Δδ (arcsec)
40
20
0
−20
−40
−60
Δα (arcsec)

Figure 3.6. - A contour map of the 350 μ continuum emission in Sgr B2. The FWHM beam size is 20.4″. The conversion from the output voltage to unpolarized flux density is 1040 Jy V^{-1}. The peak flux densities from the northern and middle sources are 3140 Jy and 3960 Jy, respectively. The contour levels are 0.9, 0.8, 0.7, 0.6, 0.5, 0.4, 0.3, 0.2, and 0.1 of the peak flux density. A row of bad pixels close to the middle source is responsible for the division in the emission between the middle and northern sources. The coordinates of the (0,0) position are: $\alpha_{1950} = 17^h 44^m 10.5^s$, $\delta_{1950} = -28°22'05''$.

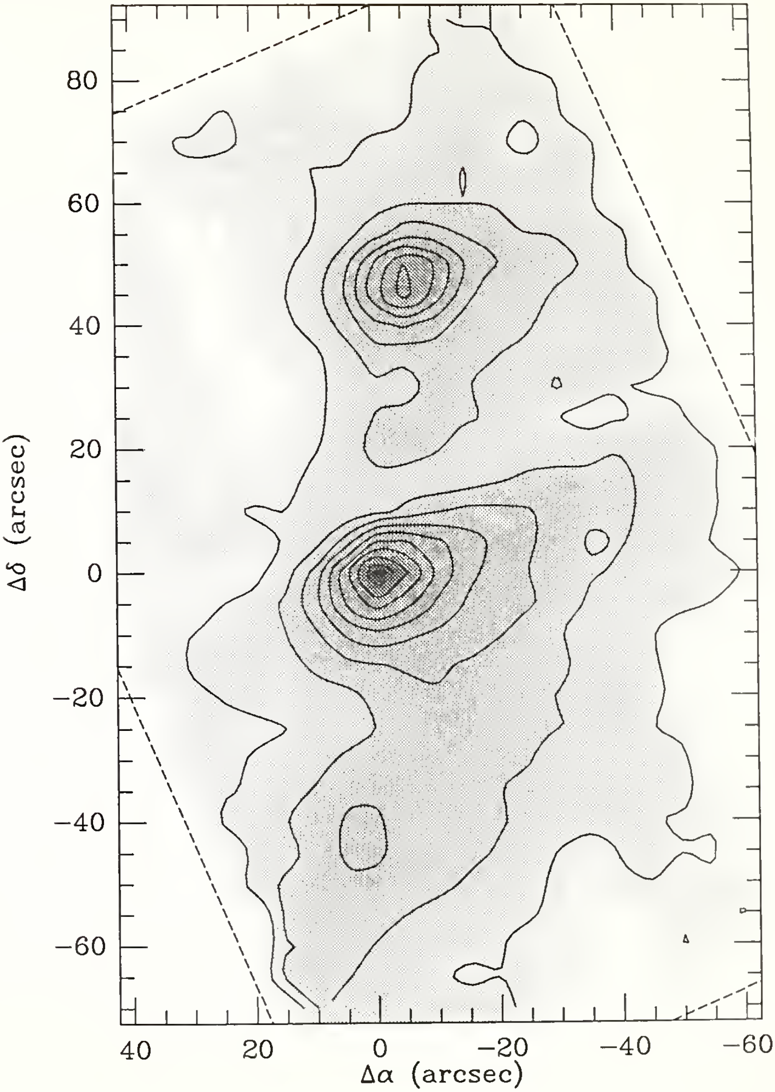
80
60
40
20
0
−20
−40
−60
Δδ (arcsec)
40
20
0
−20
−40
−60
Δα (arcsec)

Figure 3.7 - The effect of the optical depth on the IR spectrum. The 100 μ optical depths are 2.3 (dotted line), 3.1 (solid line), and 3.9 (dashed line). Increasing optical depth results in higher flux densities at long wavelengths, and lower flux densities at short wavelengths. The peak of the observed spectrum is shifted to longer wavelengths. The 1100 μ flux in a 60″ beam is 118 Jy, 156 Jy, and 193 Jy, for $\tau = 2.3$, 3.1, and 3.9, respectively. The long wavelength flux density is, therefore, approximately proportional to the 100 μ optical depth. The short wavelength flux density changes faster than the optical depth. The corresponding flux densities at 50 μ are: 12.9 kJy, 9.1 kJy, and 6.5 kJy. The wavelength of the peak of the spectrum is also approximately proportional to the optical depth. The corresponding values are 95 μ, 110 μ, and 120 μ.

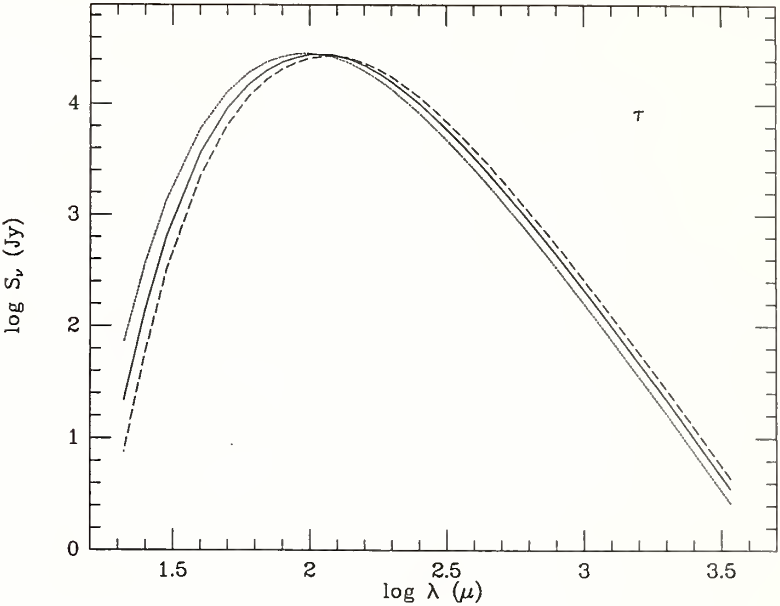
log S_ν (Jy)
log λ (μ)
0
1
2
3
4
1.5
2
2.5
3
3.5
τ

Figure 3.8 - The effect of the central luminosity on the IR spectrum. The long wavelength part of the spectrum is only slightly affected by the luminosity. The model luminosities are 5.6×10^6 $L_\odot$ (dotted line), 7.5×10^6 $L_\odot$ (solid line), and 9.4×10^6 $L_\odot$ (dashed line). The 1100 μ flux density changes from 144 Jy to 166 Jy. To the first approximation the effect is linear. The peak flux in a 60″ beam increases with L irrespective of wavelength. The corresponding values are 23 kJy, 28 kJy, and 33 kJy. The wavelength of the peak decreases from 120 μ to 100 μ, and the short wavelength flux density also increases. The corresponding flux densities at 50 μ are: 6.4 kJy, 9.1 kJy, and 11.9 kJy.

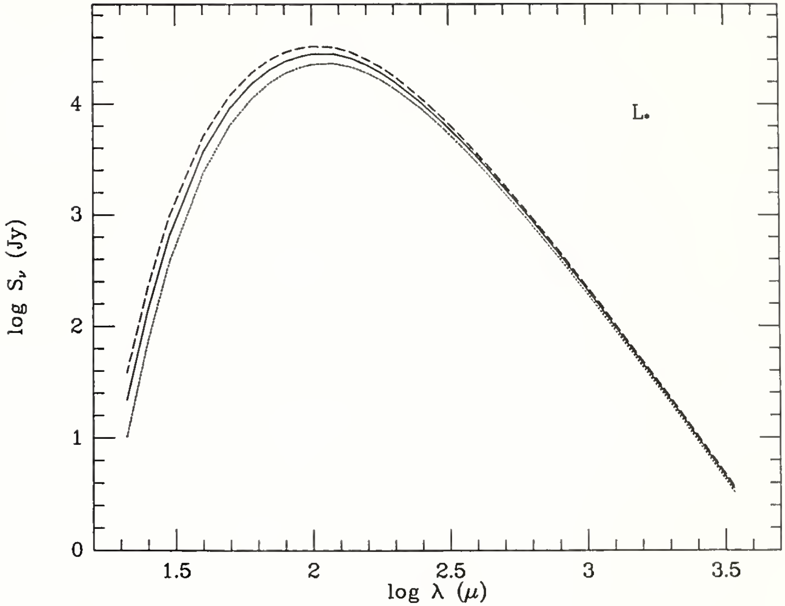
L.
log S$_\nu$ (Jy)
0
1
2
3
4
1.5
2
2.5
3
3.5
log λ (μ)

Figure 3.9 - The effect of the central source temperature on the IR spectrum. The central source temperatures are 40000 K (solid line), and 20000 K (dashed line). The spectrum is almost uneffected by the temperature.

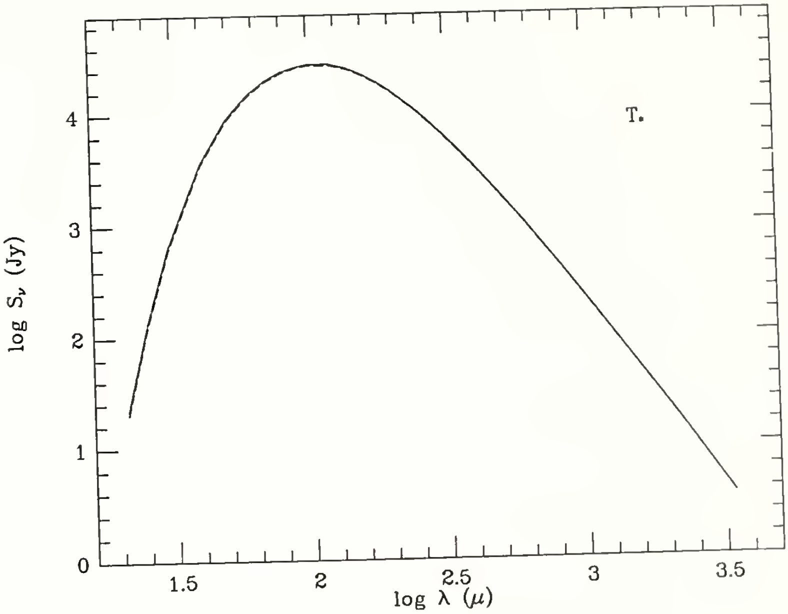
T.
log S_ν (Jy)
0
1
2
3
4
1.5
2
2.5
3
3.5
log λ (μ)

Figure 3.10. - The effect of the grain emissivity on the IR spectrum. The slopes of the grain emissivity law for wavelengths longer than 100 µ are: -1.75 (dotted line), -1.5 (solid line), and -1.25 (dashed line). Only the long wavelength flux density is affected. The 1100 µ flux density changes from 88 Jy to 272 Jy.

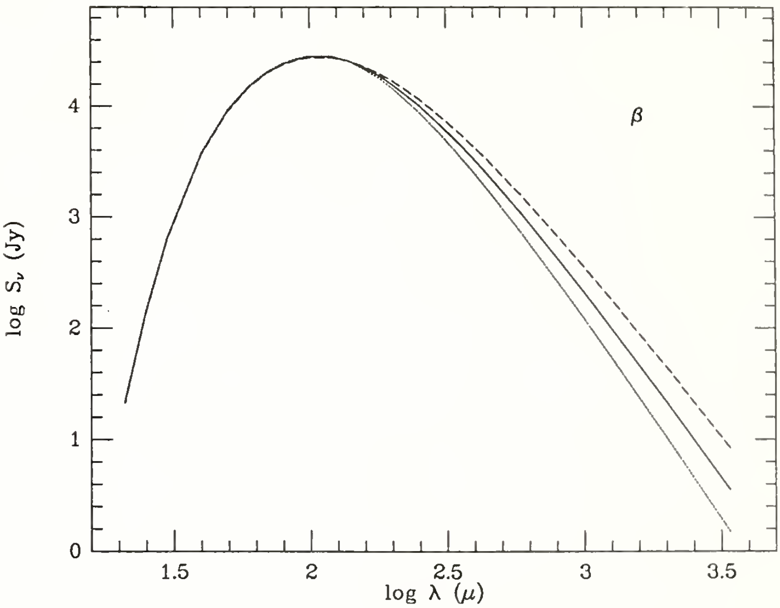
β
log S$_\nu$ (Jy)
0
1
2
3
4
log λ (μ)
1.5
2
2.5
3
3.5

Figure 3.11. - Temperature distribution for Sgr B2(M) models. Increasing luminosity of the central source increase the dust temperature in the inner ~ 1 pc region. The dust away from the center of the cloud is not affected by the luminosity change, because higher luminosities are accompanied by higher optical depths through the core. The upper dotted line corresponds to the analytic solution given by eq. (3.2) for Model C.

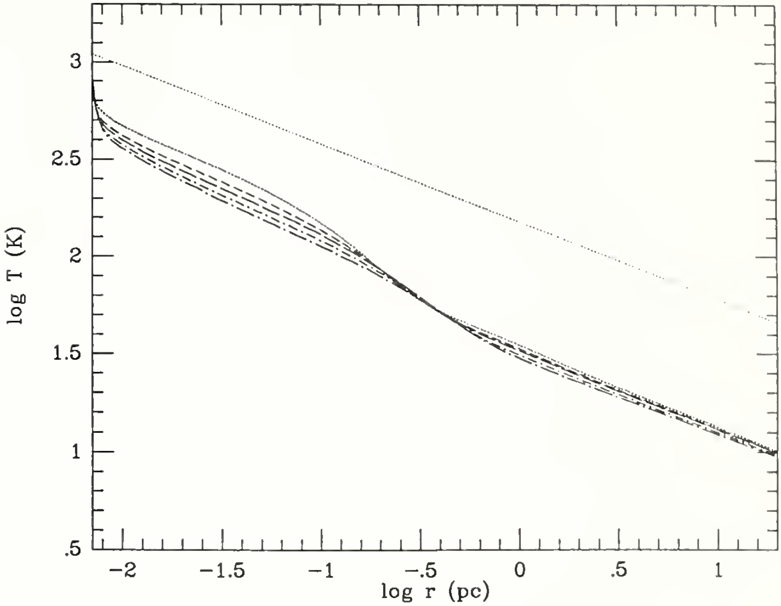
log T (K)
3
2.5
2
1.5
1
.5
−2
−1.5
−1
−.5
0
.5
1
log r (pc)

Figure 3.12. - The geometry of Sgr B2 models. The extended molecular cloud has a radius of ~ 22.5 pc and consists of a constant density component and a power law density component with an exponent of -2 extending outward from ~ 1.25 pc. The continuum emission comes from two small cores embedded in the extended cloud, which due to small beam filling factor and high temperature do not show up in the $J=1\rightarrow0$ transition of $C^{18}O$. The Sgr B2(M) continuum source has a diameter of ~ 0.5 pc and is situated at the center of the molecular cloud. The Sgr B2(N) continuum source is a small, dense clump of material situated in the envelope behind the central region of the cloud, and its emission at short wavelengths is attenuated by foreground dust. The lower panel shows the density distribution in the cloud which consists of constant density component, power law component with radial exponent of -2 extending outward from 1.25 pc, and Gaussian density core.

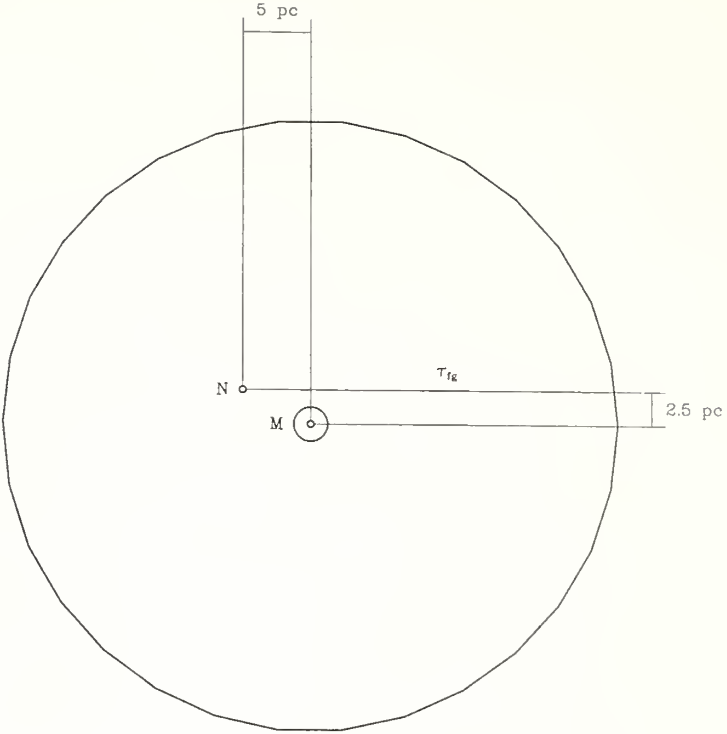
5 pc
N
M
r_fg
2.5 pc

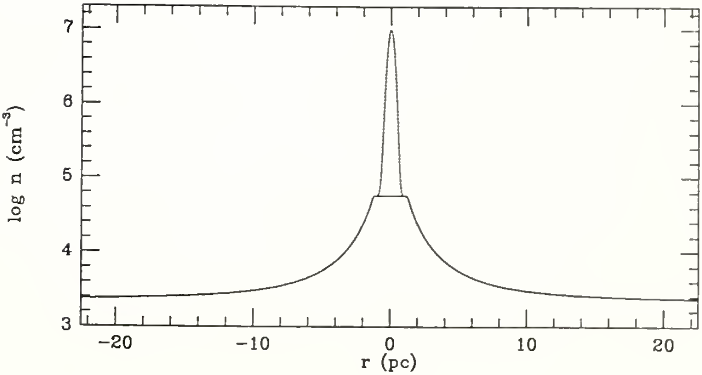
log n (cm^-3)
7
6
5
4
3
−20
−10
0
10
20
r (pc)

Figure 3.13. - Predicted spectra for constant temperature models. The average dust temperatures along the line of sight are: 31 K (dotted line), 32 K (short dashed line), and 33 K (long dashed line). The 100 μ optical depths are 1.15, 1.0, and 0.85 respectively. I assumed the same grain emissivity law as discussed in section B and the effective solid angle corresponding to 60 FWHM beam width. The constant temperature models fail to reproduce the observed spectrum at short wavelengths, predicting too low flux densities. The dashed dotted line correspond to the model of Gordon (1988).

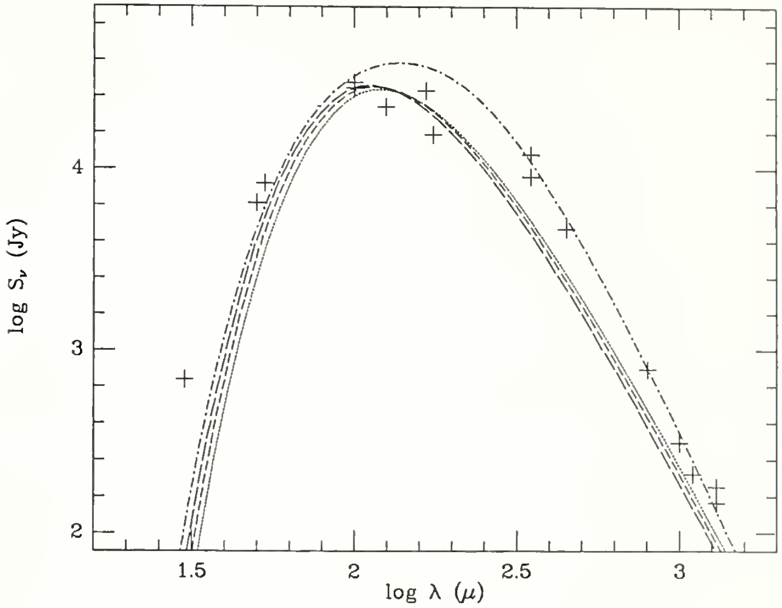
log S_ν (Jy)
4
3
2
1.5
2
2.5
3
log λ (μ)

Figure 3.14. - Predicted spectra for complete cloud models. The models plotted are: AB (solid line), BB (dotted line), CB (short dashed line), CD (long dashed line), and DE (dashed-dotted line) from Table 3.8. The spectra are almost identical and reproduce the observational data well even at short wavelengths. The error bars correspond to estimated errors of the observational data of ± 25%. The filled squares are the new data discussed in the text. The model are optimized for ~ 20″ and 30″ beams. The predicted flux in large beams is slightly underestimated for $\lambda > 300\ \mu$.

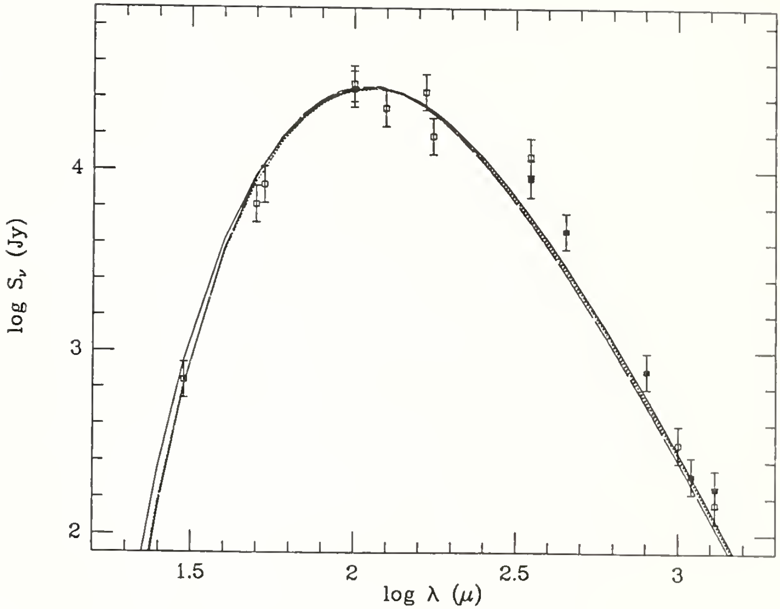
log S$_\nu$ (Jy)
4
3
2
1.5
2
2.5
3
log λ (μ)

CHAPTER IV

MULTITRANSITION CO ISOTOPE STUDIES

In Chapter II I presented a simple analysis of the $J=1\rightarrow0$ transitions of ^{13}CO and C^{18}O based on the assumption of constant excitation temperature through the cloud. I derived the density distribution in the envelope and gave estimate of the total mass of the molecular material. In the present chapter I present observations of higher transitions of CO isotopes, which are modeled using the Monte Carlo code of Bernes (1979). Because higher transitions of CO isotopes (especially the $J=2\rightarrow1$ transition of C^{18}O having moderate optical depth, and observed with high angular resolution) should be much more sensitive to the conditions in the cloud core than the $J=1\rightarrow0$ transition, the data may help to distinguish between different models of the cloud core presented in the previous chapter. The higher transitions are much more difficult to observe than the $J=1\rightarrow0$ transition. It is, therefore, important to determine how much can be learned about the cloud from them, compared to using the $J=1\rightarrow0$ data alone. I also calculate the thermal balance in the cloud in order to compare the importance of different heating sources in the region and to determine the kinetic temperature of the gas. Knowledge of the kinetic temperature is essential for the Monte Carlo calculations.

A. Observations

The $J=2\rightarrow1$ transitions of ^{13}CO and C^{18}O were observed in 1988 January and February, using the 14 m FCRAO antenna. The receiver system employed a Schottky diode mixer and 1.1 - 1.7 GHz FET IF amplifier, both operating at ~ 20 K inside a vacuum dewar (Erickson 1985). Local oscillator power was provided by a frequency tripler, with LO injection and sideband filtering accomplished through quasi-optical interferometers. The image sideband was terminated in a cryogenic load with an effective temperature of 33 K. The receiver had a useful IF bandwidth of over 600 MHz. A single-sideband receiver temperature was ~ 330 K. The typical system temperature (referred to above the Earth's atmosphere) at the low elevation characteristic of Sgr B2 was 1000 - 1700 K (SSB). Saturn was used for pointing measurements and calibration. The FWHM beam width was determined to be 23″. The aperture efficiency based on measurements of Saturn was only ~ 10%. The energy in the error pattern, however, was quite significant and the beam efficiency for an extended source is estimated to be ~ 20%. We used a spectrometer with resolution of 1 MHz, equivalent to 1.4 km s^{-1}. The ^{13}CO emission was observed at 70 positions spaced by 20″ (Table 4.1). The integration time varied from 120 to 640 seconds, depending on the system temperature. A typical r.m.s. fluctuation level is ~ 0.1 K (signal-to-noise ratio of ~ 10:1 - 15:1). The emission is confined to the velocity range 30 - 110 km s^{-1}. A contour map of the integrated intensity is shown in Figure 4.1. The emission peaks in the vicinity of the Sgr B2(M) continuum source. No secondary peak associated with the northern source is observed. This can be easily seen from a plot of the integrated intensity as a function of declination offset for $\Delta\alpha = 0$ (Figure 4.2). The emission falls off smoothly as declination offset increases. Five spectra from a north-south cut st $\Delta\alpha = 0$ with 20″ spacing are shown in Figure 4.3. The self-absorption in the main velocity component at the VLSR of ~ 62 km s^{-1} is more prominent than in the $J = 1 \rightarrow 0$ transition, suggesting higher optical depth.

The $C^{18}O$ emission was observed at 34 positions spaced by 20″ (Table 4.2). The integration time varied from 120 to 480 seconds. The typical r.m.s. noise in the spectra is smaller than 0.2 K (signal-to-noise ratio greater than 5:1). A contour map of the integrated intensity is shown in Figure 4.4. Although the map does not extend far in the southern direction it shows emission peaking in the vicinity of the position of Sgr B2(M) continuum source, similar to ^{13}CO. This is easily seen from the plot of the integrated intensity as a function of the declination offset (Figure 4.5 - solid line). A sample of five spectra from a north-south cut is shown in Figure 4.6. The line is not self-absorbed, suggesting low or moderate optical depth. The line center velocity shifts from ~ 60 km s^{-1} at $\Delta\delta = -0.33'$ to ~ 70 km s^{-1} at $\Delta\delta > 0.66'$. This is most likely a result of a change in relative intensity of different velocity components observed in the spectra. The integrated intensity in the velocity range 45 - 65 km s^{-1} peaks at the position of Sgr B2(M) (dotted line in Figure 4.5). The integrated density in the velocity range 65 - 85 km s^{-1} has more extended distribution, but it clearly peaks in the vicinity of Sgr B2(N). The relatively high noise of the data does not allow for unambiguous decomposition of the spectra into different velocity components, but there seem to be at least four clumps with VLSRs of ~ 55, 62, 70, and 85 km s^{-1} present in the core of the cloud. Similar velocity components are present in the HC_3N data as discussed in Chapter V. Additional C^{18}O data with better signal-to-noise ratio will be very helpful for studying kinematics of the core.

The $J = 3 \rightarrow 2$ transitions of ^{12}CO and ^{13}CO were observed in 1988 February at Wyoming Infrared Observatory on Jelm Mountain, Wyoming. The receiver, located at the Cassegrain focus of the telescope, employed a cooled Schottky diode mixer (Tauber *et al.* 1989). The signal and local oscillator were injected into the mixer using a quasi-optical diplexer. The receiver was tuned for double sideband operation. The IF signal centered at 1.45 GHz was first amplified by a cooled three-stage FET amplificr, and then downconverted to the center frequency of the backends consisting of two 64-channel filterbank spectrometers, with frequency resolutions of 2 MHz (1.7 km s^{-1}), and 5 MHz (4.5 km s^{-1}). The receiver noise temperature was measured in the laboratory to be ~ 800 K (DSB) at 345.8 GHz. The observations were calibrated using the chopper-wheel method (Penzias and Burrus 1973).

The submillimeter beam was aligned with the crosshair in an optical eyepiece attached to the receiver, using a strong source such as Jupiter, so the pointing of the telescope could be checked on a bright star near the source of interest using the eyepiece. Total pointing errors during observations should not exceed a few arcseconds. The beam size was determined from observations of Jupiter. The FWHM beam width of 87″ was close to the diffraction limit. The exact beam shape was determined during an earlier observing run by scanning across the lunar limb. It can be fitted by two Gaussians, one with the FWHM of 87″ and another with FWHM ~ 5 times larger. The main beam efficiency at the elevation of Sgr B2 is estimated to be ~ 0.50. ^{12}CO was observed at 26 positions with 1′ spacing. The line parameters are given in Table 4.3 and a contour map of the integrated intensity of the main velocity component between 45 and 85 km s^{-1} is shown in Figure 4.7. A sample of five spectra from a north-south cut is shown in Figure 4.8. ^{13}CO emission was observed at 5 positions with 1′ spacing. The line parameters are given in Table 4.3 and four spectra from a north-south cut are shown in Figure 4.9. For a comparison I observed the $J = 1 \rightarrow 0$ transition of ^{12}CO. The data were taken in 1988 June using the FCRAO antenna and the receiver system described in Chapter II. The beam size was 45″ and the beam efficiency ~ 0.45. The emission was observed at 35 positions with 1′ spacing. The line parameters are presented in Table 4.4 and a contour map of the integrated intensity in the same velocity range as for the $J = 3 \rightarrow 2$ transition is shown in Figure 4.10. A sample of five spectra from a north-south cut is shown in Figure 4.11. The $J = 1 \rightarrow 0$ spectra of ^{12}CO are almost identical with the $J = 3 \rightarrow 2$ spectra shown in Figure 4.8 suggesting that the first three transitions of CO are thermalized throughout the cloud.

The observational data which should be reproduced by a satisfactory model of the cloud are summarized in Table 4.5. They include the peak antenna temperature and integrated intensity at the center of the cloud for each transition observed, as well as the integrated intensity distribution as a function of the offset from the center of the cloud in the inner 2′ region, as given by ratios of integrated intensities at offsets of 2.5 pc and 5.0 pc to the peak integrated intensity. Because the absolute calibration at 230 GHz is uncertain, one should pay close attention to the distribution of the emission and to the ratio of the ^{13}CO and C^{18}O integrated intensities rather than to the absolute values of the antenna temperature and integrated intensities.

B. Monte Carlo Simulations

Modeling the molecular line emission is much more difficult than modeling the continuum emission from the dust. This is a result of the complicated kinematic structure of the cloud which consists of many clumps of molecular material with different LSR velocities. Radiation emitted in one clump can be absorbed in another clump only if their relative velocity is small compared to the line width. This does not significantly affect optically thin lines, because if the optical depth is low, each photon emitted inside the cloud escapes: velocity shifts between different portions of the cloud change the observed line profile, but do not change the total integrated intensity of the line. The intensity of optically thick lines, however, can be underestimated when the motions of the fragments are neglected. Because the radiation transfer code of Bernes (1979) which has been used in the calculations allows only for systematic motions, such as collapse, this fact has to be kept in mind when comparing the results of model calculations with the observational data.

In Chapter III I presented five models of the cloud (Table 3.5). Four of them (Models A - D) I considered to be consistent with the continuum data. In this chapter I calculate the intensities of ^{13}CO and C^{18}O emission for these models and compare the results with the molecular data presented above. The goal of the calculations is to reproduce the observed intensity distribution as a function of the offset from the center of the cloud. In order to have as few free parameters as possible, I assumed the same density distribution as discussed in Chapter III and a constant velocity dispersion and fractional abundance throughout the cloud. The velocity dispersion and the fractional abundance are the only parameters varied in the calculations. The kinetic temperature of the gas is a very important parameter of the model. The detailed calculations of heating and cooling of the gas are discussed below. Because the cooling and heating rates are highly uncertain, it seems reasonable to start with a simple assumption of equal temperatures of gas and dust, and molecular fractional abundances derived in Chapter II, scaled by the factor *X* from Table 3.7.

Each model cloud was divided into 30 shells, 10 of them in the inner part of the cloud, 1.25 pc in radius, and 20 between 1.25 pc and 22.5 pc. Because the Monte Carlo code uses Λ-iteration it can be applied only to models with the total optical depth less than ~ 100. It is, therefore, only possible to calculate models for ^{13}CO and C^{18}O, and not for ^{12}CO. The results of the calculations for models equivalent to dust models from Table 3.5 are presented in Table 4.6. The difference between the models is best seen in the C^{18}O emission. The intensity of the $J=1\rightarrow0$ transition at the center of the cloud increases significantly as the core size varies from 0.3 pc for Model A to 0.75 pc for Model E. For Model E it is almost a factor of two higher than the observed value. The C^{18}O integrated intensity, however, is almost a linear function of the assumed fractional abundance and can be easily scaled. I therefore consider the distribution of the emission to be much better test of the agreement of the model predictions with the observational data. ^{13}CO emission is much less affected by the size of the core. Because of the relatively high line center optical depth it is not very sensitive to the conditions in the core. It is puzzling, however, that even models with biggest cores predict much too low intensity for the $J=1\rightarrow0$ transition of this molecule. This may suggest that the true ^{13}CO to C^{18}O abundance ratio is higher than derived in Chapter II. The biggest difference between the models is seen in the $J=2\rightarrow1$ transition of C^{18}O. As I mentioned above, the calibration of the data represents a big problem. From the distribution of the integrated intensity it is clear, however, that the source size predicted by models with big core sizes (Models D and E) is too small. This is a combined result of lower H_2 density in the envelope and larger beam filling factor of the core. While the integrated intensity at the center of the cloud increases with increasing core size as a result of increasing beam filling factor of the core, the intensity at off-center positions decreases as a result of lower H_2 density, producing high contrast between center and off-center positions for models with big cores. Also, the ratio of the ^{13}CO to C^{18}O integrated intensity in the $J=2\rightarrow1$ transition, which is not affected by calibration, is too small for models with bigger cores. The ratio of 2.3, predicted by Model A, is very close to the observed ratio of 2.1. One should keep in mind, however, that this ratio, although not affected by calibration, may be a function of assumed gas kinetic temperature in the envelope. The excitation conditions in the envelope can change significantly the degree of self-absorption of ^{13}CO lines and, therefore, affect significantly intensities of ^{13}CO lines without changing significantly intensities of C^{18}O lines. Based on the model calculations with gas kinetic temperature equal to dust temperature I conclude that the observational data seems to favor small core sizes (Models A-C). It is not clear, however, how much the results will change after including heating and cooling of the gas. The ^{12}CO data suggest relatively high temperatures of ~ 15 - 20 K to be present over most of the region. This suggests that gas temperature is higher in the envelope than dust temperature. As I will show later, this results from the fact that turbulence is the main heating source in the region. Higher kinetic temperatures should help to increase the observed source size in the J=2→1 transition of $C^{18}O$ for models with bigger cores.

C. Thermal Balance

Different mechanisms of heating and cooling of the interstellar gas have been discussed by Black (1987). Heating sources of the gas in dense molecular clouds include cosmic rays, turbulence, dissipation of Alfvén waves, photoelectric effect on grains (cloud edges) and collisions with warm dust. The rate for cosmic ray heating (Black 1987) is given by

$$\Gamma_{cr} = 4\times10^{-28} \frac{\zeta_p}{4\times10^{-17}} \frac{\varepsilon_h}{6\,eV} n_{H_2} \quad erg\ s^{-1}\ cm^{-3}\ , \tag{4.1}$$

where ζ_p is the primary ionization rate, ε_h is the mean heating input per primary ionization, and n_{H_2} is the molecular hydrogen volume density. Turbulent heating of a molecular cloud (Boland and de Jong 1984) is given by

$$\Gamma_{turb} = 5.4\times10^{-30} \frac{\alpha^3}{1+\alpha^2} n_{H_2} T^{1.5} \quad erg\ s^{-1}\ cm^{-3}\ , \tag{4.2}$$

where $\alpha = v_{turb}(\frac{\pi m}{8kT})^{-1/2}$ is a parameter characterizing both turbulent velocity and length scale, and an average mass per particle, m =2.34, assuming the standard helium abundance. Magnetic heating (Hartquist 1977) is given by

$$\Gamma_{Alfv\acute{e}n} = 3.2\times10^{-27} f\, n_{H_2}\ , \tag{4.3}$$

where f is the energy stored in Alfvén waves as a fraction of the total gravitational energy of the cloud, and the magnetic field strength is assumed to vary as $n_{H_2}^{1/2}$. In the calculations I assumed the energy fraction stored in Alfvén waves to be equal to 0.2. The value of f does not affect the calculations, because magnetic heating gives a rather minor contribution to the total heating rate.

Photoelectric effect on dust grains is an important heating source of molecular cloud edges. The photoelectric heating rate in an unattenuated radiation field is given by

$$\Gamma_{ph} = 8\times10^{-26}\, n_{H_2}\,, \tag{4.4}$$

(Black 1987). I assumed that inside the cloud the heating rate varies as $\exp(-\beta\tau)$, where τ is the dust optical depth from the edge of the cloud, and β accounts for clumpy structure of the cloud. The radiation fields penetrates deeper into a clumpy cloud cloud than it would into a cloud with uniform density distribution. In the calculations I assumed β to be equal to 0.5. The value of β affects the temperature distribution at the edge of the cloud, but it has little effect on the intensity of observed lines as long as it is not extremely small. Finally heating by collisions with warm dust has been discussed by Burke and Hollenbach (1983). The heating rate is given by

$$\Gamma_{gr} = n_{gr} n_H \sigma_{gr} \left(\frac{8kT}{\pi M_H}\right)^{1/2} \alpha_T 2k(T_{gr}-T)\,, \tag{4.5}$$

where the thermal accommodation coefficient $\alpha \approx 0.35$, and n_H is hydrogen *nucleon* density. Assuming the same dust parameters as discussed in Chapter III (0.1 μ radius, 3 g cm^{-3} density, and a gas to dust ratio of 100 by mass), I obtain the following formula

$$\Gamma_{gr} = 2.3\times10^{-33}\, n_{H_2}^2\, T^{1/2}\,(T_{gr}-T)\,. \tag{4.6}$$

The coefficient of 2.3×10^{-33}, used in the calculations is a factor of 4 lower than that given by Black (1987). This is a result of different parameters of dust grains used, and produces rather minor change in intensities of observed lines.

Different cooling mechanisms of dense molecular clouds have been discussed by Goldsmith and Langer (1978). In my analysis I used the same functional form of total cooling rates on kinetic temperature and H_2 density as given by Goldsmith and Langer. It has to be kept in mind, however, that the rates depend critically on fractional abundances of different molecular species and radiation transfer effects and can involve significant uncertainties. The total cooling rate can be written in the form

$$\Lambda = a\,T^{b}\ . \tag{4.7}$$

The parameters a and b given by Goldsmith and Langer (1978) for different H_2 densities. I fitted the density dependence of the parameters a and b with second order polynomials in order to obtain an analytic formula for the total cooling rate. The fits are shown in Figures 4.12 and 4.13. Because best fit curves turn over at high densities, I simply assumed a constant values of a and b for densities higher than those corresponding to the peak of the fitted parabolas. This can result in underestimating the cooling rates at densities of ~ 10^6 cm^{-3} and higher. The total heating rate in this density range, however, is entirely dominated by interaction with dust grains, and the gas and dust are well coupled regardless of the cooling rates. The final formulae for a and b are

$$\log_{10} a = \begin{cases} -0.115\,x^2 + 1.25\,x - 28.80 & x<5.44 \\ -25.40 & x\geq 5.44 \end{cases} \tag{4.8}$$

$$b = \begin{cases} -0.086\,x^2 + 1.12\,x - 0.54 & x<6.53 \\ 3.12 & x\geq 6.53 \end{cases}$$

where $x = \log_{10} n_{H_2}$. I used Model C with an intermediate size of the core as a test for cooling and heating rates. The results of the calculations can be tested by comparing the calculated kinetic temperature distribution with the peak ^{12}CO radiation temperature as a function of the offset from the center of the cloud. The kinetic temperature in the envelope calculated using the heating and cooling rates discussed above is relatively high, ~ 40 K, a factor of 2 - 3 higher than the temperature suggested by ^{12}CO data (*cf.* Figure 4.14). This is not very surprising, since the cooling and heating rates are highly uncertain. The temperature in the envelope can be decreased by either increasing the total cooling rate or decreasing the turbulent heating rate which turns out to be a dominant heating source in the region. The first possibility is explored in Figure 4.14 which presents results of the calculations for the cooling rate scaling factors of 1, 2, 3, 4, and 5, upper to lower curve, respectively. The solid line corresponds to the dust temperature. The filled squares, corresponding to the peak ^{12}CO radiation temperature, suggest a scaling factor of ~ 4. Results for models with decreased turbulent heating rate are presented in Figure 4.15. The scaling factors are: 1., 0.5, 0.3, 0.2, and 0.1, upper to lower curve, respectively. A scaling factor of ~ 0.2 seems consistent with ^{12}CO data. The only clear conclusion is that since the cooling and heating rates are indeed not known accurately a scaling factor of ~ 4 does not seem unreasonable. The cooling rate may be in error due to poorly known fractional abundances, radiative transfer effects, etc. The cooling rate is also highly uncertain due to lack of knowledge about density structure and velocity field. The data presented in Chapters II and III suggest that ^{12}CO, which is a dominant coolant included in the calculations of Goldsmith and Langer (1978), may be significantly less abundant in Sgr B2 than in disk clouds. This would have the effect of reducing the cooling rate, but the magnitude of the effect depends not only on the abundance of the cooling agent, but also on the radiation trapping effects and hence is uncertain. Models with the cooling rate scaling factor of 4 and the turbulent heating rate scaling factor of 0.2 give very similar temperature distributions in the envelope. In the final Monte Carlo models I used the reduced turbulent heating rate. One can simply look at this as at a useful parametrization of the temperature distribution in the envelope, consistent with ^{12}CO data. As I mentioned above, the total heating rate is almost entirely dominated by the turbulent dissipation (Figure 4.16), except of the inner 0.1 pc region where dust heating dominates, and at the outer edge of the envelope where photoelectric heating becomes important. Both cosmic ray heating and magnetic heating are insignificant. For distances from the center bigger than ~ 5 pc the gas kinetic temperature is higher than the dust temperature and dust acts as a coolant for the gas.

D. Final Models

Figures 4.17 - 4.20 show the predicted intensity of C^{18}O and ^{13}CO emission for Models A - D as a function of the offset from the center of the cloud. The parameters of the models are given in Table 4.7. The fractional abundances of C^{18}O and ^{13}CO, which have been adjusted to give the correct integrated intensity in the J=1→0 transitions increase slowly with the size of the core to compensate for the decrease in the column density caused by lower H_2 density in the envelope. All models (except of Model E which is unable to reproduce the data) predict an essentially correct intensity distribution in the J=1→0 transitions of C^{18}O and ^{13}CO. This again confirms that the J=1→0 transitions are not sensitive to the conditions in the core. The predicted intensity of the J=2→1 transition of C^{18}O is slightly too low for all models, but it is marginally consistent with the data talking into account the ~ 25 % calibration error. The biggest discrepancy is observed for the J =2→1 transition of ^{13}CO. The model predictions are ~ 50 % higher than the observed intensities. The microturbulent models fail to reproduce the observed ratios of the J =2→1 and J =1→0 transitions of C^{18}O and ^{13}CO at the same time. This may be related to the issue of the clumpy structure of the envelope mentioned briefly in Chapter II. In the framework of the model of Kwan and Sanders (1986) the kinetic temperature inside the clumps is a few times higher than the peak ^{12}CO radiation temperature. The higher kinetic temperature would help to increase the intensity of the $J=2\rightarrow1$ transition of C^{18}O relative to the $J=1\rightarrow0$ transition of this molecule. The optical depth of the $J=1\rightarrow0$ and $J=2\rightarrow1$ transitions of ^{13}CO becomes relatively large in the clumpy model, so the intensities of the two transitions should be almost identical. Although no quantitative calculations have been performed, it seems that the clumpy structure of the envelope may be essential for accurately reproducing the observational data.

The ^{13}CO to C^{18}O abundance ratio for the models presented in Table 4.8 is close to 17, as opposed to the value of 10 derived in Chapter II, under the assumption of equal excitation temperatures. I found it impossible to fit the observational data assuming the fractional abundance ratio of 10. The predicted intensity of the $J=1\rightarrow0$ transition of ^{13}CO is ~ 30 % too low under this assumption. The predicted line profiles of ^{13}CO and C^{18}O transitions for cloud Model C are shown Figure 4.19. They are in qualitative agreement with the observed profiles shown as dotted lines. The largest discrepancy is for the $J=3\rightarrow2$ transition of ^{13}CO (lowest panel). The discrepancy may be produced by large error pattern of the beam. If the energy fraction in the error pattern is as determined for the previous observing run (Tauber *et al.* 1989), the observed profile represents an average over much bigger region than the theoretical main beam profile. Velocity shifts at different positions may obscure the self-absorption of the line. For any model of the cloud the optical depths of the $J=2\rightarrow1$ and $3\rightarrow2$ transitions of ^{13}CO at the center of the cloud are very similar, so the two transitions should have similar self absorption if observed with comparable beams. As I pointed out before, the complicated kinematic structure of the cloud makes it impossible to match exactly the observed profiles with theoretical profiles based on models neglecting relative motions of different fragments. For example all the observed spectra reveal existence of a distinctive fragment with line center velocity of ~ 90 km s^{-1}, which is not present in theoretical profiles. The model allow for making some predictions concerning higher transitions of CO isotopes. The $J=7\rightarrow6$ can now be observed with the KAO with angular resolution of ~ 1.6′. My models predict the peak antenna temperatures of ~ 0.6 K and 3 K for C^{18}O and ^{13}CO respectively. The predicted integrated intensities are ~ 15 and 110 K km s^{-1}. They drop to ~ 25 % of the peak value at an offset of 2.5 pc from the center of the cloud.

Finally I would like to address the issue of how the results of the Monte Carlo calculations compare to the simple model based on constant excitation temperature assumption presented in Chapter II. In Figure 4.21 I plot the average excitation temperature of the two lowest transitions of ^{13}CO and C^{18}O for Model C, calculated according to the formula

$$T_{ex} = \frac{T_o}{\log[\frac{T_o}{T_r}(1-e^{-\tau}) + 1\,]}\,, \tag{4.8}$$

as a function of the projected distance from the center of the cloud. In the above formula T_r is the observed radiation temperature, τ is the line center optical depth, and T_o is the frequency of the transition in Kelvins. The excitation temperature plotted in Figure 4.21 has not been convolved with the telescope beam. The solid line corresponds to the $J=1\rightarrow0$ transition of C^{18}O, dotted line to the $J=2\rightarrow1$ transition of C^{18}O, short dashed line to the $J=1\rightarrow0$ transition of ^{13}CO, and long dashed line to the $J=2\rightarrow1$ transition of ^{13}CO. The excitation temperatures for all transitions are, indeed, constant over relatively large range of projected offsets. For the $J=1\rightarrow0$ transition of C^{18}O the average excitation temperature is ~ 16 K, slightly lower than the value used in

Chapter II. Using the higher excitation temperature results in overestimating the total $C^{18}O$ column density by a factor of 1.3 for off center positions. The excitation temperature at the center of the cloud is ~ 32 K, but beam averaging will lower this value. The 20 K excitation temperature seems to be very close to the beam averaged excitation temperature at the center of the cloud because the peak $C^{18}O$ column density derived in Chapter II is very close to predictions of Models A - D. The lower $C^{18}O$ fractional abundance used in the models is simply a result of higher beam averaged H_2 column density. The only conclusion of Chapter II which seems to be incorrect based on the Monte Carlo simulations is the ^{13}CO to $C^{18}O$ fractional abundance ratio of 10. In Figure 4.22 I plot again the observed correlation between ^{13}CO and $C^{18}O$ integrated intensities together with predictions for Models A - D. Results of model calculations suggest that the slope corresponding to the true abundance ratio is observed only for very low $C^{18}O$ intensities. The fact that points below $C^{18}O$ integrated intensity of ~ 7 K km s^{-1} tend to lie above the line given by the fractional abundance ratio of 9 derived in Chapter II has been attributed to non-LTE excitation of $C^{18}O$ at the edge of the cloud. Model calculations suggest that this conclusion is incorrect.

It is rather difficult to explain the observed constancy of the ^{13}CO to $C^{18}O$ antenna temperature as a function of LSR velocity shown in Figure 2.6. The predicted ratio for Model C is shown in Figure 4.23. The upper panel corresponds to the center of the cloud, lower panel to an off-center position with a projected distance of 10 pc. The ^{13}CO to $C^{18}O$ abundance ratio for Model C is equal to 16. The antenna temperature ratios of 13 to 15 are observed in line wings. There is only one channel with the antenna temperature ratio of ~ 13 present in Figure 2.6. The discrepancy between observed and predicted antenna temperature ratios may be related to the clumpy structure of the cloud. If the emission comes from clumps spread over broad velocity range the observed antenna temperature ratio corresponds to the line center ratios of different clumps. If different clumps have similar line center optical depths the ratio may seem to be constant over broad range of velocities without implying optically thin emission. Even in this case one would expect to see a ratio close to the true abundance ratio in the line wings of outermost clumps. The radiation temperature in the region where the true abundance ratio should be observed is rather low, however, and emission from other regions along the line of sight may entirely confuse the data.

E. Conclusion

The Monte Carlo models of line emission of ^{13}CO and $C^{18}O$ provide a final test for the dust models presented in Chapter III. Comparison of predicted line intensities for three lowest transition of ^{13}CO and two lowest transitions of $C^{18}O$ with observational data further support the conclusion of Chapter III that Models A - D may be considered as consistent with observations. Model E fails to reproduce the data predicting too small source sizes in all transitions observed. Calculations of the thermal balance of the gas suggest that turbulence is the main source of heating throughout most of the region, except of the edge and center of the cloud. Gas heating in the central ~ 0.1 pc region is dominated by collisions with dust, while photoelectric heating dominates at the edge. The kinetic temperature in the envelope based on "standard" heating and cooling rates is too high compared to the peak ^{12}CO radiation temperature suggesting that the rates may need revision. A kinetic temperature distribution consistent with observations can be obtained by either increasing the cooling rate by a factor of ~ 4 or by reducing the turbulent heating rate by a factor of ~ 5. Calculations also confirm the assumption made in Chapter II that the emission in the lowest transitions of ^{13}CO and $C^{18}O$ are not very sensitive to the conditions in the core of the cloud. The peak $C^{18}O$ column density based on Models A - D is very close the value obtained in Chapter II, assuming constant $C^{18}O$ excitation temperature. The ^{13}CO to $C^{18}O$ fractional abundance ratio of

9 derived in Chapter II is not supported by Monte Carlo calculations. Models with this abundance ratio predict much too low intensity of the $J = 1 \rightarrow 0$ transition of ^{13}CO. The ^{13}CO to C^{18}O abundance ratio suggested by Monte Carlo models is ~ 17. The observed constancy of the ^{13}CO to C^{18}O antenna temperature ratio as a function of LSR velocity is not reproduced by the Monte Carlo models and may be related to the clumpy structure of the envelope. If the emission comes from several velocity components, spread over wide velocity range, the ^{13}CO to C^{18}O antenna temperature ratio will be a more uniform function of velocity. The ^{13}CO to C^{18}O ratio will be somewhere between its line-wing and line-center values for the one-component case (between 7 and 15 for the off-center position shown in Figure 4.23). The observed ratio of 9 - 10 may be, therefore, reproduced, but rigorous calculations remain to be carried out.

Table 4.1. - Line Parameters of ^{13}CO $J=2\rightarrow1$ Emission in Sgr B2.

$\Delta\alpha$	$\Delta\delta$	V_{mean}	σ_V	$\int T_A^* dv$	T_A^*	σ_T
-1.0	2.0	71.5	18.7	52.3	1.2	0.11
-0.7	2.0	71.2	17.2	59.3	1.3	0.09
-0.3	2.0	70.4	17.1	54.1	1.4	0.14
0.0	2.0	68.4	14.7	53.1	1.5	0.11
0.3	2.0	72.3	15.4	57.0	1.5	0.10
0.7	2.0	69.0	15.5	60.6	1.6	0.13
1.0	2.0	65.7	14.4	47.0	1.4	0.11
-1.0	1.7	72.2	17.1	51.5	1.2	0.09
-0.7	1.7	73.0	17.3	47.7	1.2	0.06
-0.3	1.7	72.1	16.7	51.1	1.4	0.10
0.0	1.7	69.3	15.8	54.9	1.5	0.11
0.3	1.7	71.4	13.0	49.9	1.5	0.10
0.7	1.7	69.1	11.7	41.3	1.4	0.10
1.0	1.7	65.9	11.9	42.1	1.3	0.08
-1.0	1.3	72.6	15.7	45.6	1.2	0.09
-0.7	1.3	72.8	16.0	51.5	1.3	0.09
-0.3	1.3	74.0	16.0	58.9	1.4	0.12
0.0	1.3	70.3	17.4	64.0	1.3	0.08
0.3	1.3	72.9	14.5	58.9	1.8	0.14
0.7	1.3	71.2	15.0	73.3	2.1	0.15
1.0	1.3	66.7	15.8	47.3	1.3	0.11
-1.0	1.0	73.3	17.5	58.5	1.5	0.11
-0.7	1.0	74.4	15.7	65.3	1.7	0.11
-0.3	1.0	74.2	15.6	70.3	2.0	0.09
0.0	1.0	72.6	16.1	68.1	1.8	0.09
0.3	1.0	71.9	15.5	67.6	1.9	0.07
0.7	1.0	68.7	15.2	56.7	1.5	0.10
1.0	1.0	67.1	16.5	51.5	1.1	0.10
-1.0	0.7	74.3	17.1	54.7	1.3	0.16
-0.7	0.7	72.7	17.9	70.3	1.6	0.13
-0.3	0.7	73.7	15.7	59.5	1.5	0.12
0.0	0.7	72.0	16.7	76.0	2.0	0.10
0.3	0.7	69.4	18.1	73.2	1.5	0.14
0.7	0.7	68.1	15.4	48.5	1.2	0.08
1.0	0.7	68.6	17.0	43.5	1.0	0.10
-1.0	0.3	74.9	17.3	61.3	1.3	0.13
-0.7	0.3	75.1	16.2	71.2	1.6	0.13
-0.3	0.3	72.4	17.5	90.4	2.2	0.09
0.0	0.3	71.0	17.7	96.1	2.6	0.08
0.3	0.3	71.2	17.1	76.7	1.8	0.11
0.7	0.3	67.9	16.6	69.6	1.7	0.09
1.0	0.3	67.9	18.2	61.9	1.3	0.08
-1.0	0.0	73.6	17.6	62.0	1.3	0.13
-0.7	0.0	72.1	17.0	78.7	2.0	0.11
-0.3	0.0	69.6	17.6	91.1	2.2	0.10

continued on next page

Table 4.1. - Continued.

$\Delta\alpha$	$\Delta\delta$	V_{mean}	σ_V	$\int T_A^* dv$	T_A^*	σ_T
0.0	0.0	69.4	17.1	96.5	2.7	0.06
0.3	0.0	68.5	17.4	70.4	1.8	0.11
0.7	0.0	67.8	17.4	74.9	1.8	0.11
1.0	0.0	67.0	18.0	67.8	1.5	0.10
-1.0	-0.3	72.7	16.5	58.6	1.6	0.12
-0.7	-0.3	72.0	15.7	70.1	1.6	0.11
-0.3	-0.3	68.5	15.9	70.9	1.9	0.10
0.0	-0.3	69.8	16.8	85.2	2.2	0.09
0.3	-0.3	67.5	16.3	63.7	2.0	0.12
0.7	-0.3	67.5	18.1	77.7	2.0	0.09
1.0	-0.3	66.7	15.9	62.7	1.5	0.10
-1.0	-0.7	75.1	17.1	60.0	1.5	0.13
-0.7	-0.7	74.5	15.9	68.8	1.7	0.11
-0.3	-0.7	71.3	17.7	76.4	1.7	0.09
0.0	-0.7	68.4	17.5	80.2	2.2	0.11
0.3	-0.7	69.8	17.9	72.4	1.8	0.10
0.7	-0.7	69.2	16.3	68.4	1.6	0.09
1.0	-0.7	66.6	16.1	53.8	1.4	0.10
-1.0	-1.0	74.6	17.0	56.1	1.5	0.11
-0.7	-1.0	71.9	17.3	67.3	1.5	0.09
-0.3	-1.0	71.8	17.8	73.9	1.6	0.07
0.0	-1.0	69.9	17.3	65.6	1.5	0.09
0.3	-1.0	70.1	17.6	65.6	1.5	0.12
0.7	-1.0	69.1	17.8	66.2	1.5	0.07
1.0	-1.0	65.7	17.7	64.3	1.6	0.08

The entries in the table are: offsets from the cloud center (arcminutes), mean line velocity (km s^{-1}), velocity dispersion (km s^{-1}), integrated intensity between 0 and 110 km s^{-1} (K km s^{-1}), peak antenna temperature corrected for atmospheric attenuation and warm losses but not corrected for the beam efficiency (K), and r.m.s. noise in the spectrum (K).

Table 4.2. - Line Parameters of $C^{18}O$ $J=2\rightarrow1$ Emission in Sgr B2.

$\Delta\alpha$	$\Delta\delta$	V_{mean}	σ_V	$\int T_A^* dv$	T_A^*	σ_T
0.0	-1.0	64.2	13.1	23.1	1.0	0.16
0.0	-0.7	64.9	9.2	29.1	1.3	0.13
0.0	-0.3	63.8	10.2	30.4	1.7	0.15
1.0	0.0	59.5	15.2	23.3	0.9	0.17
0.7	0.0	64.0	17.1	26.3	1.1	0.18
0.3	0.0	66.4	11.6	20.5	1.2	0.21
0.0	0.0	64.3	12.8	46.5	2.0	0.07
-0.3	0.0	65.1	13.5	35.1	1.4	0.21
-0.7	0.0	71.6	16.6	29.0	0.9	0.18
-1.0	0.0	73.9	13.7	16.8	0.8	0.17
1.0	0.3	65.0	13.2	18.4	1.0	0.20
0.7	0.3	65.4	0.0	12.5	1.0	0.18
0.3	0.3	63.5	12.6	25.9	1.0	0.21
0.0	0.3	69.2	14.1	39.2	1.3	0.12
-0.3	0.3	66.9	11.1	22.5	1.0	0.19
-0.7	0.3	71.2	12.8	17.5	1.0	0.20
-1.0	0.3	77.4	14.9	10.1	0.8	0.19
1.0	0.7	65.3	17.1	23.5	0.8	0.20
0.7	0.7	66.6	12.2	19.3	1.0	0.18
0.3	0.7	65.4	12.3	17.9	0.9	0.20
0.0	0.7	69.4	8.8	26.8	1.2	0.13
-0.3	0.7	75.2	0.0	15.2	0.9	0.20
-0.7	0.7	74.7	10.4	16.6	0.7	0.19
-1.0	0.7	74.9	0.0	12.5	1.0	0.21
1.0	1.0	57.0	8.7	11.1	0.6	0.18
0.7	1.0	72.7	11.0	14.4	0.7	0.19
0.3	1.0	66.6	13.5	27.5	1.0	0.16
0.0	1.0	67.3	10.9	25.5	1.1	0.11
-0.3	1.0	68.4	10.6	21.9	1.0	0.18
-0.7	1.0	71.3	0.0	13.9	0.9	0.16
-1.0	1.0	74.5	14.5	22.4	0.9	0.17
0.0	1.3	70.2	4.9	14.2	0.7	0.11
0.0	1.7	73.9	7.2	14.8	0.7	0.11
0.0	2.0	68.7	15.0	13.5	0.5	0.10
1.0	2.0	64.4	13.3	12.0	0.5	0.14
2.0	2.0	58.8	16.5	8.9	0.5	0.19
3.0	2.0	68.6	20.8	10.7	0.5	0.18

The entries in the table are: offsets from the cloud center (arcminutes), mean line velocity (km s^{-1}), velocity dispersion (km s^{-1}), integrated intensity between 0 and 110 km s^{-1} (K km s^{-1}), peak antenna temperature corrected for atmospheric attenuation and warm losses but not corrected for the beam efficiency (K), and r.m.s. noise in the spectrum (K).

Table 4.3. - Line Parameters of ^{13}CO and ^{12}CO $J = 3 \rightarrow 2$ Emission.

$\Delta\alpha$	$\Delta\delta$	V_{mean}	σ_V	$\int T_A^* dv$	T_A^*	σ_T
0.0	2.0	58.1	20.9	84.9	2.6	0.71
0.0	1.0	71.1	18.8	136.8	2.8	0.58
0.0	0.0	66.1	19.2	176.8	4.1	0.49
0.0	-1.0	67.0	19.6	121.3	4.4	0.58
-1.0	1.0	56.4	19.2	81.1	2.1	0.72
0.0	-2.0	68.9	27.8	785.8	14.0	1.25
-1.0	-2.0	68.4	30.0	947.3	14.3	2.69
2.0	-1.0	60.2	26.9	824.8	11.8	1.79
1.0	-1.0	66.5	26.0	688.2	10.5	0.92
0.0	-1.0	68.7	27.4	798.6	13.9	1.29
-1.0	-1.0	70.5	29.4	847.3	13.6	2.26
-2.0	-1.0	64.4	31.3	842.8	11.4	2.23
2.0	0.0	56.0	29.3	861.7	10.6	1.68
1.0	0.0	61.8	27.4	814.9	11.2	0.74
0.0	0.0	66.9	28.1	843.8	14.3	0.84
-1.0	0.0	70.3	28.5	888.8	14.7	1.87
2.0	1.0	51.7	28.8	948.7	12.6	2.07
1.0	1.0	59.9	28.5	788.1	10.2	1.26
0.0	1.0	61.7	29.2	810.1	11.8	0.97
-1.0	1.0	67.5	30.4	779.8	10.9	1.98
-2.0	1.0	58.9	29.6	703.8	9.9	1.93
2.0	2.0	53.2	28.9	924.1	12.9	2.47
1.0	2.0	54.5	28.5	809.8	11.5	1.51
0.0	2.0	59.3	28.9	749.4	11.0	0.90
-1.0	2.0	63.4	30.1	730.7	10.0	1.52
-2.0	2.0	55.3	29.0	787.6	11.4	2.46
1.0	3.0	53.5	30.6	916.3	11.6	1.93
0.0	3.0	57.1	31.3	788.1	9.3	1.41
-1.0	3.0	56.9	30.5	628.6	8.6	1.96

The entries in the table are: offsets from the cloud center (arcminutes), mean line velocity (km s^{-1}), velocity dispersion (km s^{-1}), integrated intensity between 0 and 110 km s^{-1} (K km s^{-1}), peak antenna temperature corrected for atmospheric attenuation and warm losses but not corrected for the beam efficiency (K), and r.m.s. noise in the spectrum (K). The first five lines correspond to ^{13}CO; the remaining lines to ^{12}CO.

Table 4.4. - Line Parameters of ^{12}CO $J=1\rightarrow0$ Emission in Sgr B2.

$\Delta\alpha$	$\Delta\delta$	V_{mean}	σ_V	$\int T_A^* dv$	T_A^*	σ_T
2.0	3.0	53.2	27.2	675.5	9.2	0.34
1.0	3.0	54.7	27.5	695.6	8.8	0.42
0.0	3.0	55.7	27.5	669.5	8.8	0.36
-1.0	3.0	58.0	28.6	637.4	8.8	0.31
-2.0	3.0	58.1	27.8	615.7	8.7	0.26
2.0	2.0	53.7	27.1	744.4	9.8	0.22
1.0	2.0	54.3	26.7	762.7	11.1	0.25
0.0	2.0	58.7	26.8	755.6	11.4	0.23
-1.0	2.0	63.1	27.5	673.8	9.6	0.22
-2.0	2.0	59.3	28.5	608.6	8.2	0.31
2.0	1.0	56.0	27.9	695.5	9.0	0.25
1.0	1.0	57.7	27.0	663.6	9.9	0.21
0.0	1.0	62.4	27.3	651.6	10.8	0.35
-1.0	1.0	64.9	29.2	713.9	9.6	0.30
-2.0	1.0	65.7	28.4	646.7	9.1	0.25
2.0	0.0	58.3	26.6	616.8	8.2	0.26
1.0	0.0	60.6	26.2	638.8	9.0	0.25
0.0	0.0	66.7	26.6	764.0	13.8	0.24
-1.0	0.0	67.6	28.3	798.2	11.9	0.29
-2.0	0.0	66.6	28.6	694.6	9.6	0.26
2.0	-1.0	60.4	27.2	636.0	8.4	0.25
1.0	-1.0	62.6	25.5	647.5	9.9	0.25
0.0	-1.0	65.3	26.9	656.8	10.4	0.26
-1.0	-1.0	67.6	28.1	745.7	11.7	0.24
-2.0	-1.0	66.5	27.9	664.0	9.6	0.34
2.0	-2.0	60.9	25.7	515.8	7.6	0.37
1.0	-2.0	63.7	26.1	563.2	8.4	0.31
0.0	-2.0	65.5	26.7	588.3	9.6	0.37
-1.0	-2.0	66.9	28.5	648.5	10.3	0.32
-2.0	-2.0	66.0	28.9	674.0	10.0	0.27

The entries in the table are: offsets from the cloud center (arcminutes), mean line velocity (km s^{-1}), velocity dispersion (km s^{-1}), integrated intensity between 0 and 110 km s^{-1} (K km s^{-1}), peak antenna temperature corrected for atmospheric attenuation and warm losses but not corrected for the beam efficiency (K), and r.m.s. noise in the spectrum (K).

Table 4.5. - Summary of CO Isotope Observations of Sgr B2.

Transition	η	θ	T_R	$\int T_R dv$	Δv_{FWHM}	$<R_{2.5}>$	$<R_{5.0}>$
$C^{18}O$ (1-0)	0.45	45.	3.6	84.	23.	0.60	0.40
^{13}CO (1-0)	0.45	45.	14.	535	38.	0.74	0.58
^{12}CO (1-0)	0.45	45.	30.	1590.	53.	0.90	0.86
$C^{18}O$ (2-1)	0.20	23.	10.	230.	24.	0.47	0.30
^{13}CO (2-1)	0.20	23.	13.5	485	36.	0.69	0.55
^{13}CO (3-2)	0.50	90.	8.	350.	44.	0.74	0.49
^{12}CO (3-2)	0.50	90.	29.	1690.	59.	0.98	0.95

The entries in the Table are: molecular transition observed, beam efficiency used for correcting the observed spectra, FWHM beam width, peak antenna temperature and integrated intensity in the 0 - 110 km s^{-1} velocity range corrected for the beam efficiency, FWHM line width, and average ratios of integrated intensities at 2.5 pc and 5.0 pc offsets from the cloud center to the integrated intensity at the center of the cloud.

Table 4.6. - Monte Carlo Predictions for $T_g = T_d$.

Model	T_R	$\int T_R dv$	Δv_{FWHM}	$R_{2.5}$	$R_{5.0}$
		$C^{18}O\ J=1\rightarrow0$			
Observed	3.6	84.	23.	0.60	0.40
A	3.8	85.	22.	0.68	0.55
B	4.0	90.	22.	0.64	0.52
C	4.2	94.	22.	0.64	0.51
D	4.8	108.	23.	0.56	0.44
E	6.5	151.	23.	0.40	0.30
		$^{13}CO\ J=1\rightarrow0$			
Observed	14.	535.	38.	0.74	0.58
A	11.9	377.	32.	0.72	0.60
B	11.7	381.	33.	0.70	0.59
C	11.5	382.	33.	0.69	0.58
D	11.6	398.	34.	0.64	0.54
E	12.3	440.	36.	0.53	0.46
		$C^{18}O\ J=2\rightarrow1$			
Observed	10.	230.	24.	0.47	0.30
A	7.6	185.	24.	0.43	0.28
B	8.4	207.	25.	0.37	0.23
C	9.0	225.	25.	0.32	0.20
D	10.7	278.	26.	0.23	0.14
E	15.0	428.	29.	0.12	0.07
		$^{13}CO\ J=2\rightarrow1$			
Observed	13.5	485.	36.	0.69	0.55
A	12.4	424.	34.	0.60	0.48
B	12.5	426.	34.	0.55	0.44
C	12.7	435.	34.	0.52	0.41
D	14.2	446.	32.	0.46	0.36
E	17.8	511.	29.	0.34	0.25
		$^{13}CO\ J=3\rightarrow2$			
Observed	8.	350.	44.	0.74	0.49
A	8.2	283.	35.	0.68	0.43
B	8.0	274.	34.	0.66	0.38
C	7.7	265.	35.	0.65	0.37
D	7.0	244.	35.	0.60	0.32
E	7.2	258.	36.	0.52	0.23

The entries in the Table are: model, peak radiation temperature and integrated intensity, FWHM line width, and ratios of integrated intensities for 2.5 pc and 5.0 pc offsets from the cloud center to the peak integrated intensity.

Table 4.7. - Parameters of Final Cloud Models.

Model	X_{18}^{a}	X_{13}^{b}	N_{H_2} $(45'')^{c}$	N_{18} $(45'')^{d}$
A	4.9×10^{-8}	8.5×10^{-7}	1.8×10^{24}	8.8×10^{16}
B	5.3×10^{-8}	9.4×10^{-7}	1.7×10^{24}	9.0×10^{16}
C	6.3×10^{-8}	1.0×10^{-6}	1.5×10^{24}	9.5×10^{16}
D	7.3×10^{-8}	1.3×10^{-6}	1.4×10^{24}	1.0×10^{17}
E	8.5×10^{-8}	1.4×10^{-6}	1.3×10^{24}	1.1×10^{17}
Chapter II	10^{-7}	10^{-6}	10^{24}	10^{17}

[a] Fractional abundance of ^{13}CO.

[b] Fractional abundance of $C^{18}O$.

[c] H_2 column density at the center of the cloud in a 45″

[d] $C^{18}O$ column density at the center of the cloud in a 45″ beam.

Figure 4.1. - A contour map of the ^{13}CO $J=2\rightarrow1$ integrated intensity in Sgr B2. The intensity in the velocity range 0 - 110 km s^{-1} has been corrected for atmospheric attenuation and warm losses, but not corrected for forward scattering and spillover and coupling efficiencies ($\eta_{FSS}\eta_C = 0.2$). The contour levels are: 65, 75, 85, and 95 K km s^{-1}. The coordinates of the (0,0) position are $\alpha_{1950} = 17^h44^m10.5^s$, $\delta_{1950} = -28°22'\ 5''$.

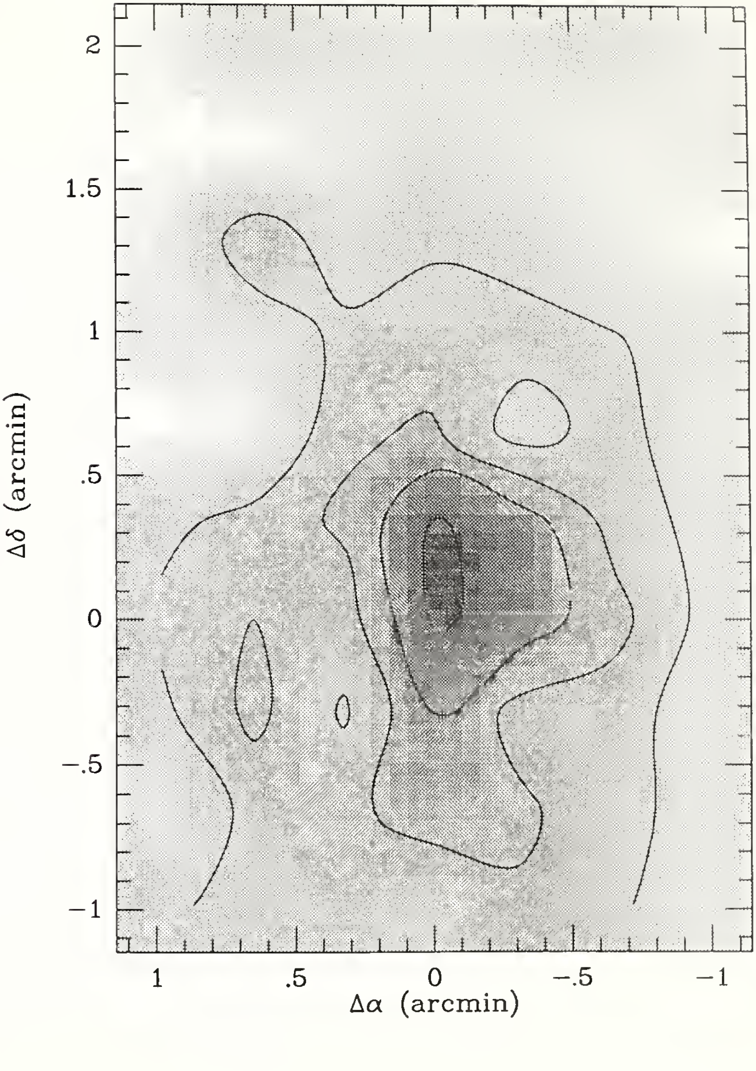
2
1.5
1
.5
0
−.5
−1
Δδ (arcmin)
1
.5
0
−.5
−1
Δα (arcmin)

Figure 4.2. - ^{13}CO $J = 2 \rightarrow 1$ integrated intensity for $\Delta\alpha = 0$. The emission peaks close to the position of the middle continuum source. No secondary peak associated with the northern source is present.

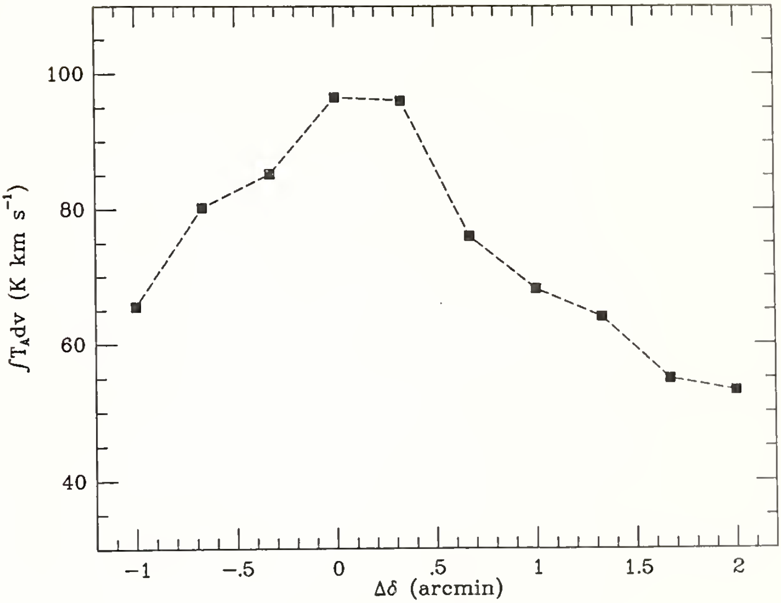
100
80
60
40
$\int T_A dv$ (K km s^{-1})
−1
−.5
0
.5
1
1.5
2
$\Delta\delta$ (arcmin)

Figure 4.3. - ^{13}CO $J = 2 \rightarrow 1$ spectra in Sgr B2. The spectra are from a north-south cut at $\Delta\alpha = 0$ with 0.33′ spacing. The lines show more prominent self-absorption than the $J = 1 \rightarrow 0$ transition, suggesting higher optical depth.

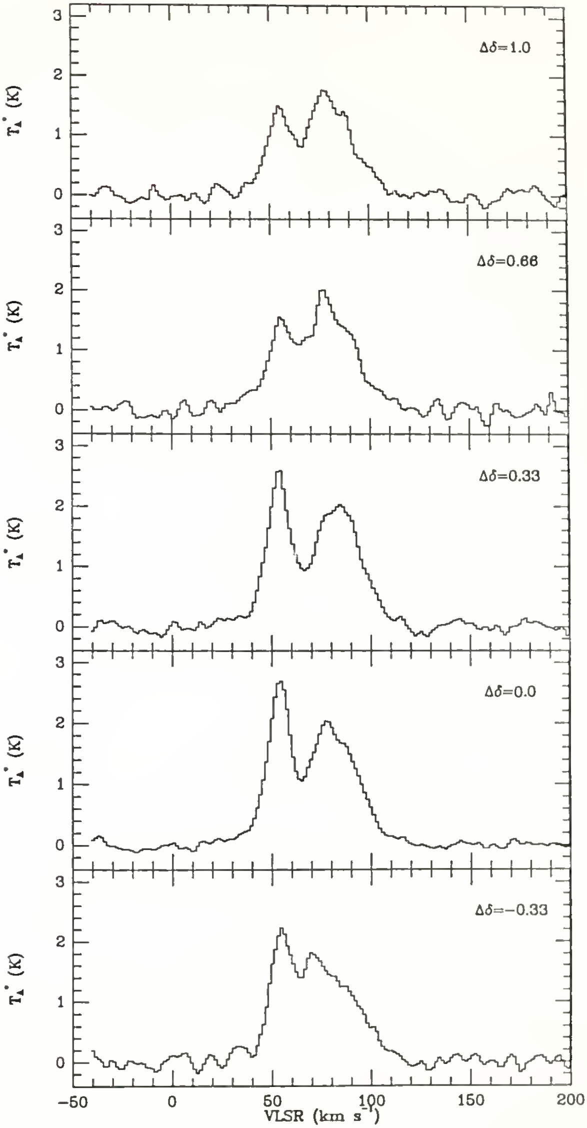
Δδ=1.0
Δδ=0.66
Δδ=0.33
Δδ=0.0
Δδ=−0.33
T_A^* (K)
0
1
2
3
−50
0
50
100
150
200
VLSR (km s^{-1})

Figure 4.4. - A contour map of the $C^{18}O$ $J=2\rightarrow1$ integrated intensity in Sgr B2. The integrated intensity in the velocity range 0 - 110 km s^{-1} has been corrected for atmospheric attenuation and warm losses, but not corrected for forward scattering and spillover and coupling efficiencies ($\eta_{FSS}\eta_C = 0.2$). The contour levels are: 15, 20, 25, 30, 35, 40, and 45 K km s^{-1}. The coordinates of the (0,0) position are $\alpha_{1950} = 17^h44^m10.5^s$, $\delta_{1950} = -28°22'\ 5''$.

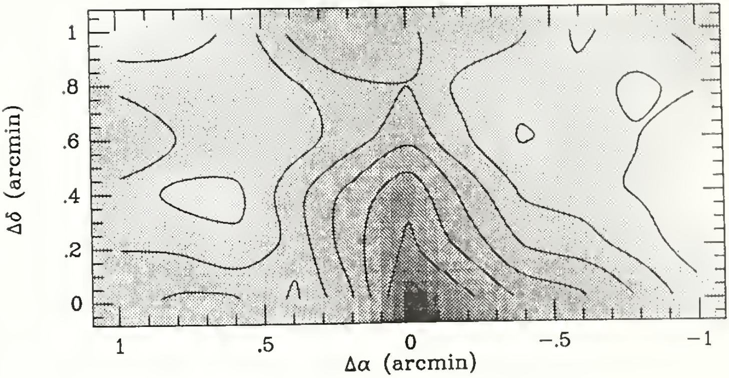
Δδ (arcmin)
1
.8
.6
.4
.2
0
1
.5
0
−.5
−1
Δα (arcmin)

Figure 4.5. - $C^{18}O$ $J=2\rightarrow1$ integrated intensity for $\Delta\alpha=0$. The solid line presents the total integrated intensity between 0 and 110 km s^{-1}. The emission in the velocity range 45 - 65 km s^{-1} (dotted line) shows a prominent peak associated with Sgr B2(M). The emission in the velocity range 65 - 85 km s^{-1} (dashed line) is more extended and it peaks close to the position of Sgr B2(N). The data suggest that the molecular clumps associated with the middle and northern continuum sources have LSR velocities of ~ 60 km s^{-1}, and 70 km s^{-1}, respectively.

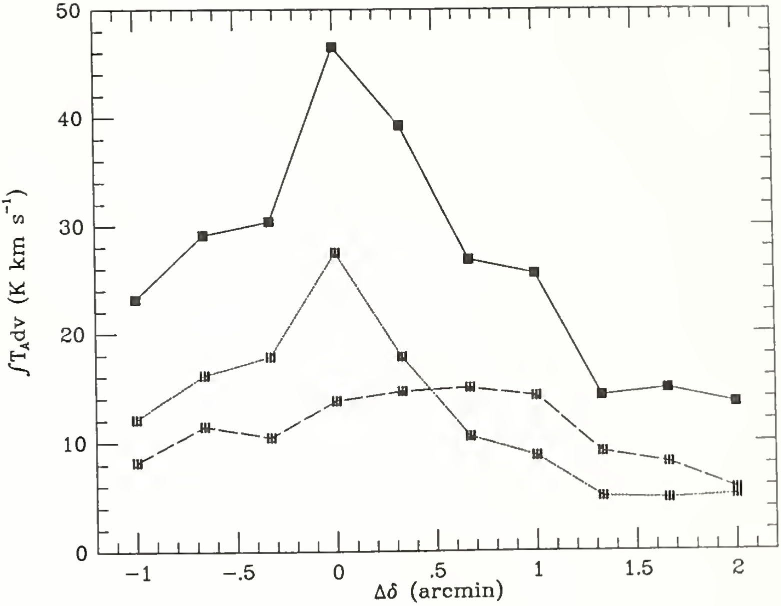
50
40
30
20
10
0
$\int T_A dv$ (K km s^{-1})
−1
−.5
0
.5
1
1.5
2
Δδ (arcmin)

Figure 4.6. - $C^{18}O$ $J=2\rightarrow1$ spectra in Sgr B2. The spectra are from north-south cut at $\Delta\alpha = 0$ with 0.33′ spacing. The line is not self-absorbed, suggesting low or moderate optical depth. The line center velocity shift is most likely a result of a change in relative intensity of different velocity components present in the spectra. Additional observations with higher signal-to-noise ratio will allow for decomposition of the spectra into different velocity components.

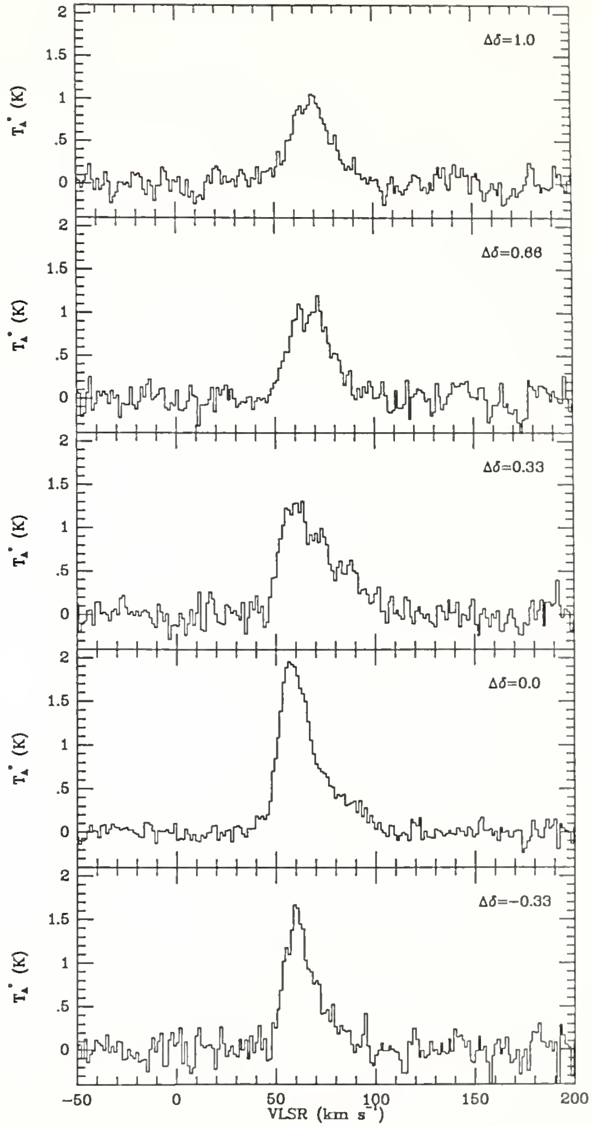
Δδ=1.0
Δδ=0.66
Δδ=0.33
Δδ=0.0
Δδ=−0.33
T_A^* (K)
2
1.5
1
.5
0
−50
0
50
100
150
200
VLSR (km s^{-1})

Figure 4.7. - A contour map of the ^{12}CO $J = 3 \rightarrow 2$ integrated intensity in Sgr B2. The integrated intensity in the velocity range 45 - 85 km s^{-1} has been corrected for atmospheric attenuation and warm losses, but not corrected for beam efficiency ($\eta_{FSS}\eta_C = 0.5$). The contour levels are: 450, 500, 550, and 600 K km s^{-1}.

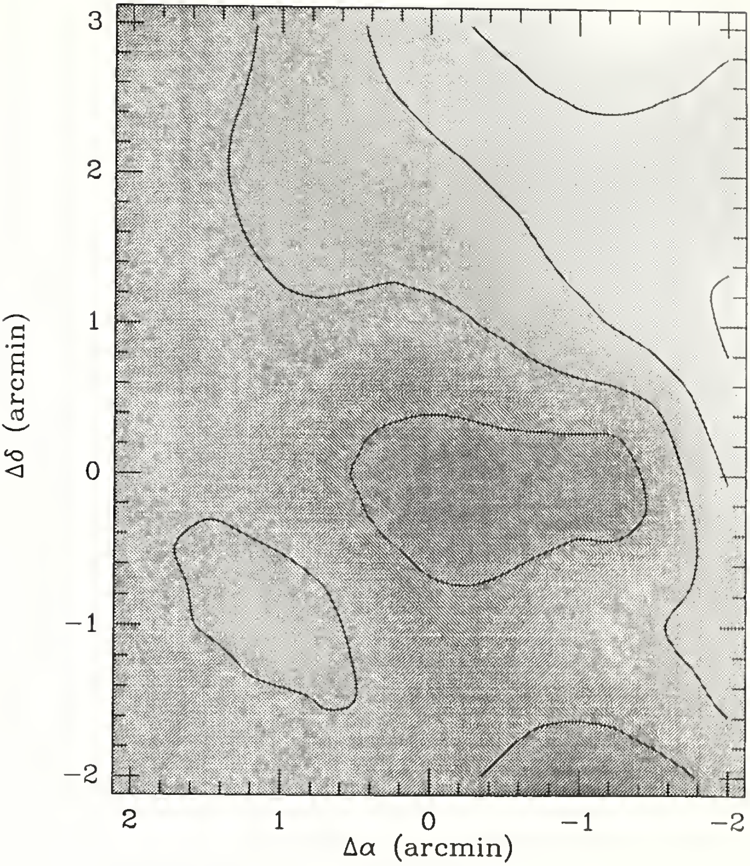
3
2
1
0
−1
−2
Δδ (arcmin)
2
1
0
−1
−2
Δα (arcmin)

Figure 4.8. - ^{12}CO $J=3\rightarrow2$ in Sgr B2. The spectra are from a north-south cut at $\Delta\alpha = 0$ with 1′ spacing. Because the beam efficiencies at 345 GHz and 115 GHz are very similar, the spectra can be directly compared with the $J=1\rightarrow0$ spectra shown in Figure 4.11.

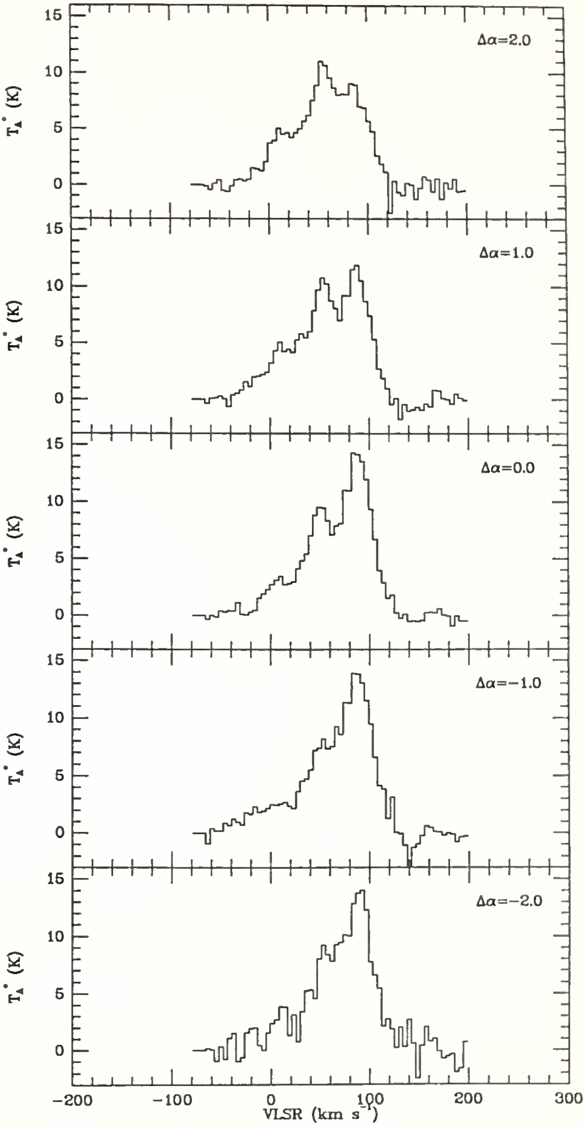
Δα=2.0
Δα=1.0
Δα=0.0
Δα=−1.0
Δα=−2.0
T_A^* (K)
15
10
5
0
−200
−100
0
100
200
300
VLSR (km s^{-1})

Figure 4.9. - ^{13}CO $J = 3 \rightarrow 2$ spectra in Sgr B2. The spectra are from a north-south cut at $\Delta\alpha = 0$ with $1'$ spacing. Notice much smaller self-absorption than for the $J = 2 \rightarrow 1$ transition, resulting from a bigger beam size.

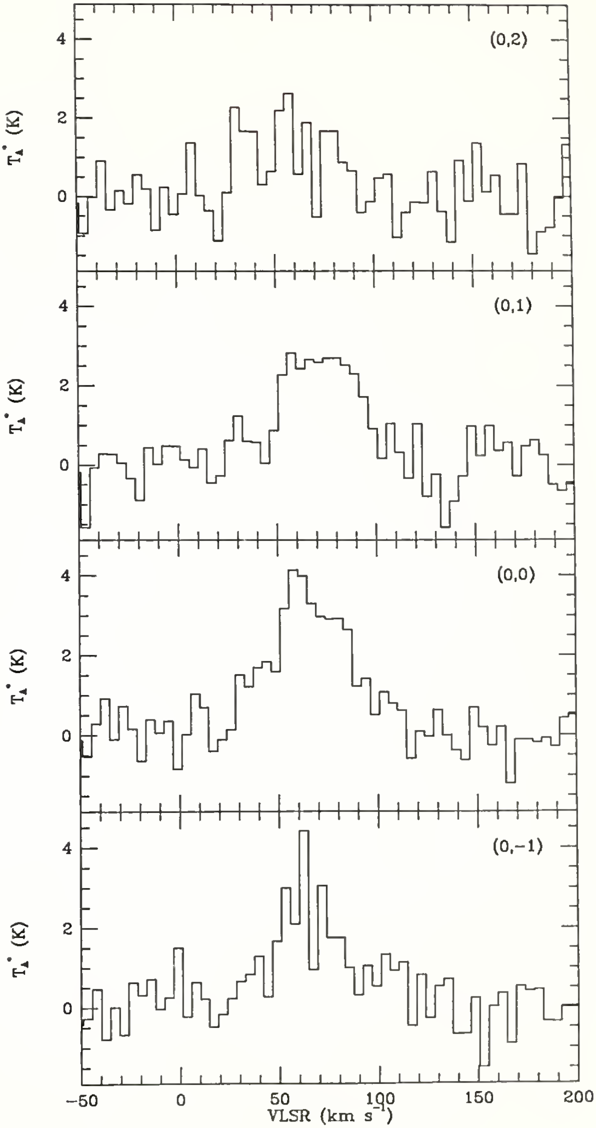
(0,2)
(0,1)
(0,0)
(0,−1)
4
2
0
T_A^* (K)
−50
0
50
100
150
200
VLSR (km s^{-1})

Figure 4.10. - A contour map of the ^{12}CO $J = 1 \rightarrow 0$ integrated intensity in Sgr B2. The integrated intensity in the velocity range 45 - 85 km s^{-1} corrected for atmospheric attenuation and warm losses, but not corrected for beam efficiency ($\eta_{FSS}\eta_{C}$ = 0.6). The contour levels are: 400, 450, 500, and 550 K km s^{-1}.

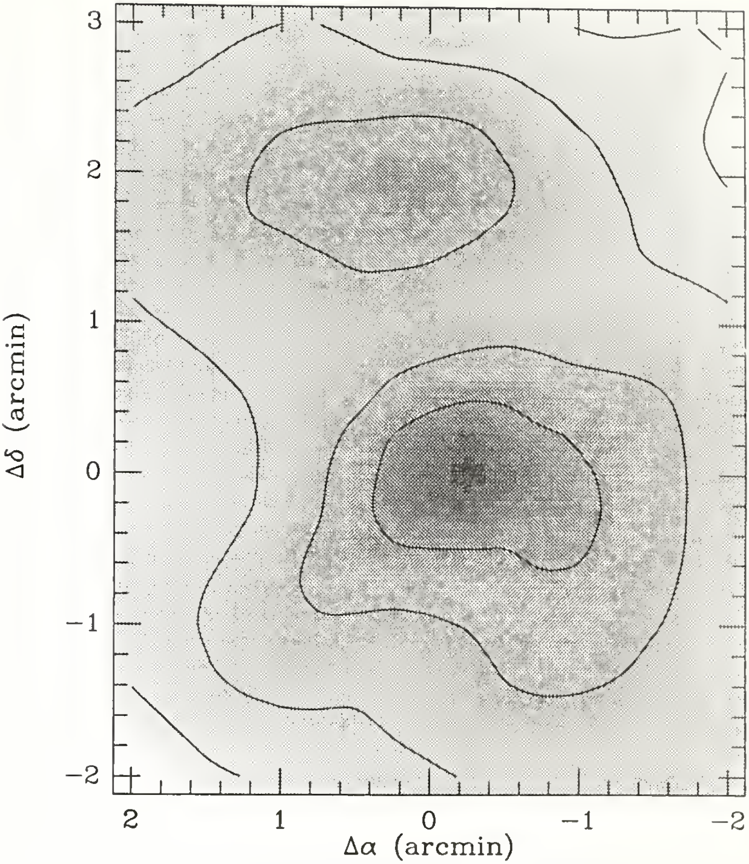
3
2
1
0
−1
−2
Δδ (arcmin)
2
1
0
−1
−2
Δα (arcmin)

Figure 4.11. - ^{12}CO $J = 1 \rightarrow 0$ spectra in Sgr B2. The spectra are from a north-south cut at $\Delta\alpha = 0$ with $1'$ spacing. Because the beam efficiencies at 345 GHz and 115 GHz are very similar, the spectra can be directly compared with the $J = 3 \rightarrow 2$ spectra shown in Figure 4.8.

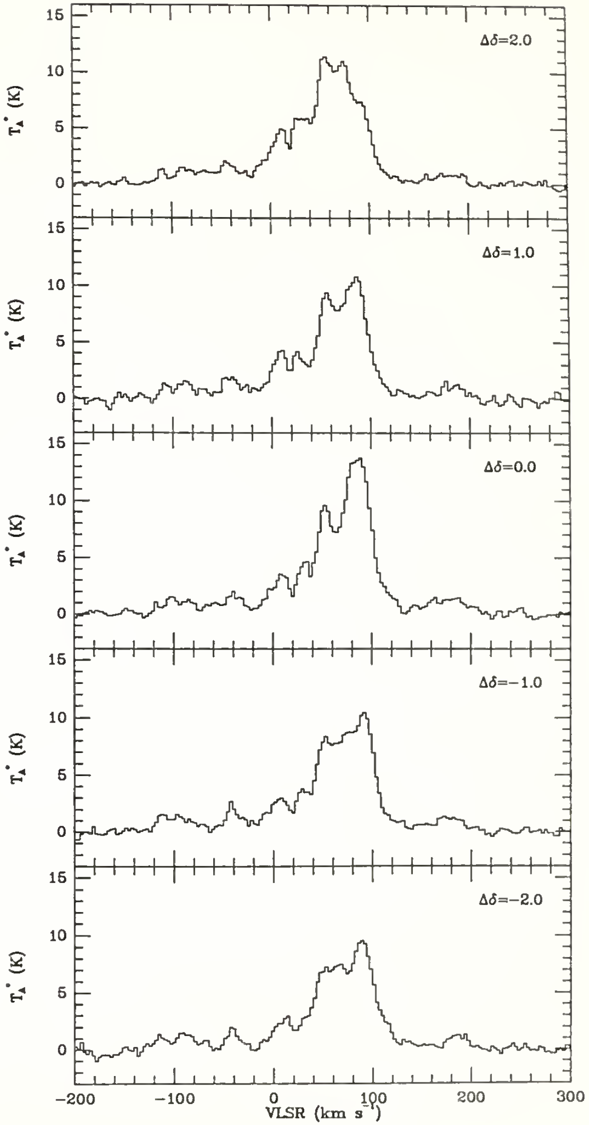
15
10
5
0
T_A^* (K)
Δδ=2.0
Δδ=1.0
Δδ=0.0
Δδ=−1.0
Δδ=−2.0
−200
−100
0
100
200
300
VLSR (km s^{-1})

Figure 4.12. - Parabolic fit to the cooling rate coefficient *a*. The filled squares represents data points taken from Goldsmith and Langer (1978). The fitted curve turns over for densities higher than ~ 2×10^5 cm^{-3} and the coefficient was assumed to be constant above this density.

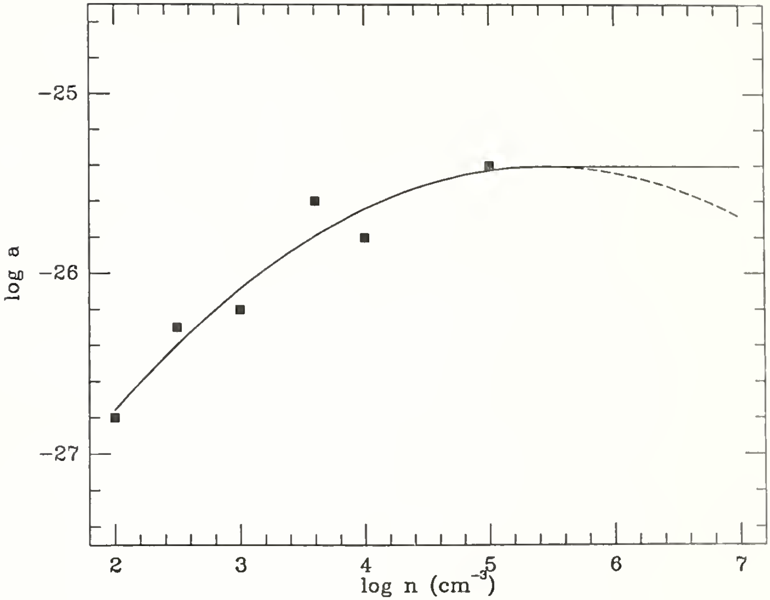
-25
-26
-27
log a
2
3
4
5
6
7
log n (cm^{-3})

Figure 4.13. - Parabolic fit to the cooling rate coefficient *b*. The filled squares represents data points taken from Goldsmith and Langer (1978).

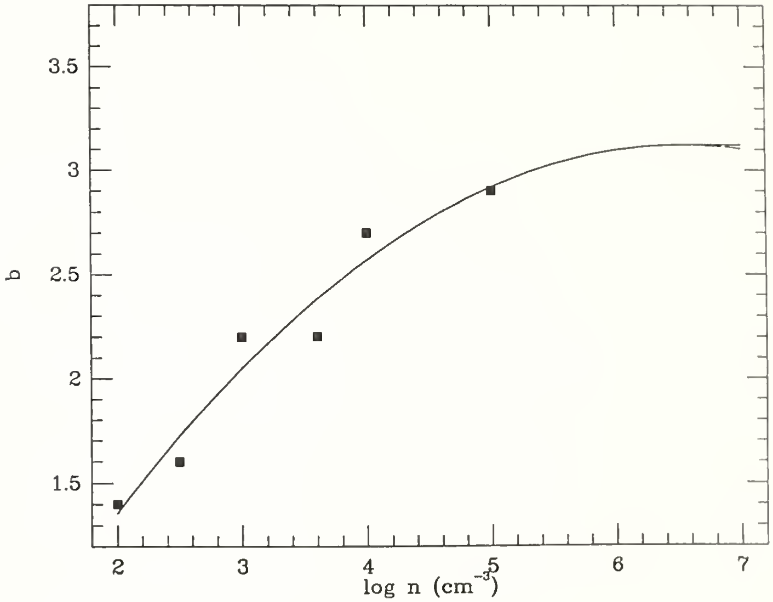
b
3.5
3
2.5
2
1.5
2
3
4
5
6
7
log n (cm^{-3})

Figure 4.14. - Kinetic temperature for different cooling rates. The solid line represents the dust temperature distribution. The dashed lines represents kinetic temperatures for the cooling rate scaling factors of 1, 2, 3, 4, and 5, upper to lower curve, respectively. The filled squares correspond to the peak ^{12}CO radiation temperature (^{12}CO antenna temperature corrected for $\eta_{FSS}\eta_C$ =0.6). The cooling rate scaling factor of ~ 4 gives results consistent with ^{12}CO data.

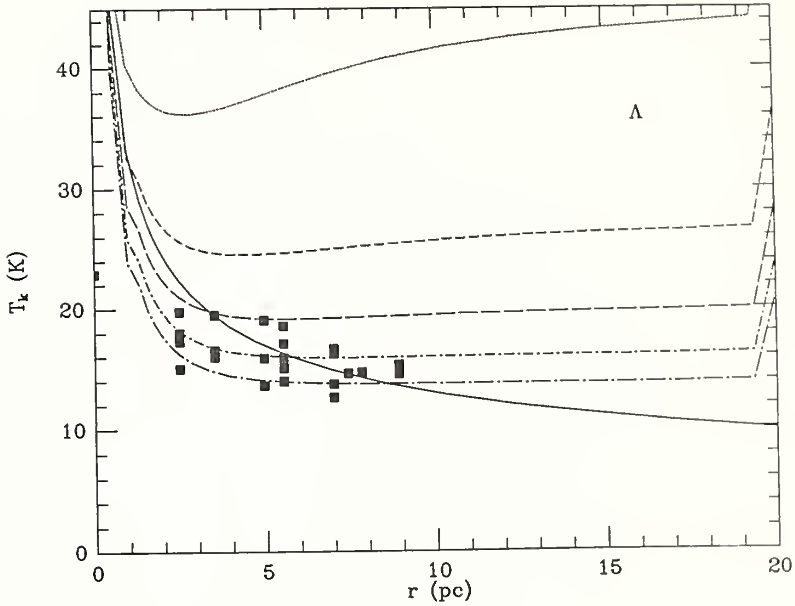
Λ
40
30
20
10
0
0
5
10
15
20
T_k (K)
r (pc)

Figure 4.15. - Kinetic temperature for different turbulent heating rates. The solid line represents the dust temperature distribution. The dotted lines represents kinetic temperatures for the turbulent heating rate scaling factors of 1, 0.5, 0.3, 0.2, and 0.1, upper to lower curves, respectively. The filled squares correspond to the peak ^{12}CO radiation temperature (^{12}CO antenna temperature corrected for $\eta_{FSS}\eta_{C}$ =0.6). The turbulent heating rate scaling factor of ~ 0.2 gives results consistent with ^{12}CO data.

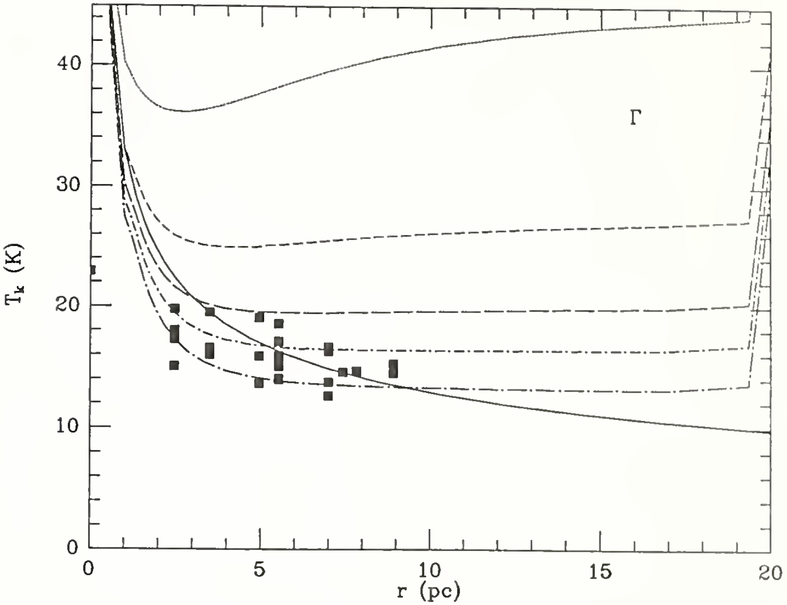

Γ
T_k (K)
r (pc)
0
10
20
30
40
0
5
10
15
20

Figure 4.16. - Heating rates as a function of the distance from the center. The results are for Model C with turbulent heating rate reduced by a factor of 5. The solid line represents the total heating rate. Within inner ~ 0.1 pc region heating is dominated by dust (long dashed-dotted line). Outside this region turbulent heating (short dashed line) dominates. Magnetic heating (long dashed line) and cosmic ray heating (dotted line) are not important. The photoelectric heating (short dashed- dotted line) dominates close to the edge of the cloud, and rapidly decreases with distance from the surface as the radiation flux is attenuated. Notice that beyond ~ 6 pc from the cloud center gas temperature is higher than dust temperature and dust acts as a coolant.

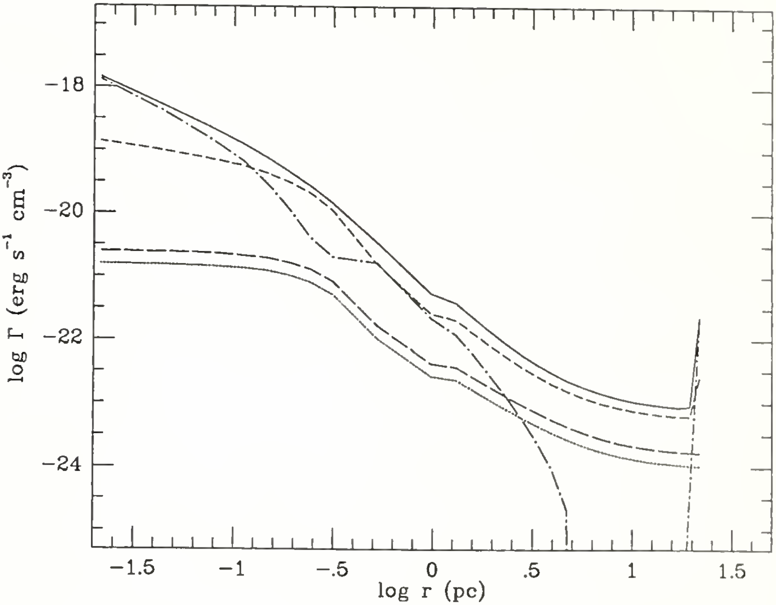

−18
−20
−22
−24
log Γ (erg s^{-1} cm^{-3})
−1.5
−1
−.5
0
.5
1
1.5
log r (pc)

Figure 4.17. - $C^{18}O$ $J = 1 \rightarrow 0$ integrated intensity for MC models. The observational data (filled squares) have been corrected for the beam efficiency of 0.45. The predicted intensities are for models: A (solid line), B (dotted line), C (short dashed line), D (long dashed line), and E (dashed-dotted line). All model except of Model E fit the observational data well.

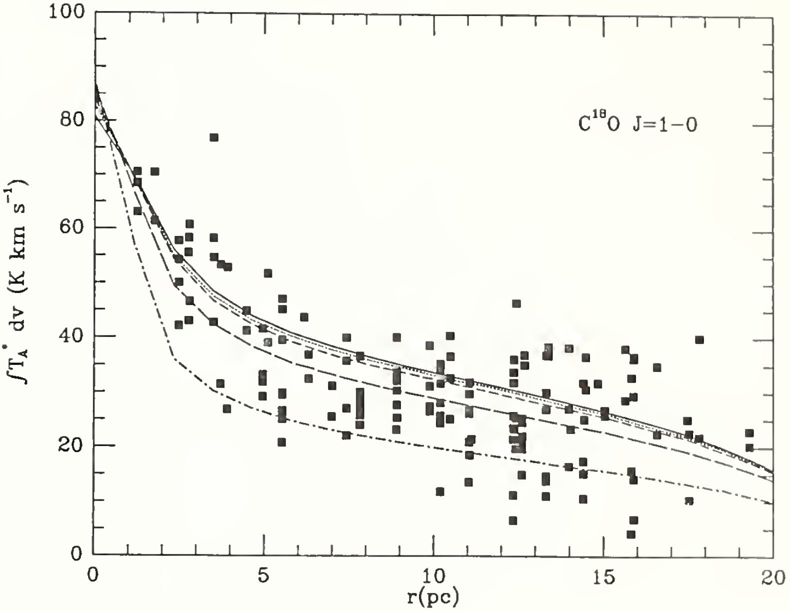
C^{18}O J=1−0
∫T$_A^*$ dv (K km s^{-1})
r(pc)
0
20
40
60
80
100
0
5
10
15
20

Figure 4.18. - ^{13}CO $J=1\rightarrow0$ integrated intensity for MC models. The observational data (filled squares) have been corrected for the beam efficiency of 0.45. The predicted intensities are for models: A (solid line), B (dotted line), C (short dashed line), D (long dashed line), and E (dashed-dotted line). All model except of Model E fit the observational data well.

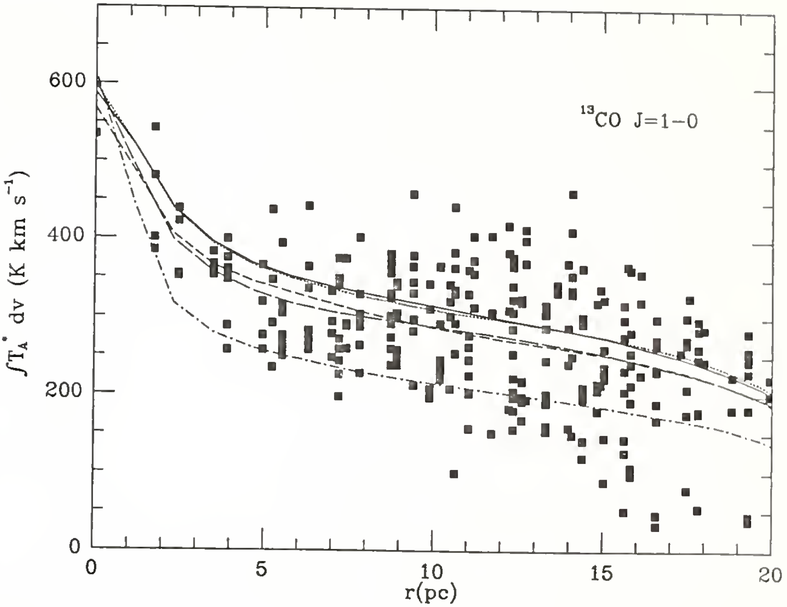
^{13}CO J=1−0
$\int T_A^* \, dv$ (K km s^{-1})
r(pc)
0
200
400
600
0
5
10
15
20

Figure 4.19. - $C^{18}O$ $J=2\rightarrow1$ integrated intensity for MC models. The observational data (filled squares) have been corrected for the beam efficiency of 0.2. The predicted intensities are for models: A (solid line), B (dotted line), C (short dashed line), D (long dashed line), and E (dashed-dotted line). The predicted intensities are marginally consistent with the data.

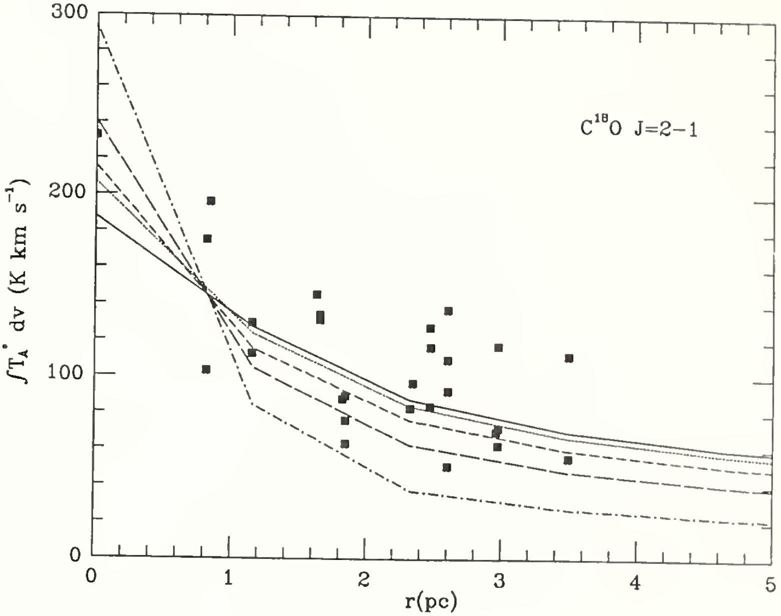
C^{18}O J=2−1
$\int T_A^* \, dv$ (K km s^{-1})
r(pc)
0
100
200
300
0
1
2
3
4
5

Figure 4.20. - ^{13}CO $J=2\rightarrow1$ integrated intensity for MC models. The observational data (filled squares) have been corrected for the beam efficiency of 0.2. The predicted intensities are for models: A (solid line), B (dotted line), C (short dashed line), D (long dashed line), and E (dashed-dotted line).

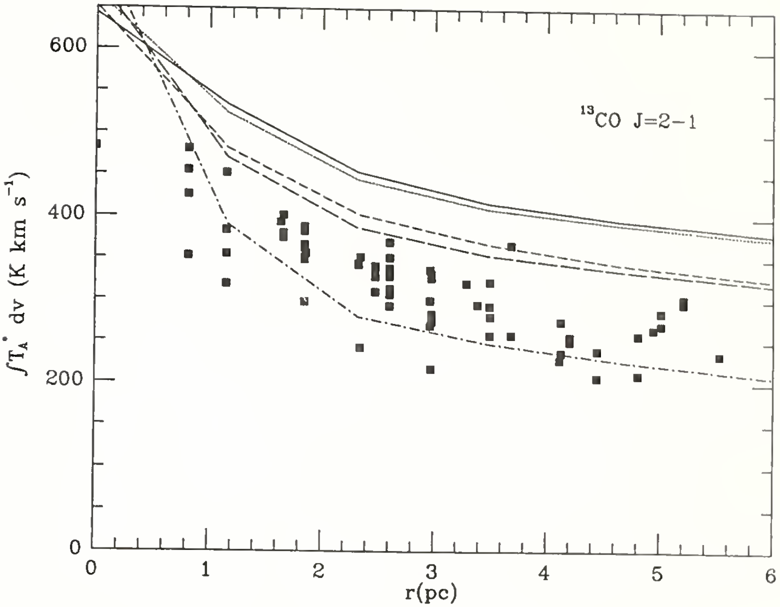

^{13}CO J=2−1
$\int T_A^* \, dv$ (K km s^{-1})
r(pc)
0
200
400
600
0
1
2
3
4
5
6

Figure 4.21. - ^{13}CO and C^{18}O model spectra. The results are for cloud Model C. The spectra correspond to (from upper to lower panel, respectively): J=1→0 transition of C^{18}O, J =1→0 transition of ^{13}CO, J =2→1 transition of C^{18}O, J =2→1 transition of ^{13}CO, and J =3→2 transition of ^{13}CO. The observational data are plotted as dotted lines. The model predictions are in *qualitative* agreement with observations. The major difference is for the J =3→2 transition of ^{13}CO which show too prominent self-absorption in the model. This may be related to the large beam error pattern which results in averaging the emission over much bigger region than it was done in the model.

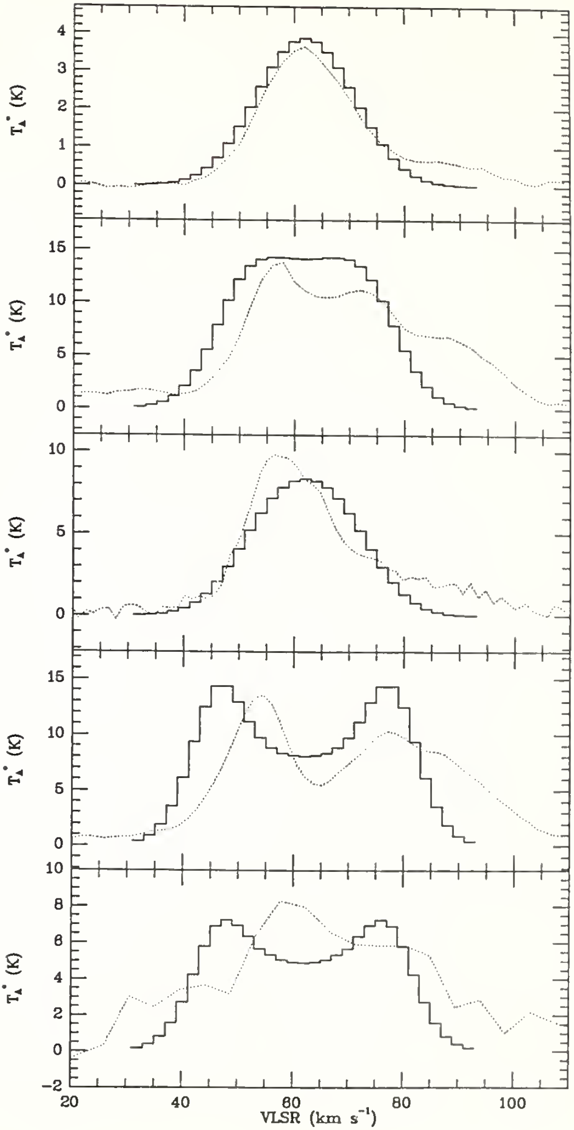
4
3
2
1
0
T_A^* (K)
15
10
5
0
T_A^* (K)
10
5
0
T_A^* (K)
15
10
5
0
T_A^* (K)
10
8
6
4
2
0
−2
T_A^* (K)
20
40
60
80
100
VLSR (km s^{-1})

Figure 4.22. - An average excitation temperature as a function of projected distance. The results plotted are for the $J = 1 \rightarrow 0$ transition of $C^{18}O$ (solid line), $J = 2 \rightarrow 1$ transition of $C^{18}O$ (dotted line), $J = 1 \rightarrow 0$ transition of ^{13}CO (short dashed line), and $J = 2 \rightarrow 1$ transition of ^{13}CO (long dotted line) for the cloud Model C.

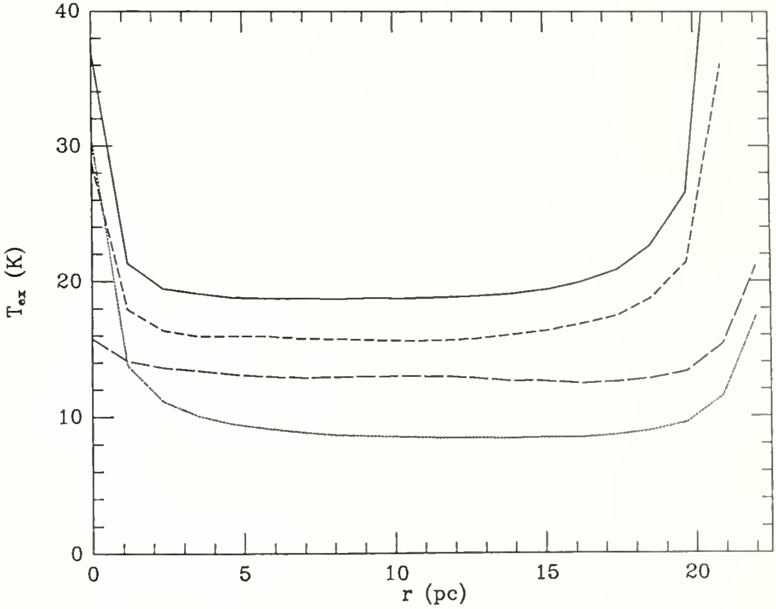
40
30
20
10
0
0
5
10
15
20
T_{ex} (K)
r (pc)

Figure 4.23. - Correlation between ^{13}CO and C^{18}O integrated intensities for MC models. The observational data points are taken from Figure 2.5. The predicted correlations are for Monte Carlo models A (solid line), B (dotted line), C (short dashed line), and D (long dashed line). The true abundance ratio is observed only for very low integrated intensities, contrary to the assumption made in Chapter II.

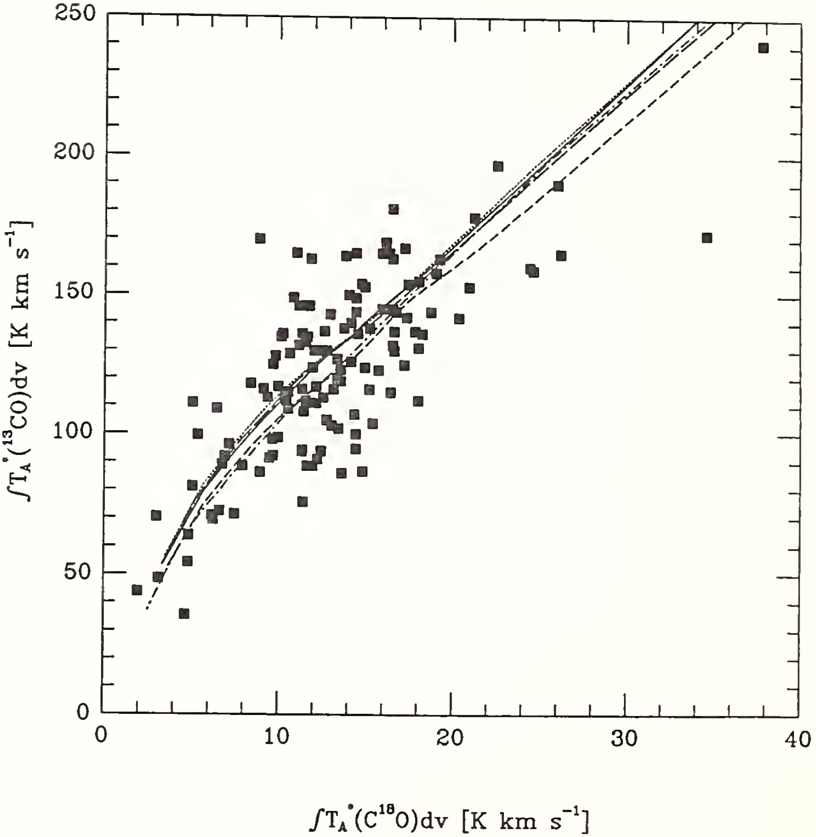

0
50
100
150
200
250
0
10
20
30
40
$\int T_A^*(^{13}CO)dv$ [K km s^{-1}]
$\int T_A^*(C^{18}O)dv$ [K km s^{-1}]

Figure 4.24. - ^{13}CO to $C^{18}O$ antenna temperature ratio. The results shown are for cloud Model C. The Monte Carlo models are not able to reproduce the observed constancy of this ratio for off-center positions discussed in Chapter II. The effect may be related to the clumpy structure of the envelope. The upper panel corresponds to the (0,0) position; the lower panel to a position with a 10 pc offset from the center of the cloud.

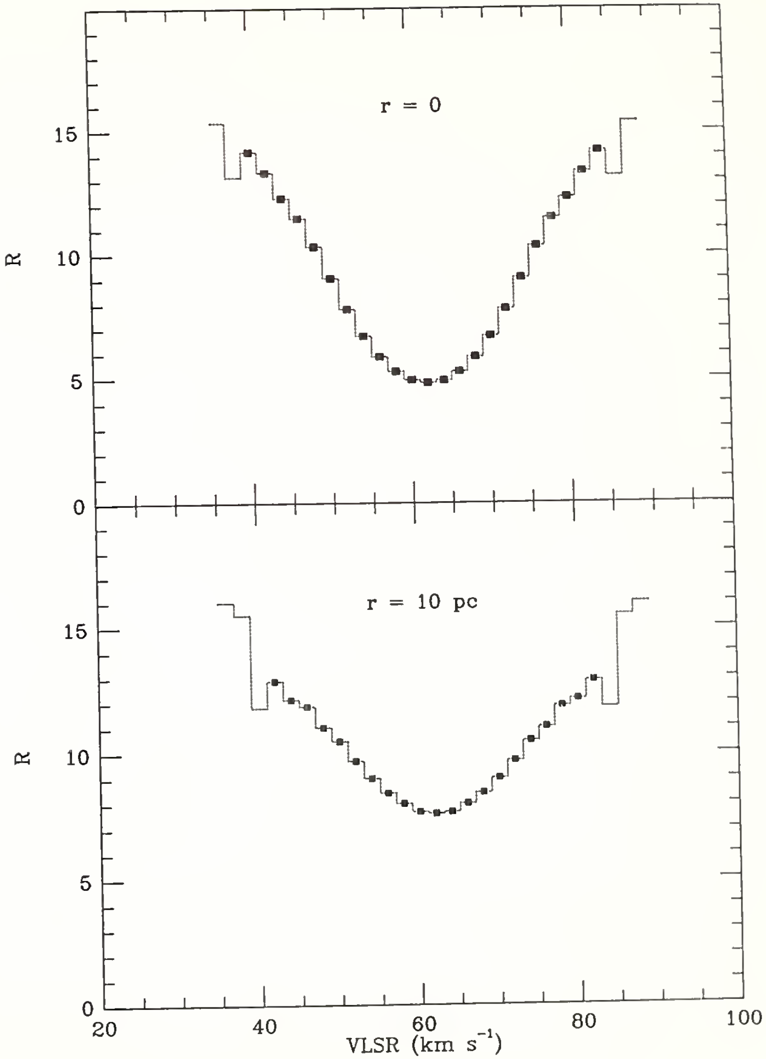
r = 0
r = 10 pc
R
R
0
5
10
15
0
5
10
15
20
40
60
80
100
VLSR (km s^{-1})

CHAPTER V

CONDITIONS IN THE CORE OF THE CLOUD

In the previous chapter I discussed results of multitransition observations of CO isotopes. I pointed out that due to the small molecular dipole moment the lower J transitions are easily excited even at relatively low densities and can be used for studying the structure of the extended cloud. In the present chapter I discuss observations of the $J = 12 \rightarrow 11$ and $5 \rightarrow 4$ transitions of cyanoacetylene, a molecule which due to its high dipole moment (~ 3.7 D) is a good tracer of the molecular material with densities of ~ 10^5 cm^{-3} and higher. Because the emission is not contaminated by contribution from low density material, the kinematic structure of the core is more easily seen. The data allow for determination of an average kinetic temperature and density at several positions where both transitions are observed. Comparison of HC_3N column densities with column densities of other molecular species suggests that significant variations of the molecular fractional abundance of this molecule may be present in the core of the cloud. I also present observations of several transitions of HC_3N in vibrationally excited states which are radiationally excited and can be used for deriving average radiation field temperatures along the line of sight.

A. HC_3N in Ground Vibrational State

The $J = 5 \rightarrow 4$ transition of HC_3N was observed between 1987 September and 1988 February using the 37 m radome enclosed antenna of Haystack Observatory at Westford, Massachusetts. The receiver system employed a refrigerator cooled maser preamplifier with instantaneous bandwidth of ~ 30 MHz. The LO has been synthesized from the Station Hydrogen Maser primary frequency standard. I used an autocorrelation spectrometer with total bandwidth of 13.3 MHz and velocity resolution of 0.26 km s^{-1}. The FWHM beam size was 50″ and the beam efficiency at the low elevations characteristic of Sgr B2 was estimated to be ~ 7%. Pointing of the antenna was checked by continuum observations of Saturn. The data consists of 24 positions with 30″ spacing. The size of the region mapped is 1.5′ × 2′. The integration time per position varied from 0.5 to 4.2 hours. A typical rms fluctuation level in a 0.26 km s^{-1} velocity element is lower than 50 mK. The highest signal to noise has been achieved for the (0,0) and (0,1) positions (the offsets are in arminutes relative to the center position: $\alpha_{1950} = 17^h44^m10.5^s$, δ_{1950} = -28°22′05″). Line parameters of the $J=5\rightarrow4$ HC_3N emission are presented in Table 5.1. A map of the integrated intensity in the 30 - 100 km s^{-1} velocity range is shown in Figure 5.1 It shows two prominent peaks at the (-0.5,1) and (0,1.75) positions. No emission peaks corresponding to the northern and middle continuum sources are present. This could be a result of excitation conditions, but is more likely related to variations in fractional abundance of HC_3N. Because of the very high spectral resolution, the data can be useful for studying the kinematic structure of the core. The $J=2\rightarrow1$ transition of $C^{18}O$ (Chapter IV) suggests existence of several distinctive kinematic components with LSR velocities of ~ 55, 70, and 85 km s^{-1}. The 55 and 70 km s^{-1} components are clearly seen in the HC_3N data (Figure 5.2). The 85 km s^{-1} component is not present, suggesting that the $C^{18}O$ emission in this velocity range originates from a region with relatively low density. The critical density (for which the collisional de-excitation rate is equal to the spontaneous emission rate) for the $J=5\rightarrow4$ transition of HC_3N is ~ 6.9×10^4 cm^{-3}.

The $J=12\rightarrow11$ transition of HC_3N (ν_o = 109.17 GHz) was observed in 1987 March and April using the FCRAO antenna and the receiver system described in Chapter II. The 45″ FWHM beam width is very close to that of the Haystack antenna at 36 GHz allowing for direct comparison of the two transitions. The data consist of 70 positions with 30″ spacing in the central region and 1′ spacing away from the center. The size of the region mapped is 4′ × 5′. Line parameters of the $J = 12 \rightarrow 11$ HC_3N emission are given in Table 5.2. A contour map of the integrated intensity in the 30 - 90 km s^{-1} velocity range is shown in Figure 5.3. The distribution of the emission differs significantly from that of the $J = 5 \rightarrow 4$ transition suggesting large variations in excitation conditions over the region mapped. The map shows a structure elongated in north-south direction, with a maximum at the (-0.5,0) position. Smaller peaks are present at the (0.5,1.75) and (-1.5,1.5) positions. Similar to the $J = 5 \rightarrow 4$ transition no peaks associated with the northern and middle sources are present in the data. Since the pointing errors are not expected to be larger than a few seconds of arc, the offset of the peak of the emission from the center of the cloud has to be, therefore, considered as real. Five $J = 12 \rightarrow 11$ HC_3N spectra from a north-south cut with $\Delta\alpha = 0$ are shown in Figure 5.4. The spectra have been smoothed to 3 km s^{-1} resolution. Similar velocity components as those seen in the $J = 5 \rightarrow 4$ spectra, however, can be distinguished.

The observed differences in the distribution of the emission in the $J = 5 \rightarrow 4$ and $12 \rightarrow 11$ transitions suggest significant variations in the excitation conditions over the region mapped. The observations of Cummins, Linke, and Thaddeus (1986) suggest that low energy HC_3N transitions are characterized by a single rotation temperature of ~ 27 K. This refers to a 2.5′ beam centered at the (0,-0.5) position. Assuming that level populations at other positions can also be characterized by a single rotation temperature, we can calculate the total molecular column density at these positions at which data from both transitions are available.

The excess antenna temperature above the cosmic background from a uniform cloud is given by

$$\frac{1}{\eta} T_A^* = \frac{c^2}{2k\nu_{ul}^2} \left[B_\nu(T_{ex}) - B_\nu(T_{bb}) \right] (1 - e^{-\tau_\nu}) , \tag{5.1}$$

where B_ν denotes the Planck's function, T_{ex} - excitation temperature, T_{bb} - temperature of the cosmic background and η - main beam efficiency. The optical depth of the transition is

$$\tau_\nu = \frac{h\nu_{ul}}{4\pi} (N_l B_{lu} - N_u B_{ul}) \Phi_{\nu,} \tag{5.2}$$

where N_u and N_l are the molecular column densities in the upper and lower states, B_{ul} and B_{lu} - Einstein's stimulated emission and absorption coefficients, and Φ_ν - normalized line profile. Substituting (5.2) into (5.1) one gets the following formula for an optically thin line

$$\frac{1}{\eta} T_A^* = \frac{c^2}{2k\nu_{ul}^2} \left[1 - \frac{B_\nu(T_{bb})}{B_\nu(T_{ex})} \right] \frac{h\nu_{ul}}{4\pi} N_u A_{ul} \Phi_\nu , \tag{5.3}$$

where A_{ul} is the spontaneous emission coefficient. The background correction in square brackets is small and can be omitted in most of practical applications. The integrated intensity of an optically thin rotational transition $J \rightarrow J-1$ is, therefore, given by

$$\frac{1}{\eta_{J\rightarrow J-1}} \int T_A^*(J \rightarrow J-1)\, du = \frac{c}{\nu_{J\rightarrow J-1}} \frac{c^2}{2k\nu_{J\rightarrow J-1}^2} \frac{h\nu_{J\rightarrow J-1}}{4\pi} A_{J\rightarrow J-1} N_J , \tag{5.4}$$

where u denotes velocity. For a linear molecule the line center frequency is given by

$$\nu_{J\rightarrow J-1} = 2JB , \tag{5.5}$$

where B is the rotational constant. The spontaneous emission rate is given by

$$A_{J\rightarrow J-1} = \frac{64\pi^4 \nu^3_{J\rightarrow J-1}}{3hc^3} \mid \mu_{J\rightarrow J-1} \mid^2 = \frac{512\pi^4 \mu^2 B^3}{3hc^3} \frac{J^4}{2J+1} \tag{5.6}$$

$$= 9.312\times 10^{-11} \; B^3[GHz] \, \mu^2[D] \, \frac{J^4}{2J+1}$$

$$= 8.425\times 10^{-7} \; B^3[K] \, \mu^2[D] \, \frac{J^4}{2J+1} \, ,$$

where the dipole moment matrix element

$$\mid \mu_{J\rightarrow J-1} \mid^2 = \frac{\mu^2 \, S_J}{2J+1}, \tag{5.7}$$

μ being the permanent dipole moment, and the line strength, $S_J = J$ for the $J \rightarrow J-1$ transition of linear molecule. If two transitions are observed an excitation temperature, T_{ex}, can be defined by

$$\frac{N_J}{N_K} = \frac{g_J}{g_K} \exp(-\frac{E_J - E_K}{kT_{ex}}) \tag{5.8}$$

$$= \frac{\eta_{K\rightarrow K-1}}{\eta_{J\rightarrow J-1}} \frac{\int T_A^*(J \rightarrow J-1) du}{\int T_A^*(K \rightarrow K-1) du} (\frac{\nu_{J\rightarrow J-1}}{\nu_{K\rightarrow K-1}})^2 \frac{A_{K\rightarrow K-1}}{A_{J\rightarrow J-1}} \, .$$

Assuming that the population of all rotational levels is described by the same excitation temperature one can calculate the total molecular column density

$$N_{tot} = N_J \frac{Z}{g_J} \exp(\frac{E_J}{kT_{ex}}) \tag{5.9}$$

$$= \frac{Z}{g_J} \exp(\frac{E_J}{kT_{ex}}) \frac{8\pi k \nu^2_{J\rightarrow J-1}}{hc^3 A_{J\rightarrow J-1}} \frac{1}{\eta_{J\rightarrow J-1}} \int T_A^*(J \rightarrow J-1) du$$

$$= \frac{4.0\times 10^{12} cm^{-2}}{J^2 \, \mu^2[D] \, B[K]} Z \exp(\frac{E_J[K]}{T_{ex}}) \frac{1}{\eta_{J\rightarrow J-1}} \int T_A^*(J \rightarrow J-1) du \; [K \; km \; s^{-1}] \, ,$$

where for $kT_{ex} \gg hB$ the partition function of a linear molecule is simply given by

$$Z = \frac{kT_{ex}}{hB} . \tag{5.10}$$

The above procedure has been applied to the observational data at 15 positions at which both transitions have been observed. The results are summarized in Table 5.3. The excitation temperature peaks at the position of the middle continuum source and falls off smoothly with the distance from the center. The only exception is the (-1,0.5) position which is characterized by a relatively high excitation temperature of ~ 20 K. The highest HC_3N column densities among the positions in Table 5.3 correspond to the (0,2), (-0.5,1), and (-0.5,0) positions. The prominent peak of the $C^{18}O$ column density at the (0,0) position does not have a correspondence in the HC_3N emission. The HC_3N data suggest presence of a relatively dense gas (~ 10^5 cm^{-3}) over a region of ~ 10 pc in size.

The simple analysis presented above does not allow for independent determination of H_2 volume density along a line of sight. The H_2 density can be independently determined by solving the system of statistical equilibrium equations and adjusting input parameters to obtain correct integrated intensity ratio of the two observed transitions, R. The ratio, which varies from 0.3 to 2.7 for different positions, depends on two parameters: density and kinetic temperature of the gas. Because only two transitions have been observed I assumed a simple model with constant temperature and density along a line of sight in order to have as few free parameters as possible. The results are presented in Figure 5.5 showing contours of constant R on the density-kinetic temperature plane. The contour levels are 0.5, 1, 2, and 3. Because to any given value of R one can ascribe an excitation temperature, contours of constant R are also contours of constant T_{ex}. The fact that constant-R contours levels off at very high densities simply means that the excitation temperature approaches the kinetic temperature. Clearly any given value of R corresponds to a range of densities and temperatures and having just two transitions observed, one cannot fit both temperature and density independently. Fortunately the kinetic temperature is a function of density via thermal balance of the cooling and heating rates discussed in the previous Chapter. One can obtain an approximate value of the kinetic temperature simply assuming turbulence as the only heating source. This reduces the number of free parameters to one: R is only a function of density. The dependence of R on density is shown in Figure 5.6. It changes rapidly for densities lower than ~ $10^{5.5}$ cm^{-3} and levels off for higher densities. In order to determine to what density range the emission in each transition is most sensitive I plot in Figure 5.7 the integrated intensity of each transition per unit hydrogen column density, assuming a constant fractional abundance of 10^{-9}. The solid line corresponds to the $J=12 \rightarrow 11$ transition and the dashed line to the $J=5 \rightarrow 4$ transition. Two vertical dotted line correspond to the critical densities of the two transitions. The "efficiency" of the $J=5 \rightarrow 4$ transition does not vary significantly for densities lower than ~ $10^{5.5}$ cm^{-3}. The "efficiency" of the $J=12 \rightarrow 11$ transition is almost constant for densities higher than $10^{5.5}$ cm^{-3} and drops very rapidly at lower densities causing large variation of the intensity ratio, R, with density. Due to the sharp cut-off of the "efficiency" of the $J=12 \rightarrow 11$ transition the SE analysis provides information about conditions in the regions with an H_2 density higher than ~ 10^5 cm^{-3}. The ratio of a yet higher transition to the $J=12 \rightarrow 11$ transition would be sensitive to higher densities. Additional data in the 2 mm or 1 mm range would allow for modeling the distribution of molecular material along the line of sight. With the observational data for two transitions, however, only a constant density model giving an average density and kinetic temperature along the line of sight seems reasonable. The results of the analysis are presented in Table 5.4. As expected the highest density is observed at the position of the middle continuum source. Morris *et al.* (1976) presented a two component model of Sgr B2 based on observations of several HC_3N transitions. They derived an H_2 density of ~ 5×10^5 and kinetic temperature of 25-50 K in the core (this refers to a beam varying from 150″ for the $J = 5 \rightarrow 4$ transition to 64″ for the $J = 12 \rightarrow 11$ transition, centered at the (0,-0.5) position). The above values are consistent with temperature and density at the (0,0) position given in Table 5.4. The total HC_3N column density in the core given by Morris *et al.*, equal to 2×10^{14} cm^{-2}, is a factor of 2 lower than the value given in Table 5.4. The 7 pc diameter of the core assumed by Morris *et al.* results in a very low HC_3N abundance of 10^{-11} in the core. Cummins, Linke, and Thaddeus also report lower HC_3N column density, of 3.5×10^{14} cm^{-2} in ~ 3′ beam centered at the (0,-0.5) position. Goldsmith *et al.* (1987), on the other hand using a 30 K excitation temperature derive a HC_3N column density of 8.1×10^{14} cm^{-2} at the (0,1) position and 4.5×10^{14} cm^{-2} at the (0,0) position, in good agreement with values reported here. The molecular column densities in Table 5.4 are slightly lower than those calculated assuming constant excitation temperature. The column density peaks at the (-0.5,0) and (-0.5,1) positions. If the fractional abundance of HC_3N were constant over the whole region, this would imply H_2 column density having maxima at the same positions. This stands in contradiction, however, with the H_2 column densities based on the $C^{18}O$ data. In Table 5.4 I give predicted integrated intensity of the $J = 1 \rightarrow 0$ transition of $C^{18}O$ from the region where HC_3N emission originates, obtained from statistical equilibrium calculations. I assumed constant fractional abundances of 10^{-9} for HC_3N, and 7×10^{-8} for $C^{18}O$. For a comparison I also give the observed $C^{18}O$ intensities. At the (0,0) position the contribution from the core is a minor fraction of the observed $C^{18}O$ intensity. This is in agreement with the assumption confirmed by Monte Carlo calculations, that $C^{18}O$ is excited throughout the cloud, and is not very sensitive to the conditions in the core. For many other positions, however, the predicted emission from the core is larger than the observed intensity questioning the assumption of constant fractional abundances. Since the $C^{18}O$ data is rather well reproduced by Monte Carlo models based on constant abundance assumption, I conclude that $C^{18}O$ abundance is indeed constant. The HC_3N abundance, on the other hand, must vary significantly in order to explain the observed emission distribution, without invoking extremely high H_2 column density through the core which are inconsistent with $C^{18}O$ data. For example the HC_3N column density of 10^{15} cm^{-2} would imply an H_2 column density 10^{24} cm^{-2} through the core at the (-0.5,1) position, assuming HC_3N fractional abundance of 10^{-9}. This is approximately equal to the peak H_2 density through the whole cloud. Significant depletion of HC_3N in the core of Sgr B2 was suggested by Morris *et al.* (1976). This depletion may have occurred, according to Morris *et al.*, through a high rate of chemical reactions in the dense medium leading to more complex molecules. This would explain why no HC_3N emission peaks associated with the northern and middle sources are observed. The idea of strong variations of molecular abundances in the core region is further supported by observations of other molecules. The 2_3-1_2 transition of SO which is observed together with HC_3N has distribution of the emission much closer resembling that of $C^{18}O$ (Figure 5.8). The emission peaks close to the position of the middle source. It is slightly elongated in the direction of the northern source. The 5_{05}-4_{04} transition of HNCO, which is observed together with $C^{18}O$, on the other hand, peaks at the (0,1.5) position similar to the $J = 5 \rightarrow 4$ transition of HC_3N. This may suggest that molecules containing nitrogen are enhanced at this position.

B. Vibrationally Excited HC_3N

Vibrationally excited HC_3N is a sensitive probe of the infrared radiation field (Goldsmith *et al.* 1982). I have searched for the $J = 12 \rightarrow 11$ HC_3N transitions in v_7=1, v_7=2, and v_6=1 vibrationally excited states, in order to obtain average radiation field temperatures at the (0,0) and (0,1) positions approximately corresponding to the middle and northern continuum sources, as well as at the (0,2) position which is close to the peak of the $J=5\rightarrow4$ transition of HC_3N and the 5_{05}-4_{04} transition of HNCO. Previous observations of the $J=12\rightarrow11$ ν_7 $(1e)$ transition (Goldsmith *et al.* 1987) showed emission confined to the immediate vicinity of the northern source. Emission at the (0,0) position was marginally detected. Rest frequencies of the lines of interest are given in Table 5.5 together with upper level energies and line strengths.

The $J=12\rightarrow11$ HC_3N spectra in the $1\nu_7$ $(1e)$ state are shown in Figure 5.10, together with the $J=9\rightarrow8$ transition of OCS (~ 8 km s^{-1} VLSR) and the 5_{15}-4_{14} transition of HNCO (~ -85 km s^{-1} VLSR). The line is blended with the $1\nu_6$ $(1f)$ transition which is shifted in velocity by +9.2 km s^{-1}. I deconvolved the two lines by using a multiple Gaussian fit with fixed line center velocities and line width of the weaker line. The fit gave a non-zero intensity of the $1\nu_6$ $(1f)$ transition only at the (0,1) position. The $1\nu_7$ $(1e)$ line is marginally detected at the (0,2) position. The integrated intensities at different positions are given in Table 5.6. The $1\nu_7$ $(1f)$ spectra are shown in Figure 5.11. The line is blended with an unidentified feature with LSR velocity of ~ 90 km s^{-1}. The spectra have been deconvolved using multiple Gaussian fitting. The $2\nu_7$ transitions (Figure 5.12) represent the biggest challenge. The emission in the 20 - 100 km s^{-1} velocity range is a blend of the $2\nu_7$ (0), $2\nu_7$ $(2e)$, and $2\nu_7$ $(2f)$ transitions of HC_3N, as well as the 5_{23}-4_{22} and 5_{24}-5_{23} transitions of HNCO. The multiple Gaussian decomposition with fixed velocities and line widths gave satisfactory results only for the (0,1) position (Figure 5.13), where lines are relatively strong. Some estimates of line intensities for the (0,0) position can also be obtained. The (0,2) position has to be considered as a non-detection. The detection of the $1\nu_6$ $(1e)$ transition (Figure 5.14) is controversial. The (0,0) and (0,2) positions are clearly non-detections. At the (0,1) position a line with a correct LSR velocity is present in the spectrum. The intensity of this line, however, seems too high compared to the $1\nu_6$ $(1f)$ and $2\nu_7$ lines (Table 5.6).

In section B of the present Chapter I derived a formula for an average excitation temperature along a line of sight based on observations of two transitions of a linear molecule. Equation (5.9) can be written in the following form

$$\log\left[\frac{8\pi k\nu_{ul}^2}{hc^3 g_u A_{ul}}\,\frac{1}{\eta}\int T_A^* du\right] = \log\frac{N}{Z} - \frac{E_u}{kT_{ex}}\,. \tag{5.11}$$

Substituting equation (5.6) one gets

$$\log\left[1.670\times10^{14}\,\frac{\int T_A^* du\ [K\ km\ s^{-1}]}{\eta\mu^2[D]\ \nu[GHz]\ S_{ul}}\right] = \log(\frac{N}{Z}) - \frac{E_u[K]}{T_{ex}}\,. \tag{5.12}$$

If several transitions are observed, one can plot the left hand side of the equation (5.12) as a function of the upper level energy. If all transitions are characterized by the same excitation temperature, its value can be determined from the slope of the straight line in the plot. This is commonly referred to as the rotation diagram method. Because the frequencies and line strengths of all the HC_3N transitions observed are very similar and the main beam efficiency is also essentially the same, one can simply plot the logarithm of the integrated intensity as a function of the upper level energy. This is done in Figure 5.15. A single excitation temperature does not seem to describe the data well. The straight line fit to the data gives a temperature of 181 K at the (0,1) position. The excitation temperature between the ground state and ν_7=1 state is only 154 K. This is significantly lower than the 286 K temperature derived by Goldsmith *et al.* based on the data taken with 15″ beam. The difference is almost certainly a result of the beam dilution. The excitation temperature between ν_7=1 and ν_7=2 states, however, is significantly higher, ~ 236 K. At the (0,0) position the excitation temperature between the ground state and ν_7=1 state is 99 K, consistent with the value given by Goldsmith, Krotkov, and Snell (1985). The excitation temperature between the first and second vibrationally excited states is 232 K, very close to the value observed at the (0,1) position. Surprisingly, this is much higher than the 128 K excitation temperature given by Goldsmith *et al.* in 15″ beam. At the (0,2) position the excitation temperature between the ground state and v_7=1 state is 84 K, only slightly lower than at the (0,0) position. This is quite surprising if HC_3N in v_7=1 vibrational state is indeed radiationally excited, because it implies existence of warm dust with temperature of ~ 80 K at this position. Figure 5.16 shows rotation diagram for HNCO which is also a tracer of the infrared radiation field due to strong b-type transitions. The excitation temperatures between the K_a=0 and K_a=1 ladders are relatively low: 16.6, 20.2, and 11.8 for the (0,0), (0,1), and (0,2) positions, respectively. Transitions in the K_a=2 ladder are detected only at the (0,0) and (0,1) positions. The excitation temperatures between the K_a=1 and K_a=2 ladders are slightly higher: 44 and 77 K for the (0,0) and (0,1) positions, respectively. For a comparison Cummins, Linke, and Thaddeus (1986) derive an excitation temperature of 61 K for the (0,-0.5) position.

C. Conclusion

Because of its large dipole moment, HC_3N was expected to be a good tracer of the high density gas in the core of the cloud. Due to possible large fluctuations in the fractional abundance of this molecule, however, the molecular column density does not correlate well with H_2 column density. The H_2 volume density and kinetic temperature derived from the statistical equilibrium calculations have to be also treated with caution. Significant variations of HC_3N may be present along any given line sight. If this is the case, the observed emission comes primarily from the region with the highest fractional abundance, and the average density and temperature for each line of sight given in Table 5.4 refer to this particular region. Therefore, it is not quite clear how representative the data in Table 5.4 is for the conditions in the core of the cloud. With all the reservations, one clear conclusion is that gas with H_2 density of ~ 10^5 cm^{-3} is present over a region at least 5 pc in diameter. Presence of such a dense gas has not been included in the Monte Carlo models for ^{13}CO and $C^{18}O$ and yet the predictions of the models seemed quite consistent with observations. This may suggest that either the fractional abundance of HC_3N is significantly lower than 10^{-9} and the contribution to $C^{18}O$ emission from regions where the HC_3N emission originates from is negligible, or that the core consists of many small and dense clumps embedded in lower density medium. If the beam filling factor of these clumps were small they would not contribute significantly to the CO isotope emission, which would still be dominated by the lower density component. HC_3N emission, however, would come exclusively from the dense clumps. The observed smoothness of the HC_3N emission suggest that the number of clumps in the telescope beam at each position has to be large. The maximum separation between clumps should not be, therefore, bigger than a few seconds of arc. Because lines in the $J=12\rightarrow11$ transition are quite strong, it should be possible to observe this emission with either Owens Valley or Hat Creek interferometers. The observations with 3-4″ angular resolution would be a test of the smoothness of the observed emission.

Vibrationally excited HC_3N and HNCO data indicate the highest excitation temperatures to be present at the position of Sgr B2(N). As discussed in Chapter III Sgr B2(M) has much higher luminosity and dust temperatures in the vicinity of the middle source are significantly higher than in the vicinity of the northern source. One possible explanation for higher excitation temperatures of radiationally excited molecules at the position of Sgr B2(N) suggested in Chapter III is the absence of molecular material in the immediate vicinity of Sgr B2(M). The very strong radiation field in this region might have resulted in destruction of molecules there. This is not the case for Sgr B2(N) because luminosity of this source is significantly lower.

Observations of vibrationally excited HC_3N can provide some information about position of the continuum sources inside the cloud. The line center velocity of the ν_7 $(1e)$ HC_3N transition at the position of the middle continuum source is 62.7 ± 0.9 km s^{-1}. This is different from the line center velocity in the ground vibrational state of ~ 55 km s^{-1} in the $J = 5 \rightarrow 4$ transition (Figure 5.2). Also the $J = 12 \rightarrow 11$ transition peaks at a velocity lower than 60 km s^{-1} (Figure 5.4). There is no distinguished velocity component with VLSR of ~ 63 km s^{-1} present in the HC_3N spectra at the (0,0) position. The $J = 2 \rightarrow 1$ transition of $C^{18}O$, however, indicates existence of a component with this LSR velocity in addition to the 55 km s^{-1} component. This suggests that the emission in the ground vibrational state of HC_3N comes primarily from regions not associated with the continuum source and that the excitation temperature between the ground state and the first vibrational state is only a lower limit to the radiation temperature in the region where the vibrationally excited emission comes from. This explains why rotation diagram for HC_3N shown in Figure 5.18 is not well described by a single rotation temperature. In this sense the excitation temperature between the first and second vibrational states seems to be much better probe of the radiation temperature, and that the radiation temperatures in the northern and middle sources are indeed comparable. At the (0,1) position the VLSR of the ν_7 $(1f)$ line is 65.4 ± 0.4 km s^{-1}, again different from velocities of the two clumps seen in the $J = 5 \rightarrow 4$ transition in the ground vibrational state but consistent with the $J = 2 \rightarrow 1$ transition of $C^{18}O$. This further confirms the conclusion that HC_3N emission in the ground vibrational state is indeed peculiar. The line center velocities of HNCO lines in $K_a = 1$ ladder are consistent with vibrationally excited HC_3N within observational errors.

Table 5.1. - Line Parameters of HC_3N $J = 5 \rightarrow 4$ Emission in Sgr B2.

$\Delta\alpha$	$\Delta\delta$	V_{mean}	σ_V	$\int T_A^* du$	T_A^*	σ_T
0.0	0.0	56.8	10.6	3.2	0.3	0.02
-0.5	0.0	61.8	11.6	9.3	0.4	0.06
-1.0	0.0	61.0	13.9	5.5	0.4	0.07
0.0	0.5	62.1	13.1	4.8	0.3	0.04
-0.5	0.5	64.7	11.1	8.9	0.4	0.04
-1.0	0.5	62.3	12.6	5.9	0.4	0.05
0.0	1.0	66.7	11.2	7.2	0.4	0.02
-0.5	1.0	65.5	11.5	13.3	0.5	0.05
-1.0	1.0	64.3	12.0	8.7	0.4	0.05
0.0	1.5	67.0	11.5	13.0	0.6	0.05
-0.5	1.5	63.1	12.8	9.6	0.4	0.05
-1.0	1.5	63.5	12.5	7.0	0.4	0.06
0.0	2.0	63.7	10.4	12.4	0.5	0.03
0.0	1.0	64.3	14.3	6.0	0.4	0.06
0.0	1.0	64.3	13.1	5.0	0.3	0.06
0.0	1.0	65.2	13.9	7.5	0.6	0.11
0.0	1.0	64.1	14.9	5.7	0.4	0.09
0.0	1.0	63.3	14.2	5.8	0.4	0.10
-0.5	2.0	63.3	10.9	11.0	0.5	0.04
-1.0	2.0	63.0	10.9	11.2	0.5	0.05
-0.5	2.5	61.0	10.6	7.9	0.5	0.05
-1.0	2.5	60.7	11.4	6.0	0.4	0.04
0.0	2.5	62.2	14.0	3.2	0.3	0.07
0.5	2.5	61.3	12.1	5.7	0.4	0.06
0.5	2.0	60.5	11.5	8.2	0.5	0.06
0.5	1.5	62.2	11.5	8.2	0.4	0.05
-1.0	3.0	59.0	12.9	4.8	0.3	0.05
0.0	2.5	61.5	10.9	6.2	0.4	0.04
0.5	1.0	61.6	11.9	5.2	0.3	0.04
0.5	0.0	58.7	11.8	6.1	0.4	0.05
0.0	1.0	64.2	13.5	6.2	0.4	0.06
0.0	2.0	61.3	16.2	-0.1	0.1	0.03
0.0	2.0	62.8	12.6	12.2	0.5	0.08
0.0	1.0	64.0	13.9	11.0	0.7	0.12
0.0	0.0	61.2	14.8	6.5	0.6	0.12

The entries in the table are: offsets from the cloud center (arcminutes), mean line velocity (km s^{-1}), velocity dispersion (km s^{-1}), integrated intensity between 30 and 100 km s^{-1}, peak antenna temperature not corrected for the main beam efficiency ($\eta = 0.07$), and rms noise in a 0.26 km s^{-1} resolution element (K).

Table 5.2. - Line Parameters of HC_3N $J=12\rightarrow11$ Emission in Sgr B2.

$\Delta\alpha$	$\Delta\delta$	V_{mean}	σ_V	$\int T_A^* du$	T_A^*	σ_T
2.0	3.0	57.9	20.4	10.6	0.4	0.05
1.0	3.0	48.5	25.5	12.5	0.3	0.05
0.0	3.0	44.7	21.0	17.5	0.5	0.04
-1.0	3.0	45.7	4.8	7.6	0.3	0.05
-2.0	3.0	47.0	4.2	9.6	0.4	0.05
-3.0	3.0	47.4	2.6	8.3	0.3	0.05
2.0	2.0	45.6	19.5	9.5	0.3	0.05
1.0	2.0	59.7	10.4	31.7	1.2	0.09
0.0	2.0	65.1	14.4	41.0	1.5	0.10
-1.0	2.0	68.5	0.0	23.7	1.2	0.06
-2.0	2.0	59.1	15.5	13.8	0.4	0.05
-3.0	2.0	50.0	19.1	13.1	0.4	0.05
1.5	1.5	52.2	17.2	19.8	0.6	0.09
0.5	1.5	62.8	15.5	56.1	2.0	0.09
-0.5	1.5	62.9	14.1	42.4	1.9	0.09
-1.5	1.5	62.5	20.0	39.0	1.2	0.09
2.0	1.0	46.4	20.5	10.2	0.3	0.05
1.0	1.0	58.2	14.7	16.0	0.7	0.06
0.5	1.0	63.3	8.4	24.9	1.1	0.09
0.0	1.0	71.8	0.0	37.3	1.9	0.10
-0.5	1.0	67.8	6.9	59.5	2.5	0.09
-1.0	1.0	70.6	0.0	36.6	1.7	0.08
-2.0	1.0	64.5	16.2	19.3	0.7	0.05
-3.0	1.0	54.1	14.5	13.6	0.4	0.05
1.5	0.5	53.8	11.6	14.8	0.6	0.08
1.0	0.5	55.6	19.9	25.3	1.0	0.09
0.5	0.5	56.6	19.5	36.1	1.2	0.09
0.0	0.5	66.2	11.4	50.6	2.1	0.08
-0.5	0.5	62.1	14.9	69.9	2.5	0.09
-1.0	0.5	65.5	7.9	64.9	2.3	0.09
-1.5	0.5	69.7	0.0	18.6	0.9	0.08
2.0	0.0	43.0	13.7	12.4	0.4	0.04
1.0	0.0	55.0	0.0	17.9	1.0	0.07
0.5	0.0	55.0	14.1	25.0	1.1	0.08
0.0	0.0	61.8	10.0	57.0	2.5	0.06
-0.5	0.0	62.8	9.9	87.4	3.9	0.08
-1.0	0.0	64.6	4.3	36.4	1.8	0.09
-2.0	0.0	60.2	14.0	11.3	0.5	0.06
-3.0	0.0	51.6	0.0	6.4	0.4	0.10
1.5	-0.5	50.0	18.6	27.5	0.8	0.09
1.0	-0.5	57.2	8.4	20.8	1.0	0.08
0.5	-0.5	56.0	14.8	34.7	1.5	0.07
0.0	-0.5	60.8	7.6	52.3	2.3	0.08
-0.5	-0.5	58.3	14.4	75.1	3.2	0.09
-1.0	-0.5	59.6	12.9	48.0	2.2	0.09

continued on next page

Table 5.2. - Continued

$\Delta\alpha$	$\Delta\delta$	V_{mean}	σ_V	$\int T_A^* du$	T_A^*	σ_T
-1.5	-0.5	59.1	13.3	18.0	0.9	0.09
2.0	-1.0	49.1	21.7	15.2	0.3	0.05
1.0	-1.0	54.9	11.0	21.8	0.9	0.08
0.5	-1.0	61.5	0.0	21.6	1.3	0.09
0.0	-1.0	55.7	0.0	32.2	1.8	0.08
-0.5	-1.0	61.3	8.5	48.0	2.2	0.08
-1.0	-1.0	64.6	10.5	18.9	0.8	0.06
-2.0	-1.0	71.0	0.0	6.9	0.3	0.05
-3.0	-1.0	0.0	0.0	0.3	0.3	0.09
1.5	-1.5	48.5	19.1	15.9	0.5	0.09
0.5	-1.5	57.5	12.5	27.1	1.3	0.08
-0.5	-1.5	56.0	15.7	38.7	1.4	0.08
-1.5	-1.5	60.0	19.1	15.5	0.6	0.08
2.0	-2.0	45.1	14.1	10.5	0.3	0.06
1.0	-2.0	51.1	11.2	8.2	0.3	0.07
0.0	-2.0	59.0	6.6	28.9	1.1	0.09
-1.0	-2.0	63.7	11.4	15.3	0.6	0.07
-2.0	-2.0	53.0	24.6	8.0	0.2	0.05
-3.0	-2.0	61.9	0.0	4.5	0.3	0.05
2.0	-3.0	72.1	0.0	6.0	0.2	0.05
1.0	-3.0	51.9	22.8	8.8	0.5	0.05
0.0	-3.0	57.6	17.2	17.8	0.9	0.07
-1.0	-3.0	54.9	20.3	11.4	0.4	0.05
-2.0	-3.0	64.3	24.3	8.0	0.3	0.05
-3.0	-3.0	74.1	15.0	4.9	0.2	0.06

The entries in the table are: offsets from the cloud center (arcminutes), mean line velocity (km s^{-1}), velocity dispersion (km s^{-1}), integrated intensity between 30 and 100 km s^{-1}, peak antenna temperature not corrected for the main beam efficiency ($\eta = 0.45$), and rms noise in a 3 km s^{-1} resolution element (K).

Table 5.3. - HC_3N Excitation Temperatures and Column Densities.

$\Delta\alpha$	$\Delta\delta$	R	T_{ex}	N_{tot}
0.0	2.0	0.51	10.4	1.0×10^{15}
-1.0	2.0	0.35	9.2	9.0×10^{14}
0.5	1.5	1.02	14.3	7.8×10^{14}
-0.5	1.5	0.65	11.6	8.4×10^{14}
0.5	1.0	0.77	12.4	4.6×10^{14}
0.0	1.0	0.88	13.2	6.6×10^{14}
-0.5	1.0	0.70	11.9	1.2×10^{15}
-1.0	1.0	0.70	11.9	7.7×10^{14}
0.0	0.5	1.67	19.2	5.3×10^{14}
-0.5	0.5	1.17	15.3	8.9×10^{14}
-1.0	0.5	1.76	19.8	6.9×10^{14}
0.5	0.0	0.60	11.2	5.1×10^{14}
0.0	0.0	2.76	29.4	5.0×10^{14}
-0.5	0.0	1.46	17.5	1.0×10^{15}
-1.0	0.0	1.00	14.1	5.5×10^{14}

The entries in the table are: offsets from the center of the cloud (arcminutes), the $J = 12 \rightarrow 11$ to $5 \rightarrow 4$ integrated intensity ratio corrected for the beam efficiencies, excitation temperature for the two transitions (K), and HC_3N column density (cm^{-3}) calculated from equation (5.9).

Table 5.4. - Results of Statistical Equilibrium Calculations.

$\Delta\alpha$	$\Delta\delta$	n_{H_2}	T_{kin}	L_z	N_{tot}	$Y_{18}(core)$	$Y_{18}(total)$
0.0	2.0	8.5×10^4	21.6	3.25	8.5×10^{14}	48.8	32.0
-1.0	2.0	6.8×10^4	20.3	3.52	7.4×10^{14}	44.9	39.6
0.5	1.5	1.4×10^5	25.1	1.55	6.7×10^{14}	34.3	26.9
-0.5	1.5	1.0×10^5	22.6	2.26	6.9×10^{14}	22.6	52.9
0.5	1.0	1.1×10^5	23.4	1.12	3.8×10^{14}	21.0	43.1
0.0	1.0	1.3×10^5	24.1	1.45	5.8×10^{14}	29.9	50.0
-0.5	1.0	1.1×10^5	23.0	3.05	1.0×10^{15}	54.0	55.6
-1.0	1.0	1.1×10^5	23.0	1.96	6.7×10^{14}	34.5	76.9
0.0	0.5	2.4×10^5	29.6	0.63	4.7×10^{14}	20.1	68.4
-0.5	0.5	1.6×10^5	26.0	1.57	7.8×10^{14}	37.8	70.4
-1.0	0.5	2.5×10^5	30.1	0.79	6.1×10^{14}	26.2	46.7
0.5	0.0	9.6×10^4	22.3	1.46	4.3×10^{14}	23.9	-
0.0	0.0	5.6×10^5	40.7	0.25	4.3×10^{14}	14.5	84.0
-0.5	0.0	1.5×10^5	25.2	2.42	1.1×10^{15}	54.5	70.4
-1.0	0.0	1.4×10^5	25.0	1.10	4.8×10^{14}	24.1	58.0

The entries in the table are: offsets from the center of the cloud (arcminutes), average hydrogen density along the line of sight (cm^{-3}), average kinetic temperature (K), size of the region in the z-direction (pc) assuming a fractional HC_3N abundance $X = 10^{-9}$, total HC_3N column density (cm^{-2}), predicted integrated intensity of the $J = 1 \rightarrow 0$ transition of $C^{18}O$ from the same region (K km s^{-1}) assuming a fractional abundance of 7×10^{-8}, and observed integrated intensity of the $J = 1 \rightarrow 0$ transition of $C^{18}O$ corrected for the beam efficiency. The size of the region in the z-direction and Y_{18} scale as $10^{-9}/X$.

Table 5.5 - Frequencies, Energies and Line Strengths of Observed Lines.

Transition	ν_o	E_u	S
HC_3N (ground)	109.173634	34.	12.0
HC_3N $1v_6(1e)$	109.352726	750.	11.9
HC_3N $1v_6(1f)$	109.438572	750.	11.9
HC_3N $1v_7(1e)$	109.441944	355.	11.9
HNCO 5_{15}-4_{14}	109.496008	59.	4.8
HC_3N $1v_7(1f)$	109.598751	355.	11.9
HC_3N $2v_7(0)$	109.862828	640.	12.0
HC_3N $2v_7(2e)$	109.865854	640.	11.7
HC_3N $2v_7(2f)$	109.870188	640.	11.7
HNCO 5_{24}-4_{23}	109.872337	186.	4.2
HNCO 5_{23}-4_{22}	109.872765	186.	4.2
HNCO 5_{05}-4_{04}	109.905753	15.8.	5.0

The entries in the table are: molecular transition, rest frequency (GHz), upper level energy (K), and line strengths.

Table 5.6. Integrated Intensities of HC_3N and HNCO Transitions.

Transition	*M*	*N*	*2N*
HC_3N (ground)	47.5	37.7	32.7
HC_3N $1\nu_6$ $(1e)^a$	-	1.8	-
HC_3N $1\nu_6$ $(1f)^b$	-	0.6	-
HC_3N $1\nu_7$ $(1e)$	1.96	4.85	0.41
HNCO 5_{15}-4_{14}	3.1	6.4	2.2
HC_3N $1\nu_7$ $(1f)$	1.80	4.63	0.98
HC_3N $2\nu_7{}^c$	0.55	1.42	-
HNCO 5_{24}-4_{23}	0.15	1.08	-
HNCO 5_{05}-4_{04}	43.5	56.8	89.8

The entries in the table are: transition, integrated intensities (K km s^{-1}) at the (0,0), (0,1), and (0,2) positions.

[a] The high intensity observed at the (0,1) position suggest that the line can be misidentified.

[b] The a multiple Gaussian fit to the spectrum shown in Figure 5.11.

[c] An average for the three blended transitions.

Figure 5.1. - A contour map of the HC_3N $J=5\rightarrow4$ integrated intensity in Sgr B2. The intensity in the 30 - 90 km s^{-1} velocity range has been corrected for atmospheric attenuation and warm losses, but has not been corrected for the main beam efficiency which is expected to be ~ 0.07 at the low elevations characteristic of Sgr B2. The contour levels are: 7, 9, 11, and 13 K km s^{-1}. Notice that no emission peaks associated with the northern and middle sources are present. The coordinates of the (0,0) position are: $\alpha_{1950} = 17^h44^m10.5^s$, $\delta_{1950} = -28°22'05''$.

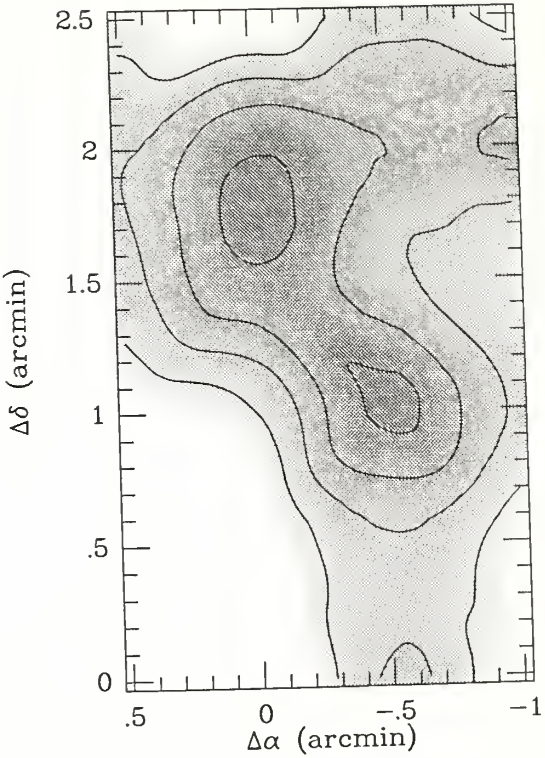
2.5
2
1.5
1
.5
0
Δδ (arcmin)
.5
0
−.5
−1
Δα (arcmin)

Figure 5.2. - HC_3N $J = 5 \rightarrow 4$ spectra in Sgr B2. The (0,0) position is the second position to the left in the lowest row. The spacing between neighboring positions is 30″ in R.A. and declination. At least two velocity components with LSR velocities of ~ 55 and 75 km s^{-1} are clearly present in the spectra. The highest signal-to-noise has been obtained for the (0,0) and (0,1) positions. Notice that the emission at the (0,0) is almost exclusively confined to the 55 km s^{-1} velocity component.

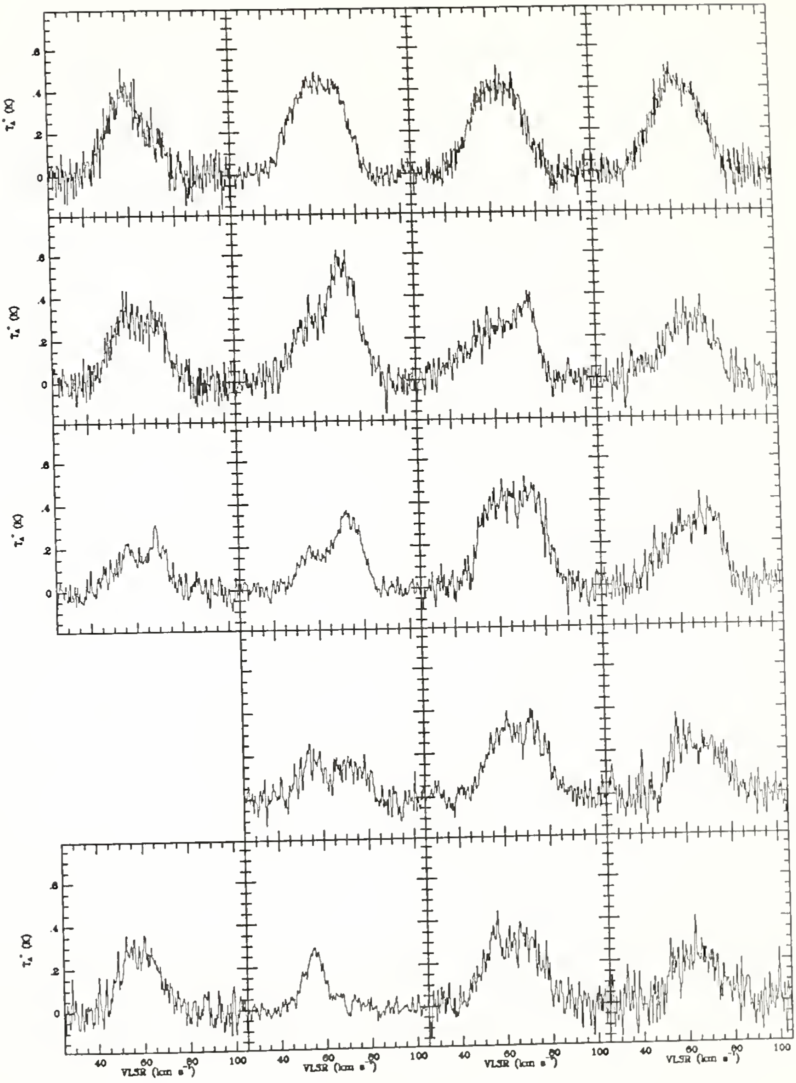

T*A (K)
.6
.4
.2
0
40
60
80
100
VLSR (km s-1)

Figure 5.3. - A contour map of the HC_3N $J=12\rightarrow11$ integrated intensity in Sgr B2. The integrated intensity in the 30 - 90 km s^{-1} velocity range has been corrected for atmospheric attenuation and warm losses, but has not been corrected for the main beam efficiency which is expected to be ~ 0.45 at the low elevation characteristic of Sgr B2. The contour levels are: 30, 35, 40, 45, 50, 55, and 60 K km s^{-1}. Notice that similar to the $J=5\rightarrow4$ transition, no emission peaks associated with the northern and middle sources are present. The coordinates of the (0,0) position are: $\alpha_{1950} = 17^h44^m10.5^s$, $\delta_{1950} = -28°22'05''$.

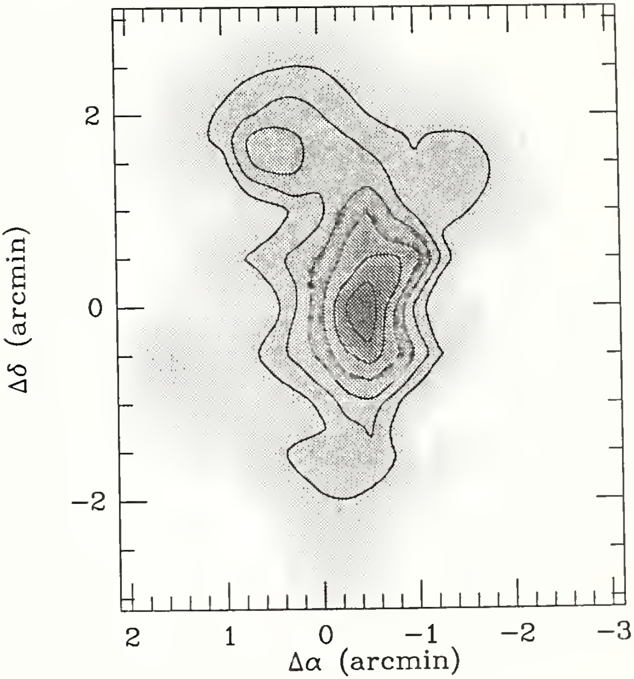
2
0
−2
Δδ (arcmin)
2
1
0
−1
−2
−3
Δα (arcmin)

Figure 5.4. - HC_3N $J = 12 \rightarrow 11$ spectra in Sgr B2. The spectra are from a north south cut with $\Delta\alpha = 0$. The emission at the VLSR of ~ 180 km s^{-1} comes from the 2_3 - 1_2 transition of SO.

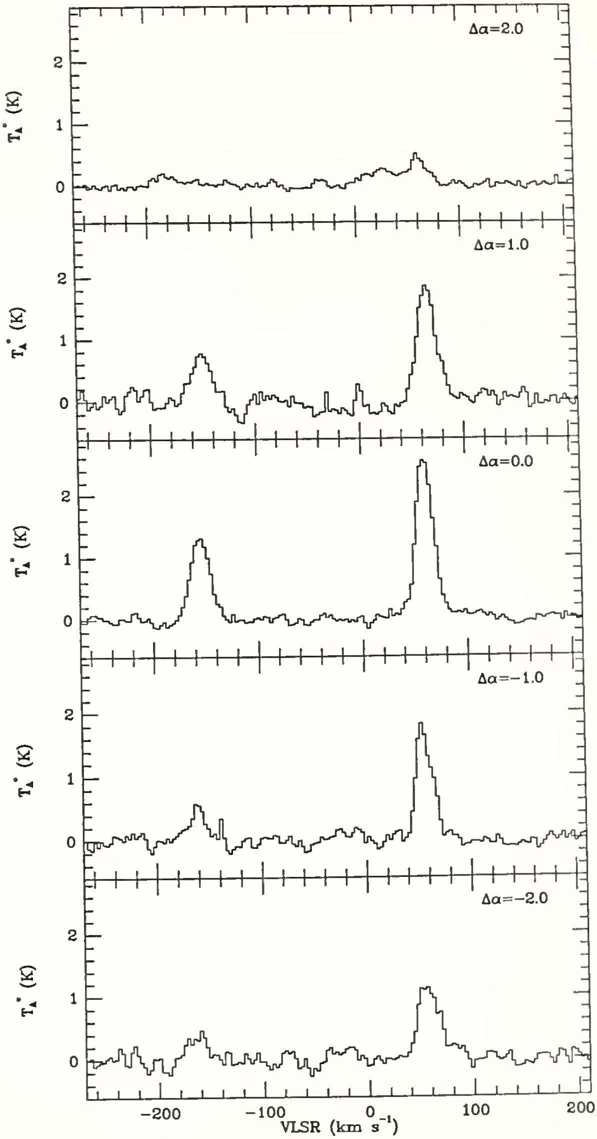
Δα=2.0
Δα=1.0
Δα=0.0
Δα=−1.0
Δα=−2.0
T_A^* (K)
0
1
2
−200
−100
0
100
200
VLSR (km s^{-1})

Figure 5.5. - Contours of constant $J = 12 \rightarrow 11$ to $5 \rightarrow 4$ integrated intensity ratio. The contour levels are 0.5, 1, 2, and 3. Constant integrated intensity ratio is equivalent to constant excitation temperature, as defined by equation 5.5. The fact that contours level off at high densities means that the excitation temperature approaches the kinetic temperature.

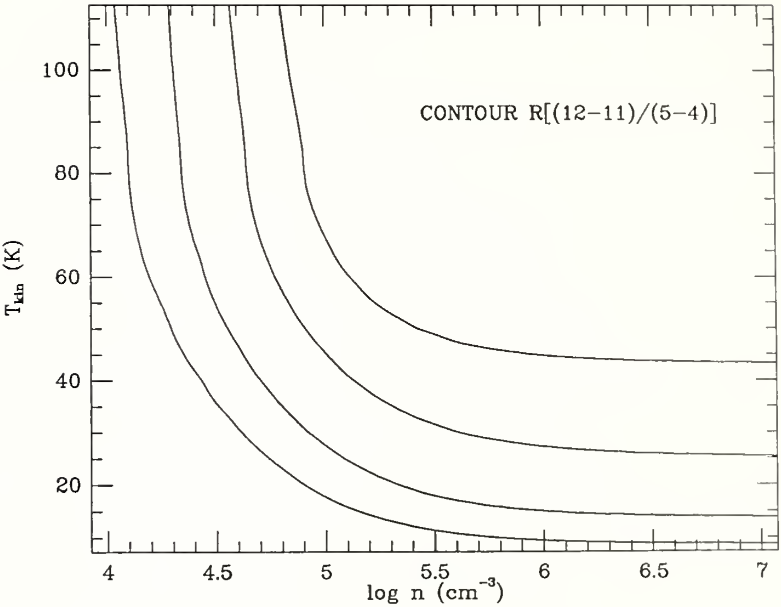
CONTOUR R[(12−11)/(5−4)]
T_{kin} (K)
100
80
60
40
20
4
4.5
5
5.5
6
6.5
7
log n (cm^{-3})

Figure 5.6. - Integrated intensity ratio as a function of density. For each density the kinetic temperature has been determined assuming turbulence as the only heating source (*cf.* Chapter IV). The ratio is a sensitive probe of gas density for densities lower than ~ $10^{5.5}$ cm^{-3}. The kinetic temperature changes from 20 K at $\log n = 4.8$ to 44 K at $\log n = 5.8$. The vertical lines correspond the the critical densities for the $J = 5 \rightarrow 4$ and $12 \rightarrow 11$ transitions.

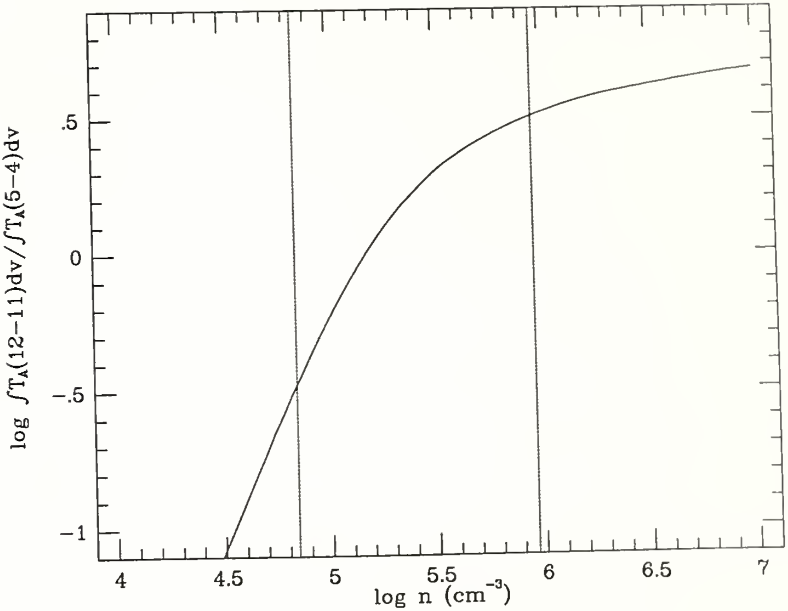
log ∫T_A(12–11)dv/∫T_A(5–4)dv
.5
0
–.5
–1
4
4.5
5
5.5
6
6.5
7
log n (cm⁻³)

Figure 5.7. - Integrated intensity per unit hydrogen column density. The HC_3N fractional abundance has been assumed to be 10^{-9}. Two vertical lines represent critical densities of the two transitions. The "efficiency" of the $J = 12 \rightarrow 11$ transition drops rapidly for densities lower than ~ $10^{5.5}$ cm^{-3} producing significant variation in the integrated intensity ratio (see Figure 5.6). The vertical lines correspond the the critical; densities for the $J = 5 \rightarrow 4$ and $12 \rightarrow 11$ transitions.

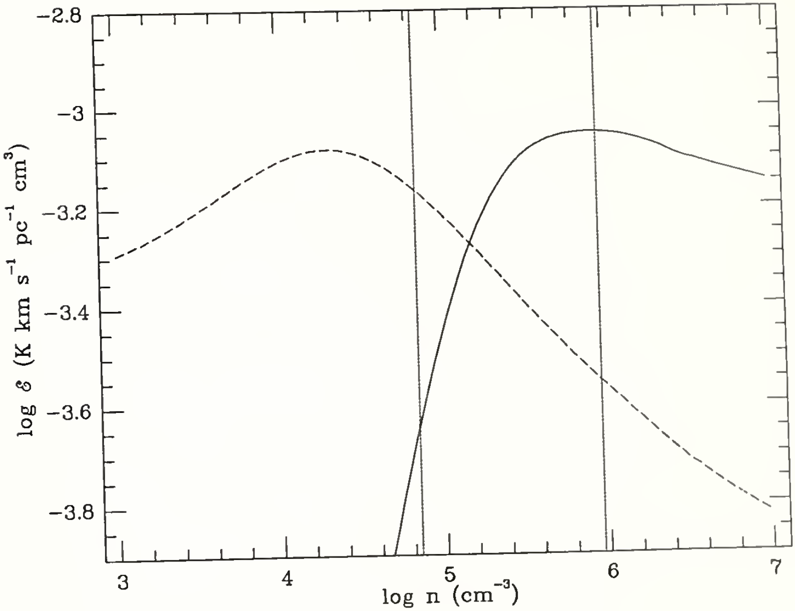
−2.8
−3
−3.2
−3.4
−3.6
−3.8
log $\mathcal{E}$ (K km s^{-1} pc^{-1} cm^{3})
3
4
5
6
7
log n (cm^{-3})

Figure 5.8. - A contour map of the SO 2_3 - 1_2 integrated intensity in Sgr B2. The integrated intensity in the 30 - 90 km s^{-1} velocity range has been corrected for atmospheric attenuation and warm losses, but has not been corrected for the main beam efficiency which is expected to be ~ 0.45 at the low elevation characteristic of Sgr B2. The contour levels are: 10, 15, 20, 25, and 30 K km s^{-1}. The emission peaks close to the (0,0) position similar to the $J = 1 \rightarrow 0$ transition of $C^{18}O$.

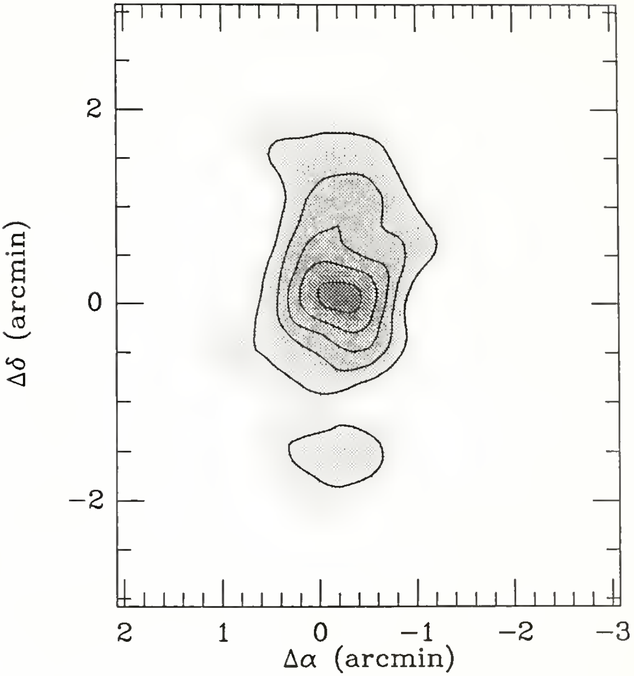
2
0
−2
Δδ (arcmin)
2
1
0
−1
−2
−3
Δα (arcmin)

Figure 5.9. - A contour map of the HNCO 5_{05} - 4_{04} integrated intensity in Sgr B2. The integrated intensity in the 30 - 90 km s^{-1} velocity range has been corrected for atmospheric attenuation and warm losses, but has not been corrected for the main beam efficiency which is expected to be ~ 0.45 at the low elevation characteristic of Sgr B2. The contour levels are: 80, 120, 160, 200, and 230 K km s^{-1}. The distribution of the emission is somewhat similar to the $J = 5 \rightarrow 4$ transition of HC_3N.

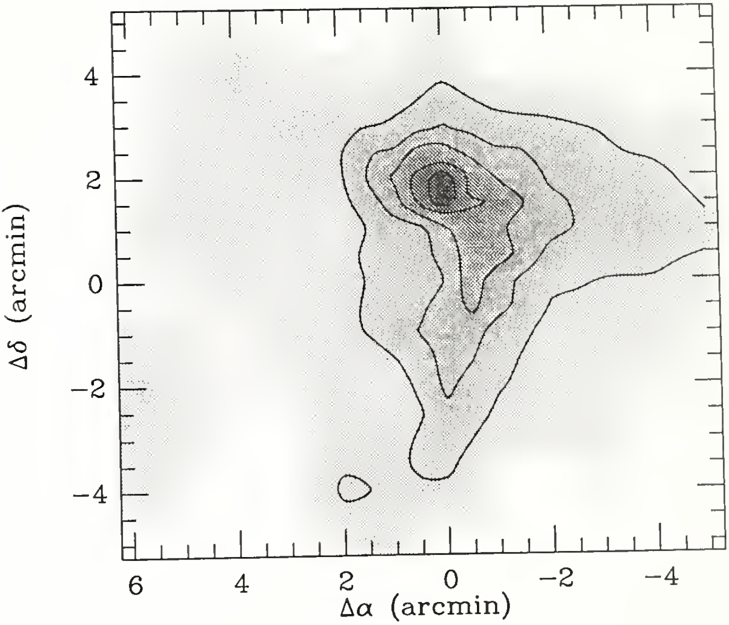
4
2
0
−2
−4
Δδ (arcmin)
6
4
2
0
−2
−4
Δα (arcmin)

Figure 5.10. - HC_3N $J=12\rightarrow11$ spectra in $\nu_7(1e)$ state. The HC_3N line (central velocity of ~ 65 km s^{-1}) is observed together with the $J=9\rightarrow8$ transition of OCS (central velocity of ~ 7 km s^{-1}) and the 5_{15}-4_{14} transition of HNCO (central velocity of ~ -85 km s^{-1}). The vibrationally excited HC_3N line is clearly detected at the (0,0) and (0,1) positions and marginally detected at the (0,2) position. It is blended with the much weaker line from the ν_6 $(1f)$ vibrational state.

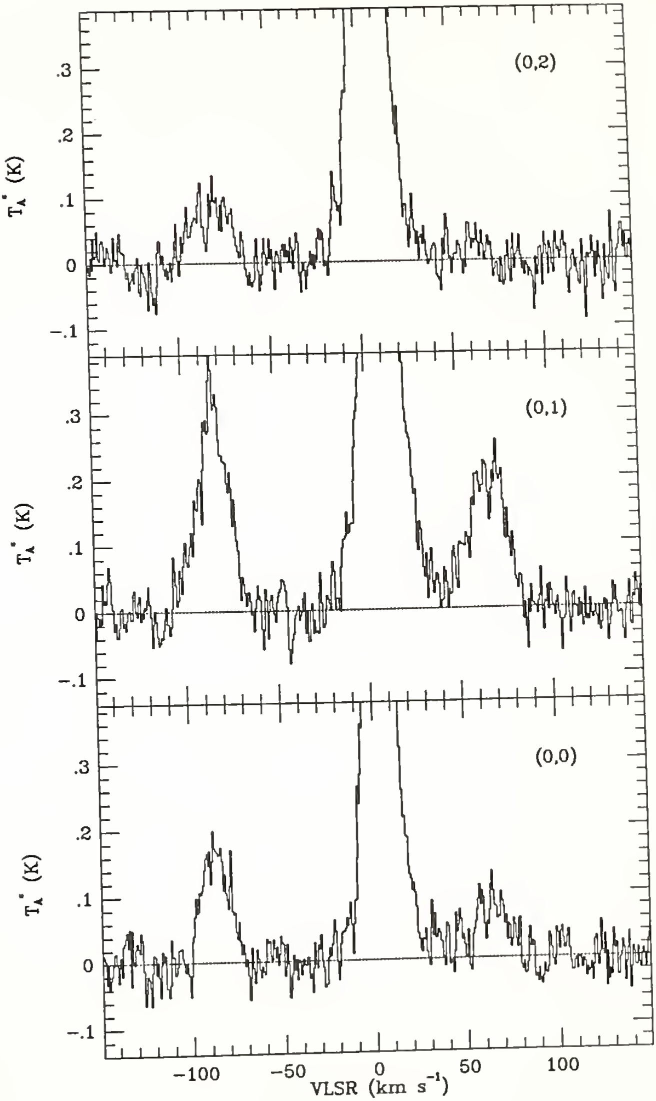
(0,2)
(0,1)
(0,0)
T_A^* (K)
.3
.2
.1
0
−.1
−100
−50
0
50
100
VLSR (km s^{-1})

Figure 5.11. - HC_3N $J=12\rightarrow11$ spectra in $\nu_7(1f)$ state. The HC_3N line is blended with an unidentified feature at ~ 90 km s^{-1} LSR velocity.

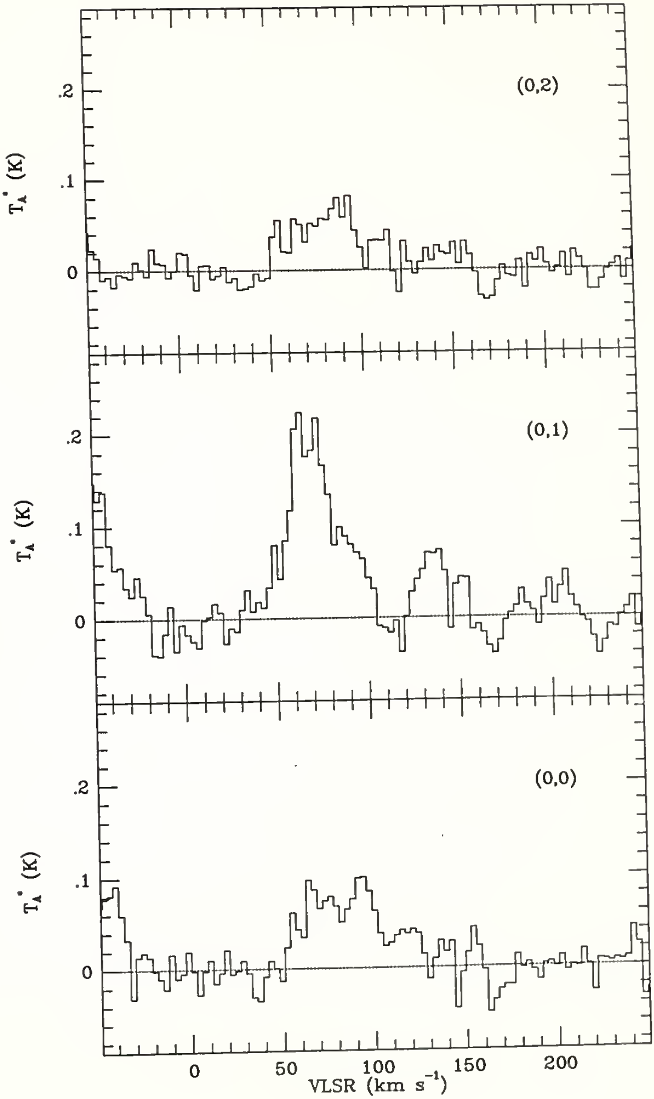
(0,2)
(0,1)
(0,0)
T_A^* (K)
.2
.1
0
0
50
100
150
200
VLSR (km s^{-1})

Figure 5.12. - HC_3N $J=12\rightarrow11$ spectra in $2\nu_7$ state. The emission in the 20 - 100 km s^{-1} velocity range is a blend of the $2\nu_7$ (0), $2\nu_7$ (2*e*), and $2\nu_7$ (2*f*) transitions of HC_3N, as well as the 5_{23}-4_{22} and 5_{24}-5_{23} transitions of HNCO. The multiple Gaussian decomposition with fixed velocities and line widths gave satisfactory results only for the (0,1) position, where lines are relatively strong. The strong line at the VLSR of ~ -40 km s^{-1} in the 5_{05}-4_{04} transition of HNCO. The line at VLSR of ~ 150 km s^{-1} may correspond to the 5_{32}-4_{31} and 5_{33}-4_{32} transitions of HNCO.

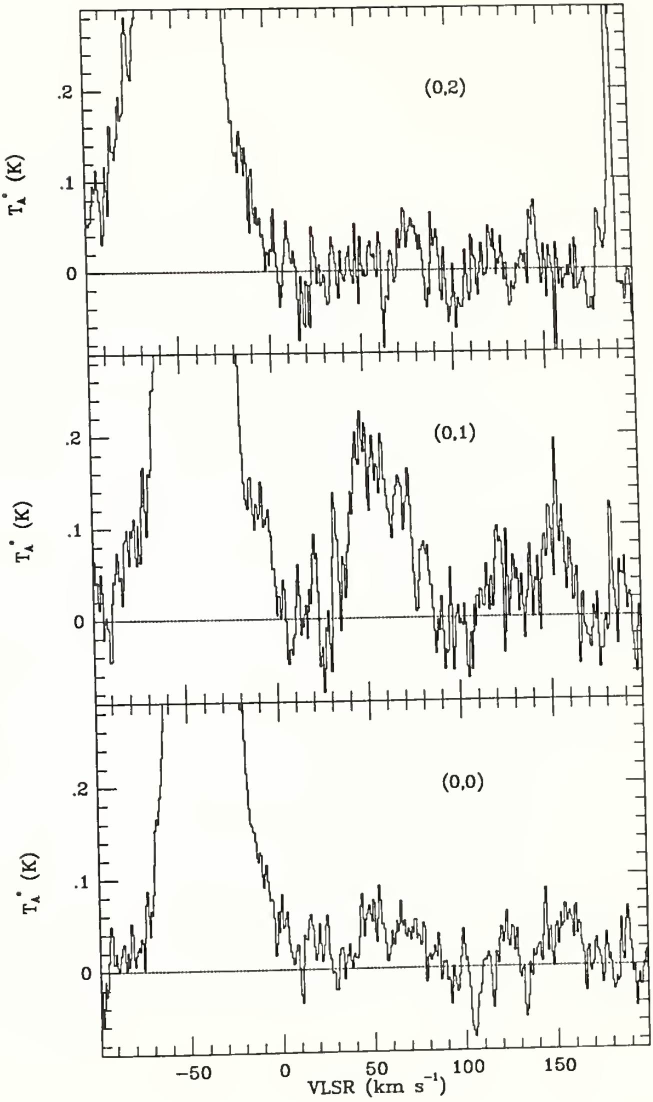
(0,2)
(0,1)
(0,0)
T_A^* (K)
.2
.1
0
−50
0
50
100
150
VLSR (km s^{-1})

Figure 5.13. - A multiple Gaussian fit to the (0,1) spectrum from Figure 5.12. The fitted lines have fixed central velocities and line widths. Integrated intensities of the three HC_3N lines in the blend between 30 and 100 km s^{-1} are similar, in agreement with the expectation based on similar line strengths.

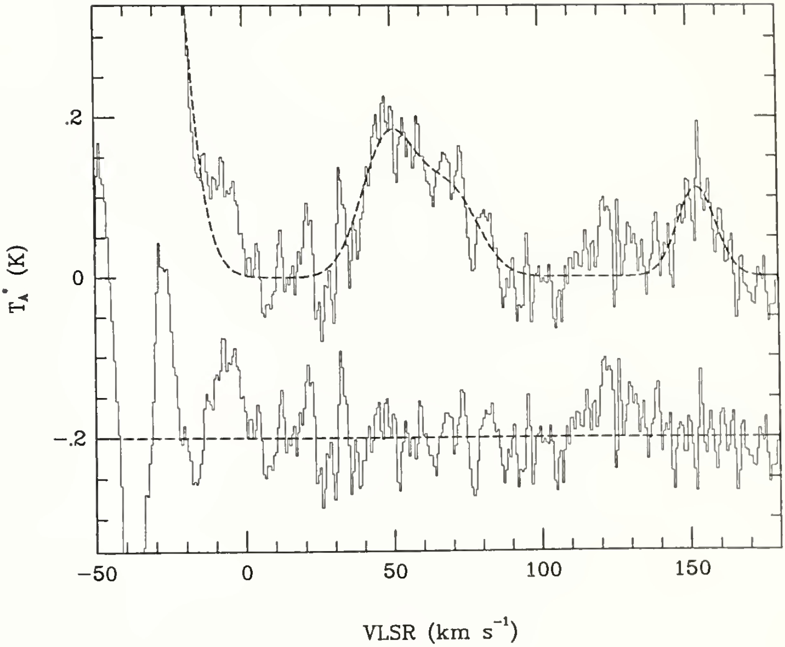
T_A^* (K)
.2
0
−.2
−50
0
50
100
150
VLSR (km s^{-1})

Figure 5.14. - Possible detection of the $J = 12 \rightarrow 11$ HC_3N transition in the $\nu_6(1e)$ state. The line observed at the (0,1) position has a correct LSR velocity; its intensity, however, seems too high compared to the $\nu_6(1f)$ transition.

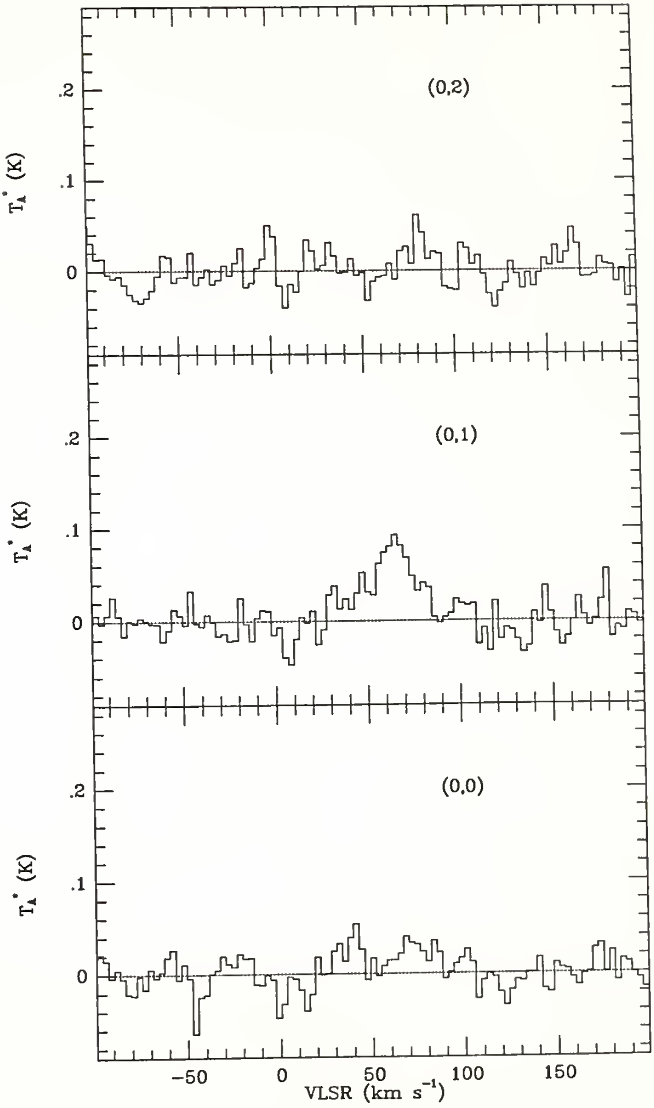
(0,2)
(0,1)
(0,0)
T_A^* (K)
T_A^* (K)
T_A^* (K)
.2
.1
0
.2
.1
0
.2
.1
0
−50
0
50
100
150
VLSR (km s^{-1})

Figure 5.15. - Rotation diagram for HC_3N. The emission cannot be described by a single rotation temperature. The excitation temperature between the ground state and v_7=1 state is 99 K, 154 K, and 84 K for the (0,0), (0,1), and (0,2) positions, respectively. The excitation temperature between the v_7=1 and v_7=2 states is 232 K and 236 K for the (0,0) and (0,1) positions. Because the ground level emission may come from regions not directly associated with the continuum sources the excitation temperature between the first and second vibrationally excited states seems to be a better estimate of the radiation field temperature in the vicinity of the continuum sources.

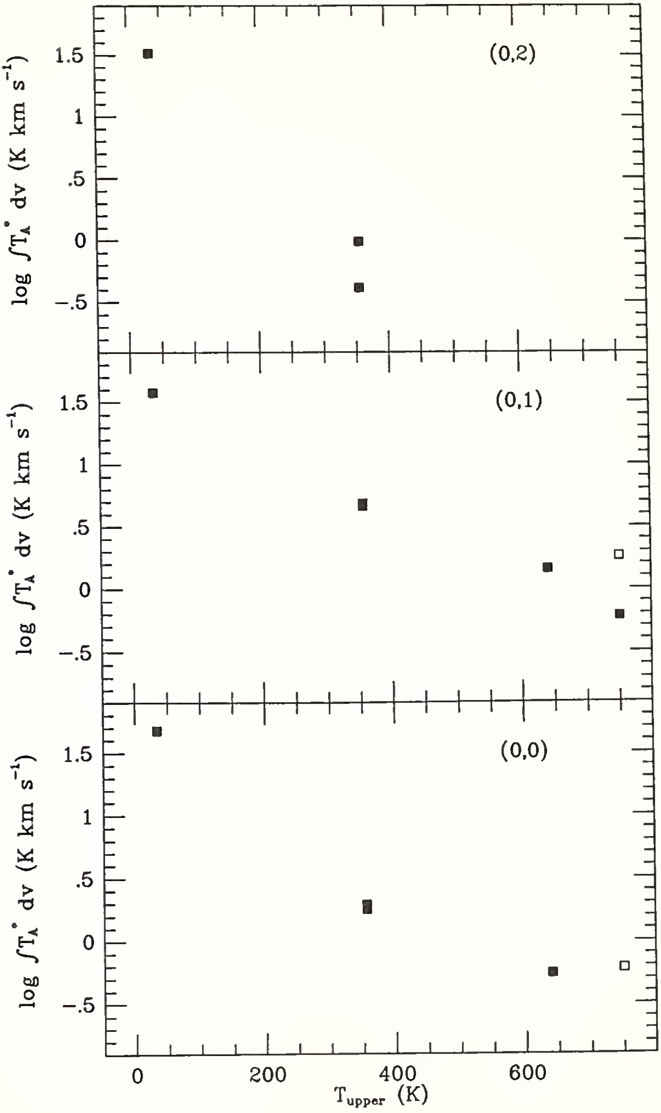
(0,2)
(0,1)
(0,0)
log ∫T_A* dv (K km s⁻¹)
1.5
1
.5
0
−.5
0
200
400
600
T_{upper} (K)

Figure 5.16. - Rotation diagram for HNCO. Similar to the case of HC_3N, the emission cannot be described by a single rotation temperature. The excitation temperature between the $K_a = 0$ and $K_a = 1$ ladders is 17 K, 20 K, and 12 K for the (0,0), (0,1), and (0,2) positions, respectively. The excitation temperatures between the $K_a = 1$ and $K_a = 2$ ladders is 44 K and 78 K for the (0,0) and (0,1) positions. The open squares correspond to a line misidentified as a transition in $K_a = 3$ ladder.

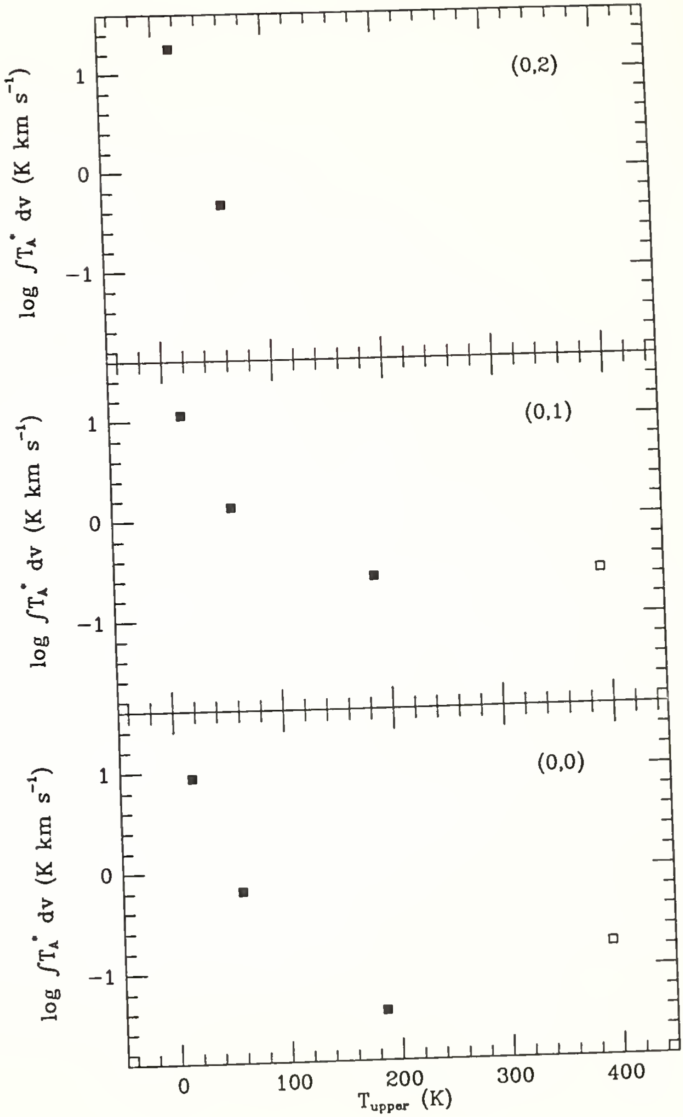
(0,2)
(0,1)
(0,0)
log ∫T*A dv (K km s-1)
1
0
−1
0
100
200
300
400
Tupper (K)

CHAPTER VI

COMPARISON WITH OTHER GALACTIC CENTER CLOUDS

In previous Chapters I have discussed the physical conditions in the Sagittarius B2 molecular cloud. I have started with a simple analysis of the $J = 1 \rightarrow 0$ transitions of ^{13}CO and C^{18}O based on constant excitation temperature assumption, and through more sophisticated models of the continuum and molecular line emission I have shown that the simple approach can be very useful for drawing conclusions about masses and column densities, provided that reasonable values of the kinetic temperature and molecular fractional abundances are chosen. In the present chapter I will use this simple approach to analyze the observations of the $J = 1 \rightarrow 0$ transition of ^{13}CO toward two other Galactic Center fields, in order to compare the characteristics of GMCs in these regions with these derived for Sgr B2. The goal of this comparison is to determine whether the high density, mass, and velocity dispersion found for Sgr B2 is characteristic for the whole population of Galactic Center GMCs.

A. Observations

The $J = 1 \rightarrow 0$ transition of ^{13}CO toward two selected Galactic Center fields, G1.1-0.1 and G359.4-0.1, was observed in 1988 June, using the 14 m FCRAO antenna and the receiver system described in Chapter II. The typical system temperature was 700 - 1700 K (SSB). Pointing was checked by continuum observations of Saturn. The FWHM beam size was 45″ and the main beam efficiency was 0.45. The integration time varied from 60 to 120 s, resulting in an rms fluctuation level of 100 - 150 mK in a 3 km s^{-1} velocity resolution element. The 1950.0 coordinates of the center positions of the two fields observed are: $\alpha = 17^h45^m30^s$, $\delta = -28°02'30''$ for G1.1-0.1, and $\alpha =$

$17^h41^m22^s$, δ = -29°26′36″ for G359.4-0.1. For both sources I used reference positions offset by -60″ in R.A. ^{13}CO emission from G1.1-0.1 was observed at 68 positions (Table 6.1) spaced over a region 12′ × 20′ in size. The typical spacing between the positions is 2′; the grid, however, is incomplete. In the case of G359.4-0.1 the size of the region mapped is 16′ × 16′, and the spacing is 4′.

For each field I observed the $J = 1 \rightarrow 0$ transition of ^{12}CO, ^{13}CO, and C^{18}O at two selected positions in order to address the issue of the optical depth of ^{13}CO lines. For G1.1-0.1 this was done at the (2,10), and (10,12) positions. For G359.4-0.1 the three CO isotopes were observed at the (-2,4), and (4,2) positions. The integration time was 16 - 20 minutes for ^{12}CO and ^{13}CO, and 40 - 80 minutes for C^{18}O. The resulting rms fluctuation level in a 3 km s^{-1} velocity channel was 150 - 200 mK for ^{12}CO, 60 - 90 mK for ^{13}CO, and 40 - 45 mK for C^{18}O.

B. G1.1-0.1

G1.1-0.1 (or KE56) is a thermal continuum source which contains a small H II region (Pauls and Mazger 1975) superimposed on a supernova remnant G1.05-0.1 (Little 1974, Swarup *et al.* 1974). Because of the strong H_2CO absorption observed toward the thermal source (Whiteoak and Gardner 1974) it is presumably located in the nuclear disk.

^{13}CO spectra at five selected positions in this region are shown in Figure 6.1. The main velocity component with a VLSR of ~ 82 km s^{-1} is present at most positions. In addition many other components spread over 200 km s^{-1} velocity range are observed. Some of them have rather narrow line widths and almost certainly originate in the local ISM. Based of the appearance of the spectra, I expect that most of the emission in the 40 - 140 km s^{-1} velocity range should come from regions physically bound to the core of the cloud. The spatial-velocity map for a cut with $\Delta\alpha=2$ (Figure 6.2) shows that the emission is, indeed, confined to this velocity range. A contour map of the integrated intensity between 40 and 140 km s^{-1} is shown in Figure 6.3. The emission is clumpy, and shows two peaks at the (2,6) and (2,10) positions. The cloud is not well isolated. The intensity at the edge of the map increase in several directions.

In order to calculate ^{13}CO column density through the cloud, one has to estimate the kinetic temperature inside the cloud and the optical depth of ^{13}CO lines. The ^{12}CO, ^{13}CO, and C^{18}O spectra at the (2,10) position corresponding to the northern peak in the core of the cloud (Figure 6.4) are very similar suggesting that even the optical depth of ^{12}CO is moderate. Ther is no evidence of self-absorption. The same is true at the (10,12) position, just outside the region mapped, close to the position of another peak of the emission. The ^{12}CO to ^{13}CO peak antenna temperature ratio of 5.3 observed at the (2,10) position gives a line center ^{13}CO optical depth of 0.19. The assumption of optically thin emission seems, therefore, fully justified. The fact that the ^{12}CO emission is not reversed may suggest that the temperature in the cloud is very uniform. If the kinetic temperature were simply constant, one would not see self absorption, even if the optical depth were large.

The peak ^{12}CO antenna temperature of ~ 8 K suggests a kinetic temperature of ~ 13 K inside the cloud. Based on the discussion of the thermal balance of the gas in Chapter IV, one can estimate the kinetic temperature simply including turbulent dissipation as the only heating source. This is done in Figure 6.6 for turbulent velocity dispersions of 10, 12, 14, 16, and 18 km s^{-1} (lower to upper curve, respectively) and the turbulent heating rate scaling factor of 0.2. Because the emission in the 40 - 140 km s^{-1} velocity range comes from several blended clumps, determination of the internal velocity dispersion inside these clumps is a non-trivial problem. Gaussian fits at ten position where the main velocity component seems to be well isolated give velocity dispersions between 9.5 and 14.5 km s^{-1} with a mean value of 11.8 km s^{-1}. The velocity dispersion within clumps is, therefore, very similar to that observed in the main component in Sgr B2. The estimate of the ^{13}CO optical depth given above suggest an H_2 column density over an order of magnitude lower than in Sgr B2, assuming the same ^{13}CO fractional abundance. Because the size of G1.1-0.1 seems to be comparable to Sgr B2 (~ 40 pc diameter), the mean H_2 density in the envelope must be significantly lower in G1.1-0.1, probably between 500 and 1000 cm^{-3}. For this density range and velocity dispersion of 12 km s^{-1} (dotted line), Figure 6.6 predicts a kinetic temperature between 12 and 15 K, quite consistent with the estimate based on the peak ^{12}CO antenna temperature. Using 13 K as an average excitation temperature for ^{13}CO I derive peak ^{13}CO column densities of 1.8 and 1.7×10^{17} cm^{-2} for the northern and southern peaks, respectively. With a ^{13}CO fractional abundance of 1×10^{-6}, as suggested by the Monte Carlo models for Sgr B2, this leads to H_2 column densities of 1.8 and 1.7×10^{23} cm^{-2} for the northern and southern peaks, respectively. The mean H_2 density along the line of sight at the position of the northern peak is ~ 1450 cm^{-3} (approximately a factor of 8 lower than for Sgr B2), assuming a diameter of ~ 40 pc (16′). The difference is much less prominent for off-center positions. At a distance of 15 pc from the center (Figure 6.7) the integrated intensity drops to ~ 55 K km s^{-1}. This is equivalent to an H_2 column density of 1.2×10^{23} cm^{-2}, ~ 65 % of the peak value. If the cloud radius is 20 pc, the mean H_2 density along the line of sight is again ~ 1450 cm^{-3}, suggesting that density contrast is indeed very low. The mean density in the envelope of G1.1-0.1 is only a factor of 2 - 3 lower than the density in the envelope of Sgr B2. The envelopes of the two cloud seem to be quite similar. The main difference is the central ~ 5 pc region which is much denser in Sgr B2. This results in much higher peak H_2 column density, explaining why so many molecular species have been detected toward Sgr B2. Because the mass of the cloud is dominated by the envelope, one can expect the total molecular mass of G1.1-0.1 to be relatively large. The total mass in the 14′ × 22′ region is 3.4×10^6 $M_\odot$, again a factor of only 2 - 3 lower than the mass of Sgr B2.

C. G359.4-0.1

G359.4-0.1 (or Sgr C) is a discrete continuum source superimposed on an extended background ridge. Radio recombination line studies (Pankonin and Downes 1976) show at least three velocity features with central velocities -4, -56 and -132 km s^{-1}. The source is thought to be in the Galactic Center region based on the observations of HI (Kazès and Aubury 1973) and formaldehyde absorption lines (Whiteoak and Gardner 1974) at velocities corresponding to the 3 kpc arm. Studies of Gatley *et al.* (1978) show that the far-infrared (30-100 μ) optical depth is low indicating that this source is not embedded in a dense molecular cloud.

The emission from this field is very complicated with many velocity components present between -150 and +50 km s^{-1}. At least two separate clouds are observed. The first one is confined to the velocity range -150 to -75 km s^{-1} (Table 6.2). It can be seen in Figure 6.8, and it it consists of several clumps with central velocities changing significantly from one position to another [compare the (0,4), (-4,4), and (0,8) positions]. Clearly the 4′ spacing of the data points is not sufficient to trace the clumps and with the present data it is impossible to determine whether they are indeed a part of one cloud. A contour map of the integrated intensity is shown in Figure 6.9. The highest integrated intensities are observed at the (0,4), and (-4,0) positions (61.8, and 62.2 K km s^{-1}, respectively). The emission is elongated and appears to peak at the (-2,4) position. The additional spectrum taken at the this position (Figure 6.10), however, has an integrated intensity of only 37.4 K km s^{-1} suggesting the presence of two separate clouds. One has to be, therefore, very careful interpreting data taken with insufficient spacing between the neighboring positions. The mean velocity of the cloud is ~ -120 km s^{-1}. Large deviations from this velocity, however, are observed. Spectra of ^{12}CO, ^{13}CO, and C^{18}O taken at the (-2,4) position (Figure 6.10) are very similar suggesting moderate optical depth of ^{12}CO. The peak ^{12}CO to ^{13}CO antenna temperature ratio of 5.4 gives a ^{13}CO line center optical depth of 0.18. The peak ^{12}CO antenna temperature of ~ 7 K suggests the kinetic temperature of ~ 12 K inside the cloud.

The emission from the second cloud (Table 6.3) (Figure 6.11) covers velocity range -80 to -20 km s^{-1}, and probably extends farther into positive velocities. The emission with VLSR close to zero, however, is strongly contaminated by local gas, and has not been included in the column density computations. A contour map of the integrated intensity is shown in Figure 6.12. The emission peaks at the (4,1) position and is elongated in the north-south direction. The additional spectrum taken at the (4,2) position (Figure 6.13) has the highest integrated intensity, suggesting that in this case we are dealing with a single, well defined cloud. The mean velocity of the cloud is ~ -45 km s^{-1}. ^{12}CO, ^{13}CO, and C^{18}O spectra at the (4,2) position, close to the peak of the emission, are shown in Figure 6.13. Contrary to the two previous cases they do not look alike. The ^{12}CO spectrum shows a very strong dip at a VLSR of ~ -52 km s^{-1}. A smaller dip at the same velocity is observed in the ^{13}CO spectrum. This is most likely produced by cold foreground gas because the velocity of the dip in ^{12}CO and ^{13}CO spectra does not correspond to the peak of C^{18}O emission. It is, therefore, plausible that ^{13}CO emission from the cloud is optically thin. The foreground absorption, however, results in underestimating the line intensities. Because the ^{12}CO line is most affected, it is difficult to estimate the peak ^{12}CO antenna temperature. A lower limit for the kinetic temperature inside the cloud based on ^{12}CO data is ~ 13 K.

Using a 13 K ^{13}CO excitation temperature I derive peak ^{13}CO column densities of 1.3×10^{17} cm^{-2} in the -120 km s^{-1} cloud at the (0,4), and (-4,4) positions. This corresponds to an H_2 column density of 1.3×10^{23} cm^{-2}. If the cloud radius is 40 pc an average H_2 density along the line of sight is 1050 cm^{-3}. The total mass contained in this velocity range in the 20′ × 20′ region is 1.9×10^{6} $M_{\odot}$. The peak ^{13}CO column density in the -45 km s^{-1} cloud is 1.5×10^{17} cm^{-2}, using a 13 K ^{13}CO excitation temperature. This corresponds to an H_2 column density of 1.5×10^{23} cm^{-2}. An average H_2 density along the line of sight is 1200 cm^{-3}. The total mass of the cloud is 1.9×10^{6} $M_{\odot}$.

D. Conclusion

The peak H_2 column densities and total cloud masses derived for G1.1-0.1 and the two components of G359.4-0.1 are very similar. The three clouds are consistent with *a typical Galactic Center GMC* with an average density of 1000 - 1500 cm^{-3}, diameter of ~ 40 pc, peak H_2 column density of $1.3 - 1.8 \times 10^{23}$ cm^{-2}, and a mass of $2 - 3 \times 10^{6}$ $M_{\odot}$. Sgr B2 has a similar size to these other Galactic Center clouds. Its average density and mass, however, are approximately a factor 3 higher. The difference in the peak H_2 column density is even more prominent (~ a factor of 10). This results from the presence of relatively dense gas with an H_2 density of ~ $5 - 8 \times 10^{4}$ cm^{-3} in the inner part of the cloud, several pc in diameter. Similar condensations are not present in the other clouds observed. The far infrared and millimeter continuum data for other Galactic Center clouds is very limited. The data of Gatley *et al.* (1978) for G359.4-0.1 suggest that very dense condensations similar to Sgr B2(N) and (M) sources are also absent. Future continuum studies with the VLA and KAO will be especially useful for making models of the continuum emission from these clouds.

The velocity dispersion of other Galactic Center clouds observed is slightly lower than the value observed in Sgr B2, 22.5 km s^{-1} for G1.1-0.1, and 18.9 and 14.7 km s^{-1} for the -120 and -45 km s^{-1} components of G359.4-0.1 compared to ~ 25 km s^{-1} for Sgr B2. The virial masses for the three clouds based given by equation (2.6) are 12, 8, and 5×10^6 $M_\odot$, respectively. The corresponding molecular masses are 3.4, 1.9, and 1.9×10^6 $M_\odot$, a factor of 3 - 4 lower. This suggest that Sgr B2 is closer to virial equilibrium than the smaller Galactic Center clouds. The galactocentric distances of ~ 160, and 90 pc suggest tidally limited densities of 1.7×10^4, and 5×10^4 cm^{-3} for G1.1-0.1 and G359.4-0.1, respectively. The discrepancy between the tidally limited densities and mean densities in the clouds is again bigger than in the case of Sgr B2, suggesting that the smaller Galactic Center clouds are less likely to be gravitationally bound than Sgr B2.

The virial masses of the smaller Galactic Center clouds are on the upper end of the virial masses of the disk cloud (Scoville *et al.* 1987). The mean H_2 densities, however, are still about an order of magnitude higher than in the disk clouds of comparable size. The average surface density is 1500 - 2700 $M_\odot$ pc^{-2}, compared to the typical value of 170 $M_\odot$ pc^{-2} for disk clouds. The Galactic Center clouds seem to be, therefore, distinctively different from the disk clouds. The difference is presumably caused by the Galactic Center environment.

Table 6.1. - Line Parameters of ^{13}CO Emission in G1.1-0.1.

$\Delta\alpha$	$\Delta\delta$	V_{mean}	σ_V	$\int T_A^* du$	T_A^*	σ_T
10.0	16.0	74.1	20.7	1.1	45.5	0.13
10.0	12.0	82.8	22.1	1.4	50.5	0.18
10.0	8.0	69.8	19.8	0.9	28.8	0.13
6.0	16.0	77.6	9.9	1.6	40.6	0.13
2.0	16.0	86.4	13.7	1.3	42.1	0.14
-2.0	16.0	90.9	17.1	1.3	42.7	0.14
8.0	14.0	73.4	16.4	1.2	43.8	0.09
4.0	14.0	77.9	19.9	1.5	61.6	0.12
0.0	14.0	101.5	22.6	1.0	43.0	0.13
-4.0	14.0	99.1	19.7	1.5	60.0	0.13
8.0	12.0	78.0	19.0	1.5	57.3	0.12
6.0	12.0	81.1	19.5	1.8	70.8	0.16
4.0	12.0	77.8	16.8	1.3	53.2	0.23
2.0	12.0	83.6	22.2	1.5	63.8	0.11
0.0	12.0	85.7	26.8	0.9	54.8	0.23
-2.0	12.0	94.1	22.8	0.9	40.6	0.17
8.0	10.0	82.3	21.7	1.6	67.8	0.09
6.0	10.0	80.8	19.5	1.9	62.2	0.15
4.0	10.0	76.3	18.1	1.5	62.2	0.15
2.0	10.0	82.6	22.3	1.8	86.5	0.19
0.0	10.0	84.3	22.3	1.3	67.6	0.09
-2.0	10.0	81.7	20.4	1.7	70.1	0.13
-4.0	10.0	82.0	19.9	1.6	55.5	0.10
8.0	8.0	84.1	19.4	1.3	50.6	0.16
6.0	8.0	82.5	17.6	1.7	58.5	0.12
4.0	8.0	81.7	19.8	1.8	69.5	0.12
2.0	8.0	83.5	18.5	1.8	76.7	0.13
0.0	8.0	82.2	20.9	1.6	75.4	0.13
-2.0	8.0	77.6	18.9	1.1	50.6	0.11
-4.0	8.0	74.7	22.1	1.2	56.0	0.12
8.0	6.0	79.3	22.7	0.9	42.9	0.17
6.0	6.0	87.8	19.3	1.5	58.0	0.11
5.0	6.0	88.5	21.4	1.5	68.2	0.12
4.0	6.0	85.2	20.7	1.4	71.0	0.13
2.0	6.0	83.8	20.3	1.8	78.3	0.13
0.0	6.0	76.3	18.5	1.5	65.9	0.11
-2.0	6.0	79.3	17.8	1.1	46.1	0.12
-4.0	6.0	76.4	18.1	1.0	39.6	0.12
8.0	4.0	82.8	24.8	0.7	27.1	0.16
4.0	4.0	91.8	25.4	0.9	48.0	0.10
2.0	4.0	83.7	25.2	1.3	73.0	0.12
0.0	4.0	72.3	18.0	1.2	58.5	0.13
-2.0	4.0	74.9	17.3	1.3	53.5	0.10
-4.0	4.0	72.0	16.7	1.2	53.5	0.11
8.0	2.0	81.1	23.9	0.5	15.3	0.17

continued on next page

Table 6.1. - Continued.

$\Delta\alpha$	$\Delta\delta$	V_{mean}	σ_V	$\int T_A^* du$	T_A^*	σ_T
4.0	2.0	84.2	24.5	1.1	49.5	0.13
2.0	2.0	80.2	22.7	1.4	63.9	0.12
0.0	2.0	88.9	24.9	1.3	73.0	0.19
-2.0	2.0	74.5	14.6	1.5	59.8	0.14
-4.0	2.0	76.7	19.4	1.6	66.3	0.12
8.0	0.0	69.4	15.7	0.8	22.8	0.15
4.0	0.0	82.7	25.1	1.2	52.4	0.14
2.0	0.0	80.3	25.1	1.5	69.1	0.22
0.0	0.0	81.4	19.3	1.0	33.3	0.20
-2.0	0.0	86.1	20.5	1.5	56.5	0.17
-4.0	0.0	79.4	19.2	1.9	62.4	0.15
8.0	-2.0	85.8	31.7	1.1	49.3	0.15
4.0	-2.0	85.0	24.6	1.0	45.6	0.21
2.0	-2.0	85.3	23.4	1.1	56.1	0.13
0.0	-2.0	90.7	26.1	1.2	55.0	0.11
-2.0	-2.0	92.8	23.6	1.3	59.2	0.14
-4.0	-2.0	94.1	18.0	1.6	54.8	0.14
8.0	-4.0	80.0	29.9	1.1	45.6	0.14
4.0	-4.0	91.4	25.6	0.8	44.5	0.12
2.0	-4.0	88.9	24.6	0.9	51.4	0.13
0.0	-4.0	93.3	26.1	1.3	62.0	0.14
-2.0	-4.0	92.3	25.9	1.4	70.6	0.29
-4.0	-4.0	102.4	17.2	1.2	40.6	0.30

The entries in the table are: offsets from the cloud center (arcminutes), mean line velocity (km s^{-1}), velocity dispersion (km s^{-1}), integrated intensity between 30 and 100 km s^{-1}, peak antenna temperature not corrected for the main beam efficiency ($\eta = 0.45$), and rms noise in a 3 km s^{-1} resolution element (K).

Table 6.2. - Line Parameters of ^{13}CO Emission in G359.4-0.1 (A).

$\Delta\alpha$	$\Delta\delta$	V_{mean}	σ_V	$\int T_A^* du$	T_A^*	σ_T
8.0	8.0	-122.7	13.0	0.5	13.8	0.12
4.0	8.0	-129.5	15.2	0.5	13.5	0.11
0.0	8.0	-96.3	13.3	2.5	47.5	0.14
-4.0	8.0	-118.9	6.2	1.2	25.0	0.16
-8.0	8.0	-119.5	18.4	0.7	19.4	0.13
8.0	4.0	-117.0	18.9	0.8	23.4	0.12
4.0	4.0	-127.8	15.6	0.6	19.9	0.12
0.0	4.0	-107.2	14.4	2.9	61.8	0.11
-4.0	4.0	-107.5	19.9	1.9	62.2	0.10
-8.0	4.0	-127.9	16.8	0.3	8.8	0.14
8.0	0.0	-123.5	18.1	0.6	19.3	0.12
4.0	0.0	-118.8	26.1	0.7	15.8	0.10
0.0	0.0	-118.1	10.9	1.1	27.1	0.13
-4.0	0.0	-125.8	13.7	1.9	49.3	0.10
-8.0	0.0	-139.5	0.0	0.3	3.5	0.12
8.0	-4.0	-121.0	17.1	0.4	13.9	0.11
4.0	-4.0	-127.2	15.3	0.8	18.1	0.15
0.0	-4.0	-123.3	19.1	0.9	23.1	0.12
-4.0	-4.0	-121.7	17.5	0.8	20.4	0.13
-8.0	-4.0	-112.8	15.0	1.4	34.3	0.13
8.0	-8.0	36.6	0.0	0.2	0.6	0.12
4.0	-8.0	-111.7	20.3	0.4	6.1	0.13
0.0	-8.0	-116.2	23.2	0.6	15.6	0.16
-4.0	-8.0	-129.0	14.3	0.6	14.5	0.14
-8.0	-8.0	-124.3	14.9	1.1	28.4	0.15

The entries in the table are: offsets from the cloud center (arcminutes), mean line velocity (km s^{-1}), velocity dispersion (km s^{-1}), integrated intensity between -150 and -75 km s^{-1}, peak antenna temperature not corrected for the main beam efficiency (η = 0.45), and rms noise in a 3 km s^{-1} resolution element (K).

Table 6.3. - Line Parameters of ^{13}CO Emission in G359.4-0.1 (B).

$\Delta\alpha$	$\Delta\delta$	V_{mean}	σ_V	$\int T_A^* du$	T_A^*	σ_T
8.0	8.0	-38.9	9.6	1.9	37.5	0.12
4.0	8.0	-41.7	11.9	1.5	29.7	0.11
0.0	8.0	-48.5	15.1	0.6	17.0	0.14
-4.0	8.0	-44.7	20.0	0.4	4.9	0.16
-8.0	8.0	-46.1	24.9	0.4	3.9	0.13
8.0	4.0	-49.3	15.8	1.3	58.0	0.12
4.0	4.0	-52.4	12.6	2.4	65.7	0.12
0.0	4.0	-56.1	12.5	1.2	25.1	0.11
-4.0	4.0	-53.3	21.6	0.6	10.4	0.10
-8.0	4.0	-39.2	23.6	0.3	2.8	0.14
8.0	0.0	-49.1	14.3	0.9	27.9	0.12
4.0	0.0	-52.3	13.2	2.0	70.8	0.10
0.0	0.0	-48.8	0.0	0.6	9.7	0.13
-4.0	0.0	-3.9	0.0	0.5	3.8	0.10
-8.0	0.0	59.7	0.0	0.3	0.8	0.12
8.0	-4.0	-43.8	14.6	0.8	27.2	0.11
4.0	-4.0	-47.4	15.0	1.3	40.5	0.15
0.0	-4.0	-49.4	13.3	1.5	42.2	0.12
-4.0	-4.0	-45.8	18.0	0.6	19.9	0.13
-8.0	-4.0	-48.3	15.3	0.5	13.8	0.13
8.0	-8.0	-57.1	10.3	0.3	6.8	0.12
4.0	-8.0	-43.1	12.5	0.6	14.1	0.13
0.0	-8.0	-43.9	12.7	0.7	21.9	0.16
-4.0	-8.0	-44.4	12.9	0.9	23.9	0.14
-8.0	-8.0	-44.9	13.1	0.4	8.5	0.15

The entries in the table are: offsets from the cloud center (arcminutes), mean line velocity (km s^{-1}), velocity dispersion (km s^{-1}), integrated intensity between -80 and 20 km s^{-1}, peak antenna temperature not corrected for the main beam efficiency ($\eta = 0.45$), and rms noise in a 3 km s^{-1} resolution element (K).

Figure 6.1. - ^{13}CO $J=1\rightarrow0$ spectra in G1.1-0.1. The emission has been corrected for atmospheric attenuation and warm losses but has not been corrected for the main beam efficiency of 0.45. The main velocity component with VLSR of ~ 82 km s^{-1} is present at most positions. The emission in the 40 - 140 km s^{-1} velocity range has been included in column density calculations.

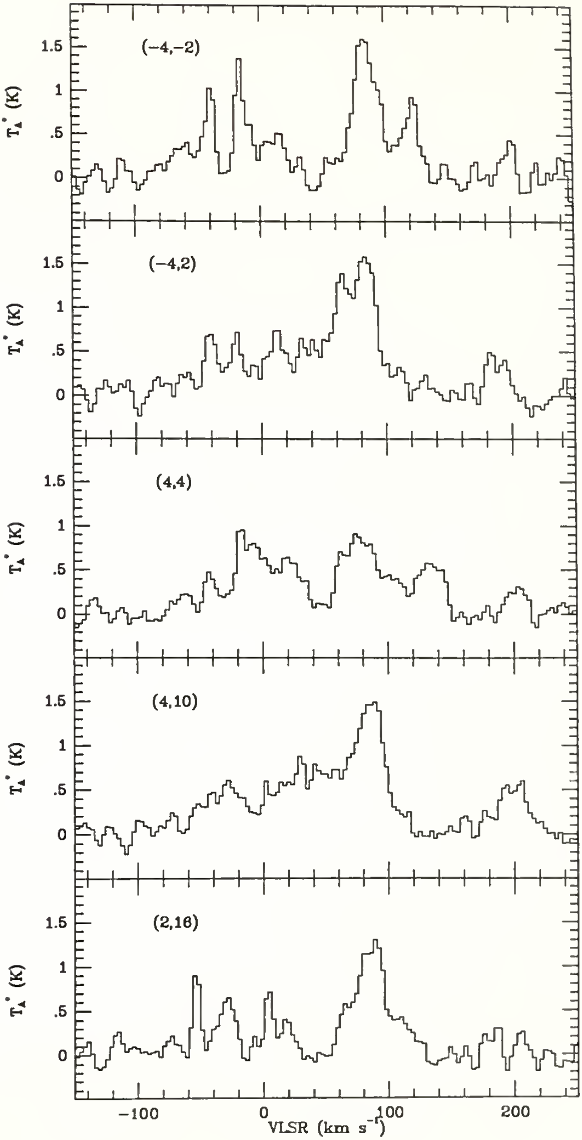
(−4,−2)
(−4,2)
(4,4)
(4,10)
(2,16)
T_A^* (K)
1.5
1
.5
0
−100
0
100
200
VLSR (km s^{-1})

Figure 6.2. - A spatial-velocity map of G1.1-0.1 for a cut with $\Delta\alpha=0$. The contour levels are 0.75, 1.0, 1.25, 1.5, and 2.0 K. The emission is clearly confined to the 40 - 140 km s^{-1} velocity range.

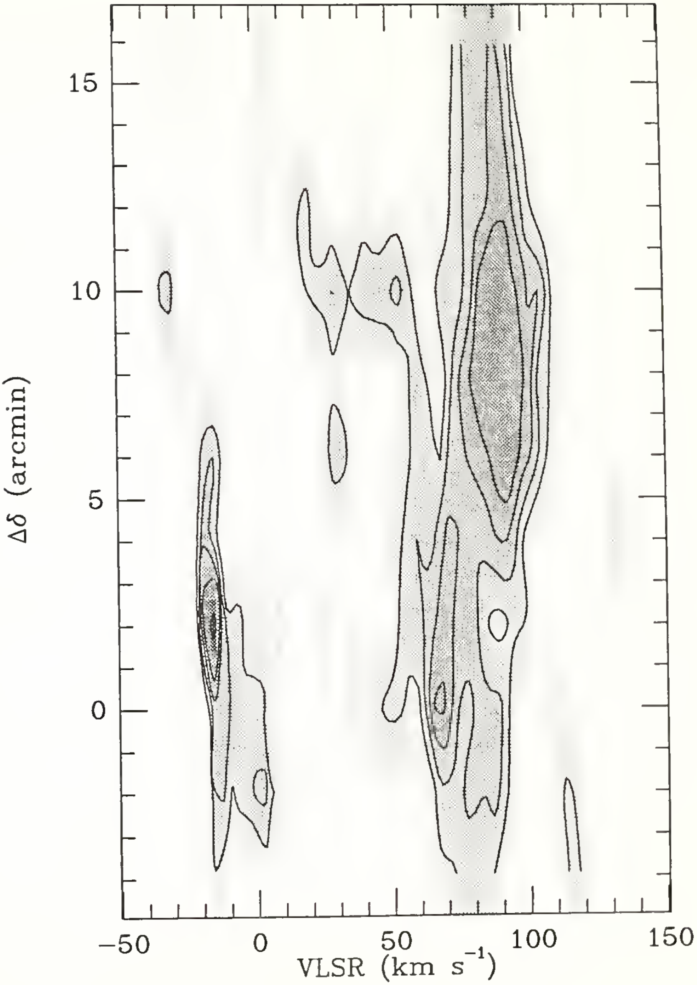
15
10
5
0
Δδ (arcmin)
−50
0
50
100
150
VLSR (km s^{-1})

Figure 6.3. - A contour map of ^{13}CO integrated intensity in G1.1-0.1. The integrated intensity in the 40 - 140 km s^{-1} velocity range has been corrected for atmospheric attenuation and warm losses but has not been corrected for the main beam efficiency of 0.45. The solid contour levels are 50, 60, 70, and 75 K km s^{-1}. The dashed contour corresponds to 50 % of the peak intensity (43 K km s^{-1}).

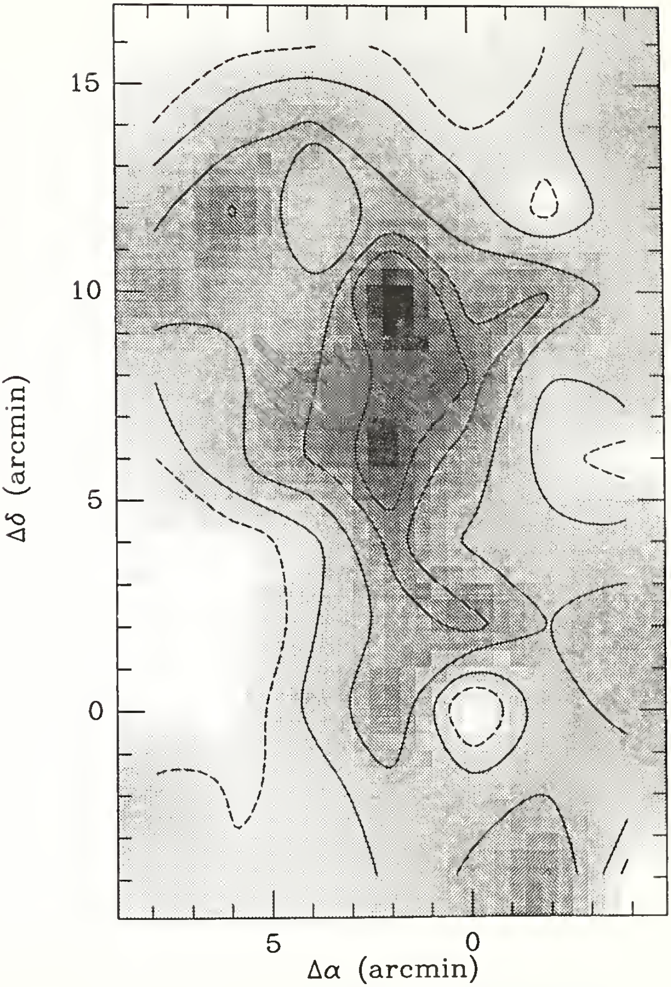
15
10
5
0
Δδ (arcmin)
5
0
Δα (arcmin)

Figure 6.4. - $C^{18}O$, ^{13}CO, and ^{12}CO spectra at the (2,10) position in G1.1-0.1. All three isotopes have very similar line shapes suggesting that the optical depth of ^{12}CO is moderate. The peak ^{12}CO to ^{13}CO antenna temperature ratio of 5.3 suggests a ^{13}CO line center optical depth of 0.19.

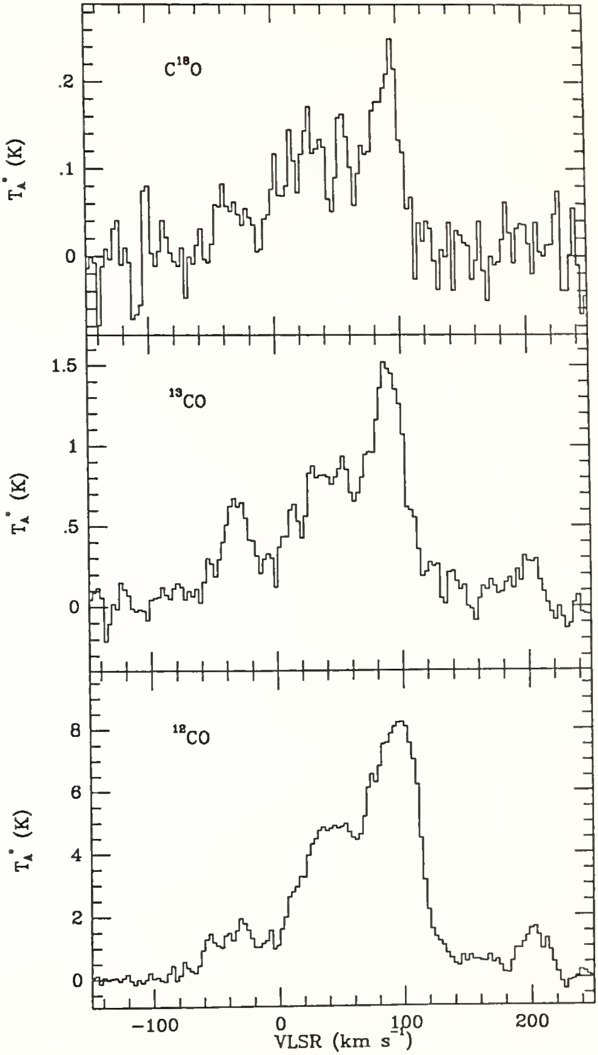
C^{18}O
^{13}CO
^{12}CO
T$_A^*$ (K)
T$_A^*$ (K)
T$_A^*$ (K)
.2
.1
0
1.5
1
.5
0
8
6
4
2
0
−100
0
100
200
VLSR (km s^{-1})

Figure 6.5. - $C^{18}O$, ^{13}CO, and ^{12}CO spectra at the (10,12) position in G1.1-0.1. Similar to the (2,10) position (Figure 6.4), all three isotopes have very similar line shapes suggesting that the optical depth of ^{12}CO is moderate.

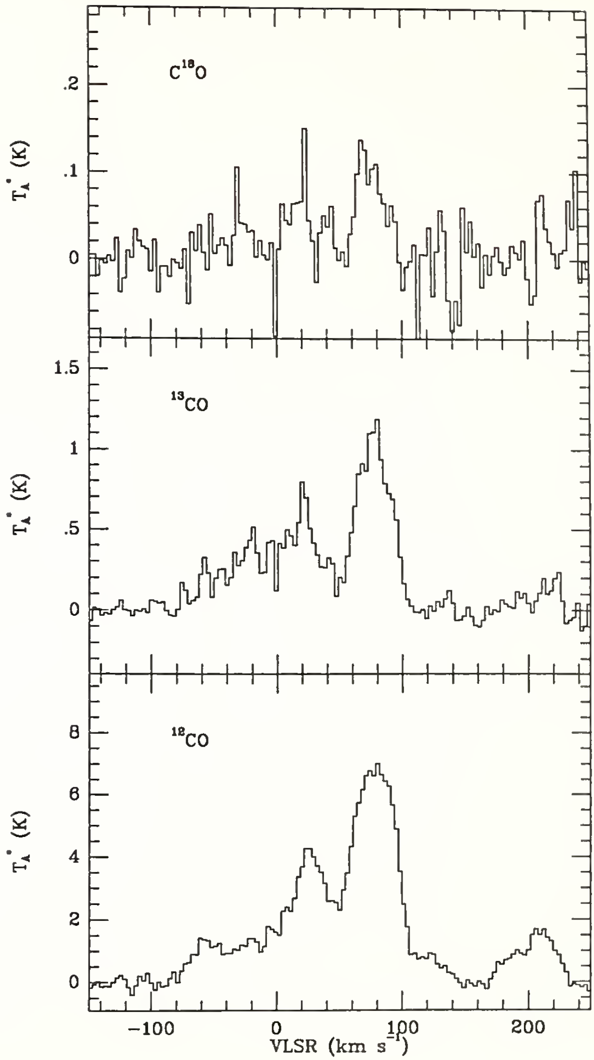
C^{18}O
T_A^* (K)
.2
.1
0
^{13}CO
T_A^* (K)
1.5
1
.5
0
^{12}CO
T_A^* (K)
8
6
4
2
0
−100
0
100
200
VLSR (km s^{-1})

Figure 6.6. - Kinetic temperature of the gas for different velocity dispersions. The five curves correspond to the velocity dispersions of 10, 12, 14, 16, and 18 km s^{-1} (lower to upper curve, respectively). Turbulent dissipation was assumed to be the only heating source. The turbulent heating rate scaling factor of 0.2 has been used in the calculations.

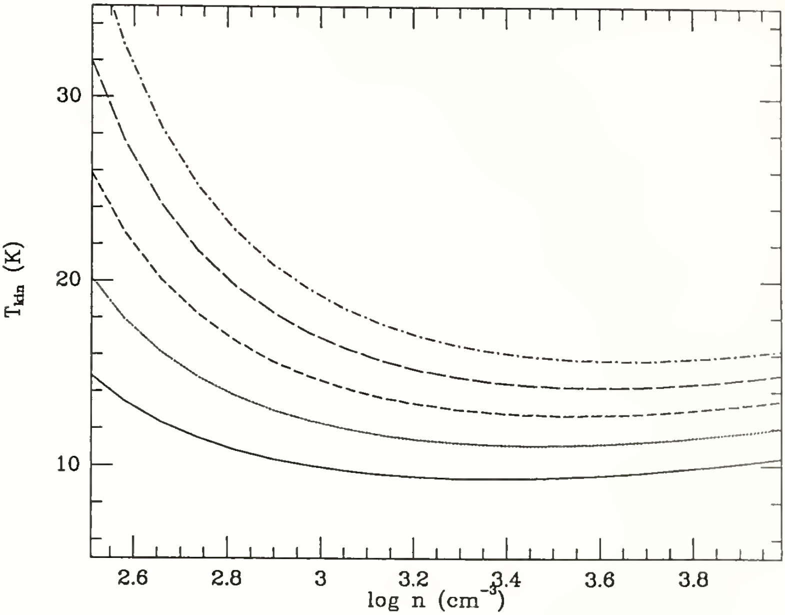
T_{kin} (K)
30
20
10
2.6
2.8
3
3.2
3.4
3.6
3.8
log n (cm^{-3})

Figure 6.7. - Integrated intensity of ^{13}CO emission in G1.1-0.1. The integrated intensity has been plotted as a function of the distance from the (2,8) position. The distribution is much less centrally peaked than that observed in Sgr B2 (Figure 4.17), suggesting much smaller density gradients inside the cloud.

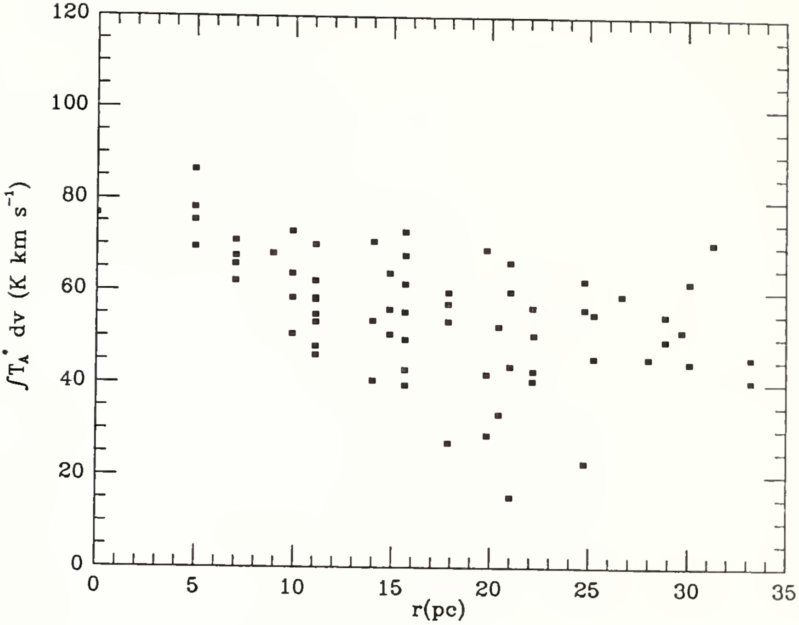
120
100
80
60
40
20
0
$\int T_A^* \, dv$ (K km s^{-1})
0
5
10
15
20
25
30
35
r(pc)

Figure 6.8. - ^{13}CO spectra showing the -120 km s^{-1} component of G359.4-0.1. The emission is confined to the -150 to -75 km s^{-1} velocity range. It is very clumpy and significant velocity shifts among neighboring positions are present. With the low angular resolution of the present data, it is not clear whether all clumps are parts of a single cloud.

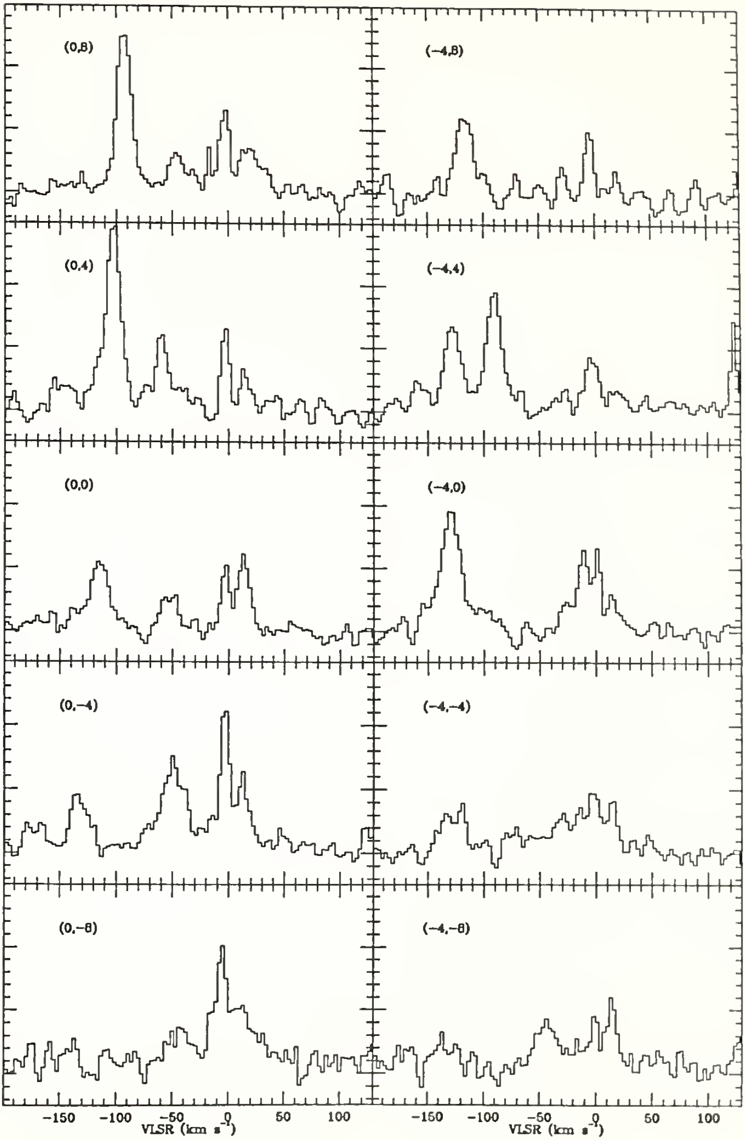
(0,8)
(-4,8)
(0,4)
(-4,4)
(0,0)
(-4,0)
(0,-4)
(-4,-4)
(0,-8)
(-4,-8)
0
1
2
-150
-100
-50
0
50
100
VLSR (km s^{-1})

Figure 6.9. - The -120 km s^{-1} component of G359.4-0.1. The contour map shows the ^{13}CO $J = 1 \rightarrow 0$ integrated intensity between -150 and -75 km s^{-1}. The solid contour levels are: 40, 50, 55, 60, and 65 K km s^{-1}. The dashed contour corresponds to 50 % of the peak intensity (31 K km s^{-1}. The data taken with 4′ spacing suggest the (-2,4) position to be the peak of the emission. The intensity at this position (Figure 6.10), however, is only 60 % of the intensities at the (-4,4) and (0,4) positions, suggesting that two separate clouds contribute to the emission.

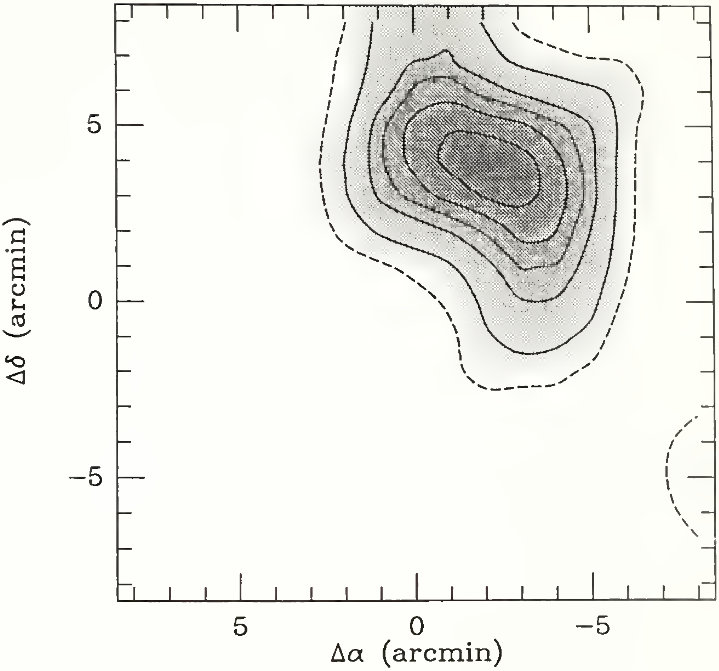
5
0
−5
Δδ (arcmin)
5
0
−5
Δα (arcmin)

Figure 6.10. - $C^{18}O$, ^{13}CO, and ^{12}CO spectra at the (-2,4) position in G359.4-0.1. Similar to the (2,10) and (10,12) positions in G1.1-0.1 (Figures 6.4 and 6.5), all three isotopes have very similar line shapes suggesting that the optical depth of ^{12}CO is moderate.

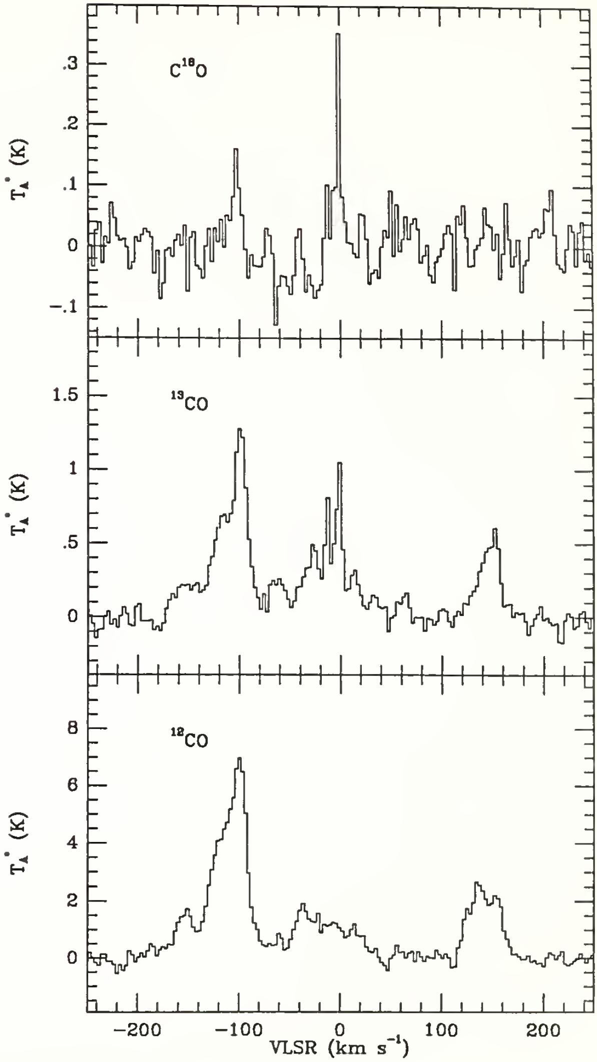
$C^{18}O$
^{13}CO
^{12}CO
T_A^* (K)
.3
.2
.1
0
−.1
1.5
1
.5
0
8
6
4
2
0
−200
−100
0
100
200
VLSR (km s^{-1})

Figure 6.11. - ^{13}CO spectra showing the -45 km s^{-1} component of G359.4-0.1. The -80 to -20 km s^{-1} velocity range was used for column density computations. The emission extends into higher velocities. It is strongly contaminated, however, by contributions from local clouds.

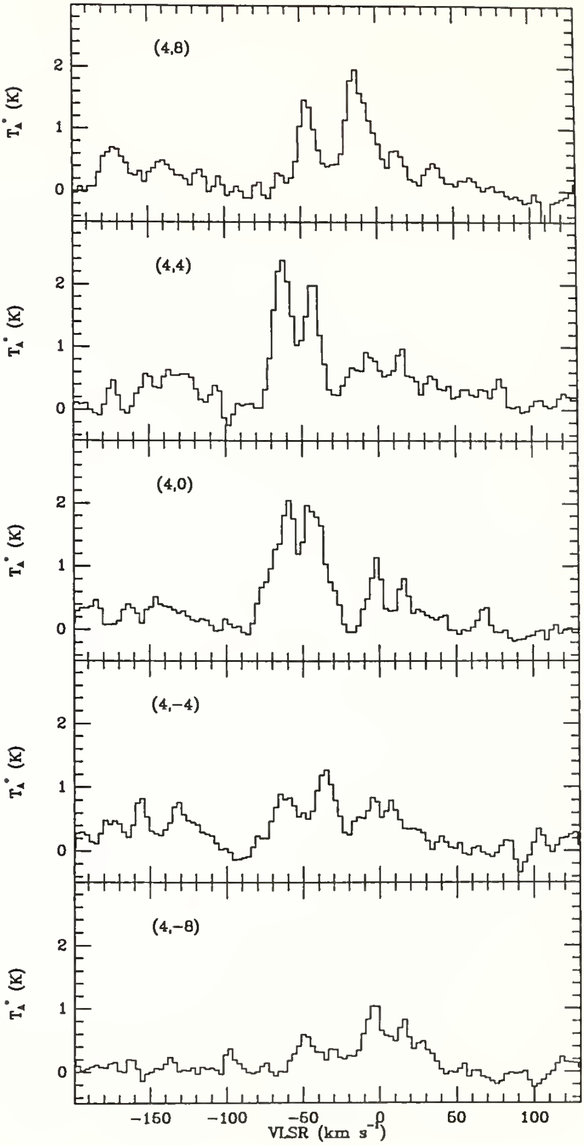
(4,8)
(4,4)
(4,0)
(4,−4)
(4,−8)
T*A (K)
0
1
2
−150
−100
−50
0
50
100
VLSR (km s⁻¹)

Figure 6.12. - The -45 km s^{-1} component of G359.4-0.1. The contour map shows the ^{13}CO integrated intensity between -80 and -20 km s^{-1}. The contour levels are: 50, 55, 60, 65, and 70 K km s^{-1}. The dashed contour corresponds to 50 % of the peak intensity. The data taken with 4′ spacing suggest the (4,1) position to be the peak of the emission.

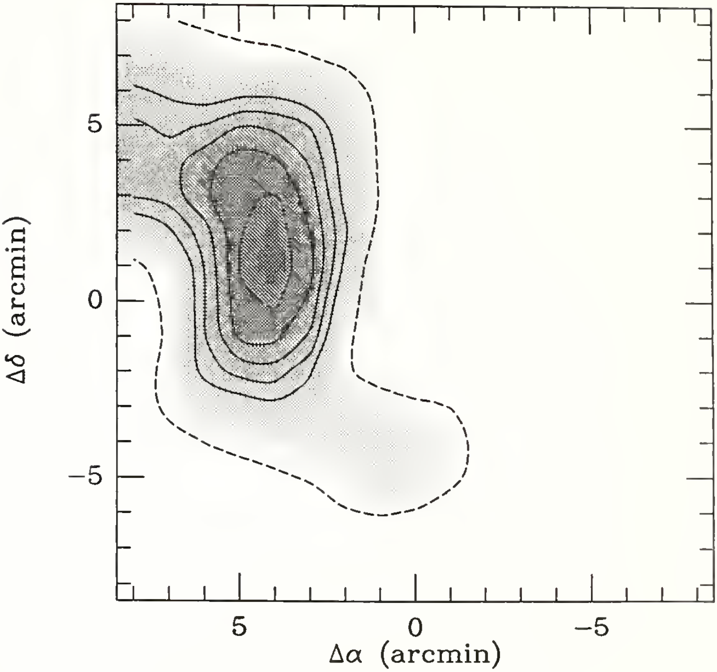
Δδ (arcmin)
5
0
−5
5
0
−5
Δα (arcmin)

Figure 6.13. - $C^{18}O$, ^{13}CO, and ^{12}CO spectra at the (4,2) position in G359.4-0.1. The -52 km s^{-1} dip in ^{12}CO and ^{13}CO spectra is most likely produced by foreground absorption because its velocity differs from the peak of the $C^{18}O$ emission. It is, therefore, plausible that ^{13}CO emission from the cloud is optically thin.

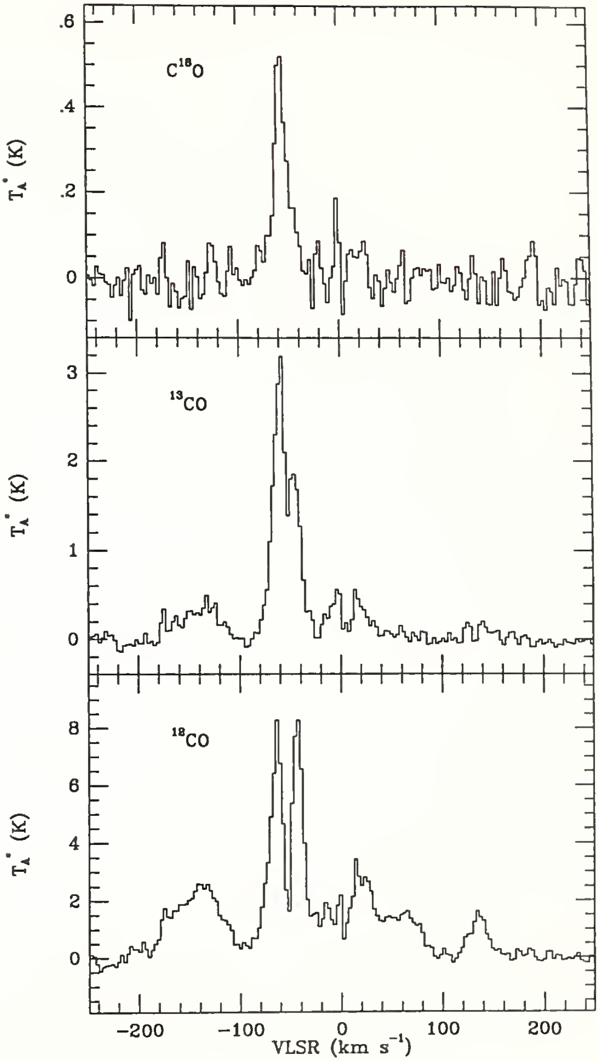
C^{18}O
^{13}CO
^{12}CO
T_A^* (K)
T_A^* (K)
T_A^* (K)
.6
.4
.2
0
3
2
1
0
8
6
4
2
0
−200
−100
0
100
200
VLSR (km s^{-1})

CHAPTER VII

CONCLUSION

The main goal of this dissertation, as stated in Chapter I, has been to develop a model of the Sgr B2 molecular cloud and to determine the physical conditions in this source. This has been done in Chapters II - V. Presenting the final model, however, has not been my exclusive goal. For sources as complicated as Sgr B2 it is important to determine a good strategy for dealing with the observational data. The number of free parameters is simply to large to adjust all of them simultaneously. The model, therefore, has to be created iteratively, starting with limited data set and large number of simplifications, and through a number of iterations it has to be refined to explain more and more aspects of the source structure. The refinement is done by incorporating more observational data and using more sophisticated methods of analysis. I consider the strategy of dealing with the problem to be equally important part of this project as the final conclusions about the cloud structure. I have presented the data in such a way that this strategy could be easily seen.

I started with the $J=1\rightarrow0$ transitions of ^{13}CO and $C^{18}O$. I choose $C^{18}O$ for determination of the density distribution inside the cloud, because the emission is optically thin and this transition is excited throughout the region, even at relatively low densities characteristic of the extended cloud. The form of the density distribution is the most important result of Chapter II. The absolute calibration of the derived density distribution involved significant uncertainties, because the H_2 column density was highly uncertain. It turned out that as a combined result of overestimating the $C^{18}O$ excitation temperature and fractional abundance the H_2 density derived in Chapter II is within the range given by Monte Carlo models. Studies of the continuum emission were a natural choice at this point of the calculations, because only the continuum emission can provide an independent estimate of the H_2 column density. The column density derived from simple analysis of Goldsmith, Snell, and Lis (1987) turned out to be entirely consistent with complete continuum radiation transfer models. The complete models, however, are clearly superior, as they allow for determination of the luminosities of the continuum sources and the dust temperature distribution. Careful comparison of flux densities in small and large beams gave an independent calibration of the density in the envelope. Having the density and dust temperature determined I went back to molecular emission, and after determining the kinetic temperature of the gas, I calculated the molecular emission from model clouds consistent with the continuum emission using the Monte Carlo method. This lead to independent determination of molecular abundances. The Monte Carlo models have problems with reproducing the observed intensity of the $J=2\rightarrow1$ transitions of $C^{18}O$ and ^{13}CO. This may indicate a clumpy structure of the envelope. The results of Monte Carlo models were compared with the preliminary analysis presented in Chapter II. The only incorrect conclusion of the simple analysis was the degree of saturation of ^{13}CO lines and the ^{13}CO to $C^{18}O$ abundance ratio. The Monte Carlo models suggest that constant excitation temperature analysis was fully justified and effective. In conclusion, the simple models give satisfactory predictions in both molecular line and continuum case. They involve, however, a large number of free parameters (excitation temperature and fractional abundance of $C^{18}O$, dust temperature and emissivity for the continuum emission). All these parameters can be independently determined in the complete models, provided that sufficient amount of observational data is available. This is the main distinction between the two approaches. Due to observing time limitations it is not always possible to obtain all the data necessary for the complete models to work.

The continuum models for Sgr B2 were effective, because they incorporated a number of observations covering wide wavelength range. Similar data base is not available for other Galactic Center clouds. The analysis of the type presented in Chapter III would not be, therefore, possible. Observations at one submillimeter or millimeter wavelength would be, however, sufficient to apply the simple analysis of the type presented by Goldsmith, Snell, and Lis (1987). It is, therefore, important to know that, at least in the case of Sgr B2, the two methods lead to similar answers.

The continuum and molecular line models lead to the following picture of Sgr B2. The total mass of the cloud is dominated by an envelope which can be represented by a two component structure. It consists of a constant density component with an H_2 density of 1800 - 3500 cm^{-3}, and a power law component with central density of 4 - 9 × 10^5 cm^{-3} and radial exponent of -2, extending inward to ~ 1.25 pc and outward to the outer radius of the envelope, ~ 22.5 pc. The total mass of the cloud is 5 - 10 × 10^6 $M_\odot$. The Sgr B2(M) continuum source has a luminosity of 1 - 2.3 × 10^7 $L_\odot$ and is situated in a dense core with diameter of 0.3 - 0.6 pc and peak H_2 density of 3 - 9 × 10^6 cm^{-3}. The core is located close to the center of the envelope. The total mass of the core is 1.5 - 4 × 10^4 $M_\odot$. The Sgr B2(N) continuum source is much less luminous (1 - 1.7 × 10^6 $L_\odot$, assuming the same grain properties in the two cores). The diameter of the northern core is 0.4 - 0.5 pc, and the peak H_2 density is 1.3 - 1.7 × 10^7 cm^{-3}. The total mass of the core is 0.7 - 1 × 10^5 $M_\odot$. The observed change in the middle-to-north peak flux ratio is primarily a result of the difference in luminosity. The peak H_2 column density at the position of the middle source is 2.6 × 10^{24} cm^{-2} in a 23″ beam, 1.4 - 1.8 × 10^{24} cm^{-2} in a 45″ beam, and 1.1 - 1.5 × 10^{24} in a 60″ beam. The average H_2 density is 2100 - 4300 cm^{-3}. The virial mass of the cloud is 9 - 16 × 10^6 $M_\odot$, suggesting that Sgr B2 is close to virial equilibrium.

A separate part of this project was to compare Sgr B2 with other Galactic Center clouds. In order to do this I choose two fields centered on the G1.1-0.1 and G359.4-0.1 continuum sources. These fields were observed in the $J = 1 \rightarrow 0$ transition of ^{13}CO. The molecular clouds observed there seem to be distinctively different from Sgr B2. They all have similar sizes of ~ 40 pc, mean H_2 density of 1000 - 1500 cm^{-3} (a factor of 3 lower than Sgr B2), peak H_2 column densities of $1.3 - 1.8 \times 10^{23}$ cm^{-2} in a 45″ beam (a factor of 10 lower than Sgr B2), and masses of $2 - 3 \times 10^6$ $M_\odot$ (a factor of 3 lower than Sgr B2). The gas with H_2 density of $4 - 6 \times 10^4$ cm^{-3} present over inner several pc of Sgr B2 seems to be absent in other Galactic Center clouds. The far-infrared optical depth is also reported to be low, suggesting that very dense cores with embedded continuum sources similar to Sgr B2(M) and (N) are absent in these objects. The galactocentric distances of the clouds observed are 90 -160 pc, similar to that of Sgr B2. The disruptive tidal forces acting on all the clouds should have similar magnitude. Sgr B2, however, seems to be much closer to the tidally limited density. It is, therefore, much more likely to be gravitationally bound than the smaller Galactic Center clouds. The discrepancy between the molecular and virial masses is also much more prominent for the smaller clouds than it is for Sgr B2.

The smaller Galactic Center clouds, although not as massive and dense as Sgr B2, are distinctively different from the disk clouds in terms of line width and average density. The high density seems to be a common characteristic of all Galactic Center GMCs. It may simply reflect the higher density of the interstellar medium from which the clouds formed. Whether the clouds are gravitationally bound remains an open issue. The discrepancy between molecular and virial masses seem significant for the smaller clouds, suggesting that they may be indeed in the process of disruption. Sgr B2 is much closer to virial equilibrium. It may be the only bound object in my sample.

There are many ways in which this project may be followed up. Several aspects of the continuum models of Sgr B2 may be answered by future observations. 1.4 mm interferometric data from OVRO will help to determine the core diameters. The 100 μ and 50 μ data from KAO will finally resolve the issue of foreground extinction at the position of the northern source which should become important at these wavelengths. Distribution of HC_3N and related issues of abundance variations and clumpiness of the core may also be answered by interferometric observations. In the case of other Galactic Center clouds the situation seems even more open to future research. High angular resolution ^{13}CO data from SEST will allow for density distribution determination. Far-infrared and submillimeter continuum data would be extremely helpful for constructing models of the dust emission. Combining molecular line and continuum data one can can again determine molecular abundances. Obtaining equally complete set of data as that presented for Sgr B2 for many Galactic Center clouds will take a lot of effort. The model of Sgr B2 suggest, however, that much can be learned about other Galactic Center GMCs applying simple methods of analysis to a limited set of *carefully selected* data.

APPENDIX

DETAILS OF THE DUST MODEL COMPUTATIONS

Because the dust emission is almost entirely confined to the northern and middle cores and the contribution from the envelope is rather insignificant especially at short wavelengths, it seemed reasonable to treat the northern and middle sources independently, without any interaction between the two sources. The problem has been, therefore, reduced to two spherically symmetric models. I assumed that the middle source is situated at the center of the molecular cloud defined by $C^{18}O$ emission. I used the functional form of the density distribution in the envelope derived in Chapter II, scaled by the factor, X. The core itself was assumed to be a Gaussian with central density, d_{in}, and FWHM size, r_{in}. The cloud was divided into 200 shells with logarithmic spacing, and the radiation transfer computations were performed at the IBM 3091D vector computer at Cornell University. For several values of r_{in} other input parameters (d_{in}, X, L, τ_{100}) were varied until the required flux distribution was obtained. The output of the main radiation transfer code in the form of the specific intensity at 200 impact parameters and 26 selected wavelengths was used by another code performing the beam convolution. The radial integral in the flux computations was done using Romberg method. For the final models including both sources the integral was evaluated at 20 different angles. The method was tested for Gaussian intensity distributions, where the integral can be evaluated analytically, and has proven to be very accurate even for small source sizes compared to the telescope beam. Although the flux density in a small beam (~ 20″) is entirely dominated by the core, the contribution from the envelope in a 30″ beam becomes important enough, so that models with different envelope densities can be distinguished based on the flux ratio in the two beams. The scaling factor of the density in the envelope can be, therefore, determined. One should keep in mind, however, that the results may be sensitive to the assumed form of the density distribution in the core.

Having the parameter of the middle core and the envelope determined, I started calculations for the northern core. In order to keep the same radial grid as for used the middle core, I assumed the density distribution to be a Gaussian plus a constant density envelope with an H_2 density of ~ 100 cm^{-3}, and the same outer radius of 22.5 pc as used in the middle core models. One could think that an envelope with an H_2 density of ~ 2000 - 3000 cm^{-3}, corresponding to the constant density component in the middle source model, would seem more appropriate. This would lead, however, to underestimating the flux at the position from the northern source at short wavelengths, because the foreground extinction would be taken into account twice, in the model of the northern core, and in equation (3.3). If instead of using the equation (3.3), the total flux was simply calculated as a sum of the contributions from the two sources, the contribution from the envelope would be counted twice and the flux in large beams would be overestimated. Taking into account the fact that the luminosity of the middle source is much higher than that of the northern source, and that the dust temperature in the envelope is, therefore, determined by the middle source, it seems reasonable to model the northern core without envelope (the 100 cm^{-3} envelope does not affect the flux and is added *only* to keep the same radial grid for the two models), and to calculate the total flux according to the formula (3.3).

BIBLIOGRAPHY

Bahcall, J. N., and Tremaine, S. 1981, *Ap. J.*, **244**, 805.

Bally, J., Stark, A. A., Wilson, R. W., and Henkel, C. 1987, *Ap. J. Suppl.*, **65**, 13.

Bania, T. M., Stark, A. A., and Heiligman, G. M. 1986, *Ap. J.*, **307**, 350.

Benson, J. M., and Johnston, K. J. 1984, *Ap. J.*, **277**, 181.

Bernes, C. 1979, *Astr. Ap.*, **73**, 67.

Black, J. H. 1987, in *Interstellar Processes*, D. J. Hollenbach, and H. A. Thronson, ed. (Dordrecht: Reidel), p. 731.

Blitz, L. 1980, in *Giant Molecular Clouds in the Galaxy*, P. M. Solomon, and M. G. Edmunds, ed. (Pergamon Press), p. 41.

Boland, W., and de Jong, T. 1982, *Astr. Ap.*, **134**, 87.

Boland, W., and de Jong, T. 1982, *Ap. J.*, **261**, 110.

Burke, J. R., and Hollenbach, D. J. 1983, *Ap. J.*, **265**, 223.

Carlstrom, J. E., and Vogel, S. N. 1989, *Ap. J.*, **337**, 408.

Gaume, R. A., and Claussen, M. J. 1988, preprint.

Dame, T. M., Elmegreen, R. S., Cohen, R. S., and Thaddeus, P. 1986, *Ap. J.*, **305**, 892.

Dame, T. M., Ungerechts, H., Cohen, R. S., de Geus, E. J., Grenier, I. A., May, J., Murphy, D. C., Nyman, L. A., and Thaddeus, P., 1987, *Ap. J.*, **322**, 706.

Dickman, R. L. 1978, *Ap. J. Suppl.*, **37**, 407.

Dickman, R. L., and Clemens, P. 1983, *Ap. J.*, **271**, 143.

Downes, D., Goss, W.M., Schwartz, U. J., and Wouterloot, J. G. A. 1976, *Astr. Ap. Suppl.*, **35**, 1.

Downes, D., Maxwell, A., and Rinehart, R. 1970, *Ap. J. (Letters)*, **161**, L123.

Draine, B. T., and Lee, H. M. 1984, *Ap. J.*, **285**, 89.

Egan, M. P., Leung, C. M., and Spagna, G. F. 1988, *Comput. Phys. Commun.*, **48**, 271.

Erickson, N. R. 1985, *IEEE Trans. Micr. Theor. Tech.*, **MTT33**, 1179.

Erickson, E. F., Caroff, L. J., Simpson, J. P., Strecker, D. W., and Goorvitch, D. 1977, *Ap. J.*, **216**, 404.

Garey, G. 1986, in *Submillimeter Astronomy*, P. Q. Shaur, and K. Kjät, ed. (Munich: European Southern), p 517.

Gatley, I., Becklin, E. E., Werner, M. W., and Harper, D. A. 1978, *Ap. J.*, **220**, 822.

Goldsmith, P. F., and Langer, W. D. 1978, *Ap. J.*, **222**, 881.

Goldsmith, P. F., Snell, R. L., Deguchi, S., Krotkov, R., and Linke, R.A. 1982, *Ap. J.*, **260**, 147.

Goldsmith, P. F., Krotkov, R., and Snell, R. L. 1985, *Ap. J.*, **299**, 405.

Goldsmith, P. F., Snell, R. L., Hasegawa, T., and Ukita, N. 1987, *Ap. J.*, **314**, 525.

Goldsmith, P. F., Snell, R. L., and Lis, D. C. 1987, *Ap. J.*, **313**, L5.

Gordon, G. 1988, *Ap. J.*, **331**, 509.

Heiligman, G. M. 1987, *Ap. J.*, **314**, 747.

Hartquist, T. W. 1977, *Ap. J. (Letters)*, **217**, L45.

Harvey, P. M., Campbell, M. F., and Hoffmann, W. F. 1977, *Ap. J.*, **211**, 786.

Irvine, W. M., Goldsmith, P. F., and Hjalmarson, A. 1987, in *Interstellar Processes*, D.J. Hollenbach, and H.A. Thronson, ed. (Dordrecht: Reidel), 561.

Kapitzky, J. E., and Dent, W. A. 1974, *Ap. J.*, **188**, 27.

Kazès, I., and Aubury, D. 1973, *Astr. Ap.*, **22**, 413.

Kerr, F., and Lynden-Bell D. 1986, *M.N.R.A.S.*, **221**, 1023.

Kwan, J., and Sanders, D. B. 1986, *Ap. J.*, **309**, 783.

Langer, W. D. 1976, *Ap. J.*, **210**, 328.

Langer, W. D. 1977, *Ap. J.*, **212**, L39.

Langer, W. D., Wilson, R. W., Goldsmith, P. F., and Beichman, C. A. 1989, *Ap. J.*, **337**, 355.

Lovas, F. J. 1986, *Journ. Phys. Chem. Ref. Data*, **15**, 251.

Little, A. G. 1974, in *Galactic Radio Astronomy, IAU Symp. No. 60*, F. J. Kerr, and S. C. Simonson, ed. (Dordrecht: Reidel), p. 491.

Morris, M., Turner, B. E., Palmer, P., and Zukerman, B. 1976, *Ap. J.*, **205**, 82.

Myers, P. C., and Goodman, A. A. 1988, *Ap. J.*, **329**, 392.

Oort, J. H. 1977, *Ann. Rev. Astr. Astrophys.*, **15**, 295.

Pankonin, V., and Downes, D. 1976, *Astr. Ap.*, **47**, 303.

Pauls, T. A., and Mazger, P. G. 1975, *Astr. Ap.*, **44**, 259.

Penzias, A. A., and Burres C. A. 1979, *Ann. Rev. Astr. Ap.*, **11**, 51.

Penzias, A. A. 1980, *Science*, **208**, 663.

Penzias, A. A. 1981, *Ap. J.*, **249**, 518.

Righini, G., Simon, M., and Joyce, R. R. 1977, *Ap. J.*, **207**, 119.

Scoville, N. Z., Solomon, P., and Penzias, A. A. 1975, *Ap. J.*, **201**, 352.

Scoville, N. Z., and Kwan, J. 1976, *Ap. J.*, **206**, 718.

Scoville, N. Z. 1980, in *Giant Molecular Clouds in the Galaxy*, P. M. Solomon, and M. G. Edmunds, ed. (Pergamon Press), p. 41.

Scoville, N. Z., Yun, M. S., Clemens, D. P., Sanders, D. B., and Waller, W. H. 1987, *Ap. J. Suppl.*, **63**, 821.

Solomon, P. M., and Sanders, D. B. 1980, in *Giant Molecular Clouds in the Galaxy*, P. M. Solomon, and M. G. Edmunds, ed. (Pergamon Press), p. 41.

Solomon, P. M., Rivolo, A. R., Barrett, J., and Yahil, A. 1987, *Ap. J.*, **319**, 730.

Stark, A. A., and Blitz, L. 1978, *Ap. J.*, **225**, L15.

Sutton, E. C., Blake, G. A., Masson, C. R., and Phillips, P. G. 1985, *Ap. J. Suppl.*, **58**, 341.

Swarup, G., Gopal-Krishna, and Sarma, N. V. G. 1974, in *Galactic Radio Astronomy, IAU Symp. No. 60*, F. J. Kerr, and S. C. Simonson, ed. (Dordrecht: Reidel), p. 491.

Tauber, J., Kwan, J. Y., Goldsmith, P. F., Snell, R.L., and Erickson, N. R. 1989, *Astr. J.*, **97**, 236.

Thronson, H. A., and Harper, D. A. 1986, *Ap. J.*, **300**, 396.

Watson, W. D., Anicich, V. G., and Huntress, W. T. 1976, *Ap. J.*, **205**, L165.

Werner, M. W., Neugebauer, G., Houck, J. R., and Hauser, M. G. 1978, *Icarus*, **35**, 289.

Westerbrook, W. E., Werner, M. W., Elias, J. H., Gezari, D.Y., Hauser, M. G., Lo, K. Y., Neugebauer, G. 1976, *Ap. J.*, **209**, 94.

Whiteoak, J.B., and Gardner, F.F. 1974, *Astr. Ap.*, **37**, 389.